

Luis Fernando Garcia Rodriguez

**OTIMIZAÇÃO TOPOLÓGICA DE ESCOAMENTO COMPRESSÍVEL
SUBSÔNICO CONSIDERANDO TURBULÊNCIA E GASES REAIS**

São Paulo
2022

Luis Fernando Garcia Rodriguez

**TOPOLOGY OPTIMIZATION OF COMPRESSIBLE SUBSONIC FLOW
CONSIDERING TURBULENCE AND REAL GASES**

Reviewed Version

Submitted in partial fulfilment of the requirements for obtaining the degree of Doctor of Science in Mechanical Engineering.

Concentration area: Control and Mechanical Automation Engineering (3152)

Advisor:
Prof. Dr. Emílio Carlos Nelli Silva

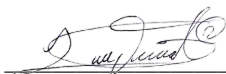
São Paulo
2022

Autorizo a reprodução e divulgação total ou parcial deste trabalho, por qualquer meio convencional ou eletrônico, para fins de estudo e pesquisa, desde que citada a fonte.

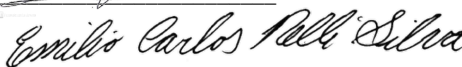
Este exemplar foi revisado e corrigido em relação à versão original, sob responsabilidade única do autor e com a anuência de seu orientador.

São Paulo, 20 de Dezembro de 2022

Assinatura do autor:



Assinatura do orientador:



Catálogo-na-publicação

Rodriguez, Luis Fernando Garcia
OTIMIZAÇÃO TOPOLÓGICA DE ESCOAMENTO COMPRESSÍVEL
SUBSÔNICO CONSIDERANDO TURBULÊNCIA E GASES REAIS / L. F. G.
Rodriguez -- versão corr. -- São Paulo, 2022.
140 p.

Tese (Doutorado) - Escola Politécnica da Universidade de São Paulo.
Departamento de Engenharia Mecatrônica e de Sistemas Mecânicos.

1.MÉTODOS TOPOLÓGICOS 2.OTIMIZAÇÃO MATEMÁTICA
3.TURBULÊNCIA 4.COMPRESSIBILIDADE DO FLUXO DOS FLUÍDOS
5.COMPRESSIBILIDADE DOS GASES I.Universidade de São Paulo. Escola
Politécnica. Departamento de Engenharia Mecatrônica e de Sistemas
Mecânicos II.t.

ABSTRACT

GARCIA RODRIGUEZ, L. F. **Topology optimization of compressible subsonic flow considering turbulence and real gases.** 2022. 65 p. Doctor of Science Thesis – Mechanical Engineering, University of Sao Paulo, Sao Paulo, 2022.

The optimization of compressible turbulent flow is fundamental to improve the performance of turbo-machinery and fluid devices used at cutting-edge energy transition technologies such as the carbon, capture and storage industry. From the different fluid flow optimization methods, the topology optimization offers a flexibility and robustness in the design as handles different objective functions and independence on initial domains that helps to create innovative and non-intuitive domains with splitters and fluid directors. The topology optimization method is performed by changing the permeability of the domain cells through the characterization of the fluid flow through CFD modelling, which is coupled to optimization methods based on the calculation of derivatives acquisition of a Lagrange system. To guarantee a successful topology optimization stable CFD models to be employed, which for compressible turbulent flow are available at subsonic regime according to the literature review. Therefore, the current research develops the topology optimization formulation for compressible turbulent subsonic flow, which demands the use of compressibility effects, rotational influence, and turbulence phenomenon besides the acquisition of the compressible adjoint system. The methodology considers the finite volume method, and the proposed formulation establishes the minimization of the energy dissipation subjected to the compressible Favre Averaged Navier-Stokes equations, the permeability of the volume cells and a volume constraint. The acquisition of the compressible adjoint system is studied simultaneously at two different approaches: via the continuous forward system and the discrete adjoint-automatic differentiator, the last adapted and coupled to finite volume method applications. Also, the influence of the integer design variables-based optimizer is included, which presents a considerable advantage over the common continuous design variables optimizers used. Finally, the optimization considering real gas modelling for compressible turbulent subsonic flow is presented, where the compressibility and temperature effects are embraced by the Peng-Robinson and the Sutherlands' law. Different tests are performed in channels and rotors that validate the mentioned hypothesis in 2D and 3D domains.

Keywords: Topology, Optimization, Turbulence, Compressible flow, Real gas, OpenFoam, perfect gas, FVM, FEM, FEniCS

RESUMO

GARCIA RODRIGUEZ, L. F. **Otimização topológica de escoamento compressível subsonico considerando turbulência e gases reais**. 2022. 65 p. Tese de Doutorado em Ciências – Engenharia Mecânica, Universidade de São Paulo, São Paulo, 2022.

A otimização do fluxo turbulento compressível é fundamental para melhorar o desempenho de turbo-máquinas e dispositivos de fluidos utilizados em tecnologias de transição energética de ponta, como a indústria de captura e armazenamento de CO₂. Dos diferentes métodos de otimização de fluxo de fluido, a otimização topológica oferece flexibilidade e robustez no desenho, pois lida com diferentes funções objetivo e independência em domínios iniciais que ajudam a criar domínios inovadores e não intuitivos com splitters e direcionadores de fluidos. O método de otimização topológica é realizado alterando a permeabilidade das células do domínio através da caracterização do escoamento do fluido através da modelagem CFD, que é acoplada a métodos de otimização baseados no cálculo de aquisição de derivadas de um sistema Lagrangiano. Para garantir uma otimização topológica bem sucedida, modelos CFD estáveis a serem empregados, que para escoamento turbulento compressível estão disponíveis em regime subsônico de acordo com a revisão da literatura. Portanto, a presente pesquisa desenvolve a formulação de otimização topológica para escoamento subsônico turbulento compressível, que demanda o uso de efeitos de compressibilidade, influência rotacional e fenômeno de turbulência, além da aquisição do sistema adjunto compressível. A metodologia considera o método dos volumes finitos e a formulação proposta estabelece a minimização da dissipação de energia submetida às equações compressíveis de Favre Averaged Navier-Stokes, a permeabilidade das células de volume e uma restrição de volume. A aquisição do sistema adjunto compressível é estudada simultaneamente em duas abordagens distintas: por meio do sistema direto contínuo e do diferenciador adjunto-automático discreto, este último adaptado e acoplado a aplicações do método de volumes finitos. Além disso, a influência do otimizador baseado em variáveis de projeto inteiras está incluída, o que apresenta uma vantagem considerável sobre os otimizadores de variáveis de projeto contínuas, comumente usadas. Por fim, é apresentada a otimização considerando uma modelagem de gás real para escoamento subsônico turbulento compressível, onde os efeitos da compressibilidade e da temperatura são englobados pela lei de Peng-Robinson e pela lei de Sutherland. Diferentes testes são realizados em canais e rotores que validam a hipótese mencionada nos domínios 2D e 3D.

Palavras-chave: Topologica, Otimização, Turbulência, Escoamento compressível, Gás real, Gás perfeito, OpenFoam, FEniCS, FVM, FEM

LIST OF FIGURES

Figure 1. Measures for reducing CO ₂ in the IEA (Blue Map scenario) (Kuckshinrichs 2015)	17
Figure 2. Principles of CCS technologies (Kuckshinrichs 2015)	21
Figure 3. Optimization approaches applied to the design of a straight-blade rotor: (a) parametric, (b) shape and (c) topology optimization	24
Figure 4. Topology optimization process	26
Figure 5. Adjoint derivation system stages (Funke 2012)	29
Figure 6. Research Methodology	32
Figure 7 Material distribution equation behaviour	42
Figure 8 Influence of the penalization term on the near-wall distance calculation	43
Figure 9 Topology optimization procedure	51
Figure 10. Triangular element interpolation (Sá and Silva 2016)	61
Figure 11. Material model behaviour	63
Figure 12. FEnics TopOpt Foam Interaction	67
Figure 13. FEniCS and OpenFOAM coupling	67
Figure 14. T.O. flowchart.	71
Figure 15. Progressive strategy	72
Figure 16. (a) Nozzle domain, and (b) mesh discretization	75
Figure 17. Optimized converging nozzle under laminar incompressible regime reported by (a) literature (Borrvall and Petersson 2003) and (b) the “adjointTopOptFoam” software	75
Figure 18. T.O. of Nozzle using (a) CDV and (b) IDV optimizers at incompressible turbulent flow	76
Figure 19. Optimized nozzle using the (a) CDV and (b) IDV approach	76
Figure 20. Nozzle primal fields comparison (a) baseline design (b) optimized topology. ($ u_i $ the velocity magnitude, p is the pressure and v_t is the turbulent viscosity field)	77
Figure 21. (a) Double channel domain and (b) mesh discretization	78
Figure 22. Optimized double-channel topology layout under incompressible laminar regime reported by (a) literature (Borrvall and Petersson 2003) (b) the adjointTopOptFOAM software	78
Figure 23. Double-channel optimization process by considering the (a) CDV and (b) IDV approach	79

Figure 24. Optimization of double channel case using the CDV optimizer and the continuation method	80
Figure 25 Optimized double-channel topology considering the (a) CDV and (b) IDV approach	81
Figure 26. Optimized double-channel characteristic flow fields of the (a) CDV and (b) IDV approaches	81
Figure 27. (a) Pipe-bend Domain, (b) mesh discretization and (c) CFD modelling of initial domain	82
Figure 28. Topology layouts evolution of the pipe-bend case under incompressible turbulent regime using the (a) CDV and (b) IDV optimizers	83
Figure 29. Influence of k_u value at (a) CDV and (b) IDV optimizer.....	84
Figure 30. Primal fields comparison between (a) optimized IDV and (b) baseline design. ($ ui $ the velocity magnitude, p is the pressure and v_t is the turbulent viscosity field	84
Figure 31. (a) 2D pipe-joint domain and (b) mesh discretization	85
Figure 32. 2D pipe-joint optimization layout process by considering the (a) CDV and (b) IDV approach.....	86
Figure 33. Optimized 2D pipe-joint topology using the (a) CDV and (b) IDV approach.....	87
Figure 34. Vorticity fields of optimized 2D pipe-joint under the (a) IDV and (b) CDV approach.....	87
Figure 35. (a) 3D initial domain, (b) mesh discretization and (c) fluid flow streamlines	88
Figure 36. (a)Optimized container by using IDV optimizer at low Re_{inlet} and (b) convergence curve	88
Figure 37. Optimized container case by using the (a)CDV and (b) IDV optimizers	89
Figure 38. Optimized container under the IDV approach: (a) side and (b) superior view	89
Figure 39. Vorticity field of optimized container topology under (a) CDV and (b) IDV approaches.	90
Figure 40. 3D Baseline design (a) velocity and (b) vorticity streamlines	90
Figure 41. (a) Straight blade rotor, (b) cavity domain considered and (c) mesh (Kim et al. 2014).....	91
Figure 42. Topology optimization of straight blade rotor under incompressible turbulent regime by using the Spalart-Allmaras turbulence model (Author).	91
Figure 43. Topology optimization of rotational turbulent flow, Case 1 (a, b, c) and Case 2 (d, e, f).....	92
Figure 44. Mesh discretization of nozzle domain at compressible regime	95

Figure 45. (a) Optimized nozzle topology layout (black = solid, white = fluid) under laminar compressible flow and (b) convergence curve.	95
Figure 46. Velocity, pressure and Mach number fields of the (a) optimized nozzle and (b) baseline case under compressible low Re regime.	95
Figure 47. (a) Optimized convergence nozzle without considering a turbulence model, and (b) convergence curve	96
Figure 48. (a) Optimized converging nozzle considering the SA turbulence model, (b) convergence curve and (c) comparison of the SA turbulence model (black continuous line) to the turbulence approximation (blue-dotted line)	96
Figure 49. Velocity and vorticity fields of the optimized nozzle under compressible turbulent flow considering (a) the non-turbulence model and (b) the S-A turbulence model	97
Figure 50. (a) Mach number, (b) density and (c) temperature fields across optimized converging nozzle at compressible turbulent regime	98
Figure 51. Optimized nozzle at turbulent regime $Re_{inlet} = 3 \times 10^3$ considering (a) incompressible, and (b) compressible flow	98
Figure 52 CFD of optimized nozzle designed for incompressible regime but tested at compressible turbulent fluid flow: (a) Mach, (b) density and (c) temperature fields.....	99
Figure 53. Optimized nozzle under $Re_{inlet} = 5 \times 10^3$	99
Figure 54. Characteristics flow fields of the optimized nozzle under a $Re_{inlet} = 5 \times 10^3$: (a) Mach, (b) density, and (c) temperature distributions.....	100
Figure 55. Pipe-bend mesh discretization using 2.75×10^4 cells in (a) uniform and (b) non-uniform distribution.....	100
Figure 56. Pipe-bend optimization layout considering (a) uniform and (b) non-uniform mesh distribution.....	101
Figure 57. Optimized pipe-bend topology in a non-uniform mesh adjusting sensitivity and employing the Helmholtz filter.....	102
Figure 58. Characteristic flow fields of the optimized pipe-bend case at compressible laminar regime	102
Figure 59. Pipe-bend topology layout at compressible turbulent regime approximation	103
Figure 60. (a) Optimized pipe-bend under the compressible turbulent approximation regime and (b) convergence curve.....	103
Figure 61. (a) Optimized pipe-bend topology layout considering the Spalart-Allmaras turbulence model, (b) convergence curve.....	104

Figure 62. Pipe-bend characteristic flow fields under compressible subsonic (a) turbulence approximation and (b) SA turbulence model	104
Figure 63. Pipe-bend baseline at compressible turbulent regime: (a) velocity streamlines and (b) Mach field.	105
Figure 64. Diffuser domain (a) dimensions and (b) boundaries.....	105
Figure 65. Optimized diffuser under laminar compressible flow: (a) topology layout and (b) convergence curve	106
Figure 66. CFD of original diffuser.....	106
Figure 67. The pressure difference between inlet/outlet boundaries of optimized diffuser	107
Figure 68. Characteristic fields distribution along (a) original and (b) optimized diffuser....	107
Figure 69. (a) Optimized diffuser for compressible turbulent subsonic flow and (b) convergence curve	108
Figure 70. Primal fields of the optimized diffuser at compressible turbulent subsonic conditions.	109
Figure 71. (a) 3D initial domain, and (b) mesh discretization (4323 tetrahedral elements)...	109
Figure 72. (a) Optimized 3D topology at turbulent subsonic compressible regime and (b) convergence curve	110
Figure 73. Characteristic fluid flow fields of optimized container: (a) Mach, (b) density and (c) temperature distribution	110
Figure 74. The optimized 3D pipe joint obtained considering incompressible regime.....	111
Figure 75. Optimized straight blade rotor cavity under compressible subsonic turbulent regime approximation.....	111
Figure 76. Topology optimization of straight blade rotor under turbulent compressible regime approximation: (a) 45° section and (b) complete rotor.	112
Figure 77. Topology layout of compressible turbulent rotor (a) 45° section and (b) complete rotor (Author)	112
Figure 78. (a) 3D initial domain, and (b) mesh discretization.....	113
Figure 79. (a) Optimized 3D straight blade rotor cavity at compressible turbulent subsonic regime (b) designed rotor and (d) convergence curve.....	113
Figure 80. (a) Optimized 3D straight blade rotor cavity at compressible turbulent subsonic regime (b) designed rotor and (d) convergence curve.....	114
Figure 81. (a) 3D initial domain, and (b) mesh discretization (2.4×10^4 tetrahedral elements)	114

Figure 82. (a) Optimized 3D straight blade rotor cavity at compressible turbulent subsonic regime (b) designed rotor, (c) convergence curve.....	115
Figure 83. Primal fields of optimized rotor under compressible turbulent subsonic regime: (a) pressure, (b) density and (c) Mach number distribution.....	115
Figure 84. Optimized 3D rotor under different volume constraints: (a) 0.3, (b) 0.5 and (c) 0.7	115
Figure 85. Optimized converging nozzle under compressible turbulent subsonic regime and real gas (b) convergence curve.	116
Figure 86. Velocity field comparison between the optimized converging nozzle designed at compressible subsonic turbulent regime considering perfect and real gas modelling.	117
Figure 87. Characteristic flow fields of optimized nozzle designed for compressible turbulent subsonic regime considering real gas modelling: (a) Mach, (b) density and (c) temperature distribution.....	118
Figure 88. (a) 2D pipe-joint domain and its (b) mesh discretization.....	118
Figure 89. Optimized 2D pipe-joint domain under compressible turbulent regime considering (a) real (b) perfect gas modelling	119
Figure 90. Optimized 2D pipe-joint topology layout comparison between the perfect and real gas modelling.....	119
Figure 91. Primal fields of optimized 2D pipe-joint under compressible subsonic turbulent regime considering the (a) perfect gas and (b) real gas state equation.....	120
Figure 92. Optimized rotor under compressible turbulent subsonic regime using real gas modelling (b) convergence curve.	121
Figure 93. Flow characteristics of optimized rotor cavity under (a) perfect and (b) real gas modelling.....	121
Figure 94. Sensitivity analysis of the nozzle case: (a) velocity streamlines and (b) sensitivity field.....	134
Figure 95. Sensitivity validation graph of continuous adjoint approach.....	135
Figure 96. Analysis of the converging nozzle case: (a) sensitivity and (b) velocity gradient field.....	136
Figure 97. Converging nozzle sensitivity field under the real gas assumption	137

LIST OF TABLES

Table 1. Boundary conditions at incompressible laminar regime	74
Table 2. Primal boundary conditions at the incompressible turbulent regime	74
Table 3. Adjoint boundary conditions at incompressible turbulent regime (Munday 2010; Papoutsis-Kiachagias and Giannakoglou 2016).	74
Table 4. Calibrated T.O. parameters at the nozzle case for the CDV and IDV approaches.	75
Table 5. Nozzle IDV and CDV objective functions at incompressible turbulent flow.	77
Table 6. Calibrated T.O. parameters at the double-channel case for the CDV and IDV approaches	79
Table 7. Double-channel objective function value.	82
Table 8. Calibrated T.O. parameters at the pipe-bend case.	83
Table 9. Comparison of the objective function values for the pipe-bend examples.	84
Table 10. Calibrated T.O. parameters at the 2D pipe-joint case for the CDV and IDV approaches	85
Table 11. 2D pipe-joint objective function value.	86
Table 12. Selected optimization parameters at the 3D domain for CDV and IDV approaches	88
Table 13. Objective function comparison between the baseline and optimized container passage by considering incompressible turbulent regime.	90
Table 14. Optimization parameters at cavity straight blade rotor under incompressible turbulent flow.	92
Table 15. Thermophysical fluid properties.	93
Table 16. Primal boundary conditions used at compressible regime with low-Re.	94
Table 17. Boundary conditions at compressible turbulent regime.	94
Table 18. Optimization parameters for compressible turbulent flow.	110
Table 19. Optimization continuation method used in the fluid interchange case	110
Table 20. Optimization parameters for compressible turbulent flow.	113
Table 21. Optimization parameters for compressible turbulent flow.	114
Table 22. Cross-check validation between perfect and real gas assumption at optimized nozzle under compressible turbulent regime	117
Table 23. 2D pipe-joint optimization parameters for compressible turbulent subsonic flow.	118
Table 24. Sensitivity analysis of the continuous adjoint approach.	135
Table 25. Sensitivity analysis – fluid domain.	136

Table 26. Converging nozzle sensitivity validation under compressible turbulent subsonic regime and real gas behaviour	137
--	-----

LIST OF SYMBOLS

u	Primal velocity field
p	Primal pressure field
ρ	Fluid density
τ_{ij}	Viscous stress
S_{ij}^*	Instantaneous strain rate tensor
μ	Dynamic viscosity
\bar{u}_i	Primal average velocity field
\bar{p}	Primal average pressure field
u'	Fluctuating velocity
p'	Fluctuating pressure
$\overline{u_i' u_j'}$	Reynolds stress tensor
ω	Angular velocity
r	Radius
h	Enthalpy
δ_{ij}	Kronecker Delta
q_j	Heat flux
C_p	Specific heat at constant pressure
Pr	The Prandtl number
T	Primal Temperature Field
$\tilde{\phi}$	Mass weighted averaging
ϕ''	Doubly primed fluctuating quantity
\tilde{H}	Mass weighted averaged total enthalpy
\tilde{E}	Mass weighted averaged total energy
$\overline{\sigma_{ij}}$	Viscous stress tensor
S	Sutherland temperature coefficient
γ	Heat capacity
k	Turbulent kinetic energy
ϕ_c	Critical properties
w	Acentric factor
$\tilde{\mu}_t$	Turbulent eddy viscosity

α_t	Thermal diffusivity
$\overline{c_p \rho u_j'' T''}$	Turbulent heat flux
Pr_t	Prandtl turbulent
$\hat{\nu}$	Viscosity-like variable
$ W_{ij} $	Vorticity magnitude
Δ	Nearest wall distance
\dot{m}	Mass flux
F	Objective function
Γ	Boundary
Ω	Domain
k	Material distribution function
\bar{k}	Maximum material distribution value
\underline{k}	Minimum material distribution value
α	Design variable
q_ϕ	Material distribution stabilizer
R^ϕ	Constraint
\bar{V}_{frac}	Volume constraint
V_{tar}	Target volume
L	Lagrange function
λ_k	Lagrange multipliers
w_f	Scalar weight factor
L_{aug}	Augmented Lagrange function
q	Adjoint pressure field
v_i	Adjoint velocity field
T_a	Adjoint Temperature field
$\tilde{\nu}_a$	Adjoint viscosity-like variable
Δ_a	Adjoint near wall distance value
δ	Total derivative
∂	Partial derivative
c_{w1}	Wall destruction SA constant term
f_w	Control function term
k	Von Karman constant term
σ	SA turbulence model constant term

c_{b2}	SA turbulence model constant term
c_{v1}	SA turbulence model constant term
χ	Auxiliary to kinematic turbulent viscosity ratio
f_{v2}	SA turbulence model function term
g	Control function term
r	Control function term ratio
\hat{v}	Auxiliary turbulent viscosity
μ_t	Turbulent dynamic viscosity

ABBREVIATIONS

CO ₂	Carbon dioxide
CCS	Carbon capture and storage
IGCC	Integrated coal gasification combined cycle
CFD	Computational fluid dynamics
SC-CO ₂	Supercritical CO ₂
Ma	Mach number
T.O.	Topology optimization
SA	Spalart-Allmaras
CDV	Continuous design variables
IDV	Integer design variables
PDE	Partial differential equation
FD	Finite difference
RANS	Reynolds Averaged Navier-Stokes
FANS	Favre Averaged Navier-Stokes
MMA	Method of moving asymptotes
TOBS	Topology optimization of binary structures
FEM	Finite element method
FVM	Finite volume method
iPOPT	Interior point optimizer
LBB	Ladyzhenskaya–Babuška–Brezzi boundary condition

CONTENTS

1. INTRODUCTION.....	17
1.1. OPTIMIZATION OF FLUID FLOW	23
1.2. TOPOLOGY OPTIMIZATION METHOD FOR FLUID FLOW DESIGN.....	25
1.3. THE CONTINUOUS AND DISCRETE ADJOINT APPROACHES	29
1.4. MOTIVATION	31
1.5. OBJECTIVES	32
1.6. METHODOLOGY	32
1.7. SCIENTIFIC CONTRIBUTIONS	33
1.8. DOCUMENT OUTLINE.....	34
2. CONTINUOUS ADJOINT APPROACH USED AT INCOMPRESSIBLE TURBULENT FLOW OPTIMIZATION	35
2.1. EQUILIBRIUM EQUATIONS OF INCOMPRESSIBLE TURBULENT FLOW	37
2.2. TURBULENCE MODEL TREATMENT	37
2.2.1. Spalart-Allmaras Turbulence Model	38
2.2.2. Near-Wall Distance Calculation.....	39
2.3. FLUID FLOW MODELLING	39
2.3.1. The Finite Volume Method Used At The OpenFoam Software.....	39
2.3.2. Resolution of the Algebraic State Equations.....	40
2.4. TOPOLOGY OPTIMIZATION FORMULATION.....	41
2.4.1. Permeability Design Variable α	42
2.4.2. Modified Equilibrium Equations of Incompressible Turbulent Flow	42
2.4.3. Topology Optimization Problem Definition.....	44
2.5. SENSITIVITY CALCULATION.....	45
2.5.1. Field Adjoint Equations.....	45
2.5.2. Objective Function Sensitivity Calculation.....	47
2.6. OPTIMIZATION ALGORITHM	48
2.6.1. Continuous Design Variable Based Optimizer: MMA	48
2.6.2. Integer Design Variable Optimizer: TOBS	49
2.7. NUMERICAL IMPLEMENTATION	50
3. DISCRETE ADJOINT APPROACH USED AT COMPRESSIBLE SUBSONIC TURBULENT FLOW OPTIMIZATION	52

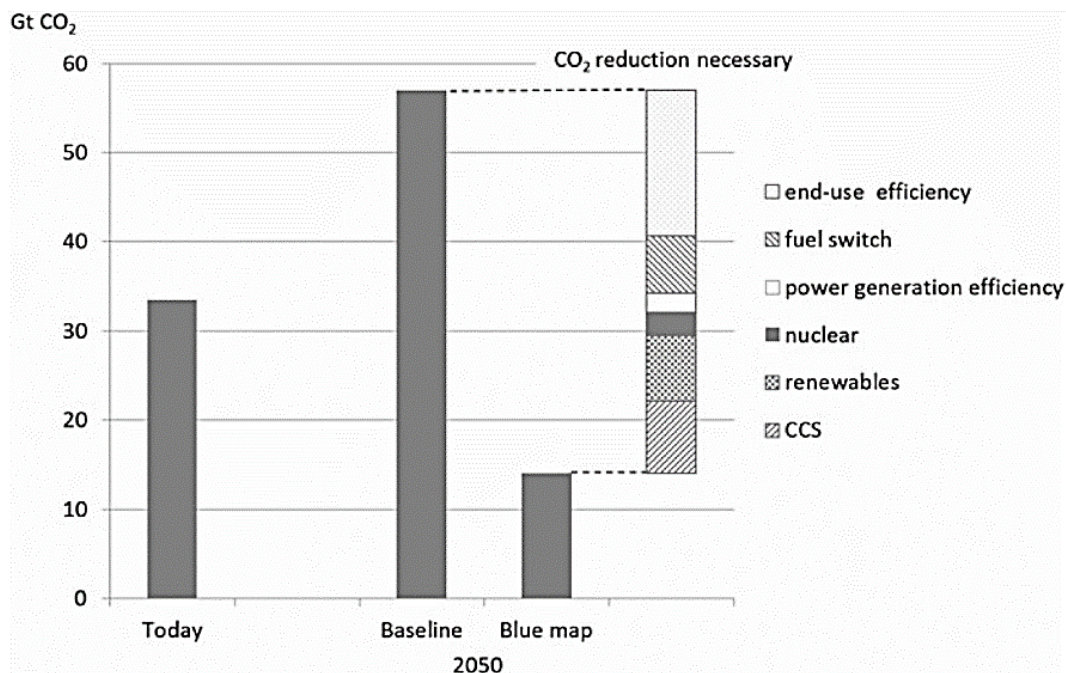
3.1.	EQUATION OF STATE.....	53
3.2.	EQUILIBRIUM EQUATIONS OF COMPRESSIBLE TURBULENT FLOW	55
3.3.	TURBULENCE MODELLING TREATMENT	57
3.3.1.	Compressible Spalart-Allmaras Turbulence Model	57
3.3.2.	Compressible Wray-Agarwal Turbulence Model.....	58
3.4.	FLUID FLOW MODELLING	60
3.4.1.	The Finite Element Method Used In The FEniCS Software	61
3.5.	TOPOLOGY OPTIMIZATION FORMULATION.....	62
3.5.1.	Permeability Design Variable (α).....	62
3.5.2.	Modified Equilibrium Equations of Compressible Turbulent Flow.....	63
3.5.3.	Topology Optimization Problem Definition.....	64
3.6.	NUMERICAL IMPLEMENTATION	65
3.6.1.	The Automatic Differentiator From FEniCS Software	65
3.6.2.	The FEniCS TopOpt Foam Software	66
3.6.3.	Weak Form Of The Equilibrium Equation Of Compressible Turbulent Flow...	68
3.6.4.	Helmholtz Pseudo-Density Filter	69
3.6.5.	Interfacing OpenFOAM with FEniCS/dolfin-adjoint	69
3.6.6.	Topology Optimization Loop	70
3.7.	PROGRESSIVE STRATEGY	71
4.	RESULTS.....	73
4.1.	TOPOLOGY OPTIMIZATION OF INCOMPRESSIBLE FLOW CONSIDERING THE CONTINUOUS ADJOINT APPROACH	73
4.1.1.	Converging Nozzle Example.....	74
4.1.2.	Double-Channel Example.....	78
4.1.3.	Pipe-bend Example.....	82
4.1.4.	2D pipe-joint Example	85
4.1.5.	3D Pipe Joint Example	87
4.1.6.	Rotor Example.....	91
4.2.	TOPOLOGY OPTIMIZATION OF COMPRESSIBLE TURBULENT SUBSONIC FLOW FOR AN IDEAL PERFECT GAS CONSIDERING THE DISCRETE ADJOINT APPROACH	93
4.2.1.	Converging Nozzle Example.....	94
4.2.2.	Pipe-bend Example.....	100

4.2.3.	Diffuser.....	105
4.2.4.	3D pipe-joint.....	109
4.2.5.	Rotor Example.....	111
4.3.	TOPOLOGY OPTIMIZATION OF COMPRESSIBLE TURBULENT SUBSONIC REGIME FOR REAL GAS CONSIDERING THE DISCRETE ADJOINT APPROACH	116
4.3.1.	Converging Nozzle Example.....	116
4.3.2.	2D pipe-joint Example	118
4.3.3.	Rotor Example.....	120
5.	CONCLUSIONS	123
6.	BIBLIOGRAPHY	126
7.	APPENDIX	134
7.1.	SENSITIVITY VALIDATION OF THE CONTINUOUS ADJOINT APPROACH 134	
7.2.	SENSITIVITY VALIDATION OF THE DISCRETE ADJOINT APPROACH....	136
7.2.1.	Sensitivity validation considering real gas modelling.....	137
7.3.	DERIVATION OF WEAK FORM EQUATIONS USED AT THE DISCRETE ADJOINT APPROACH	138

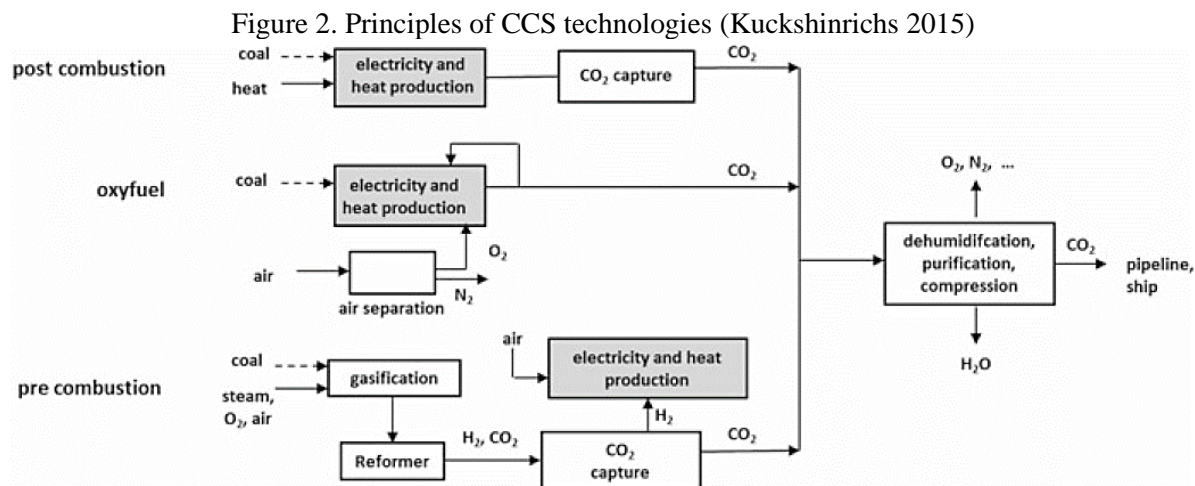
1. INTRODUCTION

Global warming has increased exponentially during the last decades, mainly due to uncontrolled CO₂ emissions (e.g. in 2010, 40% of total emissions were by fossil-fired power plants) affecting directly the greenhouse effect. Kuckshinrichs (2015) shows that CO₂ emissions must be reduced by at least 50% up to the year 2050 to limit the temperature increase by 2-3°C worldwide. To do so, the Carbon Capture and Storage (CCS) technology could reduce around 26% of the total wide range of CO₂ measures, making it the large responsible of CO₂ reduction technology (Figure 1).

Figure 1. Measures for reducing CO₂ in the IEA (Blue Map scenario) (Kuckshinrichs 2015)



The CCS technology consists of capture CO₂ emissions, applying chemical processes of gas purification and reusing them for industrial application, e.g. extraction of gases, or storing them at geological underground formations, avoiding its direct release into the atmosphere and diminishing the greenhouse effect. All technical process routes used at CCS converge in the compression stage (Figure 2), which is responsible for up to 50% performance from the whole CCS process (e.g. oxyfuel process), supporting its optimization for an efficient CCS technology.



The main challenges presented in the compression stage are related to CO₂ quantification properties, integration of CO₂ capture and compression, and systems-components design for efficient supercritical CO₂ transport (Jensen et al. 2011). The CO₂ compressor power required for an integrated coal gasification combined cycle (IGCC) power plant is approximately 5% of the plant rating (Systems 2009), therefore, any improvement on the CO₂ compressors has a significant economic impact.

The supercritical CO₂ compressor efficiency can state between 65% and 80% (Monje et al. 2014), which fundaments their study and improvement in developing elaborated thermodynamics relations, experiments (Bae et al. 2016; Kim et al. 2014; Park et al. 2022), one-dimensional models (Monje et al. 2014) and computational fluid dynamics (CFD). The one-dimensional model provides a detailed tentative design of the compressor elements by solving the thermo-fluid dynamics of the solid/fluid interfaces comprised by the turbomachinery; however, uncertainties have been found when supercritical CO₂ (SC-CO₂) is analyzed (Monge 2014) due to its unconventional behaviour in the critical point and the lack of experimental information. The CFD approaches reveal similar information as the 1D models, however, complements its use on the clearance gaps analysis, the viscosity effects near the walls, tackles simultaneous modelling between components, e.g. diffuser-impeller, presents better agreement at lower speeds, and accurateness in the surge line (Monge 2014). Also, studies related to real gas influence on supercritical CO₂ compressors (Baltadjiev et al. 2015) have shown significant differences in the ideal gas conditions, such as reductions of 9% in the choke margin of the stage compressor and condensation near the critical point operating conditions, which basis the importance of study real gas influence in the design of the components. As seen, theoretical studies complemented by experiments have answered queries

about the fluid flow performance of SC-CO₂ compressors during the last decades, but the analysis phases challenges related to fluid flow modelling, expensive limited experimental tests, elaborated thermodynamic relations and high dependences on the supercritical conditions. Also, the analysis started in the compressor rotor as the first component responsible to increase the kinetic energy from the shaft and delivering it to the stator which converts the kinetic energy into pressure (Monge 2014). Therefore, the rotor analysis is a fundamental start to tackling the performance of the compression stage of SC-CO₂.

The CFD modelling of a CO₂ compressor rotor near the critical point is a challenging task as is sensible to vary its phase and is generally coupled with uncertainties to experimental results (Pecnik, Rene and Colonna 2011; Rinaldi et al. 2013; Takagi et al. 2016), e.g. 25% differences in the overall pressure ratio. These uncertainties are mainly found due to the complexity of the SC-CO₂ modelling, as the fluid faces large velocities, compressibility effects, and large temperature gradients are summarized in large Mach numbers flows (transonic and supersonic regimes), which are unstable to model due to the shock waves and real gases behaviour (Pecnik, Rene and Colonna 2011; Rinaldi et al. 2013; Takagi et al. 2016). Nevertheless, under specific operating conditions, such as operating distant from the critical point (Kim et al. 2014; Takagi et al. 2016) or under maximum Mach numbers of 0.8 (Baltadjiev et al. 2015), some similarities can be found between the CFD modelling and the experimental tests. As the fluid flow modelling of a SC-CO₂ compressor is still under research, the topology optimization (T.O.) should consider a progressive conservative strategy based on a stabilized CFD compressible regime. By definition, the compressible fluid flow is considered when the variations of the density field across the domain reach a difference of at least 3% along the domain (Fox et al. 2015), and three main regimes can be classified as compressible flow according to the Mach number: the subsonic ($0.3 < Ma < 0.7$), transonic ($0.7 < Ma < 1.2$) and supersonic ($Ma > 1.2$) regime mainly. Each regime varies principally by the fluid flow velocity (along with other fluid properties), meaning that relative low fluid velocities (subsonic regime) should present fewer instabilities than large velocities (supersonic regime). Different works fundament this statement (Dewar et al. 2019; Langlois et al. 2016; Petit and Nilsson 2013) and suggest also the analysis of ideal-perfect gases firstly before dealing with real gas behaviour (Cantwell 2018). Another challenge appears when the turbulence phenomenon is treated via CFD modelling, as Direct Numerical Simulations (DNS) show that the turbulence effects are not captured equally as the incompressible flow does, and modifications of the turbulences models for compressible regime should be considered (Grigoriev 2016). Literature has proved that the Favre Averaged Navier-

Stokes (FANS) equations (Wilcox 1993) have led to feasible results at compressible subsonic steady-state regime (Nikaido et al. 2015; Rahman and Mustapha 2015; Tüzüner et al. 2018), which gives a fluid flow settlement for the optimization.

1.1. OPTIMIZATION OF FLUID FLOW

The mentioned works have focused on the analysis and characterization of SC-CO₂ compressors by means of different strategies (CFD modelling, experimental tests, etc.); nevertheless, the optimization of such fluid flow devices requires techniques of algorithmic differentiation to reach an optimized point. In general, the optimization of fluid flows is affected by these variants: objective function (F), which depends on a vector of design variable α_n , and follows the next algorithm:

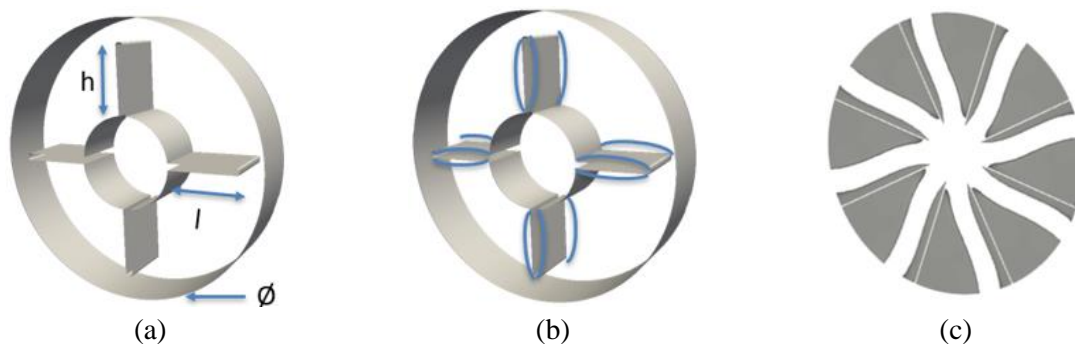
- Choose n distinct values of the depending parameter ($\alpha_1, \alpha_2, \dots, \alpha_n$), which satisfy the constraints of the T.O. formulation.
- Evaluate each objective function ($F(\alpha_1), F(\alpha_2) \dots F(\alpha_n)$) and choose a value α_j such that $F(\alpha_j) \leq F(\alpha_i)$ for $i = 1 \dots n$.

The coupling of flow control and CFD allows approaches with optimization algorithms to design and control fluid systems. This has been made for the last 40 years due to the development and implementation of efficient and robust algorithms for CFD and advances in the theory of partial differential equations and analytic algorithms (Gunzburger 2003), and despite that the simulation of fluid flows is not yet a routine endeavour. The structure of the flow control is composed of three main ingredients: objective (e.g. drag minimization), controls (shape walls) and constraints (type of flow), and they are put together in an optimization problem that seeks the optimal state (Gunzburger 2003).

The fluid flow optimization methods that applied the previous concept are the parametric, shape and topology optimization techniques (Figure 3). The parametric optimization varies the dimensions of an established domain in a simultaneous fluid flow evaluation until an optimized design is reached. The shape optimization consists on modifying the solid/fluid boundary through the Lagrange approach, which evolves the shape by gradually moving the boundary points. In this case, mesh morphing (e.g. deforming volumes, pseudo-solids and radial basis functions) is considered to vary the mesh nodes and avoid re-meshing or discontinuities in the computed objective and constraint functions (Haslinger and Mäkinen 2003). Finally, the

topology optimization technique is able to modify the entire domain by defining the permeability of each cell, which avoids remeshing the entire domain and innovative fluid flow passages (Sá and Silva 2016).

Figure 3. Optimization approaches applied to the design of a straight-blade rotor: (a) parametric, (b) shape and (c) topology optimization



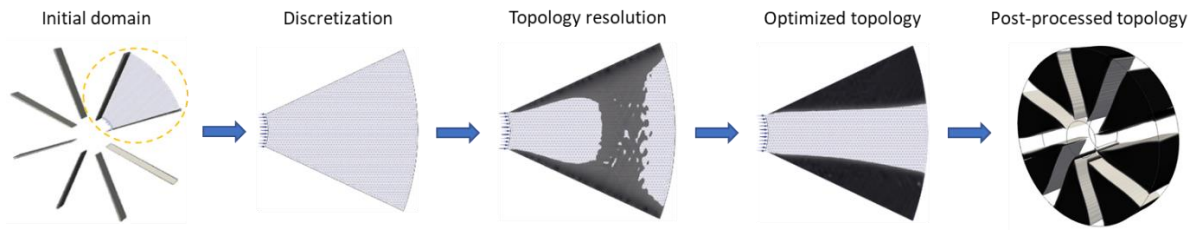
The optimization of compressible fluid flow is a challenging task as the difficulties of the optimization derivatives are related to its instabilities of fluid flow modelling: discretization to treat heat transfer processes, enthalpy variations, turbulence compressible phenomenon, compressibility factors and stable numerical schemes. The parametric optimization method has searched for solutions to optimize aerodynamics applications such as pulsating jets in unsteady compressible flow (Désidéri and Duvigneau 2019); Fosas De Pando et al. 2014), which has reduced the drag over a plate and the noise of an aerofoil through multi-objective functions and the multigradient descent algorithm. Turbomachinery has been also optimized by analysing the suction system of a reciprocating compressor for refrigeration systems (Ferreira et al. 2015), which treats the isentropic and volumetric efficiencies simultaneously. Nevertheless, the optimization on rotors has not been tackled widely and some limitations on the boundary size have been found. At shape optimization of compressible flow, aerodynamic applications have been widely studied, e.g. (Jameson et al. 1998) consider transonic regime and reduces the wing drag up to 8%. Feireisl (2003) determines a method for solving the optimized shape of profiles focusing on the viscous layer mainly in regions where the pressure distribution is given as a function of the fluid density. Kouhi Esfahani (2013) combines multi-objective function algorithms with mesh adaptation to improve the performance of aerofoils in transonic flow. Finally, (Kaźmierczak et al. 2018) propose the drag minimization of a theoretical 2D domain object by means of an approximated Stokes non-dimensional formulation. At turbomachinery applications, (Samad and Kim 2008) optimizes the fluid flow performance of a transonic axial compressor rotor by managing the total pressure and adiabatic efficiency as objective functions and modelling the fluid flow through the compressor annulus using the Reynolds-averaged

Navier–Stokes (RANS) equations. Nejadali (2021) focuses on the aerofoil compressors improvement by controlling the isothermal efficiency and the pressure coefficient as objective functions, which leads to trailing edge angles improvements of 3.17% compared to the reference case. Guo (2013) optimizes the return channel of a centrifugal compressor by means of the adjoint method derived for incompressible laminar flow and applied in a compressible turbulent regime. Iwakiri et al. (2020) attentions on the optimization of the scroll compressor of a turbocharger by means of the adjoint method allowing to reduce the recirculation flow rate and an overall efficiency improvement of 1.5%. As seen, the studies focused either on the aerofoil shape or the compressor components have been able to optimize the fluid flow performance by using both parametric and shape optimization methods, which are able to refine and make slight modifications on a preestablished domain accurately. Nevertheless, the improvements are limited to a preestablished design, maybe not made for the actual fluid flow to be transported, e.g. the transport of SC-CO₂, which might limit the accurate fluid flow path to be optimized, therefore, doubts arises from about the start domain: which blade design should be considered at first? How can we assure that the minimum space between the rotor blades is optimized based on the actual fluid flow to be transported? Should any splitter or bifurcation at the fluid flow passage be added to improve the fluid flow performance? These questions can be answered by including an innovative design technique at the first-stage design: the topology optimization method.

1.2. TOPOLOGY OPTIMIZATION METHOD FOR FLUID FLOW DESIGN

The topology optimization (T.O.) method applied to fluid flows consists on varying the permeability of a discretized cell domain in order to achieve the maximization/minimization of an established objective function (e.g. power dissipation, isentropic efficiency), which is subjected to a series of constraints that control the objective function optimization, e.g. the equations of state of the fluid flow, the permeability model, etc. The domain permeability is defined through an optimization process until a defined converge criterion is found, resulting in the optimized topology. Finally, a postprocessing is made to analyse the primal fields performance of the optimized topology. The whole process is shown sequentially at Figure 4.

Figure 4. Topology optimization process



The T.O. is a recent developed method: proposed in the year 2003 on the analysis of Stokes flow (Borrvall and Petersson 2003), and has been applied to incompressible fluid flow mainly. The challenges related to optimization of fluid flow depend not only on the fluid modelling, but also, in the implementation of the optimization algorithms, the treatment of the turbulence phenomenon, the optimizers behaviour and the boundaries between the solid/fluid definition. At following a summary of these fluid flow optimization challenges are presented.

In the laminar incompressible flow, (Borrvall and Petersson 2003) formulated the basis and methodology for T.O. of fluids in Stokes flow, which was extended to Navier-Stokes flow (Gersborg-Hansen et al. 2005), both considering the Brinkman-type model for fluid flow through porous media. Following this, (Pingen et al. 2007) considered the Lattice Boltzmann method (LBM) for modelling the fluid flow and were able to get the first three-dimensional result on a very coarse mesh. Then, the level set method for fluids, widely used at T.O. of solids, was considered by (Duan et al. 2008) at Stokes and Navier-Stokes flows, obtaining a smooth convergence of the T.O. problem.

Simultaneously, the incompressible turbulent regime has been studied through the Reynolds Averaged Navier-Stokes (RANS) modelling and the Boussinesq hypothesis to approximate the turbulence phenomenon. At first, (Othmer 2008) provides a turbulence regime approach for T.O. considering the continuous adjoint method and Finite Volume Method (FVM). However, the derivation of the turbulent viscosity is not performed, leading to the “frozen turbulence” approximation. Kontoleon et al. (2013) included the Spalart-Allmaras (SA) turbulence model to analyze incompressible turbulent internal flows, however, the near-wall distance value is approximately treated by using a high-refined mesh near the walls, which increases the computational cost and improves the accuracy in respect to the frozen turbulence approximation. Papoutsis-Kiachagias, et al. (2016) (Papoutsis-Kiachagias and Giannakoglou 2016) proposes using the stabilized Eikonal equation to approximate the near-wall distance

calculation of the SA turbulence model, and the results vary considerably from previous works. These assumptions of including the near-wall distance calculation for the SA turbulence model is tested at (Dilgen et al. 2018a; Papoutsis-Kiachagias and Giannakoglou 2016; Yoon 2016), however the analysis is made through the Hamilton-Jacobi equation resulting in a lower computational cost and accurate results too. Yoon (2016) through the discrete adjoint approach proposes an independence of the permeability constraint between the momentum and the modified Eikonal equation, to avoid inconsistencies between the selected values that define the fluid/solid domain. Finally, another turbulence models have been tested at incompressible turbulence regime, e.g. (Yoon 2020) uses a FEM-based software to analyze the $k - \epsilon$ turbulence model influence in 2D T.O. studies. In summary, these works gave us a better understanding of the challenges related with T.O. of turbulent flow, interpolation of turbulence variables and wall distance, and important discussions on the use of the frozen turbulence assumption.

Also, T.O. has been applied to the design of turbomachinery at laminar regime for both Newtonian and non-Newtonian fluids (Romero and Silva 2017; Romero and Silva 2014; Sá and Silva 2016) and 2D swirl models (Alonso et al. 2019). At first, (Romero and Silva 2014) design rotors for pumps through a T.O. formulation that minimizes the energy dissipation, the vorticity and torque as a multi-objective function. Sá, et al. (2018) (Sá et al. 2018) applied the concept to optimize the performance of small blood pumps and the method is validated successfully with experimental results. Then, (Sá et al. 2021b) optimize the performance of a rotor considering the SA incompressible turbulence model and studies the influence of a curvature correction in the turbulence treatment. Alonso (2019) (Alonso et al. 2019) considers the 2D swirl effect in the optimization of rotors minimizing the relative energy dissipation, which effects have been extended to Tesla turbine designs (Alonso and Silva 2022), non-Newtonian fluids (Alonso et al. 2020), influence of shear-stress at the blood damaging in small pumps (Alonso and Silva 2021) and the application of the Wray-Agarwal turbulence model in rotor design (Alonso et al. 2022).

Previous works were based on continuous design variables (CDV) optimizers, i.e. optimization algorithms that use permeability design values between $0 \leq \alpha \leq 1$, which are calibrated in an exhaustive process to diminish intermediate solid-fluid interfaces. These effect hinders the optimization of turbulent flow as clear information about the fluid walls is important for the accuracy of the turbulent flow simulation. Aiming to solve the lack of explicit fluid walls,

(Vrionis et al. 2021) proposes cutting the interface of the simulation cells along the optimization process under the incompressible laminar regime. In the incompressible turbulent regime, (Koch et al. 2017) proposes a shape-topology optimization method combination, which fits the solid-fluid interfaces by using non-uniform rational B-spline (NURBS) curves at the volume cells. More recently, (Picelli et al. 2022; Souza et al. 2020); (Moscatelli et al. 2022) employed an algorithm based on sequential integer linear programming to solve the fluid flow T.O. problem at incompressible laminar and turbulent regime respectively, using integer design variables (IDV), i.e. an optimization algorithm that works only with fluid ($\alpha = 0$) or solid ($\alpha = 1$) permeability values. The standard IDV approach is also based on the Brinkman-type model, however, it provides fluid walls as all elements are restricted to be only fluid or solid. Also, it reduces the dependence on optimization penalization parameters. Other methods, such as boundary descriptive or level sets, present fundamental differences in their design space and update scheme when compared to the pseudo-density methods based on CDV or IDV, being the latter ones usually simpler and simple digital (“pixelated”) approaches. Furthermore, the level set method does not allow using an automatic differentiator tool yet to derive the adjoint model.

Regarding T.O. of compressible flow, from the author's knowledge, only two works have been recently released (Okubo et al. 2022; Sá et al. 2021a), both focusing on the analysis of compressible subsonic laminar regime. The main challenge relies on the analysis of optimization of compressible flow, which has not been made previously by any literature due to the coupled difficulties of modelling compressible fluid flow and obtaining the adjoint code of compressible regime. Therefore, no commercial software offers this optimization. Sá, et al. (2021) (Sá et al. 2021a) developed FEM-based software to optimize compressible laminar regime and proposed minimizing the entropy generation on 2D cases employing the discrete adjoint. Okubo, et al. (Okubo et al. 2022) present a T.O. formulation to treat compressible laminar regime in a FVM based-software through a finite differences algorithm developed in the same code, and (Okubo and Silva 2022) presents an approximation for compressible turbulent regime by using a “frozen” turbulence scheme, where the turbulence phenomenon is not solved in the adjoint code. As seen, difficulties appear in the optimization of fluid flow related to permeability models, the transition of fluid/solid boundaries, turbulence treatment, and optimizers software... which arguments that T.O. is ongoing developing research. Now the adjoint acquisition and treatment will be explained to fundament the adjoint acquisition approach of the current work.

1.3. THE CONTINUOUS AND DISCRETE ADJOINT APPROACHES

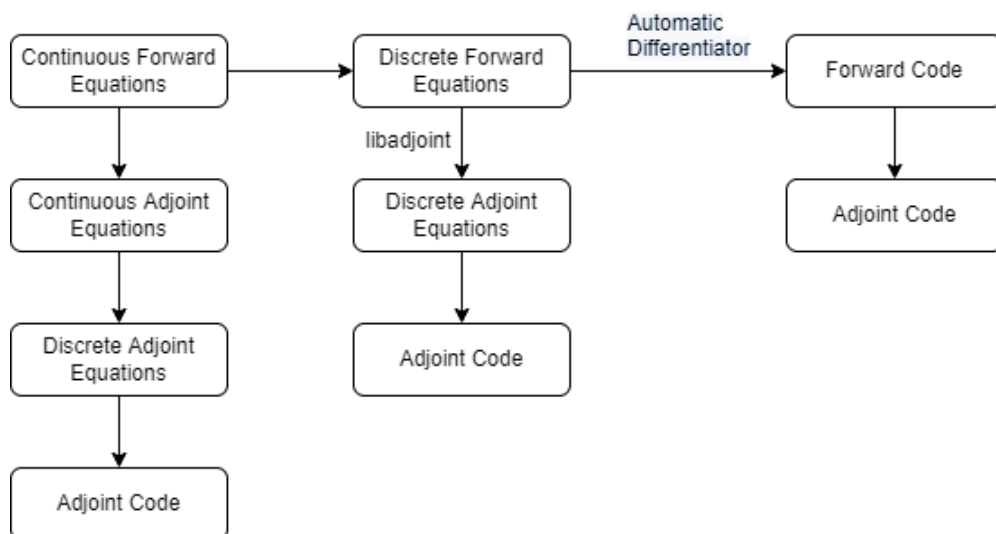
The gradient-based optimization algorithms are used to determine optimal states and controls, which requires an approximation of the functional gradient to be minimized with respect to the controls or design variables. If ϕ is defined as the state variables, g the control variables or design parameters, $J(\phi, g)$ the objective function and $F(\phi, g) = 0$ the constraints, then a typical optimization algorithm proceeds as follows:

1. Solve $F(\phi^{(m)}, g^{(m)}) = 0$ to obtain the corresponding state $\phi^{(m)} = \phi(g^{(m)})$
2. Compute the gradient of the functional $\frac{DJ}{Dg}(\phi^{(m)}, g^{(m)})$
3. Use the results of steps 1 and 2 to compute $\delta g^{(m)}$
4. Set $g^{(m+1)} = g^{(m)} + \delta g^{(m)}$

Each iteration of the optimization algorithm needs at least one solution to the flow equation. Step 3 is defined as the adjoint code acquisition and can be determined using an optimization method e.g. gradient, conjugate gradient, quasi-Newton, etc. until a convergence criterion is satisfied. The sensitivities determine what changes occur in the objective function and constraints when the design variables are changed as well.

There are three different approaches to obtaining the adjoint code of a partial differential equation (PDE) system (Figure 5): the continuous forward equation, the discrete forward equations, and the forward code (Funke 2012).

Figure 5. Adjoint derivation system stages (Funke 2012)



The derivation of the continuous adjoint is usually a handmade task, which advantage relies on its computational cost and the direct adjoint system acquisition without numerical errors related to the calculation of the derivative. The discrete forward equation approach uses an automatic differentiator to derive automatically the adjoint code via matrixial and symbolic manipulation, e.g. FEniCS software uses the “libadjoint” library to obtain the discrete adjoint equations and system, and its advantage relies on avoiding handmade derivation. Finally, the forward code, e.g. via the finite differences method (FD), derives the adjoint model from the forward model source implementation to solve the non-linear Jacobian matrix directly, it does not handle symbolic representation and in essence, solves directly the adjoint code without handmade or symbolic matrixial manipulation.

The continuous forward equations have been used in different research about T.O. of incompressible turbulent regime (Dilgen et al. 2018a; Dilgen et al. 2018b; Papoutsis-Kiachagias and Giannakoglou 2016) and its advantages on computational cost make it suitable to be adopted. On the other hand, the discrete forward equation approach via the automatic differentiator has been used in T.O. of incompressible turbulent flow (Yoon 2020; Yoon 2016) and T.O. of compressible laminar regime (Sá et al. 2021a). Despite the advantage of avoiding hand derivation, the main limitation relies on the absence of compressible fluid flow solvers, turbulence treatment for compressible flow applications and real-gas modelling. Finally, the forward code via FD has been studied for shape optimization applications in OpenFOAM by (Towara 2018) and recently for topology optimization applications by (Okubo et al. 2022), who have reached the compressible laminar regime for perfect gas applications at high costs in terms of computational cost. As seen, research in parallel computing programming should be developed, and still, the turbulence phenomenon is in doubt to be applied, besides the lack of coupling of either real gas models or inclusion of real-gas tables from an external software as the OpenFOAM-software is able to import. Therefore, the current research tackles two different approaches simultaneously aiming to obtain the turbulent adjoint code at T.O. of compressible turbulent regime for subsonic and real gas applications: firstly, via the continuous forward differentiation and secondly, the discrete forward approach based on the automatic differentiator tool.

As seen, the optimization of a compressor rotor employing the topology optimization method demands the development of T.O. of compressible turbulent flow at first. No literature has been able to reach the mentioned fluid flow regime by the complexity of including a compressible-

based solver on the fluid flow resolution besides numerical schemes and treatments of the energy equation at the fluid/solid interface. In this onset, T.O. of compressible turbulent flow could be reached by using an updated and efficient CFD software specially designed to solve fluid flow problems (OpenFOAM) and has all the necessary numerical schemes and adjustments already implemented. The only drawback is that it does not have the computation of the adjoint model, therefore, the current research develops and extends to compressible turbulent flow applications the FEniCS TopOpt Foam library (Alonso et al. 2021), which couples the automatic differentiator tool from FEniCS/dolfin-adjoint to the OpenFOAM software. The turbulence phenomenon at compressible flow is treated under the FANS equations and both, the SA and the Wray-Agarwal turbulence models are used to optimize channels and rotors respectively. The fluid flow is solved by using FVM and the proposed T.O. objective function minimizes the energy dissipation at the domain. The material modelling from (Borrvall and Petersson 2003) is adapted to penalize each property in the T.O. formulation independently. Also, the walls are considered isothermal during the optimization process, ensuring only heat transfer between the fluid regions. An interior point optimizer (iPOPT) is adopted to solve the optimization problem. Finally, the real gas influence in T.O. of compressible turbulent subsonic flow is quantified through the analysis of channels and rotors, utilizing Sutherland's law and the Peng-Robinson state equation.

1.4. MOTIVATION

The development of a flexible and robust optimized approach is essential to tackle uncertainties presented at compressible fluid evaluation as the large velocities, the compressibility effects and temperature gradients are coupled in compressible Mach numbers of ranges unstable to model due to the shock waves and the real gases behaviour. These developments are foundations to be used in the evaluation of fluid devices that manages compressible flow such as the one presented in the Carbon Capture and Storage (CCS) technology, which enhances compression stage inefficiencies.

The topology optimization technique offers the flexibility and robustness of innovating fluid flow devices that are being searched, as the efficiency of the fluid flow passages is guaranteed by the CFD modelling along with optimization algorithms that design and control the fluid systems. The optimization ensures an optimized objective function by solving the primal fluid flow system

subjected to the state equations. The topology optimization of compressible flow has been reached recently by two works considering laminar flow and perfect gases via the discrete and finite differences adjoint approach. Therefore, this research aims to solve the turbulence phenomenon and real gas influence on topology optimization of compressible turbulence by considering the discrete adjoint approach.

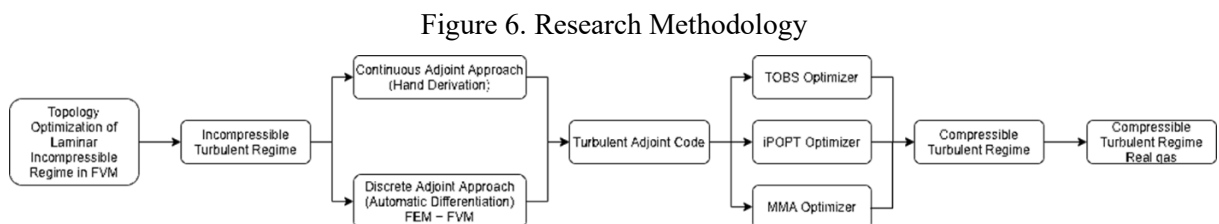
By doing so, the basis of topology optimization of compressible turbulent flow and real gases influence can be grounded, as the compressible regime is an unexplored optimization field, mainly by the challenges involved during the fluid flow modelling and the adjoint calculation of compressible systems, which fundamentals the scientific contribution of the current research.

1.5. OBJECTIVES

- Develop topology optimization formulation of subsonic compressible rotational turbulent flow considering the discrete adjoint approach (automatic differentiation) for ideal and real gases.
- Influence of continuous and integer design variables optimizers in the topology optimization of incompressible turbulent flow based on the continuous adjoint approach.
- Apply topology optimization for design channels and rotors under subsonic compressible flow considering real and perfect gases.

1.6. METHODOLOGY

Compressible turbulent rotational regime modelling for real gases is a challenging process that requires not only powerful solvers and accurate discretization methods, but also, innovative techniques for T.O. developed in the current research. The optimization process is tackled with a progressive methodology shown in Figure 6.



The work started by considering T.O. of incompressible regime, developing the continuous adjoint formulation in the CFD software OpenFOAM based on the FVM method. The primal and adjoint code are programmed along with the MMA (Svanberg 1987) and TOBS (Sivapuram and Picelli 2018) optimizers to update the material distribution. Parallel to the mentioned work, the discrete adjoint approach is developed as well, by combining OpenFOAM simulation tools with the automatic differentiator from FEniCS, which is a stabilized PDEs resolution software used to implement T.O. for incompressible flows based on FEM (Mortensen et al. 2011). The discrete approach takes the solution of the primal equation from OpenFOAM and uses its weak form to obtain the adjoint code via the automatic differentiator tool dolfin-adjoint considering the iPOPT (Wachter and Biegler 2006) optimizer. After each software capability is validated, the compressible regime is reached by the discrete adjoint approach due to its flexibility, as it can get the adjoint code employing the automatic differentiator. At first, perfect gas is considered under compressible laminar and turbulent regime, finishing with real gas modelling optimization considering the Peng-Robinson state equation.

1.7. SCIENTIFIC CONTRIBUTIONS

- Optimize compressible turbulent regime considering ideal and real gas at rotating domains;
- Analyse the influence of the IDV binary optimization algorithm for topology optimization of turbulence regime;
- Determine the influence of turbulence phenomenon at incompressible flow optimization considering FVM;
- Consider automatic differentiation to solve the adjoint code of compressible turbulent regime.

Three articles were developed with this research:

- a) D. Alonso, L. F. Garcia Rodriguez, and E. C. N. Silva, “Flexible framework for fluid topology optimization with OpenFOAM and finite element-based high-level discrete adjoint method (FEniCS / dolfin-adjoint),” *Struct. Multidiscip. Optim.*, vol. 64, pp. 4409–4440, 2021, [Online]. Available: <https://doi.org/10.1007/s00158-021-03061-4>.
- b) Garcia-Rodriguez L.; Kiyono, C; Picelli, R And Silva, E. “On the use of continuous and integer design variables in topology optimization of incompressible turbulent fluid

flow”, *App. Math. Model.*, vol. 115, pp 337-359, 2023, [Online]. Available: <https://doi.org/10.1016/j.apm.2022.10.039>

- c) Garcia-Rodriguez L.; Alonso, D. And Silva, E. “Topology optimization of turbulent subsonic compressible flow” (under review). *Journal of Structural and Multidisciplinary Optimization*, 2022.

1.8. DOCUMENT OUTLINE

The document is organized as follows: in Chapter 2, the theory of the continuous and discrete adjoint approaches is presented, each following the structure of introducing the equilibrium equations, the turbulence model treatment, followed by the topology optimization approach and the numerical implementation. In Chapter 4, the results of the optimization cases are presented, starting with the incompressible cases at laminar and turbulent regime. Then, the compressible cases are presented following the progressive strategy: laminar regime, compressible turbulence regime approximation and compressible turbulent flow. Finally, the compressible cases that consider real gas modelling are presented. In Chapter 4, some conclusions are inferred, and future work on the current research is suggested. In Chapter 6, the references used are detailed. Lastly, in Chapter 7, the appendix is shown.

2. CONTINUOUS ADJOINT APPROACH USED AT INCOMPRESSIBLE TURBULENT FLOW OPTIMIZATION

The optimization of a fluid flow system can be stated as: by the definition of “ Ω ” as an open domain in the space $R^n, n = 2, 3$, with boundary condition Γ . If ϕ denote the scalar valued state variable and $\alpha_k, k = 1, \dots, K$, denote the discrete set of control parameters or design variables. For example, a case where the constraints are of the second order nonlinear, elliptic partial differential equation (PDE)

$$-\nabla \cdot (a \nabla \phi) + b_i \cdot \nabla \phi + \phi^3 = \sum_{k=1}^K \alpha_k f_k \text{ in } \Omega \quad (1)$$

along with the boundary condition

$$\phi = 0 \text{ on } \Gamma \quad (2)$$

where a, b_i and $f_k, k = 1, \dots, K$ are given functions defined on $\bar{\Omega}$. Then, an example of an objective or cost, or performance functional is given by

$$\mathcal{J}(\phi, \alpha_1, \dots, \alpha_k) = \frac{1}{2} \int_{\Omega} (\phi - \Phi)^2 d\Omega + \frac{\sigma}{2} \sum_{k=1}^K (\alpha_k)^2 \quad (3)$$

where Φ is a given function and σ a given penalty parameter. The optimization problem is then given by:

“Find ϕ and $\alpha_k, k = 1, \dots, K$, such that the functional \mathcal{J} defined (3) is minimized subject to the requirements that ϕ and $\alpha_k, k = 1, \dots, K$, satisfy the constraints (1) and (2)”

To determine the gradient of the functional the chain rule can be applied to $\mathcal{J}(\phi(g), g)$ where $\phi(g)$ denotes the solution of the state equation $F(\phi, g) = 0$, to obtain:

$$\left. \frac{D\mathcal{J}}{Dg} \right|_{g^{(m)}} = \left. \frac{\partial \mathcal{J}}{\partial \phi} \right|_{g^{(m)}} \left. \frac{d\phi}{dg} \right|_{g^{(m)}} + \left. \frac{\partial \mathcal{J}}{\partial g} \right|_{g^{(m)}} \quad (4)$$

where $(\cdot)]_{g^{(m)}}$ denotes evaluation at the current iterate for the control, i.e. at $g^{(m)}$. The base is to calculate the sensitivities $\frac{d\phi}{dg}$. If the derivation is performed by hand, then λ is the solution of the adjoint equation, and the state problem is written as:

$$-\nabla \cdot (a \nabla \lambda) - \nabla \cdot (b \lambda) + 3\phi^2 \lambda = \phi - \Phi \text{ in } \Omega \quad (5)$$

and

$$\lambda = 0 \text{ on } \Gamma \quad (6)$$

where ϕ is the solution of the state equation (Eq.1) and its boundary conditions (Eq.2) the current values of the design variables. The gradient of its functional in terms of the adjoint equation replacing $(\phi - \Phi)$ is

$$\begin{aligned} \frac{DF}{D\alpha_k} &= \sigma\alpha_k + \int_{\Omega} (-\nabla \cdot (a\nabla\lambda) - \nabla \cdot (b\lambda) + 3\phi^2\lambda)\phi_k d\Omega, k = 1 \dots, K \\ \frac{DF}{D\alpha_k} &= \sigma\alpha_k + \int_{\Omega} (-\nabla \cdot (a\nabla\phi_k) - \nabla \cdot (b\phi_k) + 3\phi^2\phi_k)\lambda d\Omega, k = 1 \dots, K \\ \frac{DF}{D\alpha_k} &= \sigma\alpha_k + \int_{\Omega} \lambda f_k d\Omega, k = 1 \dots, K \end{aligned} \quad (7)$$

By doing so, the components of the gradient of the functional w.r.t. the design variables α_k are given in terms of the solution λ of the adjoint equations. Therefore, the resolution of the K components using the adjoint equation approach requires the solution of a single linear system and the adjoint equations, which are derived by hand according to the T.O. formulation, i.e. the adjoint system depends on the fluid flow regime, the objective function and the remaining control parameters. The T.O. literature (Giannakoglou et al.; Kontoleontos et al. 2013; Papoutsis-Kiachagias et al. 2011; Papoutsis-Kiachagias and Giannakoglou 2016) deals with the incompressible regime by the continuous adjoint approach, and none research has found yet the continuous adjoint system for a compressible flow due to the mathematical complexity that demands the hand derivation of the equilibrium state equations for compressible flow, along with the derivation of its turbulence treatment. Nevertheless, the computational cost advantage, the programming flexibility, and the straight-understanding behaviour of the continuous adjoint approach makes it attractive to study other challenges presented in fluid flow control such as optimizers influence, accurate fluid/solid boundary definition, pure diffusive problems among others. Therefore, this first stage focuses on analysing new alternatives to overcome challenges of fluid flow control apart from the adjoint system acquisition.

The T.O. formulation considers the minimization of the total pressure losses between the inlet/outlet boundaries (F) subjected to the RANS equations (expressed as PDE), the volume constraint and the permeability design variable of the volume cells. The main contribution states in the analysis of an IDV-based optimizer over the topology optimization resolution, as it defines continuously the solid-fluid boundary, which is desired for turbulence treatment. The analysis is compared to the CDV-based optimizer and the results are highlighted by its

innovation and low computational cost. The developed software is labelled as “adjointTopOptFOAM” and is implemented in the OpenFOAM extended version 1912 (OpenFOAM1912), where the turbulence model is the Spalart-Allmaras for steady-state flow. This chapter presents at first the equilibrium equations for incompressible turbulent flow, followed by the T.O. formulation, its adjoint equations and an explanation of the optimization algorithms used along with its numerical implementation.

2.1. EQUILIBRIUM EQUATIONS OF INCOMPRESSIBLE TURBULENT FLOW

Initially the incompressible, steady-state turbulent regime is considered to validate the performance of the developed T.O. software, as literature only has tackled incompressible regime for the continuous adjoint approach. The RANS equations are used to model the turbulence phenomenon (Wilcox 1993):

$$R^p = \frac{\partial \bar{u}_i}{\partial x_i} = 0 \quad (8)$$

$$R^u = \frac{\partial(\bar{u}_i \bar{u}_j)}{\partial x_j} + \frac{1}{\rho} \frac{\partial \bar{p}}{\partial x_j} - \left[(\nu) \left(\frac{\partial \bar{u}_i}{\partial x_j} + \frac{\partial \bar{u}_j}{\partial x_i} \right) - \overline{u_i' u_j'} \right] = 0 \quad (9)$$

where \bar{u}_i and \bar{p} are the average velocity and pressure respectively, ρ is the density, ν the kinematic viscosity and $\overline{u_i' u_j'}$ the Reynolds stress tensor.

2.2. TURBULENCE MODEL TREATMENT

The calculation of the Reynolds stress tensor ($\overline{u_i' u_j'}$) is a cutting-edge research fields of the fluid modelling, which is discretized according to the Reynolds number and application area. In T.O. applications the literature has shown reliable results via the Boussinesq hypothesis (Wilcox 1993):

$$\overline{u_i' u_j'} = 2\tilde{\mu}_t \left(\frac{\partial \bar{u}_i}{\partial x_j} + \frac{\partial \bar{u}_j}{\partial x_i} - \frac{1}{3} \frac{\partial \bar{u}_k}{\partial x_k} \delta_{ij} \right) - \frac{2}{3} \bar{\rho} k \delta_{ij} \quad (10)$$

As incompressible flow is considered, the terms $-\frac{2}{3} \bar{\rho} k \delta_{ij}$ and $-\frac{1}{3} \frac{\partial \bar{u}_k}{\partial x_k} \delta_{ij}$ are ignored. The $\tilde{\mu}_t$ term is the eddy viscosity obtained via the Boussinesq hypothesis and the turbulence model.

2.2.1. Spalart-Allmaras Turbulence Model

The SA turbulence model has been successfully used in T.O. of turbulent incompressible regime (Bueno-Orovio et al. 2012; Dilgen et al. 2018a; Papoutsis-Kiachagias and Giannakoglou 2016; Yoon 2020), which makes it suitable for the current research. The SA turbulence model relates the turbulent eddy viscosity ($\tilde{\mu}_t$) as following (Spalart and Allmaras 1992):

$$\tilde{\mu}_t = \rho \hat{v} f_{v1} \quad (11)$$

$$u_j \frac{\partial \hat{v}}{\partial x_j} = c_{b1}(1 - f_{t2})\hat{S}\hat{v} - \left[c_{w1}f_w - \frac{c_{b1}}{\kappa^2} f_{t2} \right] \left(\frac{\hat{v}}{\Delta} \right)^2 \frac{1}{\sigma} \left[\frac{\partial}{\partial x_j} \left((v + \hat{v}) \frac{\partial \hat{v}}{\partial x_j} \right) + c_{b2} \frac{\partial \hat{v}}{\partial x_i} \frac{\partial \hat{v}}{\partial x_i} \right] \quad (12)$$

where \hat{v} is the viscosity like variable, Δ the nearest wall distance value, and the extra terms are defined as:

$$f_{v1} = \frac{X^3}{X^3 + c_{v1}^3} \quad (13)$$

$$X = \frac{\hat{v}}{v} \quad (14)$$

$$\hat{S} = |W_{ij}| + \frac{\hat{v}}{\kappa^2 \Delta^2} f_{v2} \quad (15)$$

$$f_{v2} = 1 - \frac{X}{1 + X f_{v1}} \quad (16)$$

$$f_w = g \left[\frac{1 + c_{w3}^6}{g^6 + c_{w3}^6} \right]^{\frac{1}{6}}$$

$$g = r + c_{w2}(r^6 - r)$$

$$r = \min \left[\frac{\hat{v}}{\hat{S} \kappa^2 \Delta^2}, 10 \right] \quad (17)$$

$$f_{t2} = c_{t3} \exp(-c_{t4} X^2)$$

$$W_{ij} = \frac{1}{2} \left(\frac{\partial u_i}{\partial x_j} - \frac{\partial u_j}{\partial x_i} \right) \quad (18)$$

with constants $c_{b1} = 0.1355$, $\sigma = 2/3$, $c_{b2} = 0.622$, $\kappa = 0.41$, $c_{w1} = \frac{c_{b1}}{\kappa^2} + \frac{1+c_{b2}}{\sigma}$, $c_{w2} = 0.3$, $c_{w3} = 2$, $c_{v1} = 7.1$

2.2.2. Near-Wall Distance Calculation

The use of the SA turbulence model needs the near wall distance value (Δ), and its variation to the normal surface ($\partial\Delta/\partial n$), which is calculated specifically by the Eikonal equation (Bueno-Orovio et al. 2012):

$$\frac{\partial\Delta}{\partial x_j} \frac{\partial\Delta}{\partial x_j} = 1 \quad (19)$$

Nevertheless, its use is highly costly in terms of computational performance. Therefore, the current research establishes the use of the Hamilton-Jacobi equation, which is an approximate equivalent solution validated by the literature (Papoutsis-Kiachagias and Giannakoglou 2016; Tucker et al. 2004):

$$R^\Delta = \frac{\partial(c_j\Delta)}{\partial x_j} - \Delta \frac{\partial^2\Delta}{\partial x_j^2} - 1 = \frac{\partial\left(\frac{\partial\Delta}{\partial x_j}\Delta\right)}{\partial x_j} - \Delta \frac{\partial^2\Delta}{\partial x_j^2} - 1 = 0 \quad (20)$$

2.3. FLUID FLOW MODELLING

The fluid flow modelling is made via the computational fluid dynamics (CFD) technology, which is a computational-based method to treat the governing equation of the fluids through numerical schemes and discretization methods. There are different approaches of CFD modelling mainly based on the discretization technique: the Finite Volume Method (FVM) and the Finite Element Method (FEM). The current research stage considers the FVM through the ‘‘OpenFOAM’’ software.

2.3.1. The Finite Volume Method Used At The OpenFoam Software

In the FVM, the partial differential equations representing conservation laws are transformed into discrete algebraic equations through a finite difference analysis. The FVM is a conservative method as the flux entering into a given volume is identical to the outflow of the adjacent volume. In addition, it can be formulated at unstructured polygonal meshes as the unknown variables are evaluated at the centroids of the volumes and not at their faces. The method starts with the discretization of the geometric domain, i.e. divide the domain into non-overlapping finite volumes. Then, the partial differential equations are discretized into algebraic equations by their integration over each discrete volume. Finally, the system of algebraic equations is

solved to compute the dependent variable at each of the control volumes. By using this FVM method, some terms in the conservation equation are turned into fluxes evaluated at the faces of the finite volumes. The coupling between the pressure and velocity fields is made through the “simpleFOAM” solver, which is based on the “SIMPLE” algorithm and explained at following.

2.3.2. Resolution of the Algebraic State Equations

The SIMPLE algorithm is a numerical method used to solve the algebraic governing state equations of fluid flow and provide an accelerated convergence to stabilize steady-state solutions for incompressible and compressible flows (Rahman and Mustapha 2015). The discretized form of the momentum and mass conservation equations are presented as:

$$\sum_{f \sim nb(C)} \dot{m}_f = \dot{m}_e + \dot{m}_w = 0 \quad (21)$$

$$\begin{aligned} a_e u_e^* &= \sum a_{nb} u_{nb}^* + b + (p_p^* - p_E^*) A_e \\ a_n v_n^* &= \sum a_{nb} v_{nb}^* + b + (p_p^* - p_N^*) A_n \\ a_t w_t^* &= \sum a_{nb} w_{nb}^* + b + (p_p^* - p_T^*) A_t \end{aligned} \quad (22)$$

where \dot{m} indicates the mass flux through the face (f) from the East (e) and West (w) sides. The system can be solved only when the pressure field is given or estimated. Unless the correct pressure field is employed, the resulting velocity field will not satisfy the relation. Therefore, an initial velocity field (u^*, v^*, w^*) is calculated based on a guessed pressure distribution (p^*) to start the iterations.

$$\begin{aligned} \frac{a_p}{\alpha_u} u_p &= \sum_{c.v.} a_{c.v.} u_{c.v.} + (p_w - p_e) \Delta y + b + \frac{(1 - \alpha_u) a_p}{\alpha_u} u_p^{(n-1)} \\ \frac{a_p}{\alpha_v} v_p &= \sum_{c.v.} a_{c.v.} v_{c.v.} + (p_s - p_n) \Delta x + b + \frac{(1 - \alpha_v) a_p}{\alpha_v} v_p^{(n-1)} \end{aligned} \quad (23)$$

Then, a new value of pressure (p) is updated from the following equation.

$$p = p^* + p' \quad (24)$$

where p' is described at:

$$\begin{aligned} a_{c,c} p'_{c,c} &= a_{E,c} p'_{E,c} + a_{W,c} p'_{W,c} + a_{c,N} p'_{c,N} + a_{c,S} p'_{c,S} + b'_{c,c} \\ a_{c,c} &= a_{E,c} + a_{W,c} + a_{c,N} + a_{c,S} \end{aligned} \quad (25)$$

$$\begin{aligned}
 a_{E,c} &= (\rho dA)_{e,c} \\
 a_{W,c} &= (\rho dA)_{w,c} \\
 a_{c,s} &= (\rho dA)_{c,s} \\
 b'_{I,J} &= (\rho u^* A)_{w,c} - (\rho u^* A)_{e,c} + (\rho v^* A)_{c,s} - (\rho u^* A)_{c,n}
 \end{aligned}$$

Once the pressure is updated, the velocity is corrected with the following:

$$\begin{aligned}
 u_e &= u_e^* + d_e(p'_P - p'_E) \\
 v_n &= v_n^* + d_n(p'_P - p'_N) \\
 w_t &= w_t^* + d_t(p'_P - p'_T)
 \end{aligned} \tag{26}$$

The described process corresponds to the Semi-Implicit Method for Pressure-Linked (SIMPLE) algorithm, which can be summarized as:

- a) Guess the pressure field p^* .
- b) Solve equation 23 to obtain u^*, v^*, w^* .
- c) Solve the p' .
- d) Calculate p by adding p' to p^* .
- e) Calculate u, v, w from their previous values.
- f) Solve the discretization equation for other ϕ' 's (such as temperature, concentration, and turbulent quantities) if they influence the flow field through fluid properties, source terms, etc.
- g) Treat the corrected pressure p as a new guessed pressure p^* , return to step b) and repeat the whole pressure until convergence is reached.

After modelling the fluid flow, the adjoint code is needed to perform the topology optimization method. The path taken to derive the adjoint code is explained in the following.

2.4. TOPOLOGY OPTIMIZATION FORMULATION

The optimization problem considers the minimization of the total pressure losses between the inlet and outlet boundaries of an established domain, obeying (Papoutsis-Kiachagias and Giannakoglou 2016) formulation. It is subjected to the constraints of the fluid flow physics, established by the modified RANS equations (R^p, R^u), the modified turbulence model ($R^{\tilde{v}_t}$), the near-wall distance calculation (R^Δ), the volume constraint, (\bar{V}) and the permeability design variable (γ). Each constraint is explained as follows.

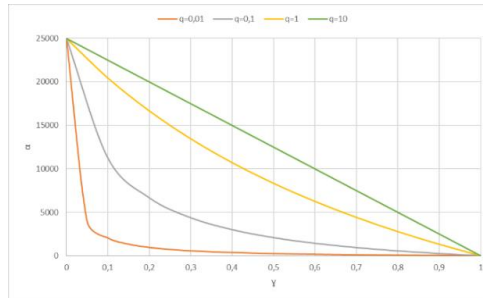
2.4.1. Permeability Design Variable (α)

The fluid topology optimization method based on the pseudo-density approach is implemented by including an additional porosity term (k_ϕ) in Eq. (9), (12) and (20), which allows the solid or fluid region definition in the domain. The idea consists of making α to assume 0 or 1 values, to represent solid and fluid, respectively. To do so, the material distribution model proposed by (Borrvall and Petersson 2003) is applied to each fluid flow equation:

$$k_\phi = \bar{k}_\phi + (\underline{k}_\phi - \bar{k}_\phi)\alpha \frac{(1 + q_\phi)}{(\alpha + q_\phi)} \quad (26)$$

where k_ϕ represents each primal variable to be considered, i.e. u , \tilde{v}_t , or Δ , as it will be described in more detail in the next sections. The model behaves like a linear or convex interpolation function depending on q_ϕ chosen value (Figure 7), which is a penalty parameter with a value greater than zero used to control the level of “grey” in the optimized design. The \underline{k}_ϕ minimum value is established as zero to represent fluid and \bar{k}_ϕ maximum is calibrated according to each case to avoid fluid entrance inside the cell. When α is equal to zero, solid regions are established, and when α equal to 1 a fluid domain is represented.

Figure 7 Material distribution equation behaviour



2.4.2. Modified Equilibrium Equations of Incompressible Turbulent Flow

Modified RANS Equations: R^p, R^u

The penalization term $k_u \bar{u}_i$ is added to the momentum equation relating velocity field (u_i) to the permeability region α that determines the domain solid/fluid regions (Borrvall and Petersson 2003). High α values overcome the momentum equation and determine a solid region, and near-zero values recover the original momentum equation, while the mass

conservation remains intact. The previous modification results in the steady-state modified averaged RANS equations for the incompressible turbulent regime:

$$R^p = \frac{\partial \bar{u}_i}{\partial x_i} = 0 \quad (27)$$

$$R^u = \frac{\partial(\bar{u}_i \bar{u}_j)}{\partial x_j} + \frac{1}{\rho} \frac{\partial \bar{p}}{\partial x_j} - \left[(\nu) \left(\frac{\partial \bar{u}_i}{\partial x_j} + \frac{\partial \bar{u}_j}{\partial x_i} \right) - \overline{u_i' u_j'} \right] + \underbrace{k_u \bar{u}_i}_{\text{Penalization Term}} = 0 \quad (28)$$

where α_u is the material modelling term of the momentum equation.

Modified Turbulence Model: $R^{\tilde{\nu}_t}$

It consists of adding the penalization term $k_{\tilde{\nu}_t} \tilde{\nu}_t$ in the modified turbulent viscosity $\tilde{\nu}$ calculation:

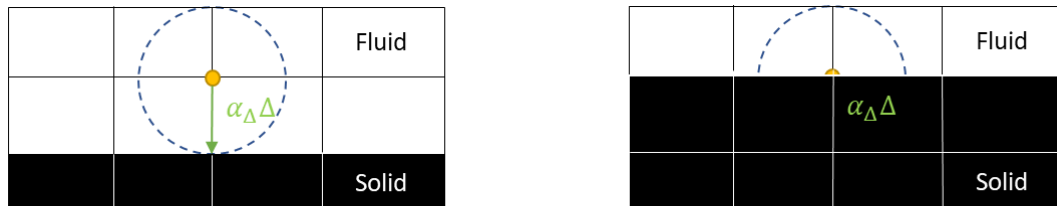
$$R^{\tilde{\nu}_t} = \nu_j \frac{\partial \tilde{\nu}}{\partial x_j} - \frac{\partial}{\partial x_j} \left[\left(\nu + \frac{\tilde{\nu}}{\sigma} \right) \frac{\partial \tilde{\nu}}{\partial x_j} \right] - \frac{c_{b2}}{\sigma} \left(\frac{\partial \tilde{\nu}}{\partial x_j} \right)^2 - \tilde{\nu} P(\tilde{\nu}) + \tilde{\nu} D(\tilde{\nu}) + \underbrace{k_{\tilde{\nu}_t} \tilde{\nu}_t}_{\text{Penalization Term}} = 0 \quad (29)$$

while the other variables remain as the original model (Spalart and Allmaras 1992). Low α_t values allow the turbulence calculation in the fluid cells, otherwise the turbulence is not considered.

Modified Near Wall Distance Calculation: R^Δ

The near-wall distance calculation is part of the equilibrium equations of the fluid flow, however, previous works have neglected its independence from the fluid/solid definition. By doing so, the wall distance is still calculated independently from the cell permeability, affecting the computational cost, and inducing numerical errors on solid cells that are already defined. To overcome such differences, the current research proposes to penalize also the near-wall distance calculation by including a penalization term $k_\Delta \Delta$ to the Hamilton-Jacobi equation (Eq(20)). By doing so, the independent performance of the $k_\Delta \Delta$ term from the momentum equation penalization term ($k_u u_i$) allows not to affect the near-wall distance calculation to the solid cells, and when the solid/fluid boundary is analyzed, the $k_\Delta \Delta$ term is zero no matter which k_Δ is selected. The definition is illustrated in Figure 8.

Figure 8 Influence of the penalization term on the near-wall distance calculation



As α_Δ definition is with low values, the Δ calculation is not affected

As Δ is zero, the α_Δ value does not influence the zero R^Δ constraint

Therefore, the modified Hamilton-Jacobi equation states as:

$$R^\Delta = \frac{\partial \left(\frac{\partial \Delta}{\partial x_j} \Delta \right)}{\partial x_j} - \Delta \frac{\partial^2 \Delta}{\partial x_j^2} - 1 + \underbrace{k_\Delta \Delta}_{\text{Penalization Term}} = 0 \quad (30)$$

2.4.3. Topology Optimization Problem Definition

The topology optimization problem is stated in Eq.(31), which establishes the minimization of the total pressure losses between the inlet/outlet boundaries subjected to the modified equilibrium equations for incompressible turbulent flow, the permeability design variable and the volume constraint. The total pressure losses objective function has been widely used in problems where the incompressible turbulent regime is optimized through the continuous adjoint approach (Kontoleontos et al. 2013; Papoutsis-Kiachagias et al. 2011; Papoutsis-Kiachagias and Giannakoglou 2016), which is an equivalent of the energy dissipation (Papoutsis-Kiachagias and Giannakoglou 2016) suitable to the analysis of compressors as by reducing the total pressure the vortex generation is reduced too. Then, the T.O. problem definition is stated at following:

Minimize

$$F = \int_\Gamma \left(\bar{p} + \frac{1}{2} \bar{u}_i^2 \right) \bar{u}_i n_i d\Gamma$$

Subject to

$$0 \leq \gamma \leq 1$$

$$R^p = \frac{\partial \bar{u}_i}{\partial x_i} = 0$$

$$R^u = \frac{\partial (\bar{u}_i \bar{u}_j)}{\partial x_j} + \frac{1}{\rho} \frac{\partial \bar{p}}{\partial x_j} - \left[(v) \left(\frac{\partial \bar{u}_i}{\partial x_j} + \frac{\partial \bar{u}_j}{\partial x_i} \right) - \overline{u_i' u_j'} \right] + \underbrace{k_u \bar{u}_i}_{\text{Penalization Term}} = 0 \quad (31)$$

$$R^{\tilde{v}_t} = v_j \frac{\partial \tilde{v}}{\partial x_j} - \frac{\partial}{\partial x_j} \left[\left(v + \frac{\tilde{v}}{\sigma} \right) \frac{\partial \tilde{v}}{\partial x_j} \right] - \frac{c_{b2}}{\sigma} \left(\frac{\partial \tilde{v}}{\partial x_j} \right)^2 - \tilde{v} P(\tilde{v}) + \tilde{v} D(\tilde{v}) + k_{\tilde{v}_t} \tilde{v}_t = 0$$

$$R^\Delta = \frac{\partial \left(\frac{\partial \Delta}{\partial x_j} \Delta \right)}{\partial x_j} - \Delta \frac{\partial^2 \Delta}{\partial x_j^2} - 1 + k_\Delta \Delta = 0$$

$$V \leq \bar{V}_{frac}$$

where the volume constraint is calculated by:

$$V = \frac{\int_\Omega \gamma d\Omega}{\int_\Omega d\Omega} \quad (32)$$

2.5. SENSITIVITY CALCULATION

As explained previously, the sensitivities are calculated to get the optimized point of the T.O. formulation and derive the optimization of the fluid flow. To do so, an Augmented Lagrange Multiplier (ALM) method is used to cope with equality constraints. Since the constraints of the state variables are set to zero, i.e. $R^p = R^u = R^{\tilde{v}} = R^\Delta = 0$, the augmented objective function L_{aug} , can be defined and minimized instead, defined as:

$$L_{aug} = F + \int_{\Omega} q R^p d\Omega + \int_{\Omega} v_i R^{u_i} d\Omega + \int_{\Omega} \tilde{v}_a R^{\tilde{v}} d\Omega + \int_{\Omega} \Delta_a R^\Delta d\Omega \quad (33)$$

where q, v_i, T_a, \tilde{v}_a and Δ_a expresses the adjoint variables of the state equations, e.g. q the adjoint pressure, v_i the adjoint velocity, and so on. Thus, the optimization formulation of Eq. (31) can be rewritten as:

$$\begin{array}{ll} \text{Minimize} & \{L_{aug} \\ \text{Subject to} & \left\{ \begin{array}{l} \bar{V}_{frac} \leq V_{tar} \\ 0 < \gamma < 1 \end{array} \right. \end{array} \quad (34)$$

To find out the optimized point, the augmented Lagrange function is differentiated to each variable and expressed as:

$$\delta L = \delta_{u_i} L + \delta_p L + \delta_\alpha L + \delta_{\tilde{v}} L + \delta_\Delta L \quad (35)$$

where $\delta_\alpha L = 0$ and $\delta_p L + \delta_{u_i} L + \delta_{\tilde{v}} L + \delta_\Delta L = 0$ allows solving the sensitivity and adjoint equations, respectively. The derivation of the adjoint system is performed by hand at the continuous adjoint approach, and the literature (Papoutsis-Kiachagias and Giannakoglou 2016) presents the derivation of the $\delta_p L, \delta_{u_i} L$ and $\delta_{\tilde{v}} L$ terms at incompressible regime. The adjoint near wall distance term ($\delta_\Delta L$) has not been considered previously, however, the current research analyses its influence by varying the permeability through the material modelling approach (Eq.26). The derivation is presented at following.

2.5.1. Field Adjoint Equations

The current research proposes a different adjoint wall distance calculation ($R^{\Delta a}$) from the literature (Papoutsis-Kiachagias and Giannakoglou 2016), as the Hamilton-Jacobi equation is

modified by including the porosity variation term ($\alpha_\Delta \Delta$). The formulation is developed as following:

$$\begin{aligned} \delta_\Delta L &= \int_\Omega \Delta_a R^\Delta d\Omega \\ \frac{\delta_\Delta L}{\delta b_n} &= \int_\Omega \Delta_a \frac{\partial R^\Delta}{\partial b_n} d\Omega + \int_{S_{wp}} \Delta_a R^\Delta n_k \frac{\delta x_k}{\delta b_n} dS \end{aligned} \quad (36)$$

By differentiating the modified Hamilton-Jacobi Equation (R^Δ):

$$\begin{aligned} \frac{\partial R^\Delta}{\partial b_n} &= \frac{\partial}{\partial b_n} \left[\frac{\partial}{\partial x_j} \left(\frac{\partial \Delta}{\partial x_j} \Delta \right) - \Delta \frac{\partial^2 \Delta}{\partial x_j^2} - 1 + k_\Delta \Delta \right] \\ \frac{\partial R^\Delta}{\partial b_n} &= \frac{\partial}{\partial x_j} \left[\frac{\partial \Delta}{\partial x_j} \frac{\partial \Delta}{\partial b_n} + \Delta \frac{\partial}{\partial x_j} \left(\frac{\partial \Delta}{\partial b_n} \right) \right] - \frac{\partial \Delta}{\partial b_n} \frac{\partial^2 \Delta}{\partial x_j^2} - \Delta \frac{\partial}{\partial x_j} \left[\frac{\partial}{\partial x_j} \left(\frac{\partial \Delta}{\partial b_n} \right) \right] + \frac{\partial k_\Delta}{\partial b_n} \Delta + k_\Delta \frac{\partial \Delta}{\partial b_n} \\ \frac{\partial R^\Delta}{\partial b_n} &= 2 \frac{\partial \Delta}{\partial x_j} \frac{\partial}{\partial x_j} \left(\frac{\partial \Delta}{\partial b_n} \right) + \frac{\partial k_\Delta}{\partial b_n} \Delta + k_\Delta \frac{\partial \Delta}{\partial b_n} \end{aligned} \quad (37)$$

As porosity value is independent of the normal boundary vector variation (∂b_n), the $\partial k_\Delta / \partial b_n$ is cancelled. Replacing Eq.(37) with Eq.(36), it is obtained:

$$\begin{aligned} \frac{\delta_\Delta L}{\delta b_n} &= \int_\Omega \Delta_a \left(2 \frac{\partial \Delta}{\partial x_j} \frac{\partial}{\partial x_j} \left(\frac{\partial \Delta}{\partial b_n} \right) + k_\Delta \frac{\partial \Delta}{\partial b_n} \right) d\Omega + \int_{S_{wp}} \Delta_a R^\Delta n_k \frac{\delta x_k}{\delta b_n} dS \\ \frac{\delta_\Delta L}{\delta b_n} &= \int_\Omega 2 \Delta_a \frac{\partial \Delta}{\partial x_j} \frac{\partial}{\partial x_j} \left(\frac{\partial \Delta}{\partial b_n} \right) d\Omega + \int_\Omega \Delta_a k_\Delta \frac{\partial \Delta}{\partial b_n} d\Omega + \int_{S_{wp}} \Delta_a R^\Delta n_k \frac{\delta x_k}{\delta b_n} dS \\ \frac{\delta_\Delta L}{\delta b_n} &= \int_\Gamma 2 \Delta_a \frac{\partial \Delta}{\partial x_j} n_j \frac{\partial \Delta}{\partial b_n} d\Gamma - \int_\Omega 2 \frac{\partial}{\partial x_j} \left(\Delta_a \frac{\partial \Delta}{\partial x_j} \right) \frac{\partial \Delta}{\partial b_n} d\Omega + \int_\Omega \Delta_a k_\Delta \frac{\partial \Delta}{\partial b_n} d\Omega \\ &\quad + \int_{\Gamma_{wp}} \Delta_a R^\Delta n_k \frac{\delta x_k}{\delta b_n} d\Gamma \end{aligned} \quad (38)$$

Eq.61 of (Papoutsis-Kiachagias and Giannakoglou 2016) shows the derivation of the primal variables, i.e. $\delta_p L / \delta b_n$, $\delta_{u_i} L / \delta b_n$, $\delta_{\tilde{v}} L / \delta b_n$, which combined with Eq.38 and by imposing the multiplier of $\partial \Delta / \partial b_n$ to be equal to zero in the resulting volume integrals, results in the modified adjoint Hamilton-Jacobi equation (R^{Aa}):

$$\begin{aligned} \int_\Omega \tilde{v} \tilde{v}_a C_\Delta \frac{\partial \Delta}{\partial b_n} d\Omega - \int_\Omega 2 \frac{\partial}{\partial x_j} \left(\Delta_a \frac{\partial \Delta}{\partial x_j} \right) \frac{\partial \Delta}{\partial b_n} d\Omega + \int_\Omega \Delta_a k_\Delta \frac{\partial \Delta}{\partial b_n} d\Omega &= 0 \\ \int_\Omega \left[\tilde{v} \tilde{v}_a C_\Delta - 2 \frac{\partial}{\partial x_j} \left(\Delta_a \frac{\partial \Delta}{\partial x_j} \right) + \Delta_a k_\Delta \right] \frac{\partial \Delta}{\partial b_n} d\Omega &= 0 \\ R^{Aa} = -2 \frac{\partial}{\partial x_j} \left(\Delta_a \frac{\partial \Delta}{\partial x_j} \right) + \tilde{v} \tilde{v}_a C_\Delta + \Delta_a k_\Delta &= 0 \end{aligned} \quad (39)$$

Therefore, the updated continuous adjoint formulation for incompressible turbulent flow developed in the current research is shown in equations (40)-(43):

$$R^q = -\frac{\partial v_j}{\partial x_j} = 0 \quad (40)$$

$$R_i^v = v_j \frac{\partial \bar{u}_j}{\partial x_i} - \frac{\partial(\bar{u}_j v_i)}{\partial x_j} - \frac{\partial}{\partial x_j} \left[(\nu + \nu_t) \left(\frac{\partial v_i}{\partial x_j} + \frac{\partial v_j}{\partial x_i} \right) \right] + \frac{\partial q}{\partial x_i} + \tilde{v}_a \frac{\partial \tilde{v}}{\partial x_i} - \frac{\partial}{\partial x_l} \left(\tilde{v}_a \tilde{v} \frac{C_Y}{Y} e_{mjk} \frac{\partial \bar{u}_k}{\partial x_j} e_{mli} \right) + k_u v_i = 0 \quad (41)$$

$$R^{\tilde{v}_a} = -\frac{\partial(\bar{u}_j \tilde{v}_a)}{\partial x_j} - \frac{\partial}{\partial x_j} \left[\left(\nu + \frac{\tilde{v}}{\sigma} \right) \frac{\partial \tilde{v}_a}{\partial x_j} \right] + \frac{1}{\sigma} \frac{\partial \tilde{v}_a}{\partial x_j} \frac{\partial \tilde{v}}{\partial x_j} + 2 \frac{c_{b2}}{\sigma} \frac{\partial}{\partial x_j} \left(\tilde{v}_a \frac{\partial \tilde{v}}{\partial x_j} \right) + \tilde{v}_a \tilde{v} C_{\tilde{v}} + \frac{\partial \nu_t}{\partial \tilde{v}} \frac{\partial v_i}{\partial x_j} \left(\frac{\partial \bar{u}_i}{\partial x_j} + \frac{\partial \bar{u}_j}{\partial x_i} \right) + (-P + D) \tilde{v}_a + k_{\tilde{v}_a} \tilde{v}_a = 0 \quad (42)$$

$$R^{\Delta_a} = -2 \frac{\partial}{\partial x_j} \left(\Delta_a \frac{\partial \Delta}{\partial x_j} \right) + \tilde{v} \tilde{v}_a C_{\Delta} + k_{\Delta} \Delta_a = 0 \quad (43)$$

2.5.2. Objective Function Sensitivity Calculation

Considering the differentiation of Eq. (33), sensitivity is found. At T.O., neither the design domain nor the mesh changes, resulting in a total derivate that is equal to the partial derivative (Papoutsis-Kiachagias and Giannakoglou 2016):

$$\frac{\delta \phi}{\delta \alpha} = \frac{\partial \phi}{\partial \alpha}, \quad \frac{\delta_S \phi}{\delta \alpha} = \frac{\partial \phi}{\partial \alpha} \quad (44)$$

therefore, the augmented Lagrange differentiation for the incompressible regime to the design variable γ is established as:

$$\frac{\delta L_{aug}}{\delta \alpha} = \frac{\delta F}{\delta \alpha} + \int_{\Omega} q \frac{\partial R^p}{\partial \alpha} d\Omega + \int_{\Omega} v_i \frac{\partial R^{u_i}}{\partial \alpha} d\Omega + \int_{\Omega} \tilde{v}_a \frac{\partial R^{\tilde{v}}}{\partial \alpha} d\Omega + \int_{\Omega} \Delta_a \frac{\partial R^{\Delta}}{\partial \alpha} d\Omega \quad (45)$$

Since F and R^p are not expressed in terms of the design variable, $\frac{\delta F}{\delta \alpha} = 0$ and $\frac{\partial R^p}{\partial \alpha} = 0$. The next three integrals are defined as:

$$\int_{\Omega} v_i \frac{\partial R^{u_i}}{\partial \alpha} d\Omega = \int_{\Omega} v_i \frac{\partial (k_u u_i)}{\partial \alpha} d\Omega = \int_{\Omega} v_i u_i \frac{\partial k_u}{\partial \alpha} d\Omega \quad (46)$$

$$\int_{\Omega} \tilde{v}_a \frac{\partial R^{\tilde{v}}}{\partial \alpha} d\Omega = \int_{\Omega} \tilde{v}_a \frac{\partial (k_{\tilde{v}_t} \tilde{v}_t)}{\partial \alpha} d\Omega = \int_{\Omega} \tilde{v}_a \tilde{v}_t \frac{\partial k_{\tilde{v}_t}}{\partial \alpha} d\Omega \quad (47)$$

$$\int_{\Omega} \Delta_a \frac{\partial R^{\Delta}}{\partial \alpha} d\Omega = \int_{\Omega} \Delta_a \frac{\partial (k_{\Delta} \Delta)}{\partial \alpha} d\Omega = \int_{\Omega} \Delta_a \Delta \frac{\partial k_{\Delta}}{\partial \alpha} d\Omega \quad (48)$$

resulting in:

$$\frac{\delta L_{aug}}{\delta \alpha} = \frac{\delta k_u}{\delta \alpha} (v_i \cdot u_i) V + \frac{\delta k_{\tilde{v}_t}}{\delta \alpha} (\tilde{v}_a \tilde{v}) V + \frac{\delta k_{\Delta}}{\delta \alpha} (\Delta_a \Delta) V \quad (49)$$

$$\frac{\delta k_{\phi}}{\delta \alpha} = \left[(k_{\phi} - \bar{k}) q \frac{(1 + q_{\phi})}{(\alpha + q_{\phi})^2} \right] \quad (50)$$

The obtained sensitivities fields are validated through the finite difference method presented in Appendix 7.1.

2.6. OPTIMIZATION ALGORITHM

As explained earlier, generally the continuous design variables (CDV) optimizers are used, i.e. optimization algorithms that use permeability design values between $0 \leq \alpha \leq 1$, which are calibrated in an exhaustive process to diminish intermediate (“grey”) solid-fluid interfaces (Borrvall and Petersson 2003). The greyscale produced by the CDV approach, however, hinders the optimization to include clear information about the fluid walls during optimization, important for the accuracy of the turbulent flow simulation. Therefore, the influence of an IDV-based optimizer is proposed, i.e. an optimization algorithm that works only with fluid ($\alpha = 0$) or solid ($\alpha = 1$) permeability values, which ensures a continuing resolution of the fluid/solid boundary during the optimization process. Both optimizers are explained as follows.

2.6.1. Continuous Design Variable Based Optimizer: MMA

The method of moving asymptotes (MMA) (Svanberg 1987) is a popular optimization algorithm due to its robust, flexible, and general gradient-based application that handles a large number of variables and constraints. The MMA is used for nonlinear programming problems in the form of minimization of the objective function, F , with inequality constraints R^{ϕ} . The MMA algorithm uses as inputs the first derivative of F and R^{ϕ} to the design variable, α of the current n iteration, the $n - 2$ iterations, and the constraints targets. This method can handle unfeasible solutions, i.e., it can reach a solution even if the constraints are not satisfied. During the

optimization process, the MMA algorithm updates the design variables iteratively to minimize the objective function and satisfy the constraints. The algorithm methodology is defined as:

Step 0: Choose a starting point $x^{(0)}$, and define the iteration index $k = 0$.

Step 1: Given an iteration point $x^{(k)}$, calculate the function value of an objective Function $F_i(x^{(k)})$ and its gradients $\nabla F(x^{(k)})$ for $i = 0, 1, \dots, m$.

Step 2: Generate a subproblem $P^{(k)}$ by replacing in P , the functions F by approximating explicit functions $F_i^{(k)}$, based on the calculation from step 1.

Step 3: Solve $P^{(k)}$ and let the optimal solution to this subproblem be the next iteration point $x^{(k+1)}$. Let $k = k + 1$ and go to step 1.

The method consists of how F_i^k should be defined and how the subproblem $P^{(k)}$ should be solved. The “dual objective function” W is defined, for $y \geq 0$ as follows:

$$W(y) = \min\{L(x, y); \alpha_j \leq x_j \leq \beta_j \text{ for all } j\}$$

$$W(y) = r_0 - y^T b + \sum_{j=1}^n l_j(x_j, y) \quad (51)$$

concluding that an objective function F that is restricted to different functions, R , can be expressed in terms of the Lagrangian function, in this case as:

$$\text{Minimize } L_{aug} = L + \int_{\Omega} q R^p d\Omega + \int_{\Omega} v_i R^{u_i} d\Omega + \int_{\Omega} T_a R^T d\Omega + \int_{\Omega} \tilde{v}_a R^{\tilde{v}} d\Omega + \int_{\Omega} \Delta_a R^{\Delta} d\Omega$$

$$\text{Subject to } \left\{ \begin{array}{l} \frac{\int_{\Omega} \gamma d\Omega}{\int_{\Omega} d\Omega} \leq \bar{V}_{frac} \\ 0 \leq \alpha \leq 1 \end{array} \right\} \quad (52)$$

2.6.2. Integer Design Variable Optimizer: TOBS

The topology optimization of binary structures (TOBS) optimizer (Sivapuram and Picelli 2018) is a gradient-based optimization method that treats the design variables as binary values (0 or 1), which makes independent the penalization for the pure fluid optimization as avoids intermediates γ values, leading to define precisely the solid/fluid interface along the optimization process and calculate accurately the near wall distance for turbulence treatment. This is made with an objective function $f(x)$ constrained by $R_i(x) \leq \bar{R}_i$, $i \in [1, N_g]$, with x

being the design variables. The linearized form of the binary variable optimization problem is formulated as follows:

$$\begin{aligned} & \underbrace{\text{Minimize}}_x && \left. \begin{aligned} & \left. \frac{\partial f}{\partial \mathbf{x}} \right|_{\mathbf{x}^k} \end{aligned} \right\} \\ & \text{Subject to} && \left. \begin{aligned} & \left. \frac{\partial g_i}{\partial \mathbf{x}} \right|_{\mathbf{x}^k} \Delta \mathbf{x}^k \leq \bar{R}_i - R_i^k \quad i \in [1, N_g] \\ & \Delta x_j \in \{-x_j, 1 - x_j\} \quad j \in [1, N_d] \end{aligned} \right\} \end{aligned} \quad (53)$$

where R_i^k is the value of the constraint R_i at iteration k of optimization. After each iteration, the design variables are updated (Eq.33):

$$\mathbf{x}^{k+1} = \mathbf{x}^k + \Delta \mathbf{x}^k \quad (54)$$

This method uses an Integer Linear Programming (ILP) algorithm to update the design variables, thus, nonlinear problems (objective function and constraints) must be sequentially linearized using Taylor first-order approximation. ILP algorithms cannot handle unfeasible solutions, thus if the constraint value is too far from the constraint target, the algorithm stops. To avoid that, whenever R_i^k is away from \bar{R}_i a constraint target relaxation is used:

$$\Delta R = \begin{cases} -\epsilon_1 R^k : \bar{R} < (1 - \epsilon_1) R^k \\ \bar{R} - R^k : \bar{R} \in (1 - \epsilon_1) R^k, (1 + \epsilon_2) R^k \\ \epsilon_2 R^k : \bar{R} > (1 + \epsilon_2) R^k \end{cases} \quad (55)$$

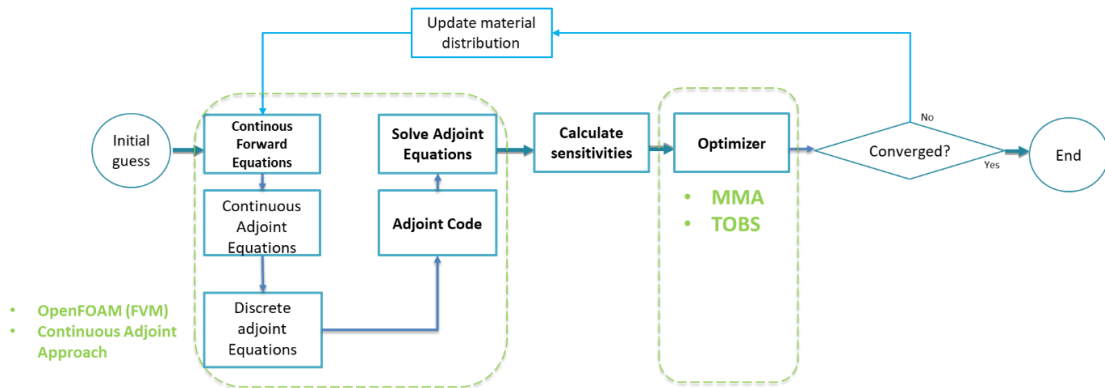
where R is any of the N_R constraints and ΔR is the right-hand side of the constraint, which is relaxed from $\bar{R} - R^k$ at iteration k . The parameters ϵ_1, ϵ_2 are chosen such that ILP has a feasible solution, usually small numbers to maintain the linearization validly. For simplicity, here it is set $\epsilon_1 = \epsilon_2$, similarly to (Picelli et al. 2020). During the optimization process, the relaxation is carried out until constraints are satisfied.

2.7. NUMERICAL IMPLEMENTATION

The implemented T.O. method is summarized in the Figure 9 flowchart. Each step is programmed in C++, following OpenFOAMv1906 structure and the “adjointOptimizationFOAM” library is modified for T.O. applications of incompressible turbulent flow using the IDV and CDV optimizers. The developed method starts by solving the fluid region through the modified RANS equations (Eq. (27)-(30) by using the finite volume method, where primal fields are obtained (p, u_i) . Then, the adjoint systems uses the primal

fields results to solve the adjoint Navier Stokes Equations (Eq. (40)-(43) to obtain the adjoint fields (q, v) and calculate the sensitivity (Eq. (50)). After that, the optimizer selected at the case is tested, either the CDV or the IDV, which is used to update the design variables along the domain establishing the solid-fluid region. The new design is then updated until satisfying the convergence criteria, which is established as 1×10^{-6} .

Figure 9 Topology optimization procedure



3. DISCRETE ADJOINT APPROACH USED AT COMPRESSIBLE SUBSONIC TURBULENT FLOW OPTIMIZATION

Another approach for determining sensitivities of the functional gradient (Eq. 4) is to differentiate the state equation $F(\phi, g) = 0$ to obtain by the chain rule, the sensitivity equation:

$$\left(\frac{\partial F}{\partial \phi} \right]_{g^{(m)}} \frac{d\phi}{dg} \Big]_{g^{(m)}} = - \frac{\partial F}{\partial g} \Big]_{g^{(m)}} \quad (56)$$

Note that $\left(\frac{\partial F}{\partial \phi} \right]_{g^{(m)}}$ and $\frac{\partial F}{\partial g} \Big]_{g^{(m)}}$ depend only on $g^{(m)}$ and $\phi(g^{(m)})$ so they are evaluated after step 1 (section 1.3), then the equation is solved for the sensitivity $\frac{d\phi}{dg} \Big]_{g^{(m)}}$. The system is linear in the sensitivities $\frac{d\phi}{dg}$, then if multiple design variables are available, an equation similar to the sensitivity equation will be obtain for each corresponding sensitivity. However, the left-hand side operator $\frac{\partial F}{\partial \phi} \Big]_{g^{(m)}}$ is independent of the particular design variable. Once the sensitivity $\frac{d\phi}{dg} \Big]_{g^{(m)}}$ is evaluated at the current values of the design variables, it can be used at Eq. 49 to determine the gradient of the functional evaluated at the current values of the design variables. Finally, the sensitivities of the state equation equation (Eq.1) can be defined by:

$$\phi_k = \frac{\partial \phi}{\partial \alpha_k}, k = 1, \dots, K \quad (57)$$

The direct differentiation w.r.t. design variables α_k , gives the derivative of the functional:

$$\frac{DF}{D\alpha_k} = \sigma \alpha_k + \int_{\Omega} (\phi - \Phi) \phi_k d\Omega, k = 1 \dots, K \quad (58)$$

The direct differentiation of the state equation with respect to the design variables α_k , results in the sensitivity equations of the system:

$$-\nabla \cdot (a \nabla \phi_k) + b \cdot \nabla \phi_k + 3\phi^2 \phi_k = f_k \text{ in } \Omega, k = 1 \dots, K \quad (59)$$

and

$$\phi_k = 0 \text{ on } \Gamma, k = 1 \dots, K \quad (60)$$

Then, the sensitivity for the gradient of the functional with respect to the control parameters can be obtained as

$$\begin{pmatrix} \frac{DF}{D\alpha_1} \\ \dots \\ \frac{DF}{D\alpha_k} \end{pmatrix} = \begin{pmatrix} \sigma\alpha_1 + \int_{\Omega} (\phi - \Phi)\phi_1 \\ \dots \\ \sigma\alpha_k + \int_{\Omega} (\phi - \Phi)\phi_k \end{pmatrix} \quad (61)$$

This is the basis of the discrete adjoint approach used at the following research stage. The proposed T.O. formulation establishes to minimize the energy dissipation through the entire domain subjected to the FANS equations, the volume constraint, and the permeability design variable of the volume cells. In this approach, the adjoint code is obtained via the automatic differentiator tool without hand-derivation. Its flexibility and robustness allow the main contribution of the research, relying on the topology optimization of compressible turbulent subsonic flow. To do so, the developed FEniCS TopOpt FOAM software is extended to compressible fluid flow applications by including the energy equation calculation, the compressible treatment of turbulence phenomenon, compressibility factors related to numerical schemes and the real gas state equation. Both the Spalart-Allmaras and the Wray-Agarwal turbulence models are implemented and analysed for different applications. This chapter follows the organization of presenting first the equilibrium equations for compressible turbulent flow, followed by the T.O. formulation, its adjoint equations and an explanation of the optimization algorithm used along with its numerical implementation.

3.1. EQUATION OF STATE

Perfect Gas Modelling

This research considers some assumptions for treating compressible turbulent flow modelling. At first, the subsonic compressible regime ($Ma < 0.7$) and the ideal-perfect gas state equation Eq.(62):

$$\rho = \frac{p}{\bar{R}T} \quad (62)$$

where ρ is the fluid density, p the pressure, T the temperature, $\bar{R} = R/M$, R is the perfect gas constant and M is the gas molar mass. Also, Stokes' hypothesis is employed to correlate the bulk viscosity (ζ) to the dynamic viscosity (μ), which is approximately the case for various other gases that are usual in CFD applications (Wilcox 1993):

$$\zeta = -\frac{2}{3}\mu \quad (63)$$

Finally, the fluid is assumed as calorically ideal-perfect so that its specific heat coefficients are constants:

$$e = c_v T \text{ and } h = c_p T \quad (64)$$

where c_v and c_p are the specific heat at constant volume and constant pressure, respectively (Wilcox 1993).

Real Gas Modelling

At the ideal-real gas assumption, the dynamic viscosity μ is modelled by Sutherland Law (White, 2006), which gives a relationship between the dynamic viscosity and the temperature of an ideal gas. In Sutherland Law, the local value of dynamic viscosity is determined by plugging the local value of temperature (T) into Eq.(65):

$$\mu = \mu_0 \left(\frac{T}{T_0}\right)^{\frac{3}{2}} \left(\frac{T_0 + S}{T + S}\right) \quad (65)$$

where $\mu_0 = 1,76 \times 10^{-5}$ [kg/ms], $T_0 = 491,6R$ and $S = 198,6R$.

Another fact for real gas modelling is the real gas compressibility, which in the current works is enabled by the Peng-Robinson model for the state equation. The equation is expressed in terms of the critical properties (T_c, p_c) and the acentric factor (w) Eq.(66):

$$p = \frac{RT}{V_m - b} - \frac{a\alpha}{V_m^2 + 2bV_m - b^2}$$

$$a \approx 0,45724 \frac{R^2 T_c^2}{p_c}$$

$$b \approx 0,07780 \frac{RT_c}{p_c} \quad (66)$$

$$\alpha = \left(1 + \kappa \left(1 - T_r^{\frac{1}{2}}\right)\right)^2$$

$$\kappa \approx 0,37464 + 1,54226w - 0,2699w^2$$

$$T_r = T/T_c$$

3.2. EQUILIBRIUM EQUATIONS OF COMPRESSIBLE TURBULENT FLOW

The compressible fluid flow is governed by the mass, momentum and energy equations of fluid flow. As turbulence phenomenon will be considered, mass-averaging operations are performed through the Favre-averaged (density-weighted) conservation equations (FANS) for steady-state compressible flow (NASA 2017; Wilcox 1993). By doing so, the compressible state equations for compressible turbulent flow are obtained (Eq.(67)(69):

$$\frac{\partial \bar{\rho} \tilde{u}_j}{\partial x_j} = 0 \quad (67)$$

$$\frac{\partial}{\partial x_j} \bar{\rho} \tilde{u}_i \tilde{u}_j = -\frac{\partial \bar{p}}{\partial x_i} + \frac{\partial \bar{\sigma}_{ij}}{\partial x_j} + \frac{\partial \tau_{ij}}{\partial x_j} \quad (68)$$

$$\frac{\partial \tilde{u}_j \bar{\rho} \tilde{H}}{\partial x_j} = \frac{\partial}{\partial x_j} (\bar{\sigma}_{ij} \tilde{u}_i + \overline{\sigma_{ij} u_i''}) - \frac{\partial}{\partial x_j} \left(\bar{q}_j + c_p \overline{\rho u_j'' T''} - \tilde{u}_i \tau_{ij} + \frac{1}{2} \overline{\rho u_i'' u_i'' u_j''} \right) \quad (69)$$

The overbar indicates the statistical time average, with the averaging time scale assumed to be long compared to turbulent fluctuations, and short compared to unsteadiness in the mean flow. The tilde symbol represents the Favre average (density-weighted), e.g. for a primal variable f , the average is defined as $\tilde{f} = \overline{\rho f} / \bar{\rho}$. Note that $f = \bar{f} + f' = \tilde{f} + f''$ (NASA 2017; Wilcox 1993). Therefore, $\bar{\rho}$, \tilde{u}_i , \bar{p} are the averaged density, velocity, and pressure, respectively. The fluctuating velocity is represented by u_i'' .

In rotating domains, the centrifugal ($2\bar{\rho}(\omega_i \times \tilde{u}_i)$) and Coriolis forces ($\bar{\rho}\omega_i \times (\omega_i \times r_i)$) are considered at the momentum FANS equation Eq.(70):

$$\frac{\partial \bar{\rho} \tilde{u}_i \tilde{u}_j}{\partial x_j} = -\frac{\partial \bar{p}}{\partial x_i} + \frac{\partial}{\partial x_j} (\bar{\sigma}_{ij} - \overline{\rho u_i'' u_j''}) + 2\bar{\rho}(\omega_i \times \tilde{u}_i) + \bar{\rho}\omega_i \times (\omega_i \times r_i) \quad (70)$$

Isothermal walls are considered, and the total specific enthalpy (H) includes the kinetic energy of the turbulent fluctuating field (k) and it is given by:

$$H = \tilde{h} + \frac{1}{2} \tilde{u}_i \tilde{u}_i + k \quad (71)$$

which differs from the total specific enthalpy of laminar flow:

$$H = h + \frac{1}{2} u_i u_i \quad (72)$$

since the mass-averaged leads to the appearance of molecular diffusion ($\overline{\tau_{ij}u_i''}$) and transport of turbulent kinetic energy ($\overline{\rho u_j'' \frac{1}{2} u_i'' u_i''}$) at the FANS energy equation (Wilcox 1993). Furthermore, since the changes in the fluid flow behaviour from the turbulence phenomenon are not small, an isentropic (ideal) flow cannot be considered.

The mass-weighted averaged specific enthalpy (\tilde{H}), statistical time-averaged heat flux (\bar{q}_j), the viscous stress tensor ($\overline{\sigma_{ij}}$) and the Reynolds stress tensor (τ_{ij}) are defined at Eq.(73)-(76), respectively (NASA 2017).

$$\tilde{H} = \tilde{E} + \frac{\bar{p}}{\bar{\rho}} \quad (73)$$

$$\bar{q}_j \approx -c_p \frac{\bar{\mu}}{Pr} \frac{\partial \tilde{T}}{\partial x_j} \quad (74)$$

$$\overline{\sigma_{ij}} \approx 2\bar{\mu} \left(\tilde{S}_{ij} - \frac{1}{3} \frac{\partial \tilde{u}_k}{\partial x_k} \delta_{ij} \right) \quad (75)$$

$$\tau_{ij} \equiv -\overline{\rho u_i'' u_j''} \quad (76)$$

where $\tilde{S}_{ij} = (\partial \tilde{u}_i / \partial x_j + \partial \tilde{u}_j / \partial x_i) / 2$ and the Prandtl number is $Pr = c_p \mu / k_{th}$. The following terms of the FANS equations need to be modelled: $c_p \overline{\rho u_j'' T''}$, $\overline{\sigma_{ij} u_i''}$, $\frac{1}{2} \overline{\rho u_i'' u_i'' u_j''}$ and $-\overline{\rho u_i'' u_j''}$. To solve the Reynolds Stress Term ($-\overline{\rho u_i'' u_j''}$) the Boussinesq approximation is used Eq.(77):

$$\tau_{ij} = 2\mu_t \left(\tilde{S}_{ij} - \frac{1}{3} \frac{\partial \tilde{u}_k}{\partial x_k} \delta_{ij} \right) - \frac{2}{3} \bar{\rho} k \delta_{ij} \quad (77)$$

where μ_t is the eddy viscosity obtained from the turbulence modelling. Since the subsonic regime is being analyzed, the $-\frac{2}{3} \bar{\rho} k \delta_{ij}$ is ignored (NASA 2017). The Reynolds analogy is used to model the turbulent heat flux Eq.(78):

$$\overline{c_p \rho u_j'' T''} \approx -\frac{c_p \mu_t}{Pr_t} \frac{\partial \tilde{T}}{\partial x_j} \quad (78)$$

where the turbulent Prandtl number for air is $Pr_t \approx 0.9$ (NASA 2017). This work considers the ideal-perfect gas law to solve the heat capacity at constant pressure, c_p . The terms associated with molecular diffusion and turbulent transport in the energy equation are modelled together, Eq.(79) (NASA 2017):

$$\overline{\sigma_{ij} u_i''} - \frac{1}{2} \overline{\rho u_i'' u_i'' u_j''} \approx \left(\bar{\mu} + \frac{\mu_t}{\sigma_k} \right) \frac{\partial k}{\partial x_j} \quad (79)$$

where σ_k is a coefficient associated with the modelling equation for k . Nevertheless, by using the SA turbulence model, k is not considered and all terms related to it are removed from the equations, e.g. $\partial k / \partial x_j = 0$.

3.3. TURBULENCE MODELLING TREATMENT

The influence of turbulence models at compressible regime is being developed mainly by LES and DNS modelling with some relative conclusions over the RANS simulations (Grigoriev 2016). In high-speed turbulent flows, the compressibility could affect the turbulence structures, the Reynolds stress-mean velocity relation, and processes of heat transfer and mixing (Gatski et al. 2019), such as found in real gas modelling. However, the analysis is extended to the different compressible regimes numbers, and literature has shown a difference between turbulence phenomena at incompressible and compressible regimes, such as that the turbulence quantities grow exponentially at a smaller rate than incompressible flow (Gatski et al. 2019) and that pressure fluctuations are not minor when temperature and density variations appear at Mach numbers greater than 0.2 (Hanifi et al. 1998). Therefore, the current research considers modifications of compressible flow to the chosen turbulence models: the Spalart-Allmaras and the Wray-Agarwal turbulence models.

3.3.1. Compressible Spalart-Allmaras Turbulence Model

The T.O. has been implemented under the SA turbulence model as literature proves its flexible applications in turbulent fluid flow. The SA formulation for compressible turbulent subsonic flow (Bueno-Orovio et al. 2012) has been validated and proved for internal flows, where its low computational cost and adaptability to work with dense meshes near the wall favour its use over other turbulence models (Deshazer 2007). Therefore, different researchers consider the SA turbulence model accuracy at compressible turbulent subsonic flow (Langlois et al. 2016; Ning and Xu 2014; Tüzüner et al. 2018), which supports its choice in the current research. The current research considers the SA-noft2 (NASA 2017) turbulence model and the Boussinesq Hypothesis, where the turbulent eddy viscosity (μ_t) is obtained by using Eq.(80)-(81):

$$\mu_t = \rho \hat{v} f_{v1} \quad (80)$$

$$\rho u_j \frac{\partial \hat{v}}{\partial x_j} = \rho c_{b1} \hat{S} \hat{v} - \rho c_{w1} f_w \left(\frac{\hat{v}}{\Delta} \right)^2 + \frac{1}{\sigma} \left[\frac{\partial}{\partial x_j} \left(\rho (v + \hat{v}) \frac{\partial \hat{v}}{\partial x_j} \right) + \rho c_{b2} \frac{\partial \hat{v}}{\partial x_i} \frac{\partial \hat{v}}{\partial x_i} \right] \quad (81)$$

where $\hat{\nu}$ is the auxiliary turbulent viscosity, and the extra terms are defined as:

$$\hat{S} = \max \left[\Omega + \frac{\hat{\nu}}{k^2 \Delta^2} f_{v2}, 0.3\Omega \right] \quad (82)$$

$$f_{v2} = 1 - \frac{\chi}{1 + \chi f_{v1}} \quad (83)$$

$$f_{v1} = \frac{\chi^3}{\chi^3 + c_{v1}^3} \quad (84)$$

$$\chi = \frac{\hat{\nu}}{\nu} \quad (85)$$

Also, W_{ij} is the vorticity field that describes the local spinning motion of a particle (i.e. its tendency to rotate, $W_{ij} = 1/2 \left(\frac{\partial u_i}{\partial x_j} - \frac{\partial u_j}{\partial x_i} \right)$), which will be used to identify regions with large turbulence. The $\Omega = \sqrt{2W_{ij}W_{ij}}$ is the vorticity magnitude and Δ the near-wall distance value. Finally, the remaining parameters are established in Eq.(88)-(87):

$$f_w = g \left[\frac{1 + c_{w3}^6}{g^6 + c_{w3}^6} \right]^{\frac{1}{6}} \quad (86)$$

$$g = r + c_{w2}(r^6 - r)$$

$$r = \min \left[\frac{\hat{\nu}}{\hat{S}k^2\Delta^2}, 10 \right] \quad (87)$$

with constants $c_{b1} = 0.1355$, $\sigma = 2/3$, $c_{b2} = 0.622$, $\kappa = 0.41$, $c_{w1} = \frac{c_{b1}}{\kappa^2} + \frac{1+c_{b2}}{\sigma}$, $c_{w2} = 0.3$, $c_{w3} = 2$, $c_{v1} = 7.1$ (Allmaras et al. 2012).

3.3.2. Compressible Wray-Agarwal Turbulence Model

The optimization of the rotational regime at large Reynolds numbers is tackled by the Wray-Agarwal turbulence model (Han et al. 2018), which combines the flexibility of the $k - \omega$ turbulence model for rotational flows, in a single equation free of the wall distance calculation. This turbulence model has been recently tested in T.O. applications (Alonso et al. 2022) and its advantage relies on diminishing the T.O. formulation complexity as the Eikonal constraint is no longer needed. The linear model is based on the Boussinesq assumption Eq.(77), which at compressible regime uses the Prandtl number as $Pr=0.72$ and the turbulent Prandtl number as

$Pr_t = 0.9$.. The model solves a variable $R = k/\omega$, at the following equation for steady-state flow:

$$\frac{\partial u_j R}{\partial x} = \frac{\partial}{\partial x_j} \left[(\sigma_R R + \nu) \frac{\partial R}{\partial x_j} \right] + C_1 R S + f_1 C_2 k \omega \frac{R}{S} \frac{\partial R}{\partial x_j} \frac{\partial S}{\partial x_j} - (1 - f_1) \min \left[C_2 k \epsilon R^2 \left(\frac{\partial S}{\partial x_j} \frac{\partial S}{\partial x_j} \right), C_m \frac{\partial R}{\partial x_j} \frac{\partial R}{\partial x_j} \right] \quad (88)$$

where the turbulent viscosity is:

$$\mu_t = \rho f_\mu R \quad (89)$$

with ρ as the density. The variable S takes on the usual definition for mean strain:

$$S = \sqrt{2 S_{IJ} S_{IJ}} \quad (90)$$

$$S_{ij} = \frac{1}{2} \left(\frac{\partial u_i}{\partial x_j} + \frac{\partial u_j}{\partial x_i} \right)$$

and $S = \max(S, 10^{-16} s^{-1})$ to avoid a zero division. The wall blocking is accounted for by the damping function:

$$f_\mu = \frac{\chi^3}{\chi^3 + C_w^3} \quad (91)$$

where $\chi = R/\nu$ and $\nu = \mu/\rho$. The wall distance free switching function is:

$$f_1 = \tanh(\arg_1^4) \quad (92)$$

$$\arg_1 = \frac{\nu + R}{2} \frac{\eta^2}{C_\mu k \omega}$$

where

$$k = \frac{\nu_t S}{\sqrt{C_\mu}}$$

$$\omega = \frac{S}{\sqrt{C_\mu}}$$

$$\eta = S \max\left(1, \left| \frac{W}{S} \right| \right) \quad (93)$$

$$W = \sqrt{2 W_{ij} W_{ij}}$$

$$W_{ij} = \frac{1}{2} \left(\frac{\partial u_i}{\partial x_j} - \frac{\partial u_j}{\partial x_i} \right)$$

The constants are defined as:

$$\begin{aligned}
 C_{1k\omega} &= 0.0829 \\
 C_{1k\epsilon} &= 0.1284 \\
 C_1 &= f_1(C_{1k\omega} - C_{1k\epsilon}) + C_{1k\epsilon} \\
 \sigma_{k\omega} &= 0.72 \\
 \sigma_{k\epsilon} &= 1.0 \\
 \sigma_R &= f_1(\sigma_{k\omega} - \sigma_{k\epsilon}) + \sigma_{k\epsilon} \\
 C_{2k\omega} &= \frac{C_{2k\omega}}{k^2} + \sigma_{k\omega} \\
 C_{2k\epsilon} &= \frac{C_{2k\epsilon}}{k^2} + \sigma_{k\epsilon} \\
 k &= 0.41 \\
 C_\omega &= 8.54 \\
 C_\mu &= 0.09 \\
 C_m &= 8.0
 \end{aligned} \tag{94}$$

Finally, the boundary conditions at solid smooth walls are defined as:

$$R_{wall} = 0 \tag{95}$$

and for the freestream:

$$R_{far-field} = 3v_\infty : to : 5v_\infty \tag{96}$$

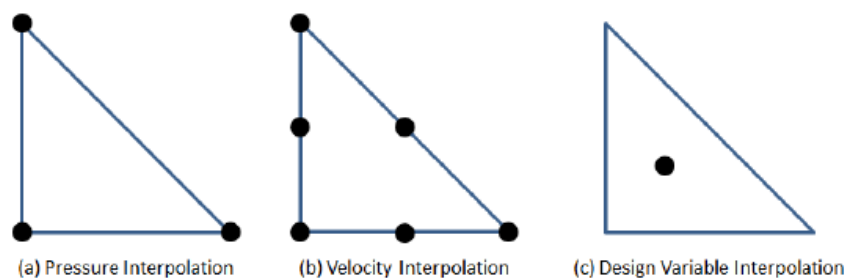
3.4. FLUID FLOW MODELLING

At this research, two different software are used to model the primal and adjoint fluid flow: the OpenFOAM and the FEniCS software. The OpenFOAM software is based on the FVM approach, explained in section 2.3 and the FEniCS software is based on the Finite Element Method (FEM), which is explained in the following.

3.4.1. The Finite Element Method Used In The FEniCS Software

The FEM is a general numerical method for solving PDEs, which subdivides a domain into finite elements. Therefore, the domain is discretized by a mesh with a finite number of points that influence the accurate representation of the geometry and the capture of the local effects. After the mesh division, the elements are set into a global system of equations for the fluid flow modelling. To solve the state equations the Galerkin method is applied, which consists of the integral construction of the inner product of the residual (trial function) and the weight functions (polynomial approximation), and then, set the integral to zero. By doing so, the error of approximation is minimized by fitting the trial function into the PDE. By doing so, the spatial derivatives from the PDE are approximated locally by a set of algebraic equations for steady-state problems. The interpolation function is used to approximate the variables inside the elements by using their nodal values. In the current research, a triangular element is used with different polynomial interpolation ranks to avoid instabilities in the resolution problem. The Taylor-Hood element (Arnold et al. 1984) is considered, where the pressure uses a triangular element with three nodes (linear interpolation) and the velocity considers a triangular element with six nodes (quadratic interpolation). Also, it helps deal with the complexity of optimizing 3D domains Finally, the inverse permeability considers one node per element (Sá and Silva 2016).

Figure 10. Triangular element interpolation (Sá and Silva 2016)



To ensure numerical stability in the fluid flow simulation at FEniCS, the Ladyzhenskaya–Babuška–Brezzi (LBB) condition is used (Brezzi and Fortin 1991). Also, the turbulence models variables pseudo-density (design variable) has a first-degree interpolation to allow the use of a Helmholtz filter when non-uniform meshes are considered, as it requires the existence of a first derivative. The Helmholtz filter influence is checked at section 4.2.2 and the precision losses when the conversion from FEM to FVM is employed is not considered yet, however, the

analysis could be performed by using different discretization schemes and meshes. To make feasible the mesh conversion it is demanded to use only triangular prisms or tetrahedron meshes for the 2D and the 3D optimizations, respectively. The FEniCS solver also considers the SIMPLE algorithm, explained in section 2.3, however, it is developed for compressible regime applications as the “OpenFOAM” considers the “rhoSimpleFOAM” solver, also based on the SIMPLE algorithm (Rahman and Mustapha 2015).

3.5. TOPOLOGY OPTIMIZATION FORMULATION

The optimization problem considers the minimization of the energy dissipation of an established domain, which is subjected to the constraints of the fluid flow physics, established by the modified FANS equations (R^p, R^u, R^T), the modified turbulence model ($R^{\tilde{v}}, R^R$), the near-wall distance calculation (R^Δ), the volume constraint, (\bar{V}) and the permeability design variable (α). Each constraint is explained as follows.

3.5.1. Permeability Design Variable (α)

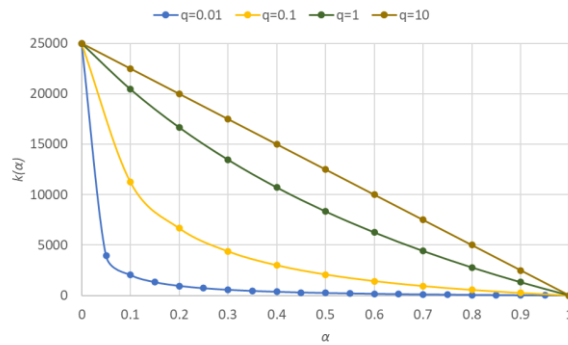
The fluid topology optimization method based on the pseudo-density approach is implemented by including an additional porosity term (k_ϕ) in Eq.(67)-(69), Eq.(81) and Eq.(88). This allows the solid or fluid region definition in the domain. The idea consists of making α to assume 0 or 1 values, to represent solid and fluid, respectively. To do so, the material distribution model proposed by (Borrvall and Petersson 2003) is applied to each fluid flow equation Eq.(97):

$$k_\phi = \bar{k}_\phi + (\underline{k}_\phi - \bar{k}_\phi)\alpha \frac{(1+q)}{(\alpha+q)} \quad (97)$$

Thus, the k_ϕ term represents each penalization to be considered, i.e. for u, \hat{v}, Δ and T , k_ϕ is defined as $k_u, k_{\hat{v}}, k_\Delta$ and k_T respectively. The penalization term proposed in the energy equation, $k_T(\alpha)(T - T_{wall})$, considers isothermal walls during the optimization process. Thus, when the modelled solid material is present, the boundaries of this material represent isothermal walls, and heat transfer is calculated only at the fluid regions and not between the solid/fluid boundaries.

The model behaves like a linear or convex interpolation function depending on the chosen value for q (Figure 11), which is a penalty parameter with a value greater than zero used to control the level of “grey” in the optimized design during topology optimization. The k_ϕ minimum value is established as zero to represent fluid and \bar{k}_ϕ maximum value is calibrated according to each case to avoid fluid entrance inside the modelled solid material. When α is equal to zero, solid regions are established, and when α equal to 1, a fluid region is represented.

Figure 11. Material model behaviour



3.5.2. Modified Equilibrium Equations of Compressible Turbulent Flow

Modified FANS Equations: R^p, R^u, R^T

To optimize fluid flow devices, T.O. is performed by maximizing/minimizing an objective function, where the domain cells permeability is changed by considering α , determining new solid/fluid regions. To do so, a penalization term is added to the momentum and energy equations relating the velocity and temperature fields, respectively, and treating the walls under isothermal conditions. High $k_\phi(\alpha)$ values raise the importance of the penalized terms in the modified equations, determining solid regions, and near-zero $k_\phi(\alpha)$ values recover the effect of the original FANS equations. Finally, the mass conservation is not penalized (Borrvall and Petersson 2003), resulting in the modified FANS equations (Eq. 98).

$$\begin{aligned}
 R^p &= \text{Continuity equation} = 0 \\
 R^u &= \text{Momentum equation} + \underbrace{k_u \tilde{u}_j}_{\text{Penalization Term}} = 0 \\
 R^T &= \text{Energy equation} + \underbrace{k_T \left(\frac{\tilde{h}}{c_p} - \frac{\tilde{h}_{wall}}{c_p} \right)}_{\text{Penalization Term}} = 0
 \end{aligned} \tag{98}$$

where the subscript "wall" indicates the values that are assumed on the walls.

Modified Spalart-Allmaras and Wray-Agarwal Turbulence Models ($\mathbf{R}^{\hat{v}}, \mathbf{R}^R$)

The SA turbulence model for the turbulent subsonic compressible flow Eq.(81) is modified by adding a penalization term ($k_{\hat{v}}\hat{v}$) in the auxiliary turbulent viscosity \hat{v} calculation:

$$R^{\hat{v}} = \text{Spalart - Allmaras equation} + \underbrace{k_{\hat{v}}\hat{v}}_{\text{Penalization Term}} = 0 \quad (99)$$

Analogously, the Wray-Agarwal turbulence model Eq.(88) is modified by adding a penalization term ($k_R R$):

$$R^R = \text{Wray - Agarwal equation} + \underbrace{k_R R}_{\text{Penalization Term}} = 0 \quad (100)$$

Modified Near-Wall Distance Calculation (\mathbf{R}^{Δ})

To calculate the near-wall distance (Δ), the modified Eikonal equation is considered (Alonso et al. 2021; Yoon 2016):

$$\frac{\partial^2 G}{\partial x_i \partial x_i} + \sigma_w G \left(\frac{\partial^2 G}{\partial x_i \partial x_i} \right) = (1 + 2\sigma_w)G^4 + \underbrace{k_{\Delta}(G - G_0)}_{\text{Penalization Term}} \quad (101)$$

where $G = G_0/(G_0\Delta + 1)$ and $G_0 = 1/\Delta_{ref}$. G is the reciprocal near-wall distance, Δ_{ref} is a reference value for the near-wall distance (in the current case, the maximum mesh element size), k_{Δ} is the near-wall distance penalization and σ_w is a relaxation factor for the near-wall distance computation.

3.5.3. Topology Optimization Problem Definition

Here, the T.O. is formulated to minimize the energy dissipation (F) across the domain, which is commonly used in T.O. of fluids. The objective function is applied to a compressible turbulent flow, where the viscous energy dissipation term can be obtained from the integral form of the energy equation. The objective function F , is subjected to the constraints of the fluid flow physics, established by the modified FANS equations (R^p, R^u, R^T), a volume constraint $\left(\bar{V}_{frac} \leq \frac{\int_{\Omega} \alpha d\Omega}{\int_{\Omega} d\Omega} \right)$ used to express the amount of fluid domain that aims to be optimized (Papoutsis-Kiachagias and Giannakoglou 2016), the modified turbulence model is selected according to the turbulence model: $R^{\hat{v}}$ for SA and R^R for Wray-Agarwal, the near-wall distance calculation (R^{Δ}), and the permeability design variable (α), resulting in the final T.O. formulation:

Minimize

$$F = \int_{\Omega} \frac{1}{2} (\mu + \mu_T) \left(\frac{\partial \tilde{u}_i}{\partial x_j} + \frac{\partial \tilde{u}_j}{\partial x_i} \right) \left(\frac{\partial \tilde{u}_i}{\partial x_j} + \frac{\partial \tilde{u}_j}{\partial x_i} \right) d\Omega + \int_{\Omega} k_u \tilde{u}_i^2 d\Omega$$

subject to

$$0 \leq \alpha \leq 1$$

$$R^p = \frac{\partial(\bar{\rho}\tilde{u}_i)}{\partial x_i} = 0$$

$$R^u = \frac{\partial(\bar{\rho}\tilde{u}_j\tilde{u}_i)}{\partial x_j} + \frac{\partial\bar{p}\delta_{ij}}{\partial x_j} - \left[(\mu) \left(\frac{\partial\tilde{u}_i}{\partial x_j} + \frac{\partial\tilde{u}_j}{\partial x_i} - \frac{2}{3} \frac{\partial\tilde{u}_k}{\partial x_k} \delta_{ij} \right) - \overline{\rho u_i'' u_j''} \right] + k_u \tilde{u}_i = 0 \quad (102)$$

$$R^T = \frac{\partial\tilde{u}_j\bar{\rho}\tilde{h}}{\partial x_j} - \frac{\partial}{\partial x_j} \{ \bar{\sigma}_{ij} \tilde{u}_i - \tilde{u}_i \overline{\rho u_i'' u_j''} \} + \frac{\partial}{\partial x_j} \left(\bar{q}_j - \frac{c_p \tilde{\mu}_t}{Pr_t} \frac{\partial \tilde{T}}{\partial x_j} - \left(\mu + \frac{\mu_t}{\sigma_k} \right) \frac{\partial k}{\partial x_j} \right) + k_T \left(\frac{\tilde{h}}{c_p} - \frac{\tilde{h}_{wall}}{c_p} \right) = 0$$

$$R^{\hat{v}} = \rho u_j \frac{\partial \hat{v}}{\partial x_j} - \rho c_{b1} \hat{S} \hat{v} + \rho c_{w1} f_w \left(\frac{\hat{v}}{\Delta} \right)^2 - \frac{1}{\sigma} \left[\frac{\partial}{\partial x_j} \left(\rho (v + \hat{v}) \frac{\partial \hat{v}}{\partial x_j} \right) - \rho c_{b2} \frac{\partial \hat{v}}{\partial x_i} \frac{\partial \hat{v}}{\partial x_i} \right] + k_{\hat{v}} \hat{v} = 0$$

$$R^{\Delta} = \frac{\partial^2 G}{\partial x_i \partial x_i} + \sigma_w G \left(\frac{\partial^2 G}{\partial x_i \partial x_i} \right) - (1 + 2\sigma_w) G^4 - k_{\Delta} (G - G_0) = 0$$

$$\bar{V}_{frac} \leq \frac{\int_{\Omega} \alpha d\Omega}{\int_{\Omega} d\Omega}$$

3.6. NUMERICAL IMPLEMENTATION

The implementation of the adjoint code becomes challenging when compressible fluid flow regime is tackled, due to large dependences on the variables to be derived by including the energy equation, compressibility effects, real gas performance, among others. Therefore, the derivation of the adjoint code is proposed by means of the discrete adjoint approach, which manipulates symbolically sensitivities of the variables by using either the automatic differentiator or the finite difference approach. The FEniCS software includes a discrete-based optimizer that uses the automatic-differentiator tool to obtain the adjoint code of fluid flow.

3.6.1. The Automatic Differentiator From FEniCS Software

In FEniCS, the variational form of the discrete equations is specified in the domain-specific language UFL, from which optimized finite element code is generated to compute their solutions. This high-level description can be algorithmically manipulated before the code. The

forward model equations implemented in the FEniCS platform can then be used by dolfin-adjoint to automatically derive the adjoint model (Alnæs et al. 2014; Farrell et al. 2013; Mitusch et al. 2019). The software library dolfin-adjoint inspects the high-level problem description provided at runtime and performs the required tasks for deriving the adjoint model automatically. The resulting adjoint model is represented in the same high-level data format as the forward problem. Therefore, the code generation technique in FEniCS can be applied to the adjoint model as easily as to the forward model.

The use of dolfin-adjoint has the advantage that the derivation and solution of the adjoint model require almost no user intervention. Besides, the adjoint derivation is generic: it applies to any PDE discretized with the finite element method (Funke 2012). The dolfin-adjoint library collects the necessary information about the discrete forward system for the automatic derivation of the adjoint model. As such, each equation in the forward model is annotated with information about which variable the equation solves for and its dependencies to any forward equation that has been solved before (chain rule).

In dolfin-adjoint, the annotation happens automatically during the execution of the forward model. This is achieved in dolfin-adjoint by overloading all FEniCS routines that modify the forward solution. These overloaded functions extract the required information from the UFL input and use the dolfin-adjoint interface to annotate the corresponding equation (Funke 2012).

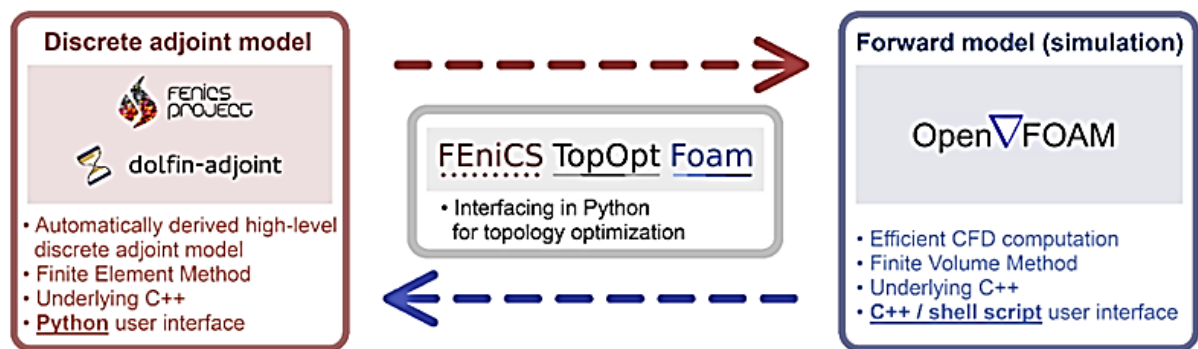
3.6.2. The FEniCS TopOpt Foam Software

The standard FEniCS version treats only laminar incompressible regimes and the implementation of a compressible turbulent based fluid flow solver is not an easy task as it demands a challenging programming to include not only the energy equation, but also the turbulence model treatment, numerical schemes to discretise accurately the energy equation variables, and even by programming such fluid flow solver it is not guaranteed a stabilized solver to treat compressible turbulent fluid flow solver. There are already fluid flow simulations software able to model compressible turbulent flow, e.g. the FVM-based OpenFOAM software. Unfortunately, these software does not incorporate an automatic-differentiator tool to manage compressible turbulent regime, and also, it has not been designed to optimize fluid flow. Some works (He et al. 2020; Okubo and Silva 2022; Okubo et al. 2022) implemented a discrete-adjoint based tool to treat compressible regime al laminar regime and turbulence via an approximated solution. Nevertheless, part of the scientific contributions of

the current research relies on solving the turbulence phenomenon at the adjoint code and coupling of the automatic differentiator tool from an efficient optimization software (FEniCS) with an efficient fluid flow modelling software (OpenFOAM), resulting in the FEniCS TopOpt Foam software. The advantage of the discrete adjoint approach relies on the automation of the adjoint model generation, which means that any objective function, turbulence model, fluid flow regime...may be considered, and only the forward model equations need to be specified at both software.

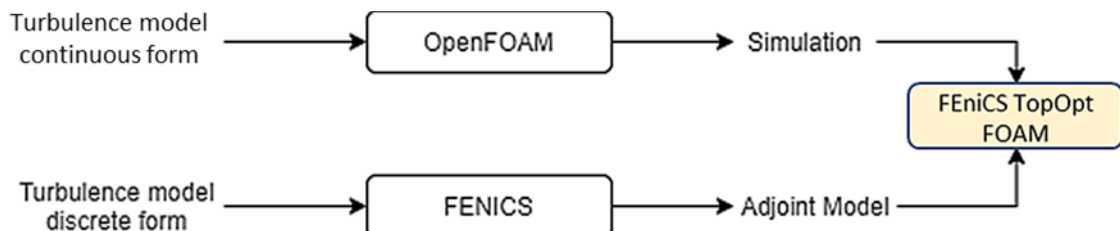
Since the automatic derivation of the adjoint model is given in this work in the FEniCS/dolfin-adjoint approach, an interface programmed in Python is used to combine with the OpenFOAM simulation (Figure 12) (Alonso et al. 2021).

Figure 12. FEniCS TopOpt Foam Interaction



The optimization using the FEniCS TopOpt FOAM software is composed of the fluid flow simulation and the adjoint model acquisition (Figure 13). The OpenFOAM software is used for the CFD modelling of the compressible turbulent flow and the “dolfin-adjoint” of FENICS to obtain the adjoint model.

Figure 13. FEniCS and OpenFOAM coupling



3.6.3. Weak Form Of The Equilibrium Equation Of Compressible Turbulent Flow

In order to automatically derive the adjoint model, it is needed to specify the weak form of the finite element method in FEniCS. The weak form of the compressible turbulent subsonic flow is developed in Appendix 7.3, and shown at following:

$$\begin{aligned}
 R_w^p &= \int_{\Omega} \left(\frac{\partial}{\partial x_i} \bar{\rho} \tilde{u}_i \right) w_p \, d\Omega = 0 \\
 R_w^u &= \int_{\Omega} \left[\frac{\partial}{\partial x_j} (\bar{\rho} \tilde{u}_j \tilde{u}_i) \right] w_{u_j} \, d\Omega + \int_{\Omega} \left[\frac{\partial}{\partial x_i} \bar{p} \right] w_{u_i} \, d\Omega - \int_{\Omega} \left\{ \left(\frac{\partial \tilde{u}_i}{\partial x_j} \right) \frac{\partial}{\partial x_j} w_{u_j} (\mu - \mu_t) \right\} \, d\Omega + \\
 &\int_{\Gamma} \left\{ w_{u_j} (\mu - \mu_t) \frac{\partial \tilde{u}_i}{\partial x_j} n_j \right\} \, d\Gamma + \int_{\Omega} \left\{ \frac{\partial}{\partial x_k} \tilde{u}_k \frac{\partial}{\partial x_k} \left[\frac{2}{3} \delta_{ij} (\mu - \mu_t) w_{u_j} \right] \right\} \, d\Omega - \int_{\Gamma} \left\{ \left[\frac{2}{3} \delta_{ij} (\mu - \mu_t) w_{u_j} \right] \frac{\partial}{\partial x_k} \tilde{u}_k n_k \right\} \, d\Gamma + \int_{\Omega} [k_u \tilde{u}_i] w_{u_j} \, d\Omega = 0 \\
 R_w^T &= \int_{\Omega} \left[\frac{\partial}{\partial x_j} (\tilde{u}_j \bar{\rho} \tilde{H}) \right] w_T \, d\Omega - \int_{\Omega} \left\{ \frac{\partial}{\partial x_j} (\tilde{u}_i \mu - \tilde{u}_i \mu_t) \right\} 2w_T \, d\Omega + \int_{\Omega} \frac{\partial \tilde{u}_i}{\partial x_j} \frac{\partial}{\partial x_j} (2w_T) \, d\Omega - \\
 &\int_{\Gamma} 2w_T \frac{\partial \tilde{u}_i}{\partial x_j} n_j \, d\Gamma - \int_{\Omega} \frac{\partial}{\partial x_k} \tilde{u}_k \frac{\partial}{\partial x_k} \left(\frac{4}{3} \delta_{ij} w_T \right) \, d\Omega + \int_{\Gamma} \frac{4}{3} \delta_{ij} w_T \frac{\partial}{\partial x_k} \tilde{u}_k n_k \, d\Gamma - \\
 &\int_{\Omega} \left(\frac{\partial \tilde{T}}{\partial x_j} \right) \frac{\partial}{\partial x_j} \left[c_p w_T \left(\frac{\mu}{Pr} + \frac{\mu_t}{Pr_t} \right) \right] \, d\Omega + \int_{\Gamma} c_p w_T \left(\frac{\mu}{Pr} + \frac{\mu_t}{Pr_t} \right) \left(\frac{\partial \tilde{T}}{\partial x_j} \right) n_j \, d\Gamma + \int_{\Omega} \left[k_T \left(\frac{\tilde{h}}{c_p} - \frac{\tilde{h}_{wall}}{c_p} \right) \right] w_T \, d\Omega = 0 \tag{103} \\
 R_w^{\Delta} &= \int_{\Omega} \left[-\frac{\partial G}{\partial x_i} (1 + \sigma_w G) \right] \frac{\partial}{\partial x_i} w_{\Delta} \, d\Omega + \int_{\Gamma} w_{\Delta} \frac{\partial}{\partial x_i} [G(1 + \sigma_w G)] n_i \, d\Gamma - \int_{\Omega} [(1 + 2\sigma_w) G^4] w_{\Delta} \, d\Omega - \int_{\Omega} [k_{\Delta} (G - G_0)] w_{\Delta} \, d\Omega = 0 \\
 R_w^{\hat{v}} &= \int_{\Omega} \left(\rho u_j \frac{\partial}{\partial x_j} \hat{v} - \rho c_{b1} \hat{S} \hat{v} + \rho c_{w1} f_w \left(\frac{\hat{v}}{\Delta} \right)^2 \right) w_{\hat{v}} \, d\Omega - \int_{\Omega} \left(\frac{1}{\sigma} \frac{\partial}{\partial x_j} \left(\rho (v + \hat{v}) \frac{\partial \hat{v}}{\partial x_j} \right) \right) w_{\hat{v}} \, d\Omega + \\
 &\frac{1}{\sigma} \rho c_{b2} \left[-\int_{\Omega} \left(\frac{\partial}{\partial x_i} \hat{v} \right) \frac{\partial}{\partial x_i} w_{\hat{v}} \, d\Omega + \int_{\Gamma} w_{\hat{v}} \frac{\partial}{\partial x_i} \hat{v} n_i \, d\Gamma \right] + \int_{\Omega} (k_{\hat{v}} \hat{v}) w_{\hat{v}} \, d\Omega = 0
 \end{aligned}$$

where $w_p, w_{\hat{v}}, w_G, w_T$ and w_u are the test functions of the state variables ($\bar{p}, \hat{v}, G, \tilde{T}$ and \tilde{u}), respectively. From the mutual independence of the test functions, the weak form equations can be established as a single equation:

$$F = R^p + R^u + R^T + R^{\Delta} + R^{\hat{v}} = 0 \tag{104}$$

3.6.4. Helmholtz Pseudo-Density Filter

In topology optimization, the use of regularization mechanisms is employed to counter numerical instabilities presented due to mesh dependency and local minima (Sigmund and Petersson 1998). The regularization used is the Helmholtz filter, which is a PDE-based topology optimization pseudo-density filter (Lazarov and Sigmund 2011). It consists of weighting the values of the original design variable (α) with a Green function that is always positive with an integral equal to 1 (Lazarov and Sigmund 2011). Smaller values of the filter length r_H , leads to a Dirac delta function ($\alpha_f \rightarrow_{r_H \rightarrow 0^+} \alpha$). The equivalent of the Green function is expressed by solving a modified Helmholtz equation with homogeneous Neumann boundary condition, which boundary is stated at (Lazarov and Sigmund 2011):

$$\begin{aligned} -r_H^2 \nabla^2 \alpha_f + \alpha_f &= \alpha \text{ in } \Pi \\ \frac{\partial \alpha_f}{\partial n} &\text{ on } \Pi \end{aligned} \quad (105)$$

where α is the original design variable, α_f is the filtered design variable and r_H is the filter length. A one-shot-like scheme is considered, which consists of solving only a few iterations (50, in the present work) of the SIMPLE solver in the direct problem, and then computing the adjoint model. Through this scheme, stabilized CFD simulations and adjoint model acquisition are guaranteed, by avoiding vortex generation along the topology optimization procedure.

3.6.5. Interfacing OpenFOAM with FEniCS/dolfin-adjoint

To solve the fluid flow modelling, the rhoSimpleFoam solver from OpenFOAM is modified by including the penalization terms to the momentum equation, the energy equation, the Spalart-Allmaras and the Wray-Agarwal turbulence model. The adjoint model is computed in the finite elements software FEniCS through dolfin-adjoint (Farrell et al. 2013). Finally, the T.O. problem is solved through the IPOPT optimizer, from the interface of the dolfin-adjoint library.

The idea of coupling FEniCS and OpenFOAM consists of solving the fluid flow modelling at first in the OpenFOAM software and derived automatically the adjoint model in FEniCS/dolfin-adjoint. FEniCS is implemented in C++ and its automatic differentiator considers UFL language to represent the weak form and functionals for the finite element matrices. By doing so, the adjoint model is automatically derived from the weak form and objective functions by the dolfin-adjoint library, which is restricted to a Python interface of FEniCS. On the other hand,

the OpenFOAM software is an open-source CFD software also programmed in C++ and based on the FVM. OpenFOAM operates in the lowest degree of finite volumes, which advantage relies on its computational cost. The difference between the FVM and the FEM is stated as the first is based on the local conservation of fluxes and the second is based on the global conservation of fluxes. Since dolfin-adjoint is written in Python, the coupling with OpenFOAM is feasible when its C++ code and shell script functionalities are accessible in Python as well. Therefore, the library that joints this code is developed and labelled as FEniCS TopOpt FOAM. The boundary conditions selected in OpenFOAM might differ from the ones available at FEniCS due to the discretization based-method of each software. For the turbulent variables, the boundary conditions can be implemented in FEniCS equally as in OpenFOAM. The wall distance is computed through the finite element method and later imported into OpenFOAM, to avoid implementing and solving a similar equation. Although in FEniCS no boundary conditions need to be explicitly imposed for the pressure and the outlet velocity, the OpenFOAM software requires all boundary conditions to be explicitly imposed: at the inlet and wall boundaries, the normal gradient of the pressure is set to zero ($\partial p / \partial n_i = 0$), and the outlet regions that consider a Dirichlet boundary condition, e.g. $p = 0$, is stated as a “stress-free” boundary condition ($(T_i + T_{R_i})n_i = 0$) in FEniCS.

3.6.6. Topology Optimization Loop

The T.O. developed method (Figure 14) computes the sensitivities as follows:

- a) starts by solving the simulation of the fluid flow: to do so, a mesh conversion between FEniCS and OpenFOAM is performed due to OpenFOAM dependence on using 3D meshes only, despite 2D simulations can be performed through the “empty” library function (Ltd.). After that, the state variables, design variables, boundary conditions and the extra setups are converted by “FEniCS TopOpt FOAM” to variable and configuration files. Then, a specific solver for OpenFOAM is selected, which will be employed simultaneously by FEniCS, e.g. the SIMPLE algorithm.
- b) Conversion from the OpenFOAM files to the FEniCS variables: when the fluid flow modelling finish, the state variables files of the result are converted to the state variables in FEniCS. At that moment, the dolfin-adjoint computes the adjoint model, which is automatically generated from the forward model specified in FEniCS. The conversion starts by mapping the internal values of the OpenFOAM variables to the element-wise variables in FEniCS ($dP_0, "DGO"$). Then, the element-wise variables are projected into the

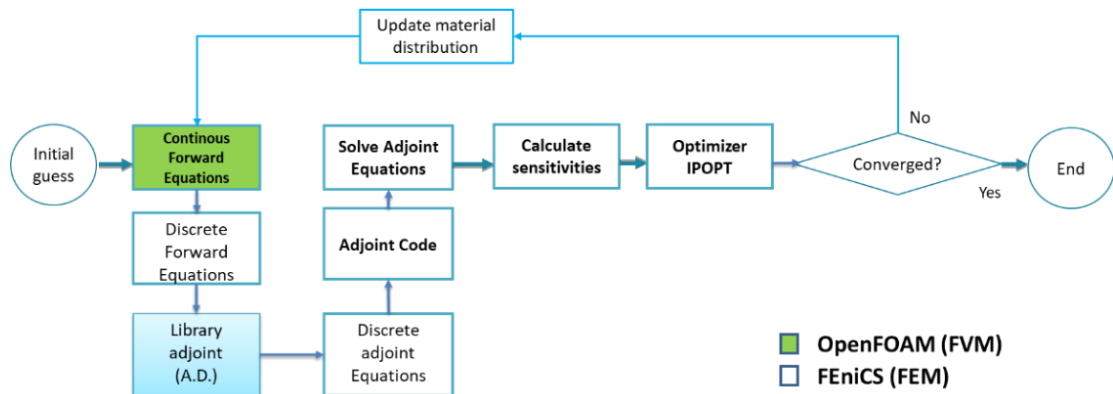
interpolation that is being used in the adjoint model. After that, the isolated state variables are joined together in a single state vector by using the “FunctionAssigner” (Copyright FEniCS Project) from FEniCS. When turbulent variables are converted, the values must remain positive and different from zero because some turbulence models depend on square roots/divisions. Also, a small-radius Helmholtz filter is applied in the turbulent variables to alleviate some sharp transitions, which may hinder post-processing operations in FEniCS. Finally, the original Dirichlet boundary conditions are reimposed onto the state vector, to consider the external faces values from the internal values taken from OpenFOAM. By doing so, numerical errors on the boundaries are avoided. A complete picture of the situation is given by the weak form of a projection function:

$$\int_{\Pi} a_{orig} w_p d\Pi = \int_{\Pi} a_p w_p d\Pi \quad (106)$$

where a_{orig} is the function being projected and a_p is the obtained projected function.

- c) Interfacing of the simulation with dolfin-adjoint: it requires “overloading” a specific internal function of the solver object in the dolfin-adjoint library, regarding the “forward simulation”.

Figure 14. T.O. flowchart.

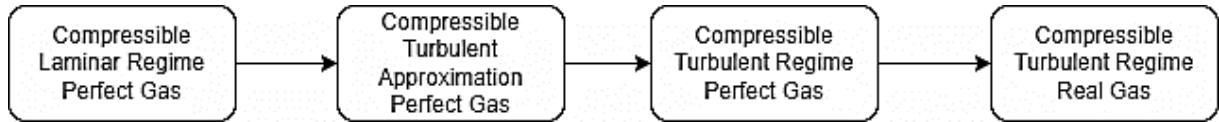


3.7. PROGRESSIVE STRATEGY

T.O. of compressible turbulent regime is a challenging process that requires not only powerful solvers and accurate discretization methods, but also the development of innovative T.O. formulations and techniques. The optimization is developed in FEniCS TopOpt Foam (Alonso et al. 2021) for compressible turbulent subsonic regime. The optimization process is tackled with a progressive strategy, which consists in optimizing the distribution of the design variable at laminar regime and taking its topology layout result as an initial guess to consider the

turbulent regime (by decreasing the fluid viscosity). This is made to facilitate the T.O. parameters calibration and to identify the turbulence influence at T.O. of compressible turbulent subsonic regime. The other fluid properties remain constant during the optimization process (Figure 15).

Figure 15. Progressive strategy



4. RESULTS

Different 2D and 3D examples are shown in the following chapter, where the incompressible regime is developed firstly to calibrate the turbulence model at T.O. Then, the compressible regime is tackled by considering the energy equation and the compressibility influence at T.O. of real gases. To discretize each regime the Mach number (Ma) is defined as Eq.(107):

$$Ma = \frac{u_{inlet}}{u_{sound}} \quad (107)$$

where u_{inlet} and u_{sound} are the inlet velocity at the domain boundary and the speed of sound of the analyzed fluid respectively. When $Ma < 0.3$ the case is considered incompressible, which results are presented in section 4.1. Then, the examples at compressible regime, i.e. $Ma > 0.3$, are presented at section 4.2.

In addition, each regime evaluates two kinds of flows: the laminar and turbulent flow, which are identified by the Reynolds numbers (Re) at the inlet domain boundary:

$$Re_{inlet} = \frac{u_{inlet} L_{inlet} \rho}{\mu} \quad (108)$$

where L_{inlet} , μ and ρ are the characteristic inlet length, density, and dynamic viscosity respectively. At the current research, the laminar flow is considered when the $Re_{inlet} < 3000$, otherwise the fluid is treated as turbulent.

4.1. TOPOLOGY OPTIMIZATION OF INCOMPRESSIBLE FLOW CONSIDERING THE CONTINUOUS ADJOINT APPROACH

As mentioned before, a progressive methodology is attempted to discretize and calibrate by steps the first T.O. formulation to reach compressible turbulent regime. The first step consists on solving the incompressible flow at laminar and turbulent regime.

Different domains are evaluated to validate the continuous-adjoint and the automatic differentiation approaches implemented at the “adjointTopOptFOAM” and the “FEniCS TopOpt Foam” software respectively. All examples of laminar regime consider Table 1 boundary conditions.

Table 1. Boundary conditions at incompressible laminar regime

	Primal Boundary Conditions		Adjoint Boundary Conditions		Design Variable Boundary Conditions
	\mathbf{u}	\mathbf{p}	\mathbf{u}_a	\mathbf{p}_a	α
inlet	u_{inlet}	$\frac{\partial p}{\partial n} = 0$	$u_a = u$	$\frac{\partial p_a}{\partial n} = \frac{\partial p}{\partial n}$	1
Outlet	$\frac{\partial u}{\partial n} = 0$	p_{out}	$\frac{\partial u_a}{\partial n} = \frac{\partial u}{\partial n}$	$p_a = p$	1
wall	$u = 0$	$\frac{\partial p}{\partial n} = 0$	$u_a = u$	$\frac{\partial p_a}{\partial n} = \frac{\partial p}{\partial n}$	0

After optimizing the laminar incompressible regime, the turbulence phenomenon is treated with the Spalart-Allmaras turbulence model. Therefore, the primal and adjoint boundary conditions need to include the turbulent viscosity (ν_t) and the modified turbulent viscosity ($\tilde{\nu}$). This update is reflected in Table 2 and Table 3 respectively.

Table 2. Primal boundary conditions at the incompressible turbulent regime

Primal Boundary Conditions	\mathbf{u}_i [m/s]	\mathbf{p} [Pa]	\mathbf{v}_t	$\tilde{\nu}$
Inlet	u_{inlet}	$\frac{\partial p}{\partial n} = 0$	$v_{t\,inlet}$	$\tilde{\nu} = cte$
Outlet	$\frac{\partial u_i}{\partial n} = 0$	$p = 0$	$v_{t\,outlet}$	$\frac{\partial \tilde{\nu}}{\partial n} = 0$
Wall	$u = 0$	$\frac{\partial p}{\partial n} = 0$	$v_t = \max\left(0, \frac{u_{T^*}^2}{ \nabla u_i + \zeta} - \nu_w\right)$	$v_t = \max\left(0, \frac{u_{T^*}^2}{ \nabla u_i + \zeta} - \nu_w\right)$

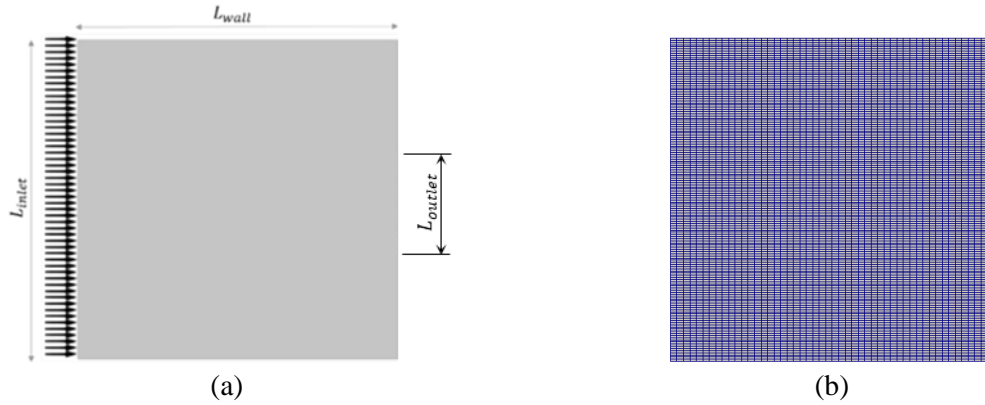
Table 3. Adjoint boundary conditions at incompressible turbulent regime (Munday 2010; Papoutsis-Kiachagias and Giannakoglou 2016).

Adjoint Boundary Conditions	\mathbf{v}_i [m/s]	\mathbf{q} [Pa]	$\hat{\nu}_a$	α
Inlet	$v_{i_a} = u_{inlet}$	$\frac{\partial q_a}{\partial n} = \frac{\partial p}{\partial n}$	$\tilde{\nu}_a = 0$	$\alpha = 1$
Outlet	$v_i = v_{i_t} u_n + (v + v_t) \left(\frac{\partial v_i}{\partial x_j} + \frac{\partial v_j}{\partial x_i} \right) n_j t_i$	$q = v_n u_n + u_i \cdot v_i + (v + v_t) \left(\frac{\partial v_i}{\partial x_j} + \frac{\partial v_j}{\partial x_i} \right) n_j n_i + \tilde{\nu}_a \tilde{\nu}$	$-\frac{\partial v_t}{\partial \tilde{\nu}} v_i \left(\frac{\partial u_i}{\partial x_j} + \frac{\partial u_j}{\partial x_i} \right) n_j + \tilde{\nu}_a u_j n_j + \left(v + \frac{\tilde{\nu}}{\sigma} \right) \frac{\partial \tilde{\nu}_a}{\partial x_j} n_j = 0$	$\alpha = 1$
Wall	$v_{w_a} = \sqrt{(v + v_t) \left(\frac{\partial v_i}{\partial x_j} + \frac{\partial v_j}{\partial x_i} \right) n_j} = 0$	$\frac{\partial q_a}{\partial n} = \frac{\partial p}{\partial n}$	$\tilde{\nu}_a = 0$	$\alpha = 0$

4.1.1. Converging Nozzle Example

The case consists of a horizontal straight channel with an inlet/outlet ratio of 3 discretized by a 100×100 hexahedral mesh (Figure 16).

Figure 16. (a) Nozzle domain, and (b) mesh discretization



At first, the case is tested in laminar incompressible regime to validate the accurate implementation of the developed “adjointTopOptFOAM” software. The inlet velocity is stated as $u_{inlet} = 1$ [m/s], and kinematic viscosity of $\nu = 1$ [m²/s], resulting in a $Re_{inlet} = 1$. The optimization parameters are calibrated to: $\bar{V}_{target} = 0.5$, $q_\phi = 0.1$, $\underline{k}_\phi = 2.5 \times 10^{-4}$ and $\bar{k}_\phi = 2.5 \times 10^4$, resulting in the optimized topologies of Figure 17.

Figure 17. Optimized converging nozzle under laminar incompressible regime reported by (a) literature (Borrvall and Petersson 2003) and (b) the “adjointTopOptFoam” software



As seen, the resemblance between the literature and the developed software is high enough to validate its implementation.

Now, the turbulence regime is treated by updating its boundary conditions to $|\bar{u}_{inlet}| = 3$ [m/s], fluid properties of $\tilde{\nu}_{inlet} = \tilde{\nu}_{outlet} = 1$ [m²/s], and $\nu = 1 \times 10^{-3}$ [m²/s], which results in a $Re_{inlet} = 3 \times 10^3$. The influence of both optimizers (the CDV and IDV approach) is evaluated during the optimization process, and each case is tested separately under the optimization parameters calibrated presented in Table 4, which results in the smooth topologies of Figure 19. An interesting case is depicted in the optimization process, where the resolution of the topology under the IDV optimizer (Figure 18b) allows a clear fluid-solid boundary region, avoiding intermediate grey regions, which occur in the CDV-based approach (Figure 18a).

Table 4. Calibrated T.O. parameters at the nozzle case for the CDV and IDV approaches.

\bar{V}_{target}	$q_{\phi_{CDV}}$	$q_{\phi_{IDV}}$	\bar{k}_u	\bar{k}_{ν_t}	\bar{k}_Δ
0.3	0.1	1.0	1×10^4	1×10^{-3}	25

Figure 18. T.O. of Nozzle using (a) CDV and (b) IDV optimizers at incompressible turbulent flow

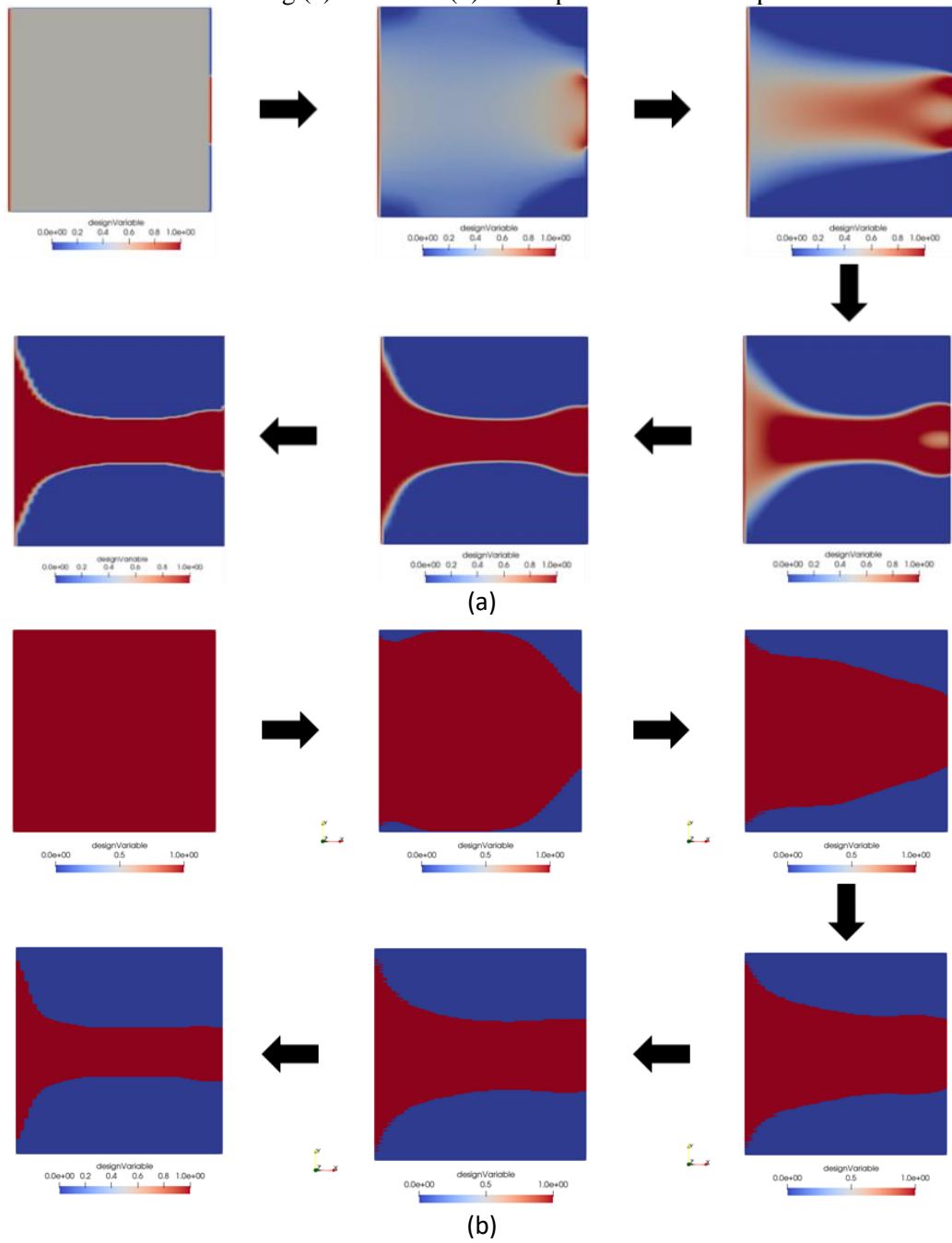
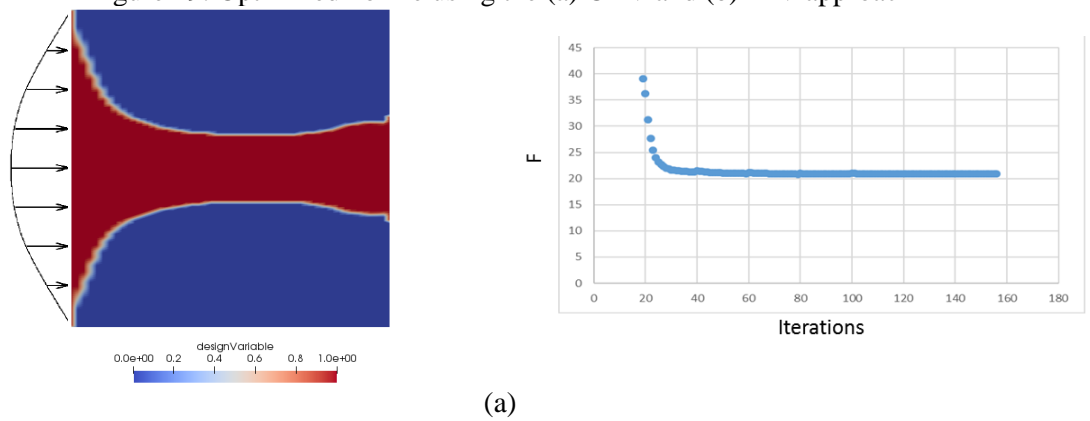


Figure 19. Optimized nozzle using the (a) CDV and (b) IDV approach



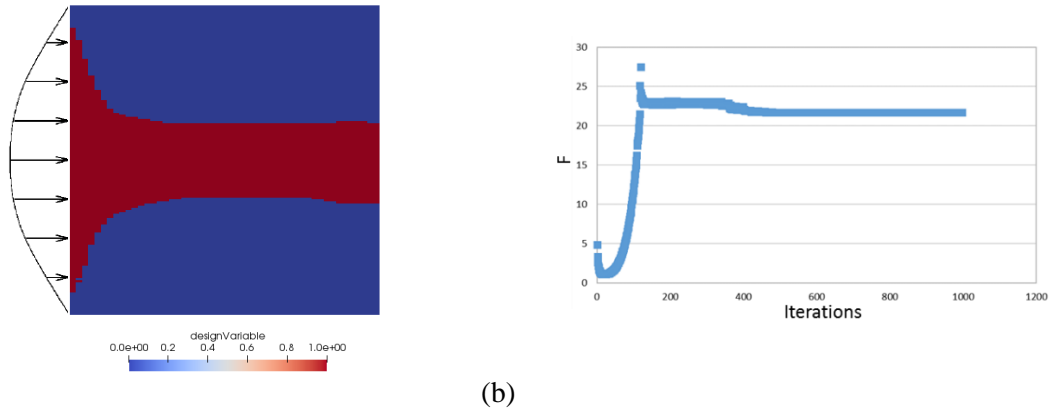
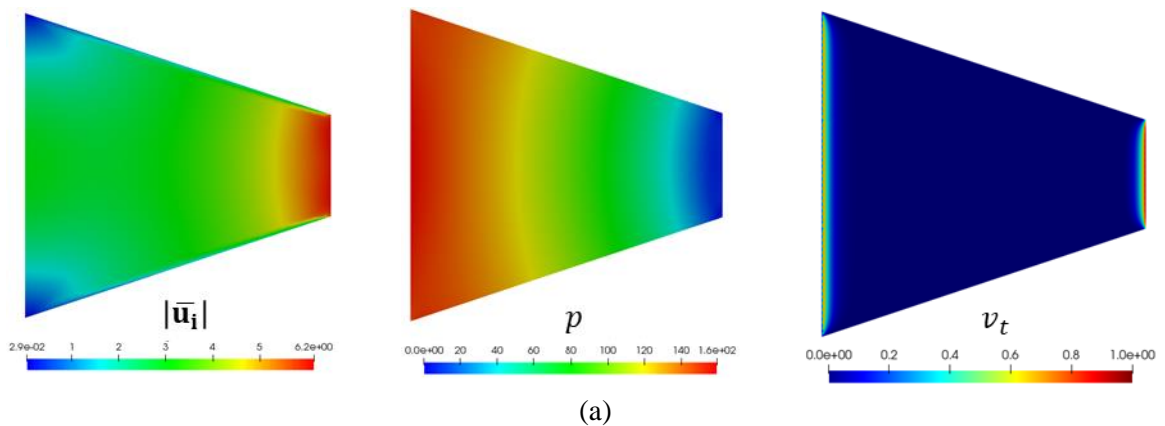


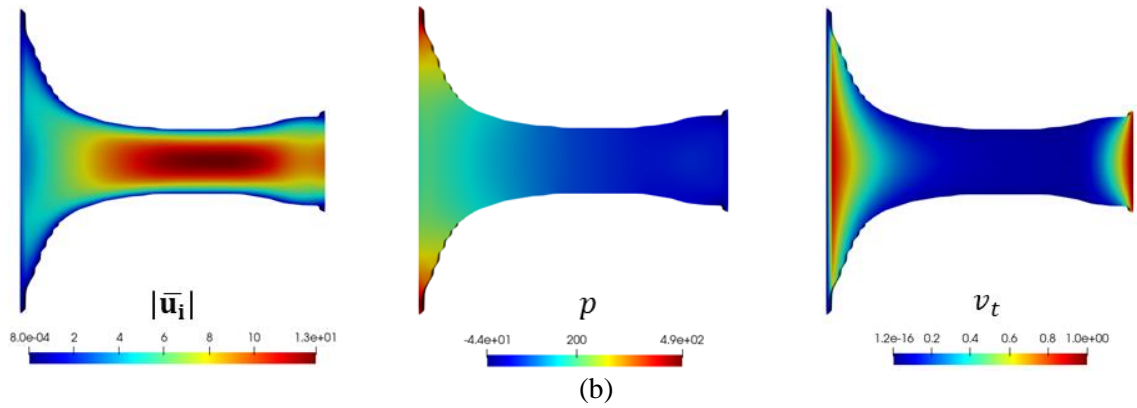
Table 5. Nozzle IDV and CDV objective functions at incompressible turbulent flow.

	Total pressure losses (F)	Difference %
IDV Optimized Topology (Figure 19b)	21.7	-
CDV Optimized Topology (Figure 19a)	20.9	3.69

Table 5 shows that the CDV-based optimizer reaches a slight improvement of 3.69% over the IDV approach. The analysis is extended by comparing a baseline nozzle design (Figure 20) to the optimized CDV-based optimizer result (Figure 19a). For example, the CFD modelling of the baseline design is performed and its total pressure losses are calculated as $F=26.3$, which is 26% greater than the optimized CDV nozzle. Such difference is depicted in the primal fields (Figure 20), where the optimized topology increases the flow velocity (Figure 20b) from 6.2 [m/s] to 13 [m/s], which is desirable when nozzles are installed. This effect increases the relative pressure difference between the inlet/outlet boundaries, resulting in a 65% difference.

Figure 20. Nozzle primal fields comparison (a) baseline design (b) optimized topology. ($|\bar{u}_i|$ the velocity magnitude, p is the pressure and v_t is the turbulent viscosity field)





4.1.2. Double-Channel Example

The case consists of a straight channel with two inlet/outlet boundaries placed parallel to each other (Figure 21). At first, the incompressible laminar regime is tested to validate the implementation of the developed “adjointTopOptFOAM” software. To do so, two δ lengths are tested: 1 and 1.5, under an inlet velocity of $u_{inlet} = 1$ [m/s] and kinematic viscosity of $\nu = 1$ [m²/s], resulting in a $Re_{inlet} = 0.167$. The optimization parameters are: $\bar{V}_{target} = 1/3$, $q = 0.01$ and a 100×100 tetrahedral mesh is considered.

Figure 21. (a) Double channel domain and (b) Mesh discretization

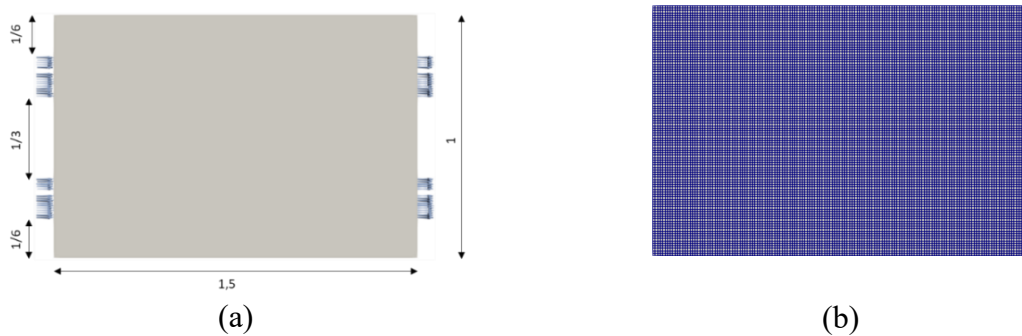
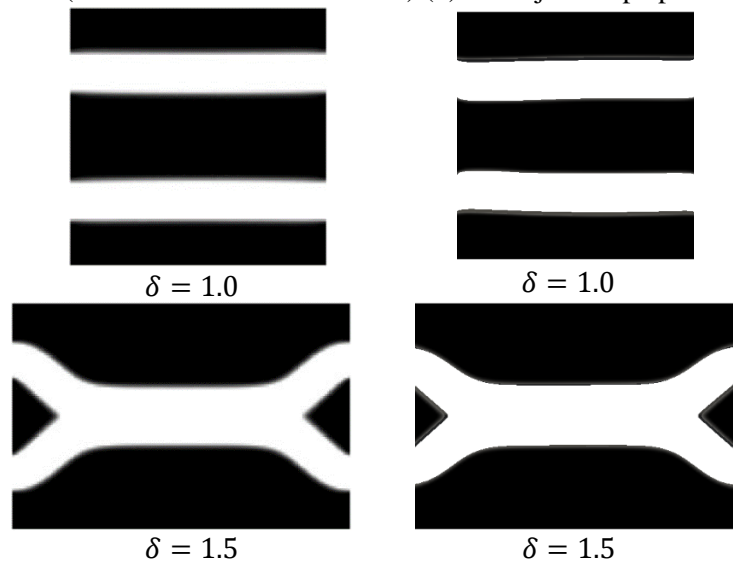


Figure 22. Optimized double-channel topology layout under incompressible laminar regime reported by (a) literature (Borrvall and Petersson 2003) (b) the adjointTopOptFOAM software



According to the chosen δ length, different topology layouts are obtained and compared in Figure 22. By the results resemblance, the developed software is validated again.

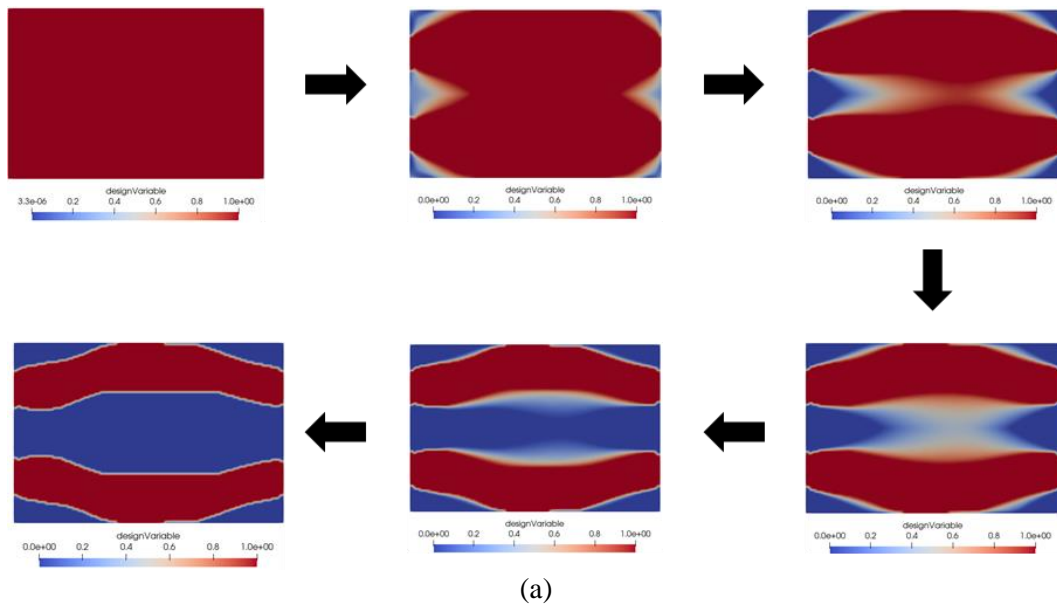
Now the case is analyzed under turbulent flow conditions and considers Table 2 and Table 3 boundary conditions with $|\overline{u}_{inlet}| = 1$ [m/s], $\tilde{v}_{inlet} = \tilde{v}_{outlet} = 0.2$ [m²/s], $\nu = 8 \times 10^{-5}$ [m²/s], which leads to a $Re_{inlet} = 3 \times 10^3$. The optimization is performed with Table 6 parameters.

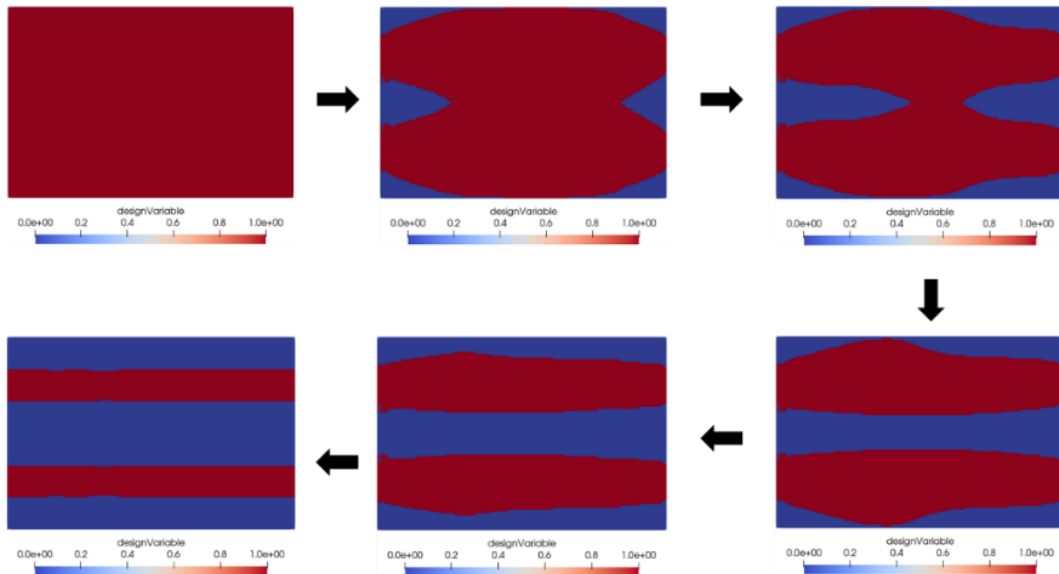
Table 6. Calibrated T.O. parameters at the double-channel case for the CDV and IDV approaches

\bar{V}_{target}	q_ϕ	\bar{k}_u	\bar{k}_{ν_t}	\bar{k}_Δ
0.33	1.0	25×10^4	1×10^{-3}	25-500

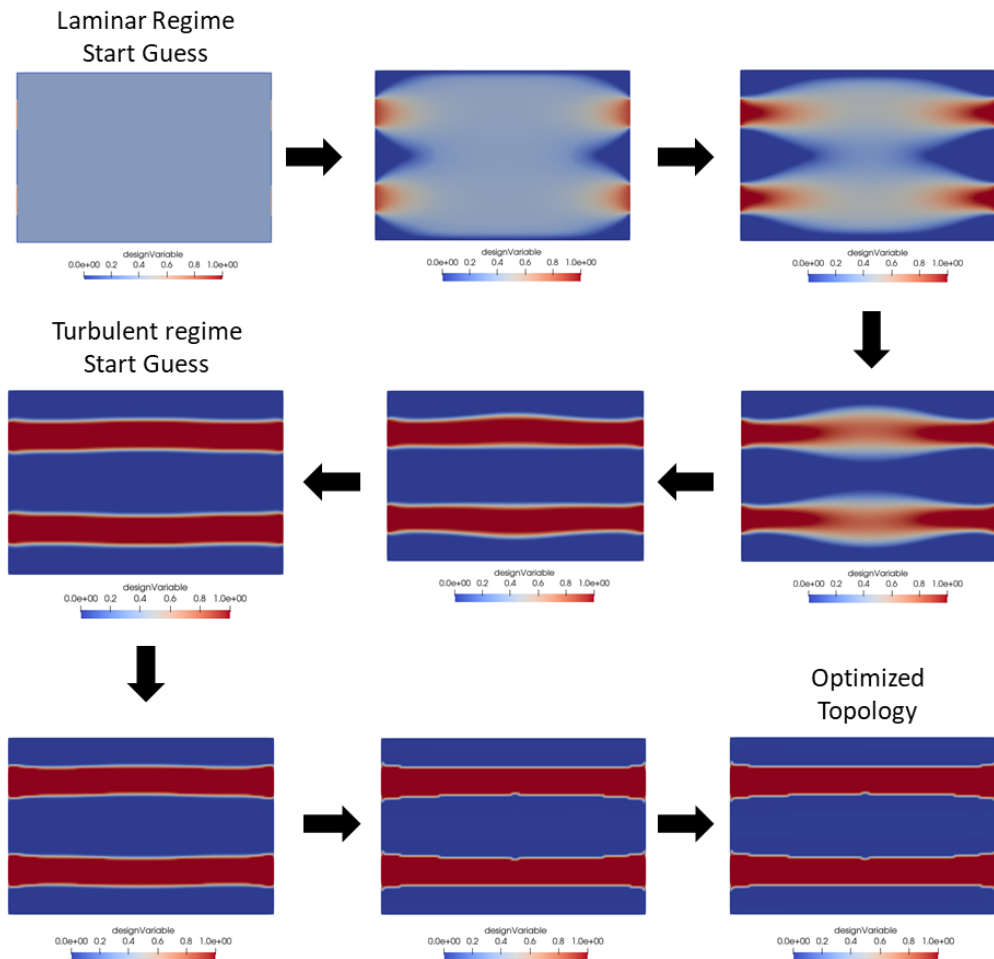
Again, the IDV approach defines a clear solid-fluid boundary along the optimization process (Figure 23b) as intermediate α values are avoided. On the other hand, the CDV approach leads to a curved pipe design (Figure 23a), due to the proximity of wall boundaries that captures fluid cells, not easy to modify by the flexibility of the CDV optimizer. This curved pipe-design shows an objective function (2.012×10^{-3}) larger than the one obtained by the IDV design (1.72×10^{-3}). Therefore, another test is made with the CDV approach by proposing a continuation method, i.e. by running the case under laminar regime at first, and then, taking its topology layout result as a start guess of the turbulence regime. Figure 24 describes the employed method.

Figure 23. Double-channel optimization process by considering the (a) CDV and (b) IDV approach





(b)Figure 24. Optimization of double channel case using the CDV optimizer and the continuation method



As Figure 24 shows, the straight-channel optimized topology is obtained by doing the progressive strategy (section 3.7), which updates the fluid viscosity along the optimization process. Both optimized topologies can be found in Figure 25. The abrupt variation in the

convergence curve of the CDV approach (Figure 25a) is presented due to the continuation method used.

Figure 25 Optimized double-channel topology considering the (a) CDV and (b) IDV approach

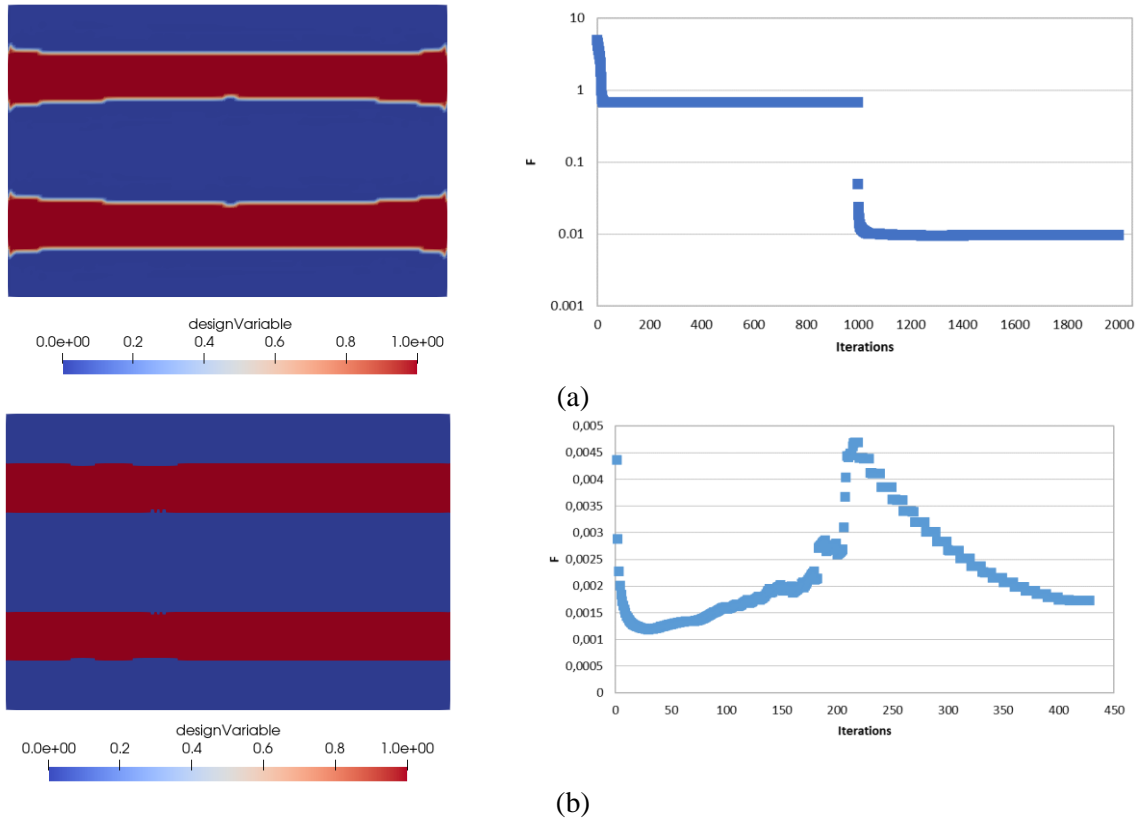
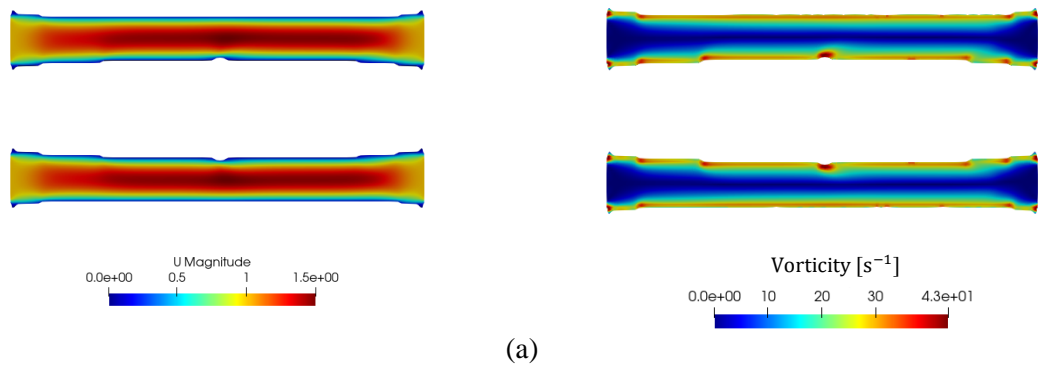


Table 7 shows the objective functions of each case, where the IDV based-approach solution is 83% more efficient than the CDV approach. This is due to the thickness of the optimized straight channels, where the CDV based-approach presents a thinner solution that accelerates the fluid flow (Figure 26), increases the vortex generation along the domain, and ends with the highest dissipated energy value.

Figure 26. Optimized double-channel characteristic flow fields of the (a) CDV and (b) IDV approaches



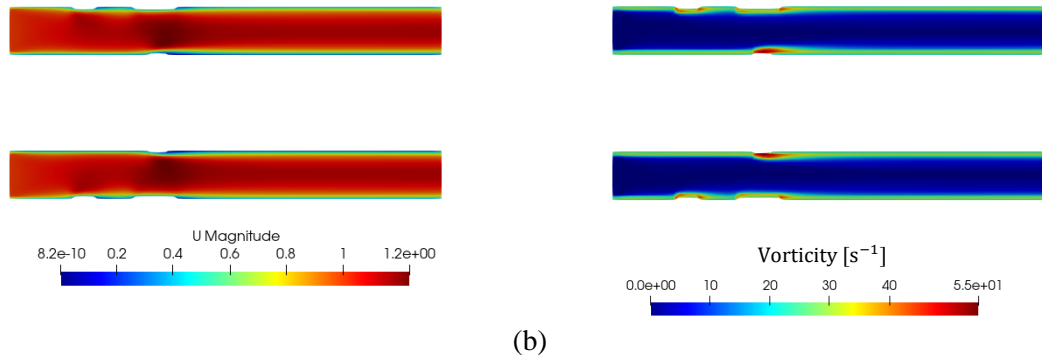


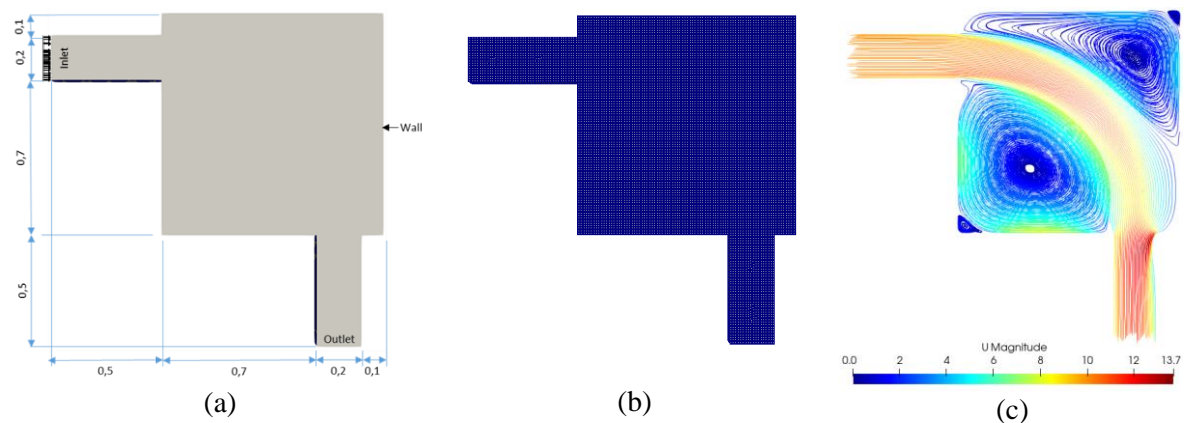
Table 7. Double-channel objective function value.

Optimized Double Channel	Total pressure losses (F)
CDV Approach (Figure 25a)	9.6×10^{-3}
IDV Approach (Figure 25b)	1.72×10^{-3}

4.1.3. Pipe-bend Example

The Pipe-bend case consists of a square domain with perpendicular boundaries representing the inlet and outlet boundaries (Figure 27a), discretized by 4.8×10^4 hexahedral mesh (Figure 27b). The inclusion of extended inlet/outlet channels facilitates the stabilization of the fluid flowing through these regions. It considers Table 2 and Table 3 boundary conditions, with constant values of $|\bar{u}_{inlet}| = 5$ [m/s], $\tilde{v}_{inlet} = 0.2$ [m²/s] and fluid properties $\nu = 2 \times 10^{-4}$ [m²/s] reaching a turbulent inlet flow characterized by $Re_{inlet} = 5 \times 10^3$. The CFD of the original domain (Figure 27c) shows large transversal vortices generated at the corners of the domains, which may be replaced by solid regions during the first iterations of the optimization process to mitigate the recirculation zone.

Figure 27. (a) Pipe-bend Domain, (b) mesh discretization and (c) CFD modelling of initial domain



The optimization is performed using the CDV and IDV approaches, where the T.O. parameters are calibrated in Table 8. At the IDV approach a constant value of the penalization parameter

(q_ϕ) is used and \bar{k}_Δ is increased 20% after 100 iterations until a maximum value is reached. Then, the optimization stops due to the convergence criteria.

Table 8. Calibrated T.O. parameters at the pipe-bend case

	\bar{V}_{target}	q_ϕ	\bar{k}_u	\bar{k}_{v_t}	\bar{k}_Δ
CDV	0.25	0.01 – 1.0	2.5×10^3	1×10^{-3}	300
IDV	0.25	1.0	2.5×10^3	1×10^{-3}	25 – 300

The T.O. process is shown in Figure 28, where the IDV approach presents clear definitions of solid and fluid regions along with iterations, meanwhile, the CDV distributes intermediate material at the first 40 iterations until a discrete result is found when q_ϕ gets maximum value. Thus, the IDV approach presents a continuum of feasible solutions along with iterations and a clear solid/fluid boundary definition. This allows a more accurate CFD modelling through the T.O. iterations, as the wall distance can be calculated continuously. Then, solid regions are placed across areas where probably vortex are generated.

Figure 28. Topology layouts evolution of the Pipe-bend case under incompressible turbulent regime using the (a) CDV and (b) IDV optimizers

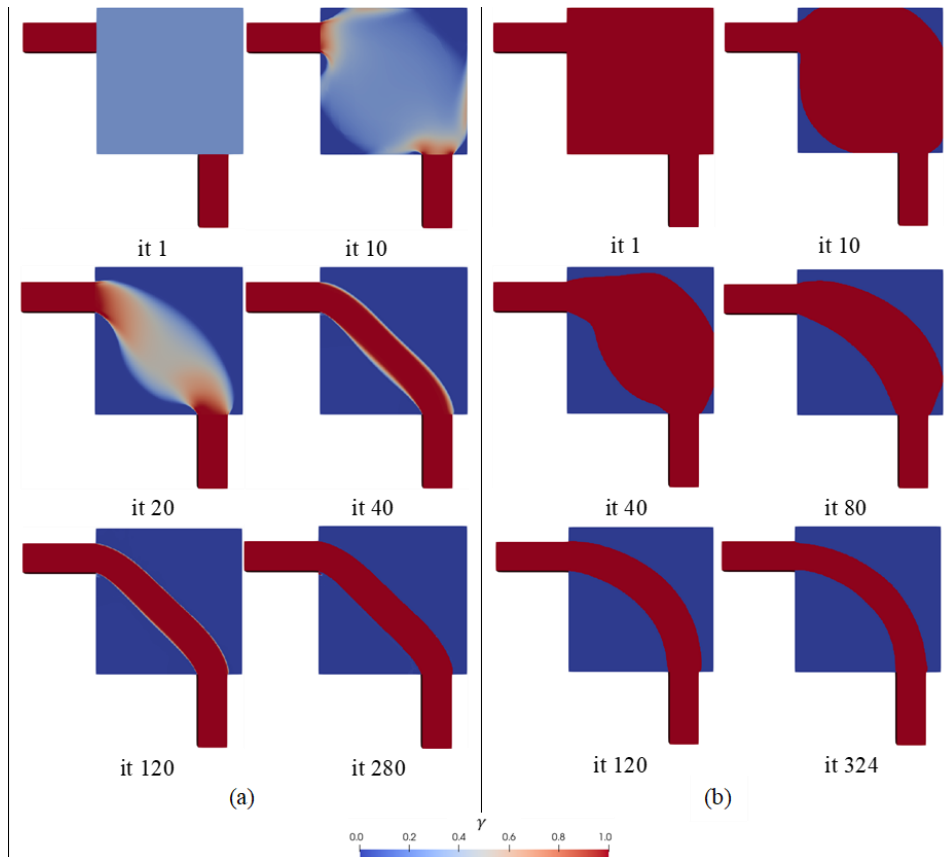
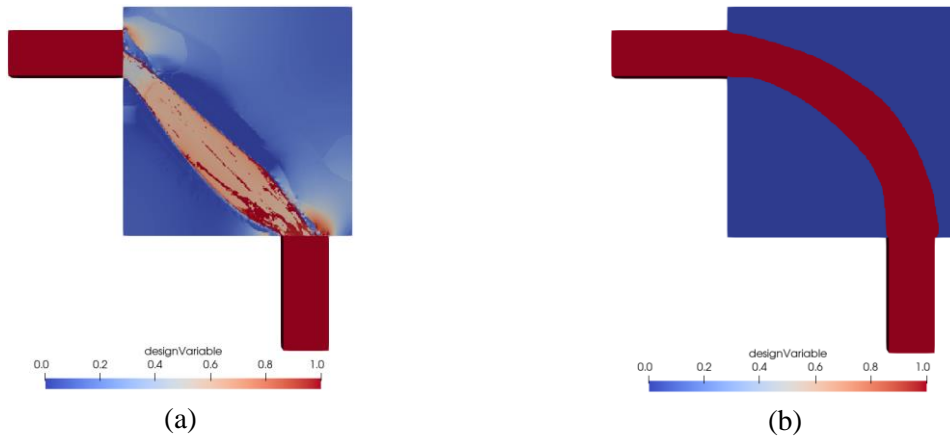


Table 9 presents the objective function values of the optimized pipe-bend case, where the CDV approach states the lowest objective function value.

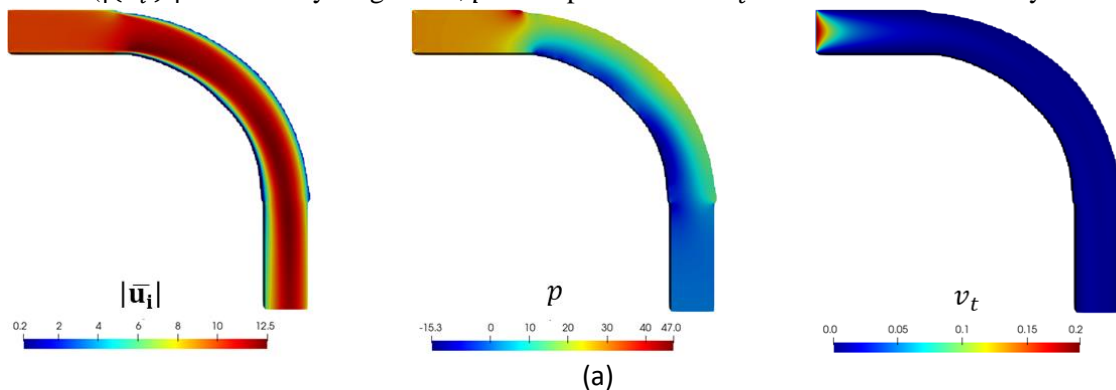
Table 9. Comparison of the objective function values for the Pipe-bend examples.

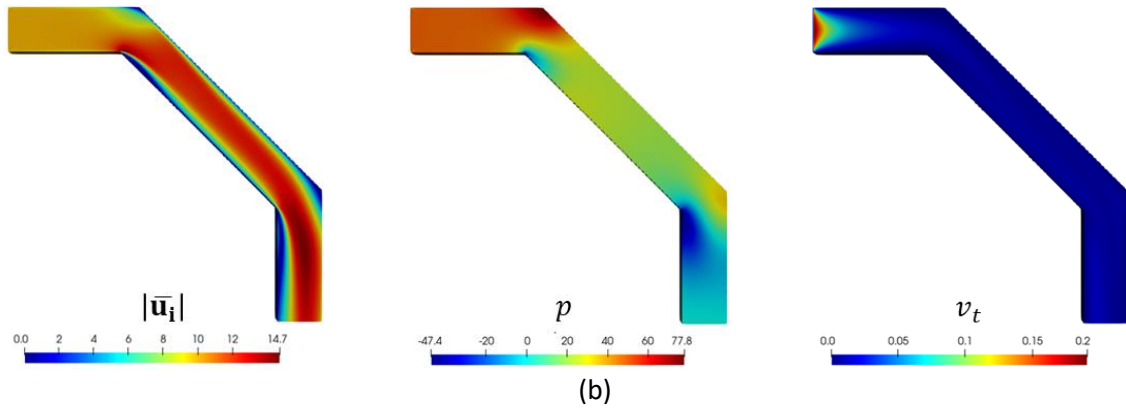
	Total pressure losses (F)	Difference from initial Domain
Baseline design (Figure 30b)	7.07	-
IDV Optimized Topology (Figure 28b)	4.90	30.7%
CDV Optimized Topology (Figure 28a)	4.48	36.6%

A remark concluded is the T.O. parameters value independence of the IDV approach, i.e. the optimization can be performed with different optimization parameters values, in contrast to the CDV approach. An example is shown in Figure 29, where the \bar{k}_u from the previous case is changed to $\bar{k}_u = 2.5 \times 10^5$. The CDV approach (Figure 29a) diverges with the new \bar{k}_u value and the IDV still presents a feasible solution (Figure 29b).

Figure 29. Influence of \bar{k}_u value at (a) CDV and (b) IDV optimizer

For example, the primal field performance of the optimized IDV design (Figure 30a) is compared to a baseline pipe (Figure 30b). Low velocities values can be seen at the baseline outlet region, which might be related to vortex generation. Also, the pressure difference between the inlet/outlet boundaries of the baseline case is larger than the IDV optimized case. Both phenomena are reflected at the baseline objective function value, which overcomes by 30.7% the IDV-based case (Table 9).

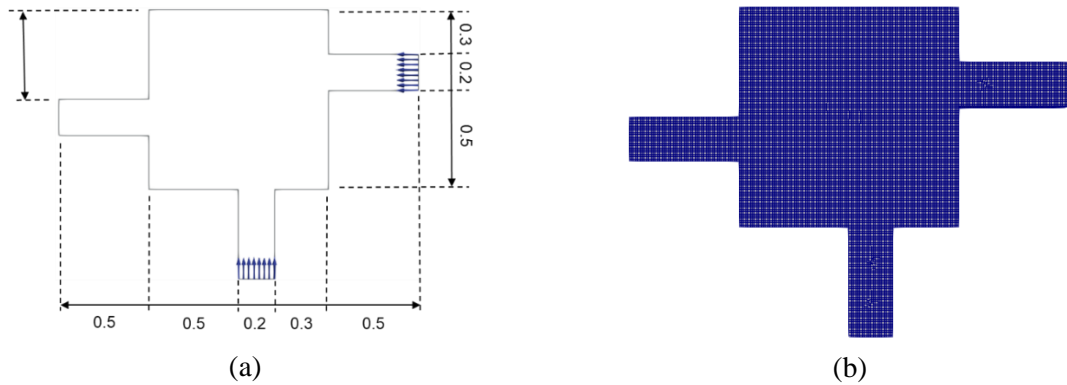
Figure 30. Primal fields comparison between (a) optimized IDV and (b) baseline design. ($|\overline{u}_i|$) the velocity magnitude, p is the pressure and v_t is the turbulent viscosity field



4.1.4. 2D pipe-joint Example

The design connects one inlet and two outlet boundaries discretized by a uniform hexahedral mesh. The boundary conditions are established in Table 2 and Table 3 with $|\bar{u}_{inlet}| = 15$ [m/s], $\bar{v}_{inlet} = 5 \times 10^{-1}$ [m²/s] and $\nu = 4.29 \times 10^{-4}$ [m²/s], resulting in a $Re_{inlet} = 7 \times 10^3$.

Figure 31. (a) 2D pipe-joint domain and (b) Mesh discretization



The optimization parameters are calibrated (Table 10) until reaching a smooth topology layout employing the CDV and IDV optimizers.

Table 10. Calibrated T.O. parameters at the 2D pipe-joint case for the CDV and IDV approaches

\bar{V}_{target}	q_ϕ	\bar{k}_u	\bar{k}_{ν_t}	\bar{k}_Δ
0.3	1.0	3×10^3	1×10^{-3}	25

The CDV and IDV approaches reach an optimized 2D pipe-joint design that joints in the middle region, avoiding the domain corners where eddies might be presented. Nevertheless, the topologies differ in the joint point and length channels. The topology variation influences each objective function value as expected (Table 11), where the IDV performs a better total pressure loss distribution between the inlet/outlet boundaries.

Figure 32. 2D pipe-joint optimization layout process by considering the (a) CDV and (b) IDV approach

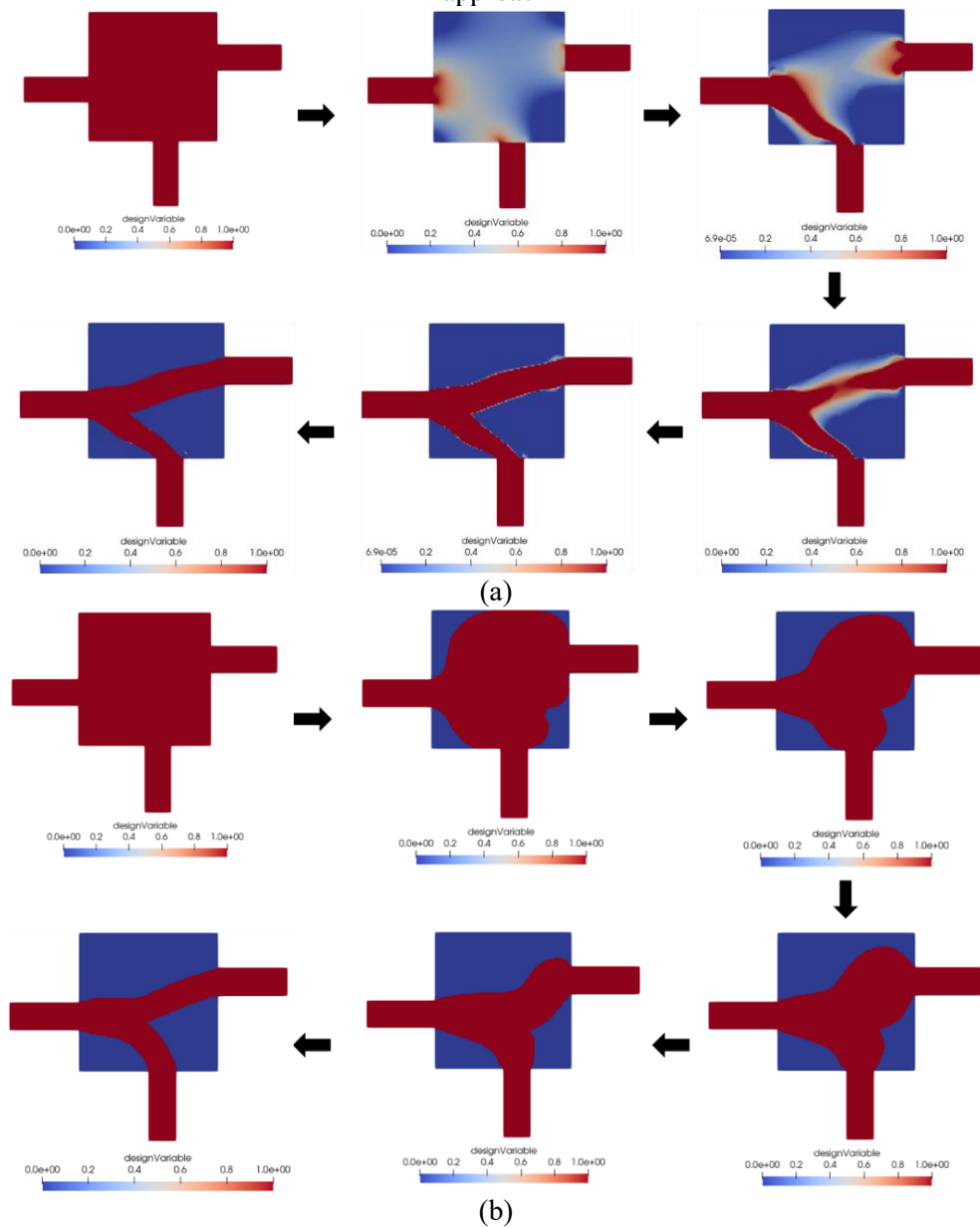


Table 11. 2D pipe-joint objective function value.

Optimized 2D pipe-joint	Total pressure losses (F)
CDV approach (Figure 33a)	71.01
IDV approach (Figure 33b)	50.4

The vorticity fields (Figure 34) justify the objective function difference: It shows that the CDV topology layout generates high vorticity due to its straight channel design mainly at the inlet bottom section. This abrupt fluid section change increases the vorticity in the regions, which is not depicted in the IDV approach topology. Its smooth curvature-designed channel decreases the vorticity generation.

Figure 33. Optimized 2D pipe-joint topology using the (a) CDV and (b) IDV approach

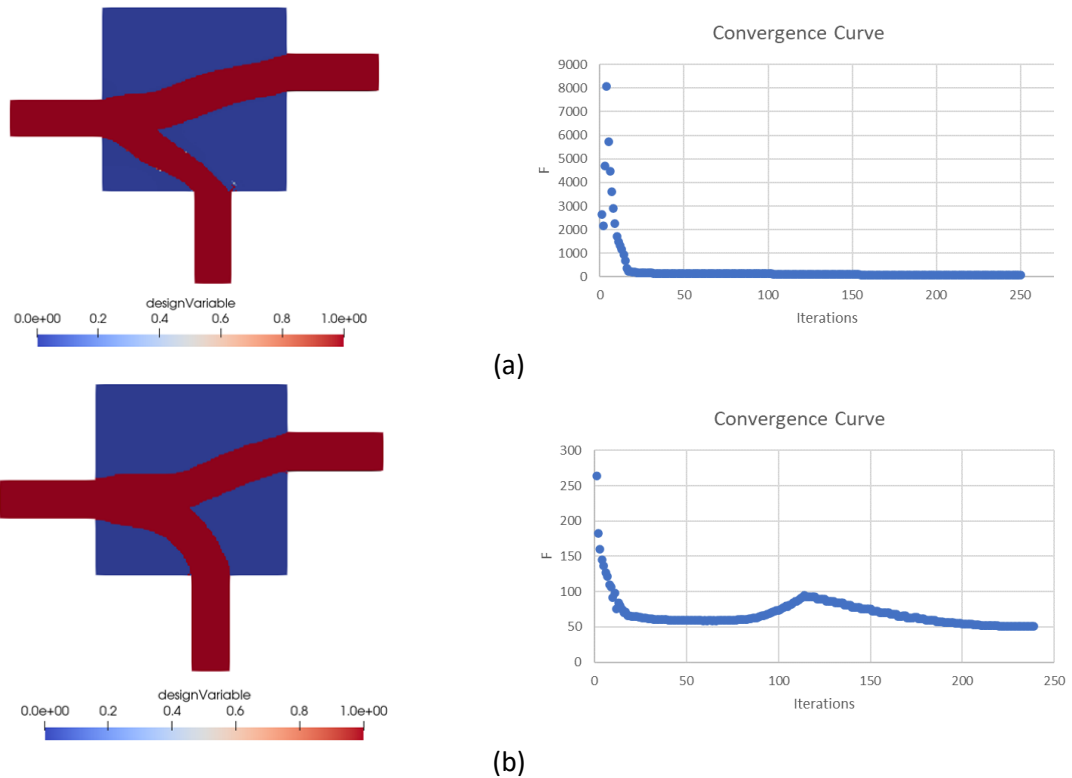
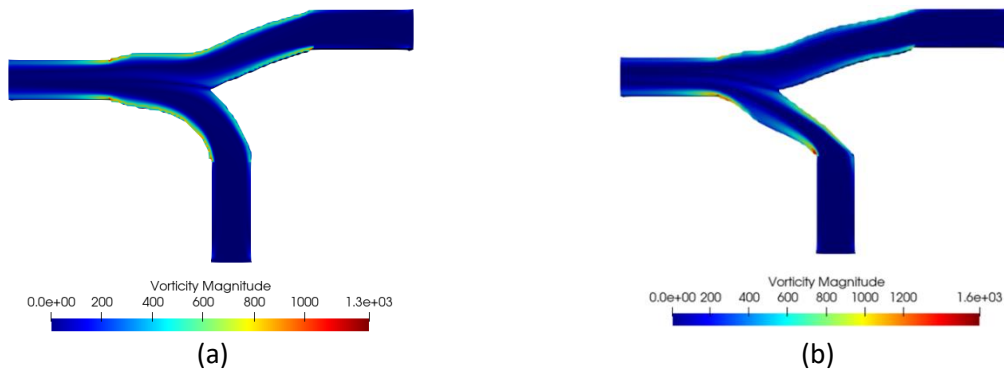


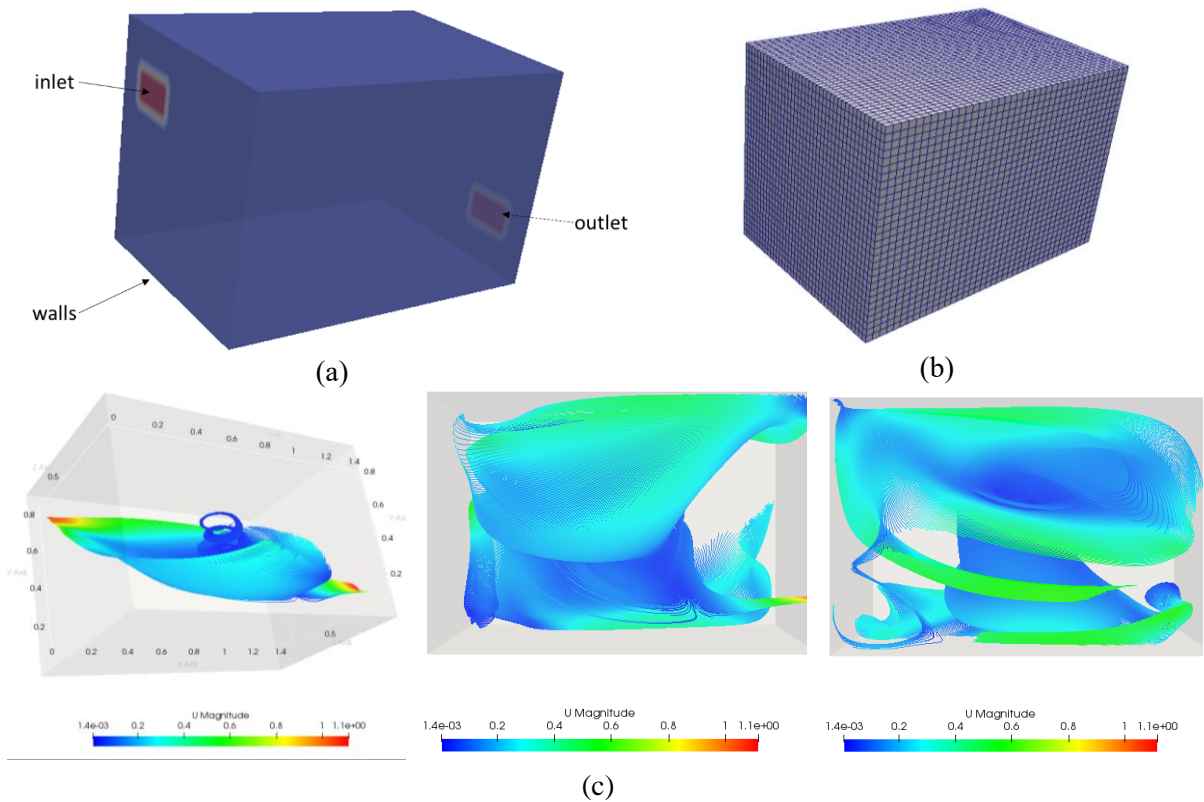
Figure 34. Vorticity fields of optimized 2D pipe-joint under the (a) IDV and (b) CDV approach.



4.1.5. 3D Pipe Joint Example

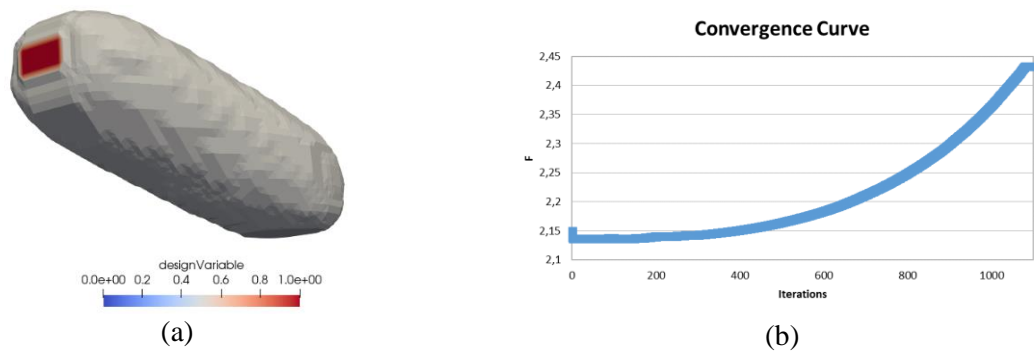
Finally, the method is tested in a 3D domain to show its flexible application. A fluid container is analyzed (Figure 35a), and which domain is discretized with an uniform hexahedral mesh (Figure 35b). It uses Table 2 and Table 3 boundary conditions, with constant values of $|\bar{u}_{inlet}| = 1$ [m/s] and fluid properties of: $\nu = 8 \times 10^{-5}$ [m²/s] ensuring a turbulent inlet flow characterized by $Re_{inlet} = 3125$. The CFD modelling of the original domain (Figure 35c) shows a chaotic flow where non-intuitive fluid passage is detected, which increases the difficulty of the optimization process.

Figure 35. (a) 3D initial domain, (b) mesh discretization and (c) fluid flow streamlines



A first guess solution could be a diagonal pipe that joins the inlet and outlet boundaries. Thus, initially, the optimization is performed considering a low Re_{inlet} value ($Re_{inlet} = 0.2$), and the diagonal pipe is obtained as expected (Figure 36).

Figure 36. (a) Optimized container by using IDV optimizer at low Re_{inlet} and (b) convergence curve

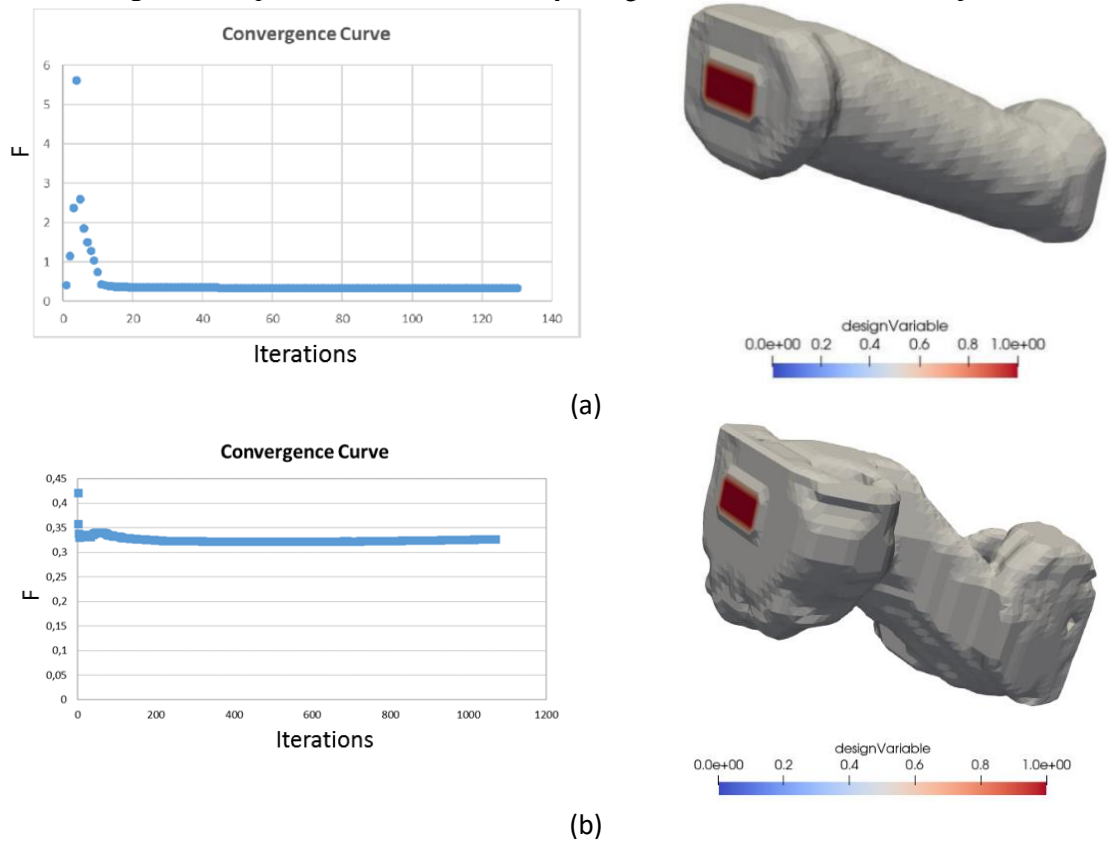


Nevertheless, at turbulent flow, the optimization parameters calibration changes, and different tests are performed by changing the volume constraint until reaching the convergence of the optimization process and getting smooth topologies. The optimized topologies considering CDV and IDV optimizers are reached (Figure 37) when Table 12 optimization parameters are calibrated.

Table 12. Selected optimization parameters at the 3D domain for CDV and IDV approaches

$\alpha_{initial}$	\bar{V}_{target}	q_{ϕ}	\bar{k}_u	\bar{k}_{v_t}	\bar{k}_{Δ}
0	0.33	1.0	2.5×10^4	1×10^{-3}	25

Figure 37. Optimized container case by using the (a)CDV and (b) IDV optimizers



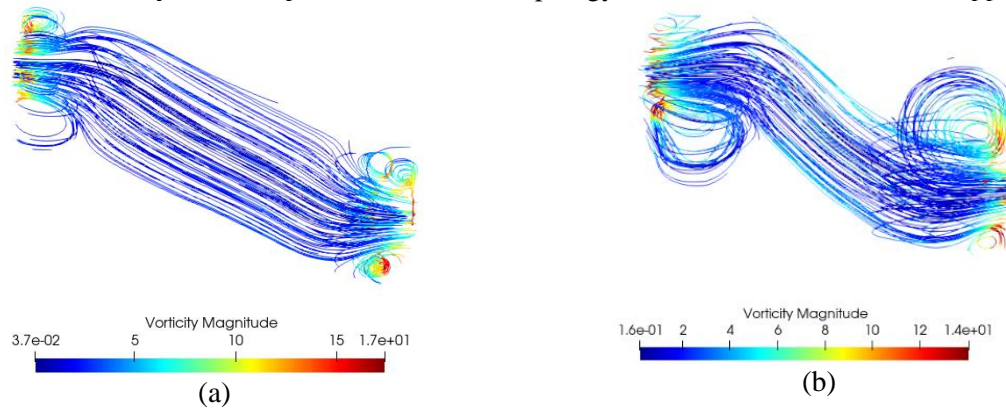
By using the CDV optimizer, the computational cost is 12.2% of the IDV computational cost, and the topologies layouts are considerably different from each other. As Figure 38 shows, the IDV binary behaviour avoids intermediate α values, creating an innovative topology where clear passages are described.

Figure 38. Optimized container under the IDV approach: (a) side and (b) superior view



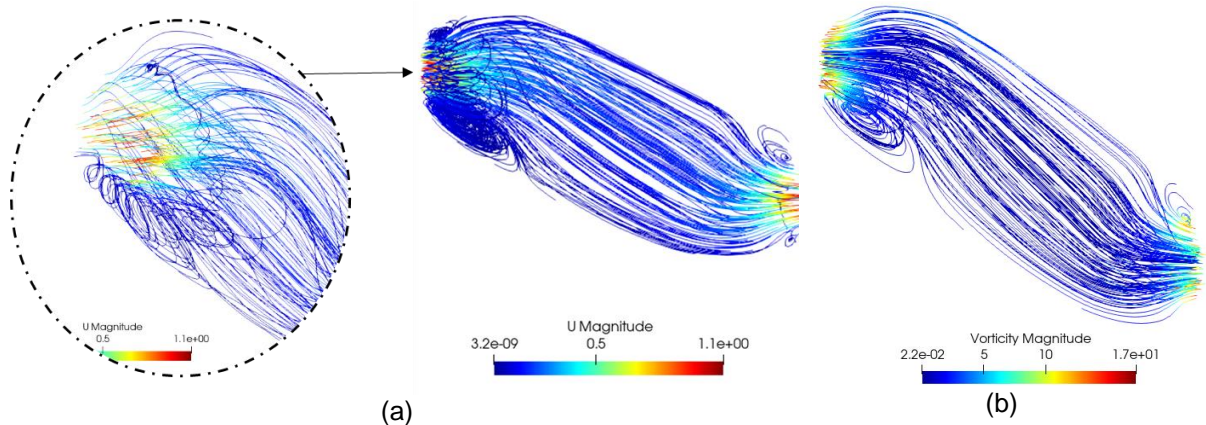
The designed passages direct the fluid flow through the domain, avoiding its chaotic random behaviour and reducing the vortex generation (Figure 39b). Therefore, the optimized topology using the IDV optimizer acts more efficiently than the CDV in the current case.

Figure 39. Vorticity field of optimized container topology under (a) CDV and (b) IDV approaches.



The IDV optimized design is compared to the baseline topology (Figure 40), by running the CFD under the same fluid flow properties, i.e. by using $\nu = 8 \times 10^{-5} [\text{m}^2/\text{s}]$, and the same \bar{V}_{target} of the optimized design (Table 12). The baseline primal fields are shown in Figure 40.

Figure 40. 3D Baseline design (a) velocity and (b) vorticity streamlines



Transversal vortices are identified at the inlet section and a swirl flow too. Both phenomena induce a turbulent flow across the domain and the outlet region too. The vorticity magnitude calculation shows an 18% peak difference between both cases. Such improvement is confirmed in the Total pressure losses value (F), where the optimized topology presents a 15% improvement over the baseline design (Table 13).

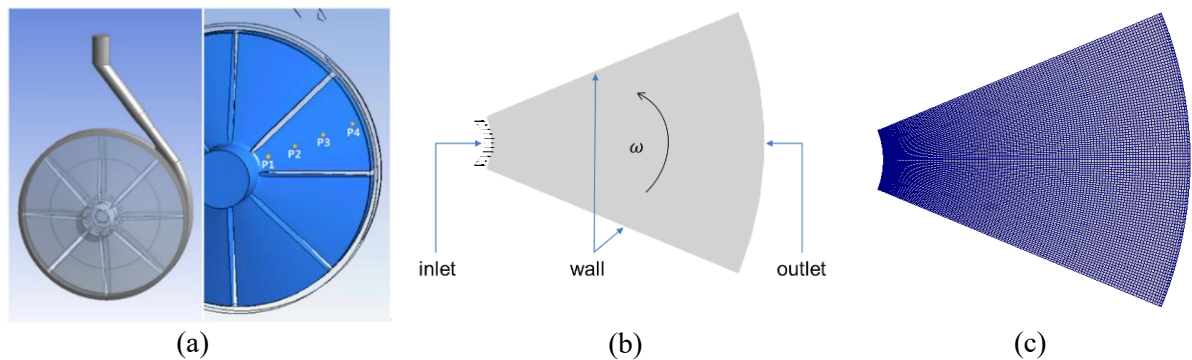
Table 13. Objective function comparison between the baseline and optimized container passage by considering incompressible turbulent regime.

	Total pressure losses (F)	Baseline Difference %
Baseline	0.384	-
Optimized Topology Layout CDV	0.344	10.4
Optimized Topology Layout IDV	0.326	15.1

4.1.6. Rotor Example

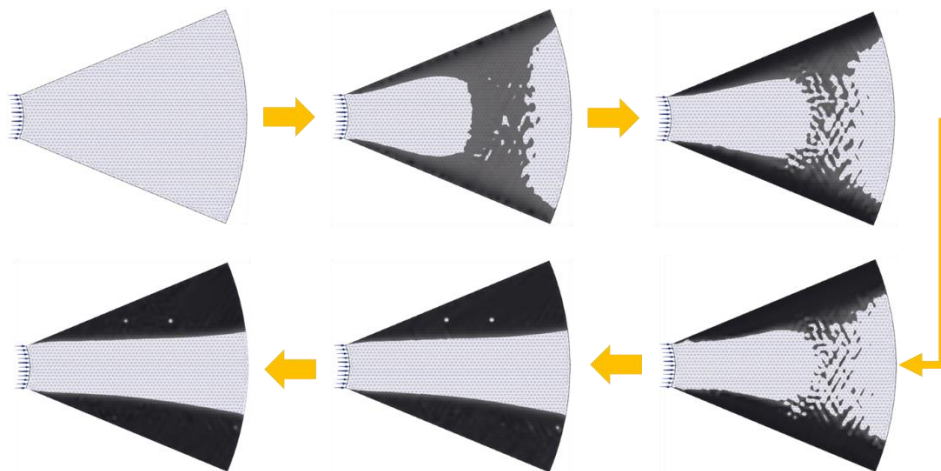
Simultaneously, the continuous adjoint method is tested with the rotational flow under the incompressible turbulent regime using the CDV approach. The domain considers the fluid cavity between two straight blades of a rotor (Figure 41). The domain is discretised considering a hexahedral mesh (Figure 41c) and its boundary conditions are taken in Table 2 and Table 3. The fluid properties are: $u_{inlet} = 10$ [m/s], $\nu = 5 \times 10^{-5}$ [m²/s], $Re_{inlet} = 4 \times 10^3$.

Figure 41. (a) Straight blade rotor, (b) Cavity domain considered and (c) mesh (Kim et al. 2014).



The CDV optimizer is used and the optimization parameters are calibrated as: $\alpha_{initial} = 0.5$, $\bar{V}_{target} = 0.3$, $q_\phi = 0.1$, $\bar{k}_u = 50$, $\bar{k}_{v_t} = 50$, $\bar{k}_\Delta = 50$. The optimization process is seen in Figure 42. The selected optimization parameters have lower values than the parameters used for the optimization of channels, due to the domain area and the fluid flow, as it requires some “freedom” to stabilize the chaotic inlet turbulent rotating flow.

Figure 42. Topology optimization of straight blade rotor under incompressible turbulent regime by using the Spalart-Allmaras turbulence model (Author).



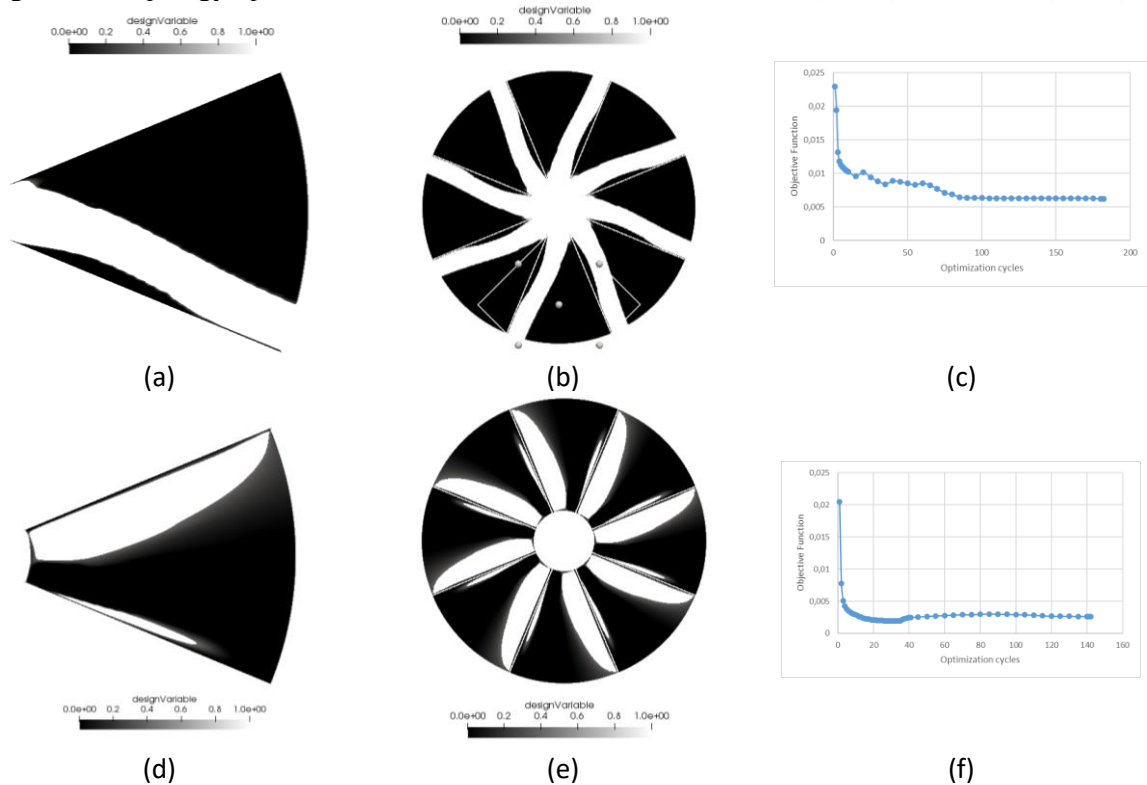
The case is tested under different rotations and fluid viscosities, (Table 14), distributing the material differently across the domain section (Figure 43).

Table 14. Optimization parameters at cavity straight blade rotor under incompressible turbulent flow.

Case	Viscosity, ν [m^2/s]	Rotational velocity [rpm]	Volume target, \bar{V}	\bar{k}_ϕ	q_ϕ
1	1×10^{-5}	20	0.3	1×10^3	0.1
2	5×10^{-5}	40	0.3	50	0.1

The T.O. tends to create a narrow blade at the suction side of the blade domain. This is expected as vortex generation from the pressure side is different from the suction side (Gaetani, (Gaetani 2018)). According to the fluid nature of entering through the cavity, e.g. inlet velocity, the centrifugal forces could predominate, increasing the mentioned differences between vortex generation across the suction and pressure side. Both tests are made using wall boundary conditions and case 2 shows how it affects the fluid flow direction, as reverse flow is found in the middle section when large Reynolds numbers are tested.

Figure 43. Topology optimization of rotational turbulent flow, Case 1 (a, b, c) and Case 2 (d, e, f)



The developed software “adjointTopOptFOAM” based on the continuous adjoint approach proves its robustness to optimise incompressible turbulent flow in channel designs, rotors domains and 3D fluids interchanges. The analysis of the IDV influence is tested in some cases to conclude its flexibility and accurate fluid/solid boundary design along the optimization iterations. Furthermore, it can optimize complex domains without treating the progressive strategy as the CDV approach demands. At the rotational regime, large rotations are tested with

the previous assumption, however, no convergence is found. The research shows that using wall boundaries at the rotor cavity restricts the space to be optimized, increases the computational cost, and creates undesired instabilities of the rotating flow. Therefore, a cyclic boundary condition is proposed to be analysed further to reach large rotational velocities. Several tests of hand-derivation to obtain the continuous adjoint code for compressible fluid flow regime were made, but challenges related to the derivatives of many variables at compressible regime, such as temperature, enthalpy, and compressible turbulent fluctuations, which depend on the sensitivity analysis difficult the process. Therefore, another path is considered to reach the compressible adjoint code, which is explained in the following.

4.2. TOPOLOGY OPTIMIZATION OF COMPRESSIBLE TURBULENT SUBSONIC FLOW FOR AN IDEAL PERFECT GAS CONSIDERING THE DISCRETE ADJOINT APPROACH

As it is explained in section 3.7, the T.O. of compressible turbulent regime is tackled via the progressive methodology (Figure 15), which consists in optimizing the domain at laminar regime and taking its topology layout result as an initial guess of the turbulent. The other fluid properties remain constant during the optimization process. A fictitious fluid is proposed to be discretized, which can be tested at different regimes by changing its dynamic viscosity and remaining its thermophysical properties as Table 15 shows.

Table 15. Thermophysical fluid properties.

c_p [J/kgK]	1004
Molar Weight [g/mol]	28.96
Gas constant (R) [J/mol K]	8.314
Thermal conductivity (k_{th}) [W/m K]	0.0263

The software “FEniCS TopOpt FOAM” (Alonso et al. 2021) is modified to deal with T.O. of compressible turbulent regime by including: firstly, the FANS equations to treat turbulence at compressible regime, and secondly, the Sutherland Law and the Peng-Robinson model to represent real gas behaviour. The optimization is performed via the CDV optimizer and the IPOPT optimizer, where the established convergence criterion of the T.O. is of 10^{-10} .

The first step of the progressive strategy considers a subsonic regime with low Reynolds numbers, which is a much simpler configuration for both simulation and optimization.

Therefore, the penalization terms related to the turbulence treatment are zero ($k_{\hat{\nu}} = k_{\Delta} = 0$) as no turbulence model is employed. Two examples are presented: a converging nozzle and a pipe-bend. Both cases consider the boundary conditions described in Table 16.

Table 16. Primal boundary conditions used at compressible regime with low-Re.

Primal Boundary Conditions	u [m/s]	p [Pa]	T [K]
Inlet	u_{inlet}	$\frac{\partial p}{\partial n} = 0$	T_{inlet}
Outlet	$\frac{\partial u}{\partial n} = 0$	$p_{total_{out}} = 101325$	$\frac{\partial T}{\partial n} = 0$
Wall	$u_{wall} = 0$	$\frac{\partial p}{\partial n} = 0$	$T_{wall} = 298.15$

As T.O. of turbulent regime demands precise calibration of the optimization parameters, a “turbulence regime approximation step” is proposed, which consists of calibrating, at first, the T.O. parameters for compressible subsonic regime, without solving the turbulence tensor part of the FANS equations, i.e. by not considering any turbulence model. By doing so, the T.O. parameters calibration is suitable as fewer variables need to be defined, i.e. \bar{k}_{Δ} and $\bar{k}_{\hat{\nu}}$ are not considered.

After performing T.O. at turbulent regime approximation, the obtained topology is used as a start guess to solve the turbulence phenomenon considering the modified SA turbulence model. Therefore, the boundary conditions are updated with the turbulence model variables, as described in Table 17.

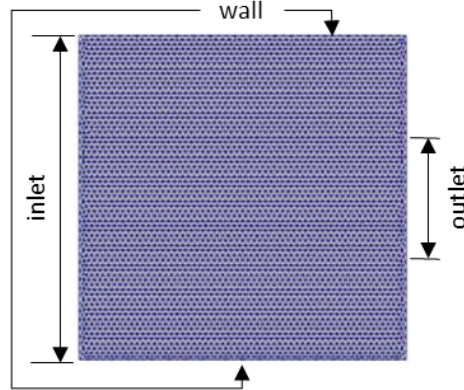
Table 17. Boundary conditions at compressible turbulent regime.

Boundary Conditions	Inlet	Outlet	Wall	Cyclic-1	Cyclic-2
u_i	u_{inlet}	$\frac{\partial u}{\partial n} = 0$	$u_{wall} = 0$	$u_{Cyclic-1} = -u_{Cyclic-2}$	
p	$\frac{\partial p}{\partial n} = 0$	$p_{total_{out}}$	$\frac{\partial p}{\partial n} = 0$	$p_{Cyclic-1} = p_{Cyclic-2}$	
T	T_{inlet}	$\frac{\partial T}{\partial n} = 0$	$T_{wall} = 298.15$	$T_{Cyclic-1} = T_{Cyclic-2}$	
$\hat{\nu}$	$\hat{\nu} = 0.023$	$\frac{\partial \hat{\nu}}{\partial n} = 0$	$\hat{\nu} = 0$	$\hat{\nu}_{Cyclic-1} = \hat{\nu}_{Cyclic-2}$	

4.2.1. Converging Nozzle Example

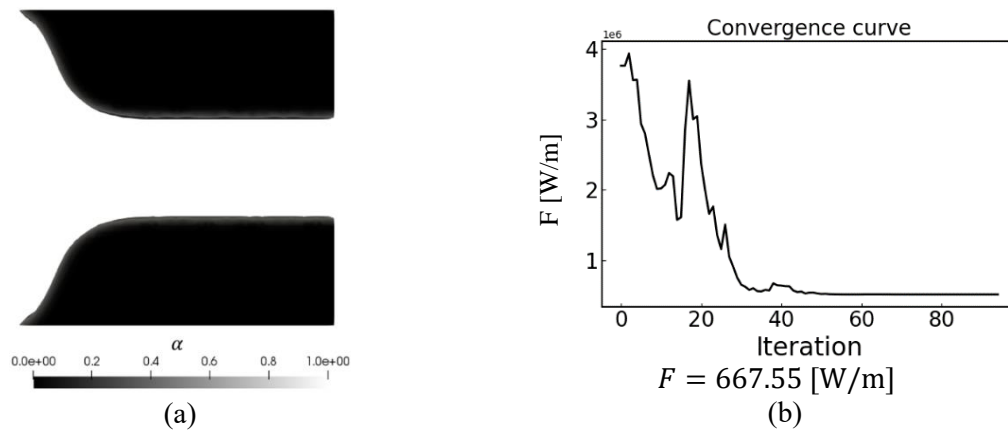
The converging nozzle case is tested at compressible regime by updating its fluid properties to: $u_{inlet} = 30$ [m/s], $\mu = 1$ [Pa · s], $Re_{inlet} = 30$, $T_{inlet} = 298$ [K] and $p_{total_{out}} = 101325$ [Pa]. The boundary conditions from Table 16 are used and the domain is discretized by 2500 triangular elements.

Figure 44. Mesh discretization of nozzle domain at compressible regime



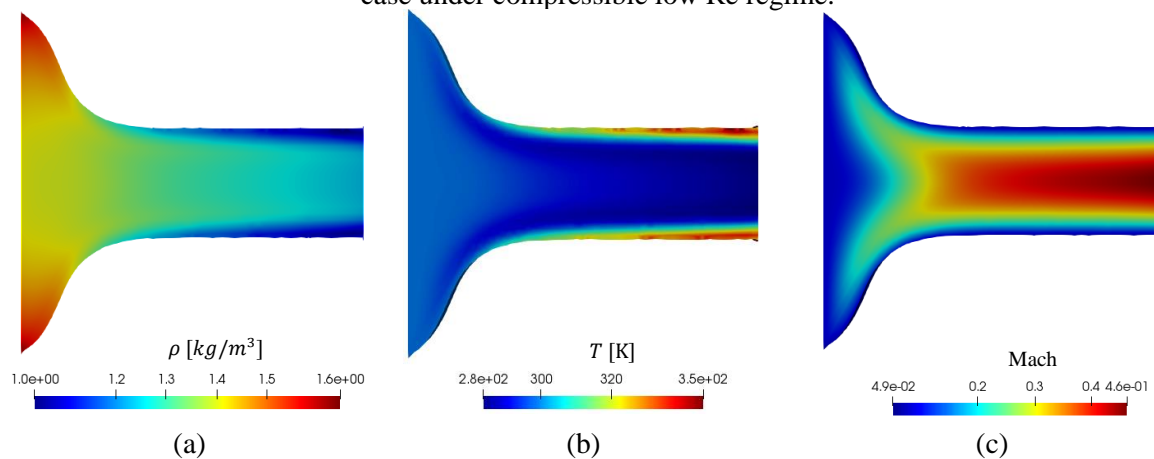
The initial guess of the domain is $\bar{V}_{frac} = 0.3 \text{ [m}^3/\text{m}^3]$, and the optimization parameters are established as $q = 0.1$, $\bar{k}_u = 5 \times 10^5 \text{ [kg}/(\text{m}^3\text{s})]$ and $\bar{k}_T = 1 \times 10^5 \text{ [kg}/(\text{m K s}^3)]$, resulting in the optimized topology layout shown in Figure 45.

Figure 45. (a) Optimized nozzle topology layout (black = solid, white = fluid) under laminar compressible flow and (b) convergence curve.



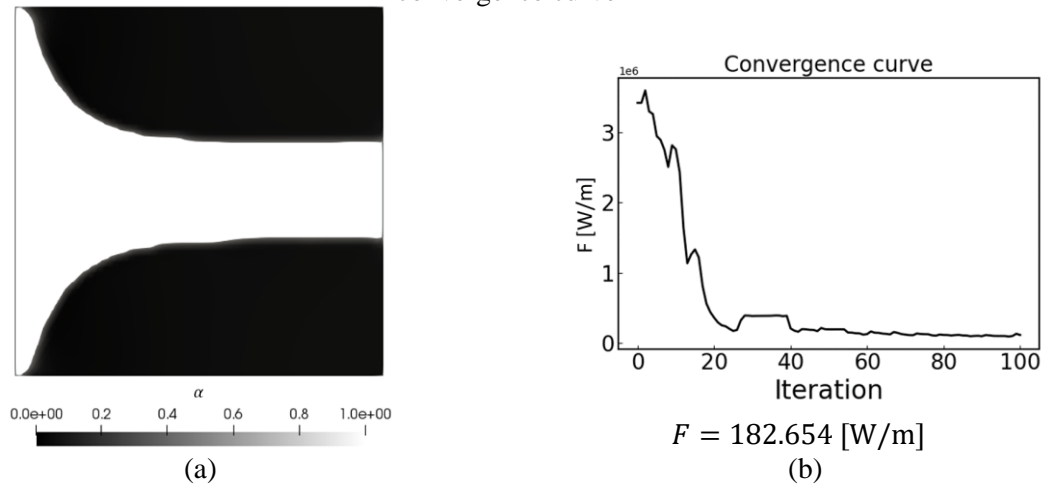
The optimized nozzle characteristic fields (Figure 46) show a peak Mach number difference of 0.46 and a density variation of 37.5% along the domain, which justifies the use of a compressible-based solver to optimize the current domain.

Figure 46. Velocity, pressure and Mach number fields of the (a) optimized nozzle and (b) baseline case under compressible low Re regime.



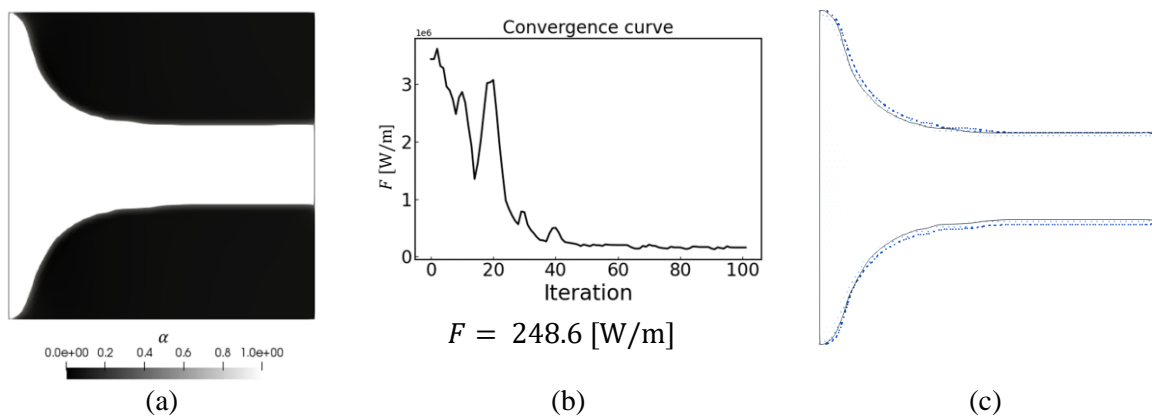
The turbulence regime is reached by updating the dynamic viscosity to $\mu = 0.01169$ [Pa · s],. The optimization parameters are calibrated to $\bar{V}_{frac} = 0.4$ [m³/m³], $q = 0.1$, $\bar{k}_u = 2.5 \times 10^7$ [kg/(m³s)] and $\bar{k}_T = 1 \times 10^2$ [kg/(m K s³)], which outcome is the optimized topology layout shown in Figure 47 with the corresponding convergence curve.

Figure 47. (a) Optimized convergence nozzle without considering a turbulence model, and (b) convergence curve



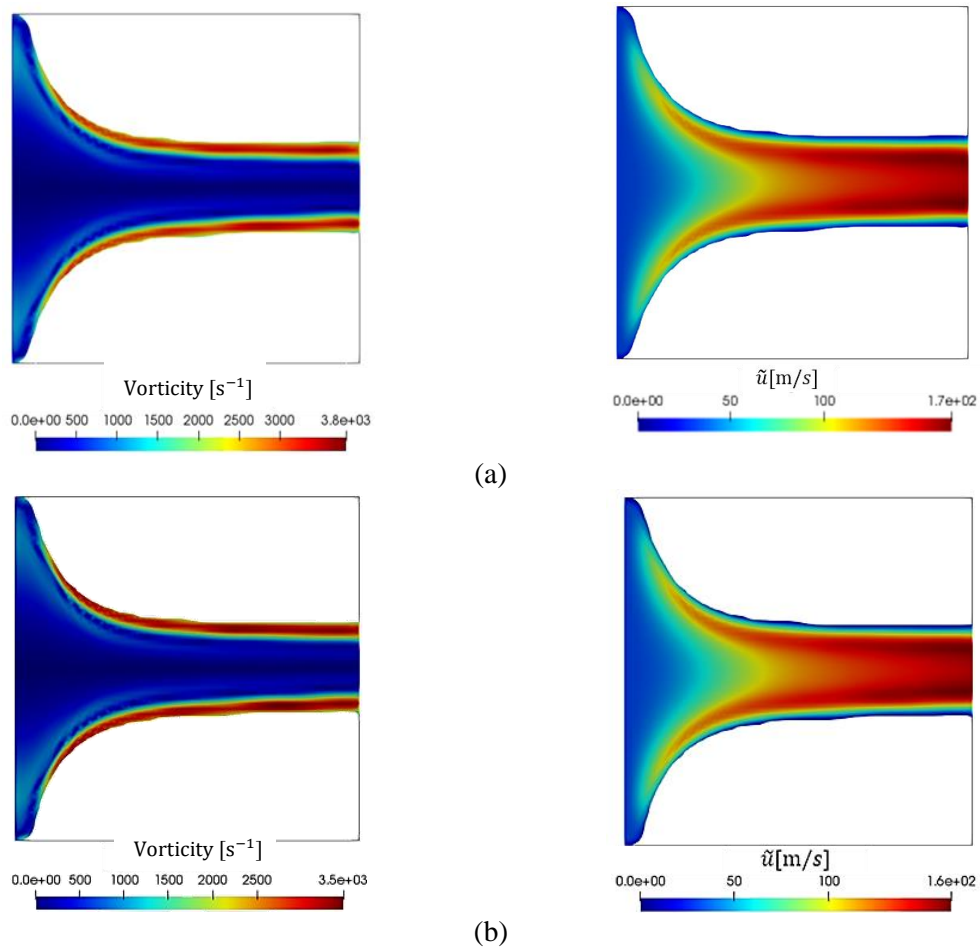
After reaching the turbulence regime approximation, the SA turbulence model is used to analyse accurately the turbulence phenomenon. Therefore, the boundary conditions of the converging nozzle case are updated in Table 17. Also, the optimization parameters related to the SA turbulence model and Eikonal equation are calibrated to $\bar{k}_\phi = 1$ [kg/m³s] and $\bar{k}_\Delta = 1 \times 10^3$ [m⁻³], respectively. The optimized topology, its convergence curve and the comparison between the turbulence approximation solution are shown in Figure 48. The optimized SA nozzle presents a slight thinner outlet channel difference than the turbulence approximation solution (Figure 48c).

Figure 48. (a) Optimized converging nozzle considering the SA turbulence model, (b) convergence curve and (c) comparison of the SA turbulence model (black continuous line) to the turbulence approximation (blue-dotted line)



Despite the influence of the turbulence model calculation is not high in the topology layout, the fluid flow presents variations (Figure 49). For example, the velocity field shows a significant difference in its peak value of 11.8%. Also, the vorticity field varies when the SA turbulence model is employed (Figure 49b), implying the influence of solving accurately the turbulence phenomenon.

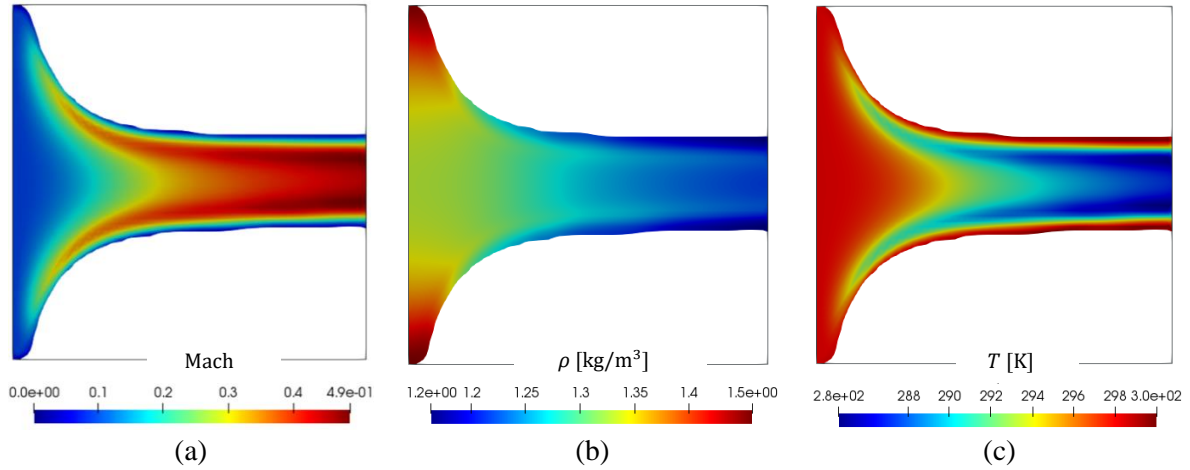
Figure 49. Velocity and vorticity fields of the optimized nozzle under compressible turbulent flow considering (a) the non-turbulence model and (b) the S-A turbulence model



The influence of the turbulent fluid flow modelling is quantified at the objective function, i.e. the optimized topology under the turbulence regime approximation presents a 182.654 [W/m] objective function, which overcomes by 24.4% the Spalart-Allmaras optimized topology (138.064 [W/m]). It can be concluded that the unsolved turbulence phenomena may lead to miscalculations of the objective function, even though, in the current case the topology layout does not vary considerably. Also, it is found that the continuation method allows a step-by-step calibration of the T.O. parameters. Another important fact is reinforced by seeing the primal fields of the case (Figure 50), where the Mach number, the density and the temperature across

the whole domain varies considerably: 20%, 7% and 6.7% respectively. This consolidates the need of using a compressible solver to optimize the topology.

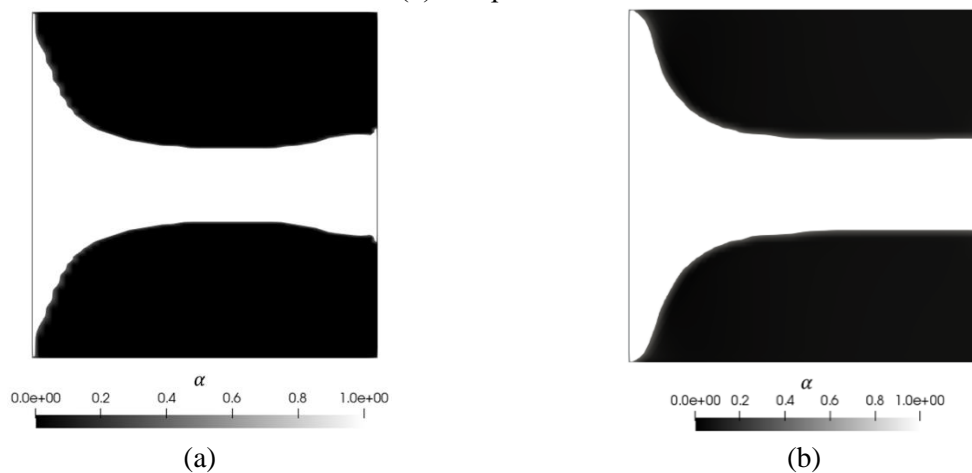
Figure 50. (a) Mach number, (b) density and (c) temperature fields across optimized converging nozzle at compressible turbulent regime



Incompressible and Compressible cross-check trial

As seen, the optimized nozzle case presents variations on its topology layout when the fluid flow regime is changed from incompressible (Mach < 0.3) to compressible flow (Mach > 0.3) (Figure 51). At the following section, the energy dissipation influence at each case is presented.

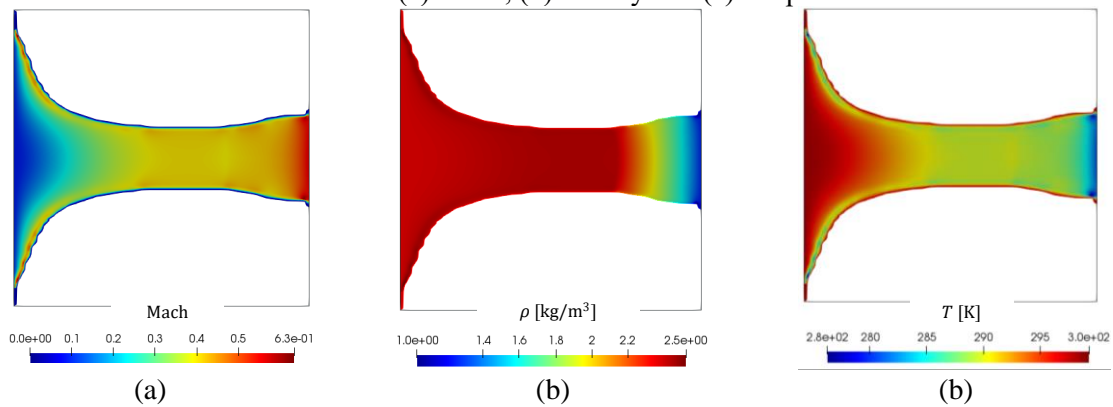
Figure 51. Optimized nozzle at turbulent regime ($Re_{inlet} = 3 \times 10^3$) considering (a) incompressible, and (b) compressible flow



Although previous tests indicated the need to use a compressible-based T.O. formulation, a cross-check trial is performed between the optimized topologies shown in Figure 51, both at the same fluid flow properties of compressible turbulent regime ($u_{inlet} = 30$ [m/s], $T_{inlet} = 298$ [K], $\rho = 1.225$ [kg/m³], and $\mu = 0.01169$ [Pa · s]).

The incompressible optimized topology ($F = 29092.40[\text{W/m}]$) dissipates more energy than the recent obtained compressible optimized topology ($F = 138.064[\text{W/m}]$), which indicates the need of using a compressible-based T.O. formulation. The topologies are remarkable different, and the fluid characteristic fields (Figure 50 and Figure 52) present differences, e.g. the peak Mach number differs 22% between each other. Also, the density variation in each case is larger than 20%, which also supports the need of using a compressible-based T.O. formulation.

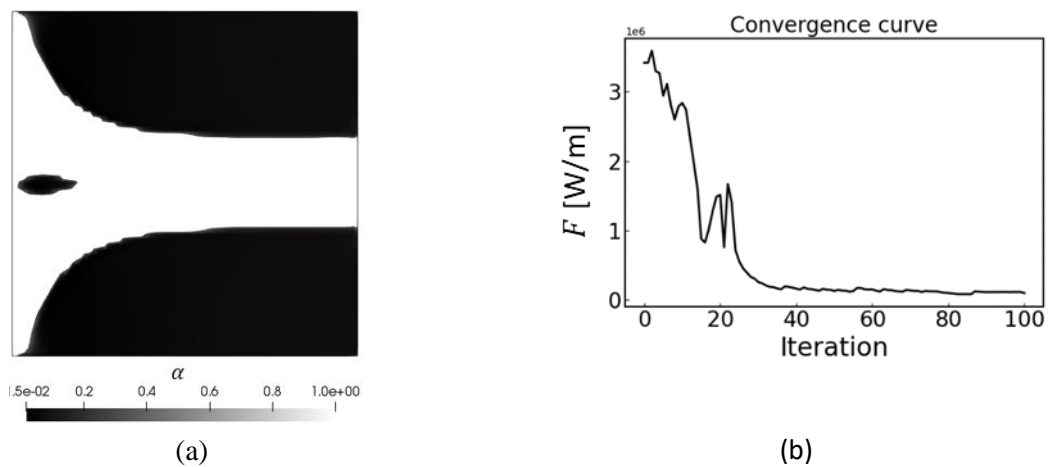
Figure 52 CFD of optimized nozzle designed for incompressible regime but tested at compressible turbulent fluid flow: (a) Mach, (b) density and (c) temperature fields



Reynolds number influence

The compressible nozzle case is tested at a higher Reynolds number by updating the dynamic viscosity to $\mu = 7 \times 10^{-3} [\text{Pa} \cdot \text{s}]$, resulting in a $Re_{inlet} = 5 \times 10^3$. The fluid properties and optimization parameters are remained as previously.

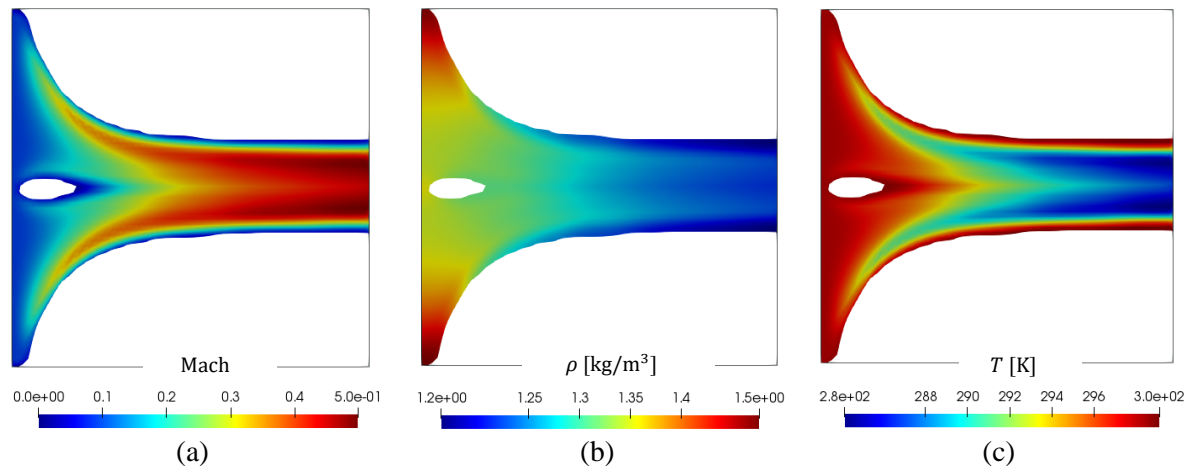
Figure 53. Optimized nozzle under $Re_{inlet} = 5 \times 10^3$



The optimized nozzle topology (Figure 53a) develops an inlet guide vane leading to an energy dissipation value of $F = 156.743 [\text{W/m}]$, which indicates an advantage of the T.O. method as it can produce non-intuitive topologies.

To compare the energy performance of the optimized nozzle, a cross-check validation is made through the CFD modelling of the previously optimized nozzle (Figure 48a) under a $Re_{inlet} = 5 \times 10^3$ as well. The calculated energy dissipation of the optimized compressible nozzle at $Re_{inlet} = 3 \times 10^3$ (Figure 48a) is larger than the Figure 53a topology, i.e. $F = 1119.019$ [W/m], proving the importance of an inlet guide-vane at the $Re_{inlet} = 5 \times 10^3$ regime. The characteristic fluid flow fields (Figure 54) display how the fluid flow bifurcation decelerates near the inlet-guide vane due to its wall boundary. The observed drop in the fluid flow velocity is most probably the reason for the decrease of the energy dissipation calculated across the domain, besides resulting in a thinner domain than the domain presented in Figure 50, which also affects the calculated volume integral.

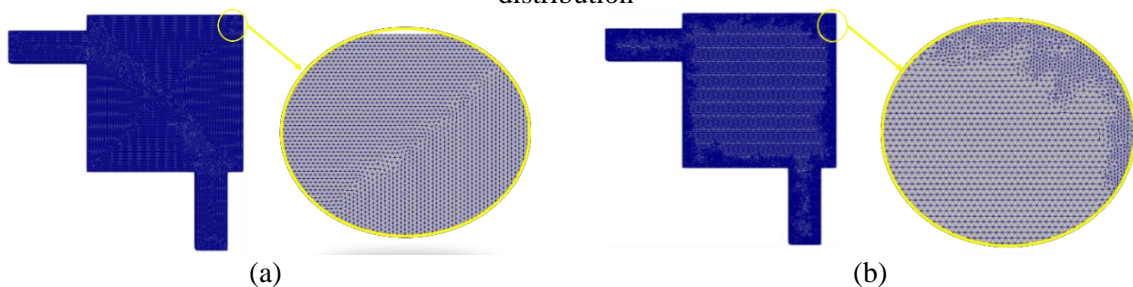
Figure 54. Characteristics flow fields of the optimized nozzle under a $Re_{inlet} = 5 \times 10^3$: (a) Mach, (b) density, and (c) temperature distributions



4.2.2. Pipe-bend Example

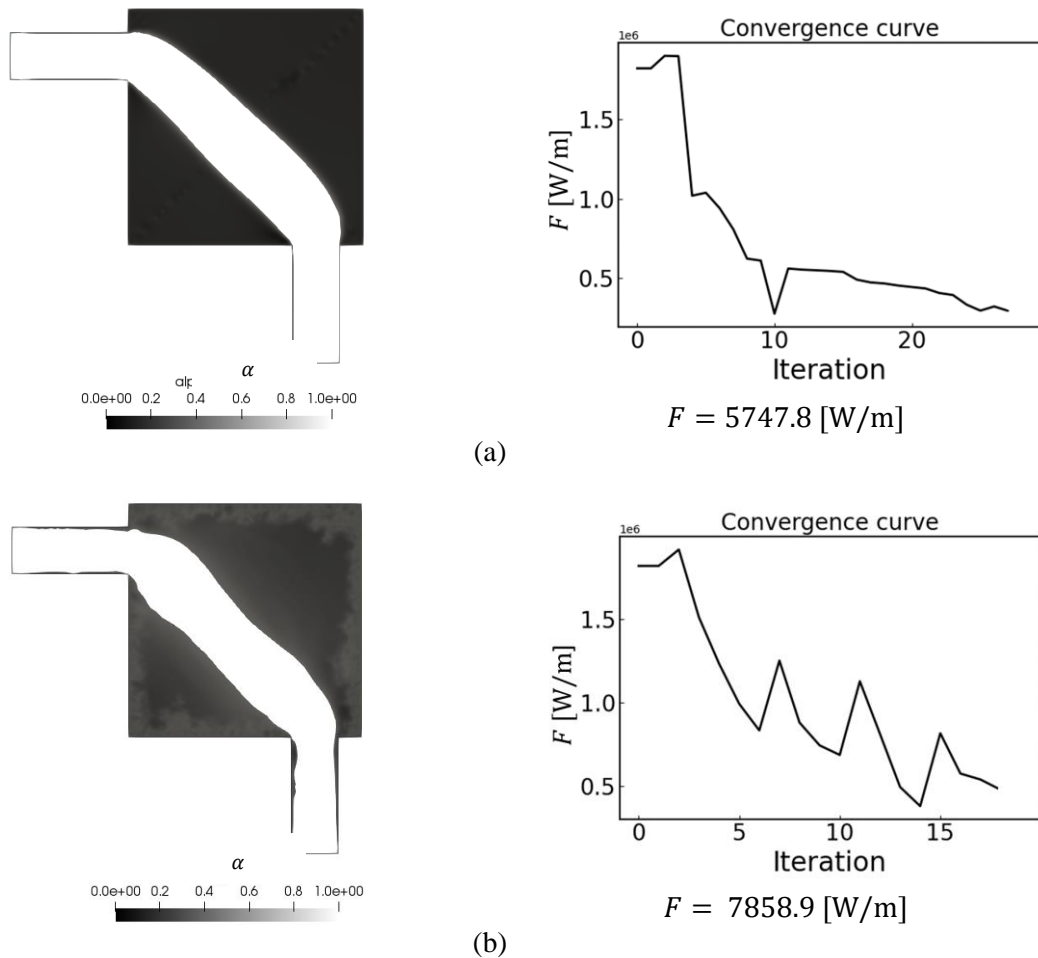
The pipe-bend case of section 0 is optimized at compressible laminar subsonic regime by updating the fluid properties to $u_{inlet} = 50$ [m/s], $T_{inlet} = 193.15$ [K] and $\mu = 1$ [Pa · s], which results in $Re_{inlet} = 60$. Each test considers a constant velocity profile at the inlet boundary. In many cases of fluid flow, complex geometries (such as pipes, nozzles, external flow cases, pumps, etc.) are commonly discretized by non-uniform mesh. Therefore, its influence is initially tested (Figure 55).

Figure 55. Pipe-bend mesh discretization using 2.75×10^4 cells in (a) uniform and (b) non-uniform distribution



The initial guess material distribution ponders $\bar{V}_{frac} = 0.5$ [m³/m³], and the optimization parameters are calibrated to $q = 0.1$, $\bar{k}_u = 2 \times 10^4$ [kg/(m³s)] and $\bar{k}_T = 2 \times 10^4$ [kg/(m K s³)]. The optimization layout from the different meshes is compared (Figure 56), depicting the influence of using non-uniform meshes in T.O., where grey regions appear in the refined mesh zones and the optimized topology reaches a local minimum.

Figure 56. Pipe-bend optimization layout considering (a) uniform and (b) non-uniform mesh distribution.



The grey regions in T.O. indicate a weak definition of volume permeability, as fluid might flow through these volume cells. Therefore, two strategies previous developed at incompressible regime are tried (Alonso et al. 2021): firstly, adjust the sensitivity calculation through its volume division, and secondly, applying the Helmholtz filter with $r_H = 0.5 \times$ (minimum element size). By doing so, the topology layout improves its solid/fluid definition and allows using non-structural meshes in the following T.O. cases (Figure 57). Nevertheless, the objective function varies 20% between the structured uniform and the unstructured non-uniform meshes optimized topologies. Since both optimized topologies are different, this shows that there is a mesh-dependency effect.

The T.O. mesh-dependency effect is not present in structured uniform meshes, however, the optimization at unstructured non-uniform meshes may feature such effect intensely. In the field of optimization, there is the mathematical concept of the Riesz map, which converts between the primal (simulation) and dual (adjoint) spaces the sensitivities to their mesh-independent variants by essentially weighting them by the volume around each node. The resulting "adjusting sensitivity method", featuring such conversion, makes the difference only when unstructured non-uniform meshes are used, e.g. when complex domains are required.

Figure 57. Optimized pipe-bend topology in a non-uniform mesh adjusting sensitivity and employing the Helmholtz filter

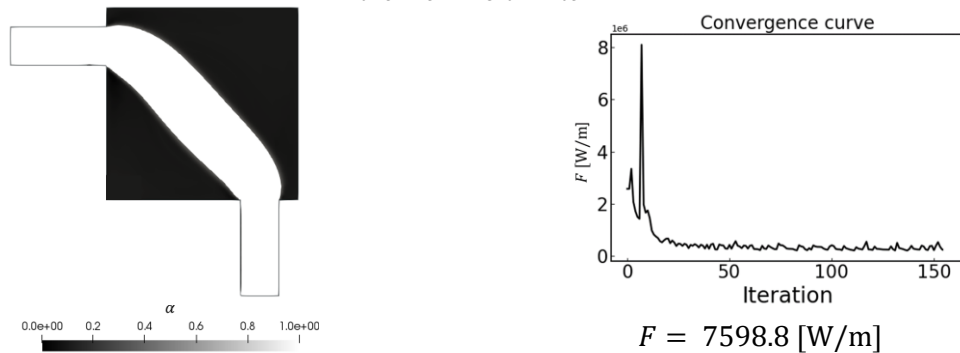


Figure 58. Characteristic flow fields of the optimized pipe-bend case at compressible laminar regime

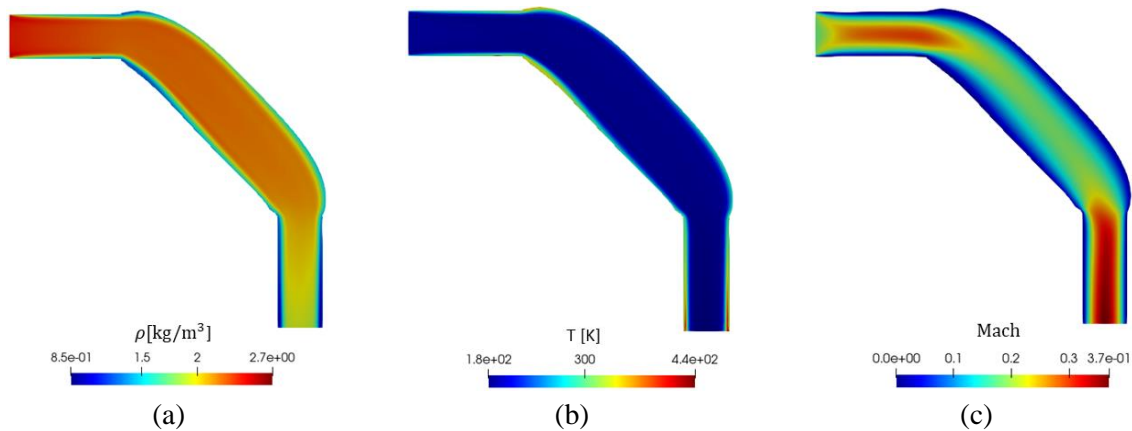


Figure 58 shows a 68.5% density variation along the optimized pipe-bend domain, which justifies again the development of a compressible-based T.O. formulation as previously. The large peak temperature gradients are found near the walls, and the achieved peak Mach number supports the optimization of compressible subsonic regime.

Then, the turbulent compressible regime is setup by updating the $u_{inlet} = 60$ [m/s] and $\mu = 5 \times 10^{-4}$ [Pa · s], reaching a $Re_{inlet} = 2.4 \times 10^4$. The optimization parameters are calibrated to $\bar{V}_{frac} = 0.5$ [m³/m³], $\bar{k}_u = 2 \times 10^4$ [kg/(m³s)], $\bar{k}_T = 2 \times 10^4$ [kg/(m K s³)] and $q = 0.1$, resulting in Figure 59 topology layout.

Note that in Figure 59 instabilities are found at the optimized topology due to lower fluid viscosity and the domain shape, which is sensitive to vortex generation at the outlet region, challenging the T.O. process. To overcome the mentioned instabilities in the topology layout, a viscosity continuation is proposed by starting with high viscosity values ($\mu_{start} = 0.5$ [Pa · s]) and taking each topology layout result to start the next optimization process until reaching the desired fluid viscosity ($\mu_{end} = 5 \times 10^{-4}$ [Pa · s]), which is depicted in Figure 60.

Figure 59. Pipe-bend topology layout at compressible turbulent regime approximation

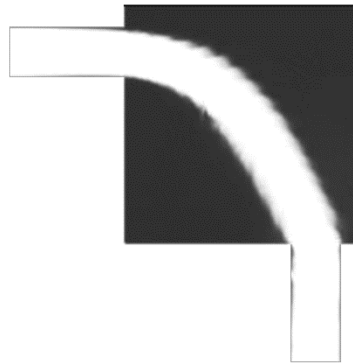
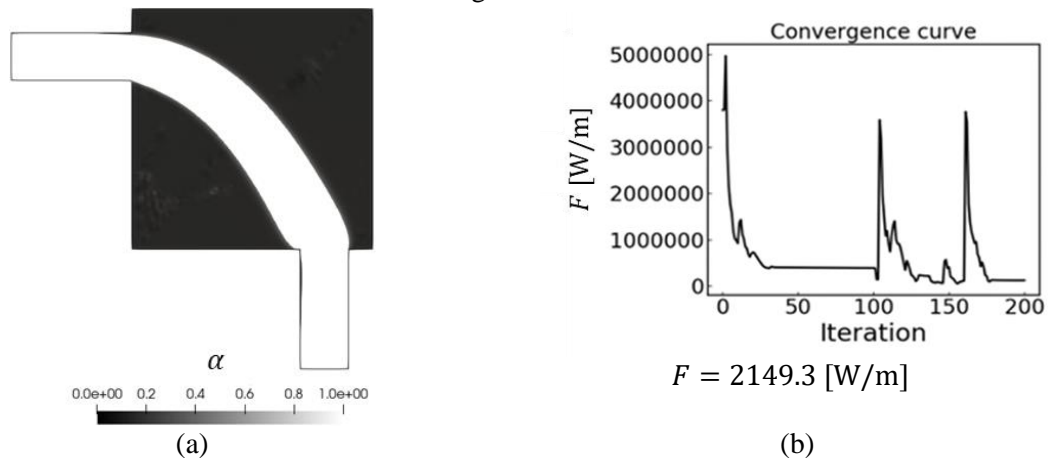


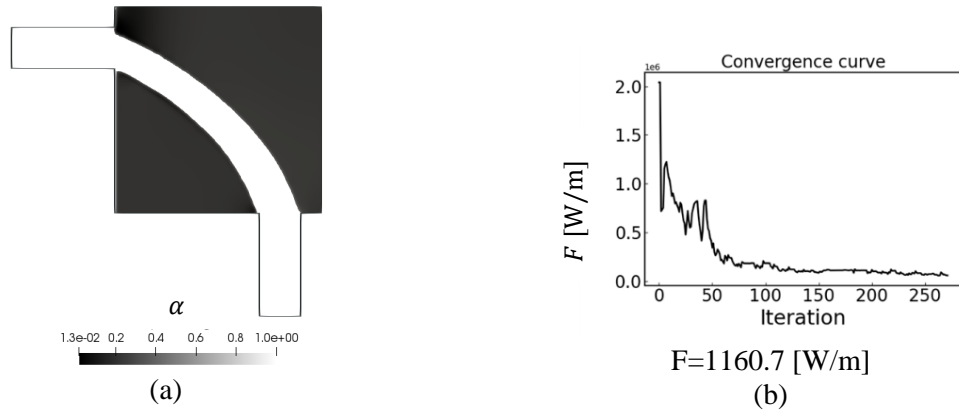
Figure 60. (a) Optimized pipe-bend under the compressible turbulent approximation regime and (b) convergence curve.



The analysed case is updated by solving the turbulence phenomenon. The T.O. parameters are calibrated for the SA turbulence model ($\bar{k}_{\varphi} = 5$ [kg/m³ s]) and the Eikonal equation ($\bar{k}_{\Delta} = 25$ [m⁻³]), resulting in the optimized topology and convergence curve presented in Figure 61.

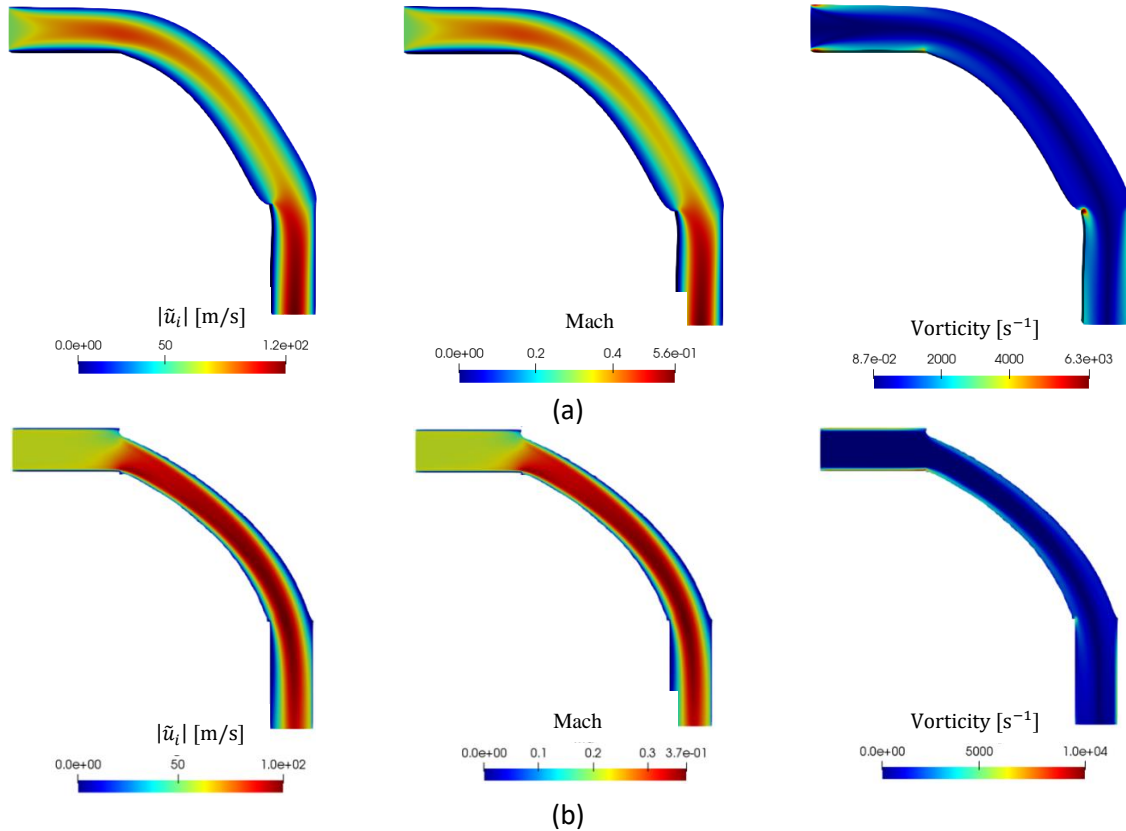
By solving the turbulence phenomenon, the pipe-bend topology decreases its thickness in comparison to the optimized pipe-bend turbulence approximation solution (Figure 60). This channel thickness variation leads to an objective function difference of 46% between the optimized cases.

Figure 61. (a) Optimized pipe-bend topology layout considering the Spalart-Allmaras turbulence model, (b) convergence curve



The characteristic flow fields (Figure 62) analysis also demonstrates that not solving the turbulence phenomenon overestimates the peak fluid acceleration by 16.7%, which influences the Mach number calculation presenting a peak difference of 33.9%. Also, the vorticity field comparison shows that not solving the turbulence phenomenon, overestimates the regions and values where eddies could be identified.

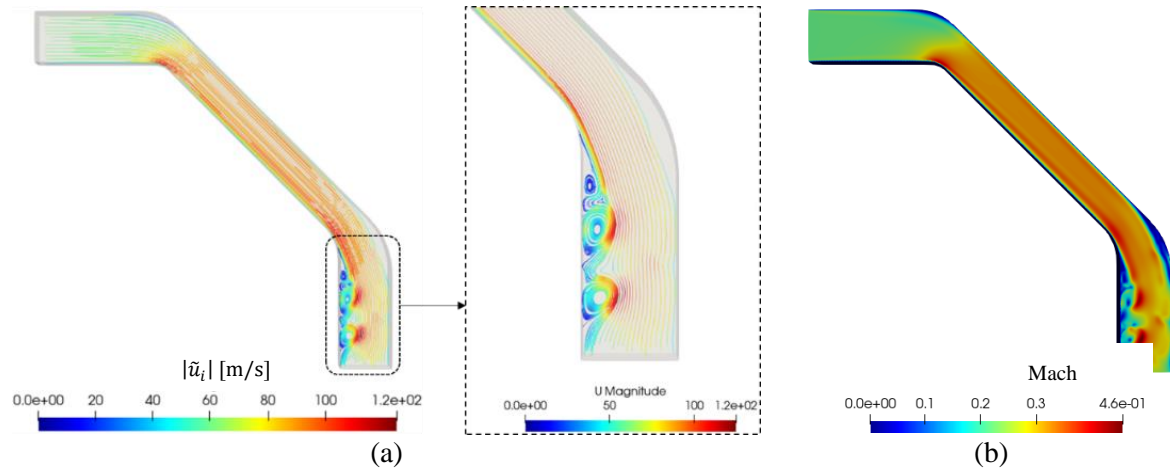
Figure 62. Pipe-bend characteristic flow fields under compressible subsonic (a) turbulence approximation and (b) SA turbulence model



Finally, the optimized pipe-bend (Figure 61) is compared to a baseline design (Figure 63) under the same fluid flow conditions.

A chaotic flow is found in the outlet region of the baseline pipe-bend, which increases its energy dissipation to $F = 3233.1$ [W/m], which is 64.1% larger than the optimized pipe-bend topology ($F = 1160.7$ [W/m]).

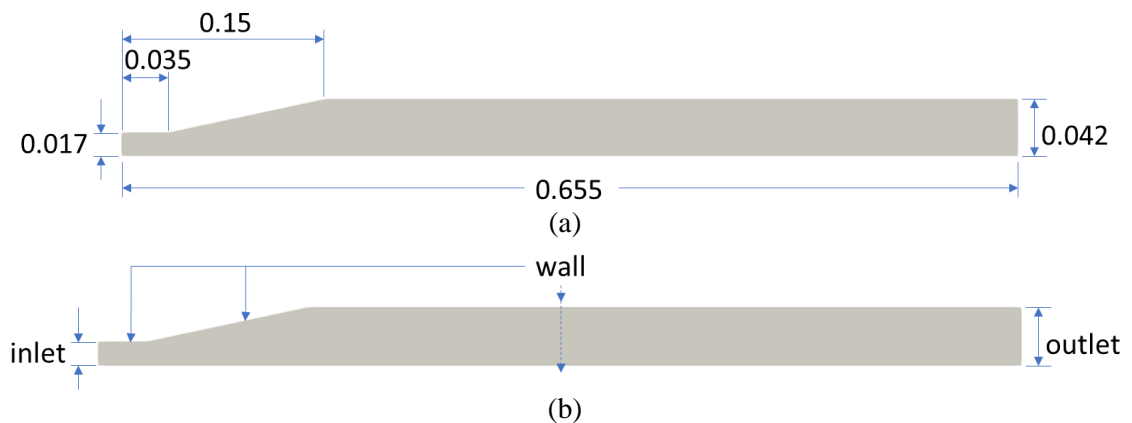
Figure 63. Pipe-bend baseline at compressible turbulent regime: (a) velocity streamlines and (b) Mach field.



4.2.3. Diffuser

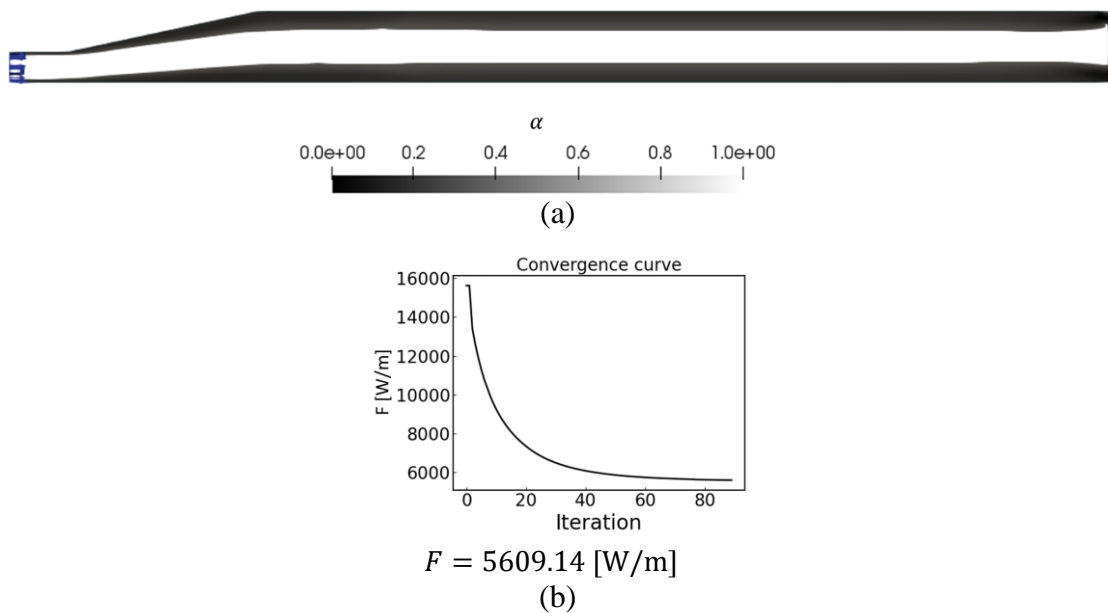
Finally, a diffuser domain from experimental tests (Alvarenga et al. 2016) at compressible subsonic flow application is brought to the current research to be optimized. The case consists of a duct with a transversal area enlargement (Figure 64). Generally, these kinds of devices are employed to diminish the kinetic energy of tube systems by increasing the cross-section, generating an increase in the pressure inlet/outlet ratio.

Figure 64. Diffuser domain (a) dimensions and (b) boundaries



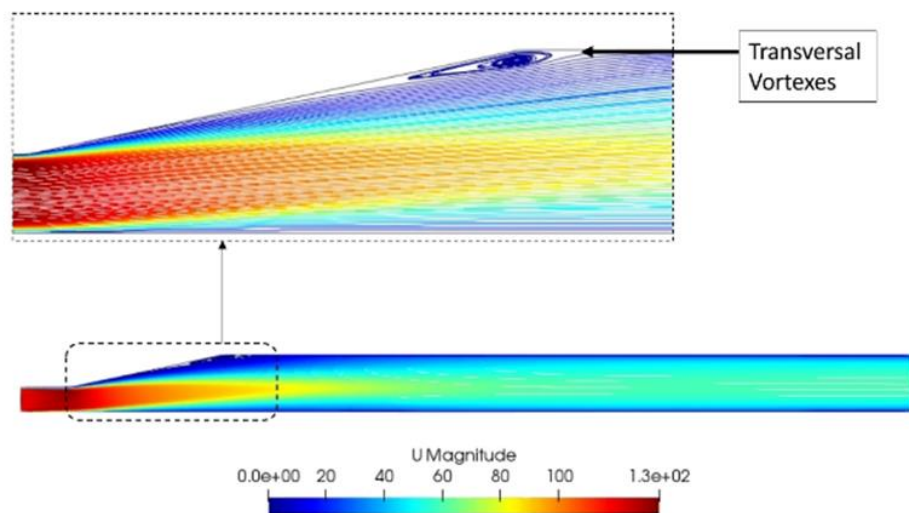
The boundary conditions are established as $p_{t_{inlet}} = 97316$ [Pa], $p_{t_{outlet}} = 101325$ [Pa], $\mu = 0.01$ [Pa · s], $\rho_{inlet} = 1.169$ [kg/m³] resulting in a $Re_{inlet} = 238$. Also, the optimization parameters are calibrated to $\bar{V}_{frac} = 0.4$ [m³/m³], $\bar{k}_u = 2.5 \times 10^7$ [kg/(m³s)], $\bar{k}_T = 1 \times 10^2$ [kg/(m K s³)] and $q = 1 \times 10^{-4}$, leading the optimization of the diffuser domain to the result shown in Figure 65.

Figure 65. Optimized diffuser under laminar compressible flow: (a) topology layout and (b) convergence curve



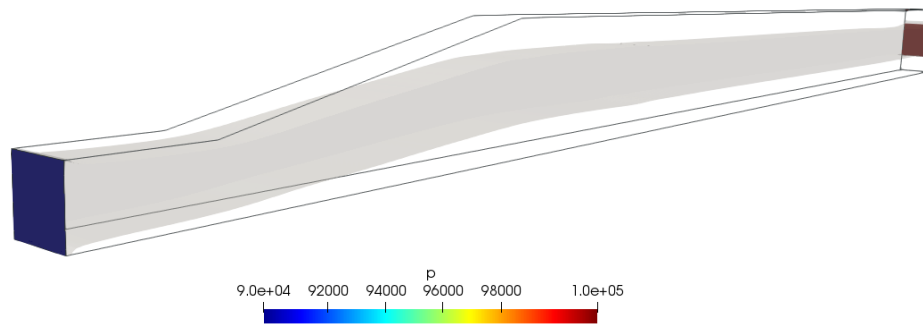
As expected, solid cells are placed at the converging transversal area after the inlet tube, to avoid vortex generation, which is commonly generated by changes in the cross-section areas (Figure 66).

Figure 66. CFD of original diffuser



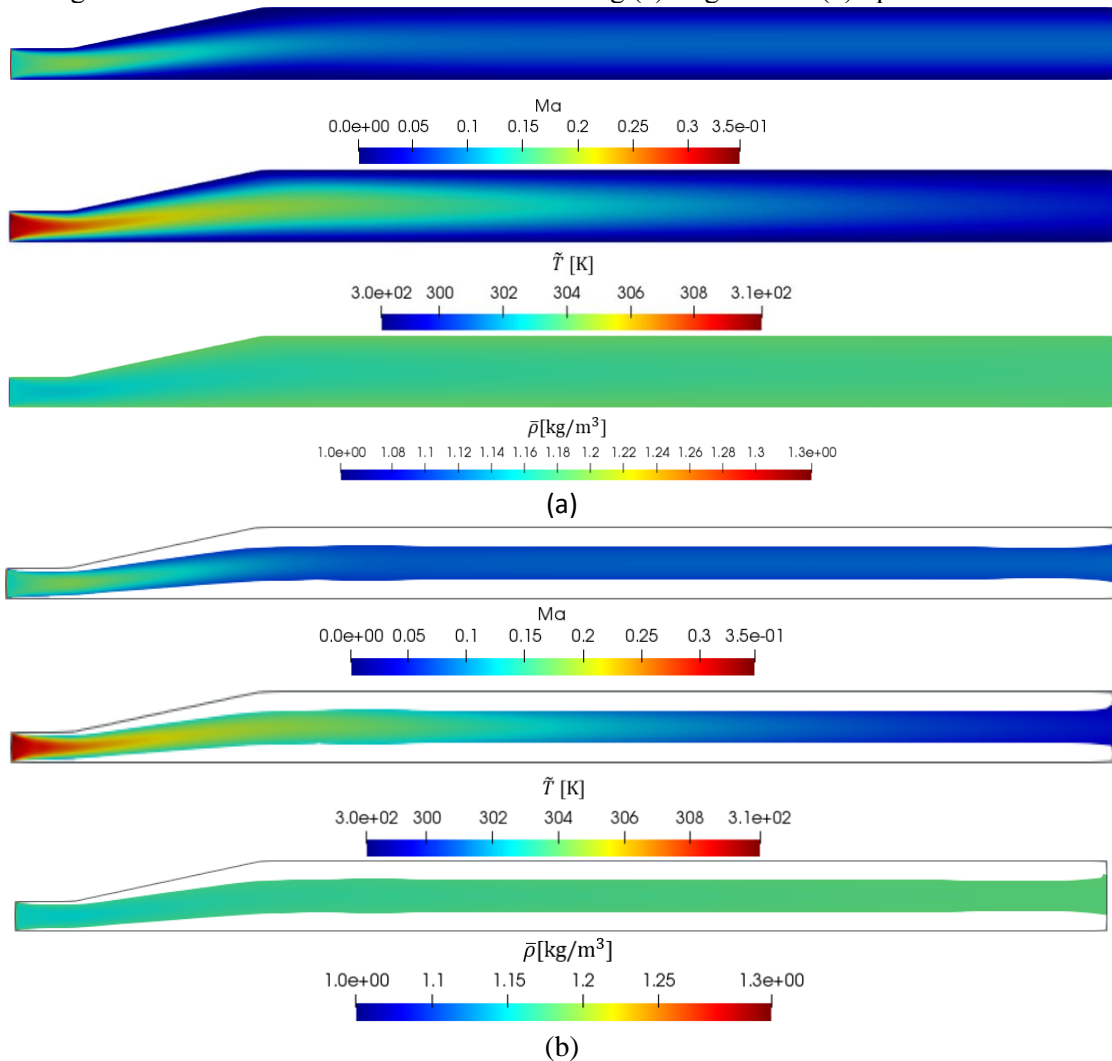
Despite some material being placed next to the wall boundaries, the optimized diffuser still guarantees the initial pressure difference established (Figure 67).

Figure 67. The pressure difference between inlet/outlet boundaries of optimized diffuse



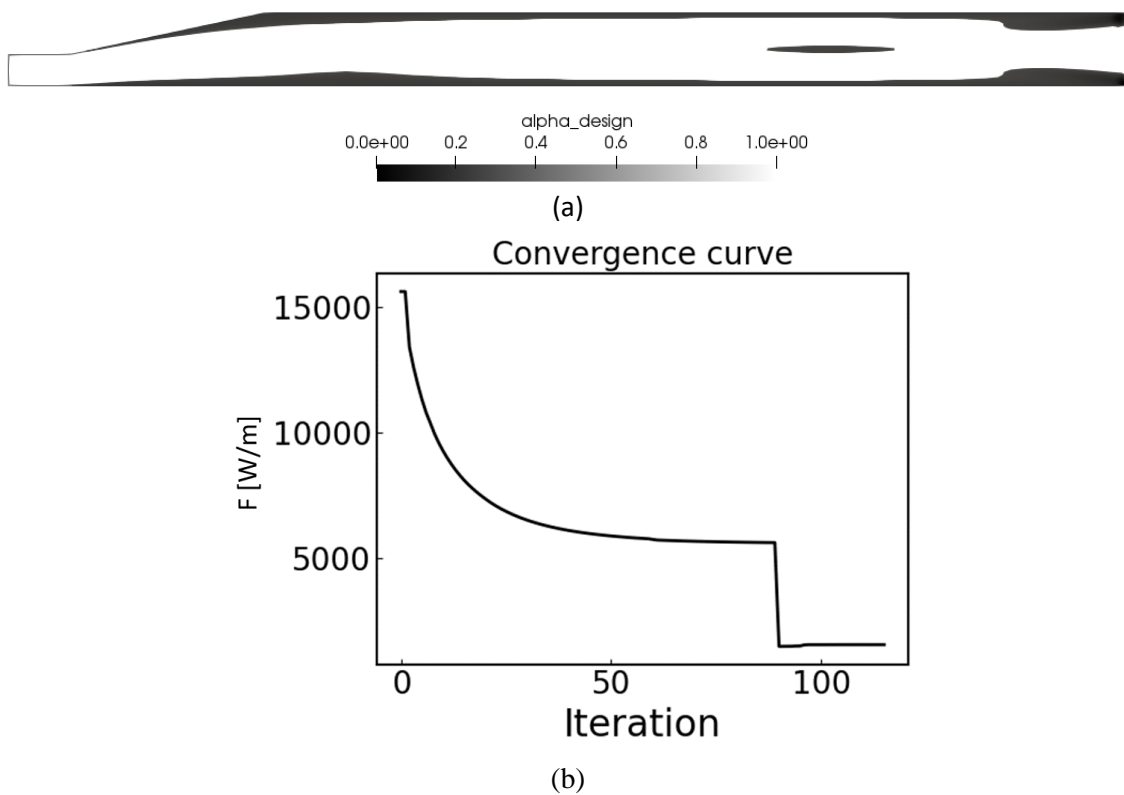
The objective functions of the optimized ($F=5609.14$ [W/m]) and original ($F=5650.61$ [W/m]) diffuser cases are similar, showing that a thinner optimized diffuser can improve by 0.74% the energy dissipation across an original design, and maintains the desired pressure difference of the initial domain. This objective function resemblance is seen in the characteristic fields of each (Figure 68), where significant variations in the density and temperature fields are found in both cases, i.e. of 23% and 3.22% respectively- These variations justify the need of using a compressible fluid-based solver.

Figure 68. Characteristic fields distribution along (a) original and (b) optimized diffuser



After optimizing the laminar compressible regime, the viscosity is updated to $\mu = 7 \times 10^{-4}$ [Pa · s], resulting in a turbulent inlet number of $Re_{inlet} = 3400$. The optimization is performed without considering the turbulence approximation approach and includes an update of the viscosity value through the optimization process, which can be seen in the convergence curve behaviour that changes drastically due to the viscosity update (Figure 69b). The turbulent variables are solved directly via the Spalart-Allmaras turbulence model applying a turbulent intensity inlet value of 5% and calibrating the T.O. turbulence parameters at $\bar{k}_\nu = 1$ [kg/m³ s] and $\bar{k}_\Delta = 1 \times -3$ [m⁻³]. The optimized layout is seen in (Figure 69a).

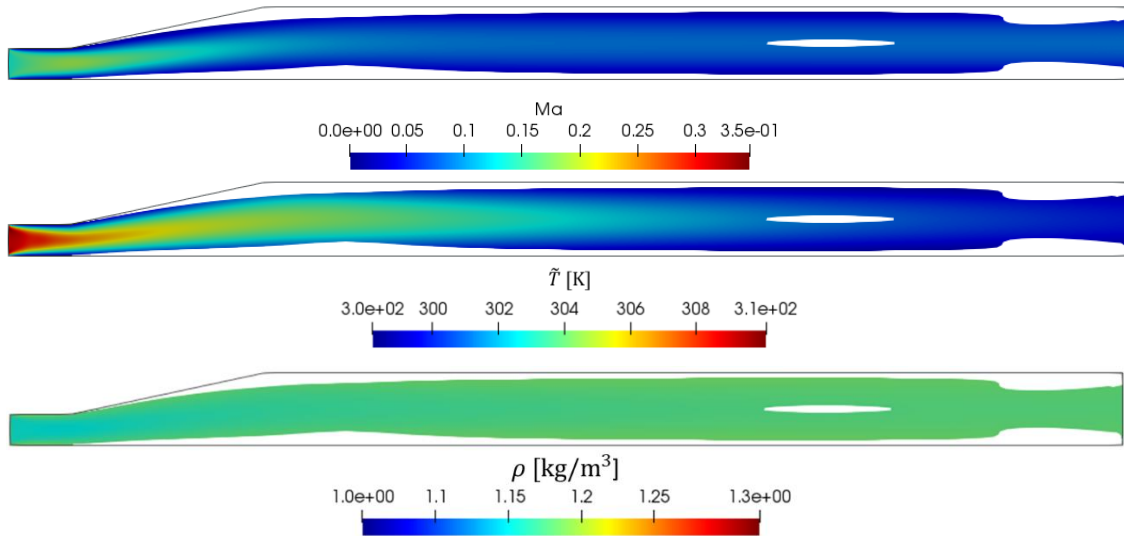
Figure 69. (a) Optimized diffuser for compressible turbulent subsonic flow and (b) convergence curve



A remarkable difference is seen between the optimized diffusers at compressible laminar (Figure 65) and turbulent (Figure 69a) regimes. At first, the optimized diffuser at compressible turbulent conditions presents a thinner channel after the inlet variation cross-section, which helps to decrease the kinematic fluid conditions. Then, a splitter is generated near the outlet region, along with a cross-section reduction. By doing so, the fluid diminishes the kinematic energy at the entrance region up to the splitter point, where it is accelerated due to the cross-section area diminution resulting in optimized energy dissipation of 1527.550 [W/m].

The primal fields of the optimized diffuser at compressible turbulent conditions (Figure 70) show a subsonic Mach number reached, framed with a temperature reduction at its outlet region and a density variation of 23% along the domain.

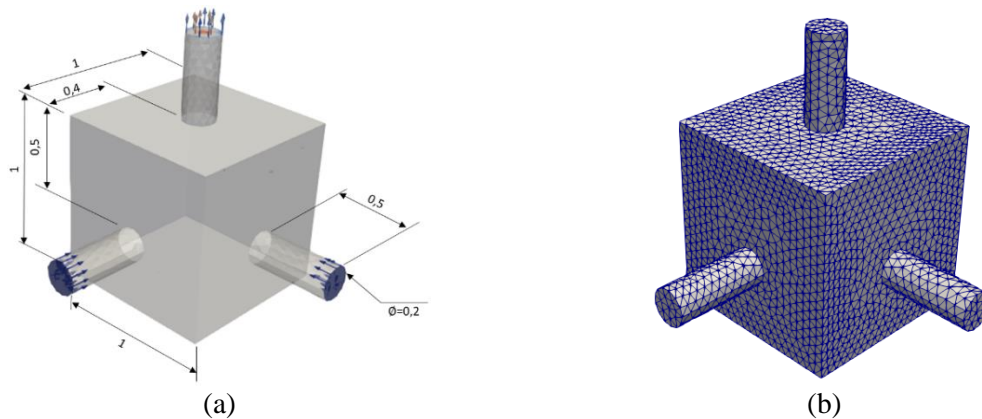
Figure 70. Primal fields of the optimized diffuser at compressible turbulent subsonic conditions.



4.2.4. 3D pipe-joint

The robustness and flexibility of the developed methodology in the FEniCS TopOpt FOAM software are tested by optimizing a 3D domain. It consists of a hexahedral space with two inlets and one outlet boundary with $L_{\text{inlet}} = L_{\text{outlet}} = 0.2$ [m] each (Figure 71a). The domain is discretized by a 5×10^4 tetrahedral elements (Figure 71b) and uses Table 17 boundary conditions. The velocity and viscosity are updated to $u_{\text{inlet}} = 40$ [m/s] and $\mu_{\text{inlet}} = 6 \times 10^{-3}$ [Pa · s], in order to ensure a subsonic turbulent flow, i.e. $Ma_{\text{max}} = 0.44$ and $Re_{\text{outlet}} = 5.6 \times 10^3$. The optimization parameters are calibrated as Table 18 shows.

Figure 71. (a) 3D initial domain, and (b) mesh discretization (4323 tetrahedral elements)



The optimization is achieved (Figure 72) by using the continuation method, which updates the fluid viscosity after a series of optimization iterations (Table 19).

Table 18. Optimization parameters for compressible turbulent flow.

T.O. parameters	Value
α_{start}	1
$\bar{V}_{fraction} [\text{m}^3/\text{m}^3]$	0.33
q	0.1
$\bar{k}_\mu [\text{kg}/(\text{m}^3\text{s})]$	1×10^4
$\bar{k}_T [\text{kg}/(\text{m K s}^3)]$	1×10^4
$\bar{k}_{\nu_t} [\text{kg}/\text{m}^3\text{s}]$	5×10^{-2}
$\bar{k}_A [\text{m}^{-3}]$	1×10^3

Table 19. Optimization continuation method used in the fluid interchange case

Viscosity $\mu_{inlet} [\text{Pa} \cdot \text{s}]$	6×10^{-1}	6×10^{-2}	6×10^{-3}
Optimization iterations	50	50	100

As expected, the inlet pipes are connected at the outlet region, forming a diagonal topology. The viscosity update influence is seen at the convergence curve peaks, where the objective function varies according to the optimization steps named in Table 19 until the topology and the objective function stop varying. The characteristic flow fields of the optimized container (Figure 73) show how the fluid reaches the compressible subsonic regime, with a peak Mach number of 0.52 and density variation of 42%, which justifies again the implementation of the compressible-based T.O. formulation.

Figure 72. (a) Optimized 3D topology at turbulent subsonic compressible regime and (b) convergence curve

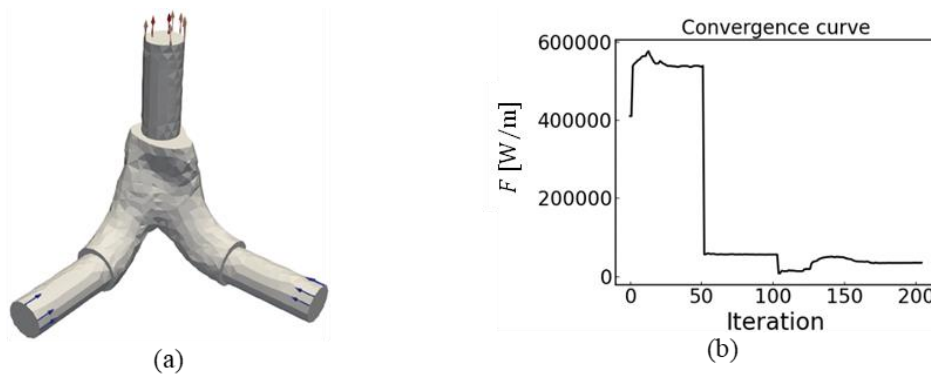
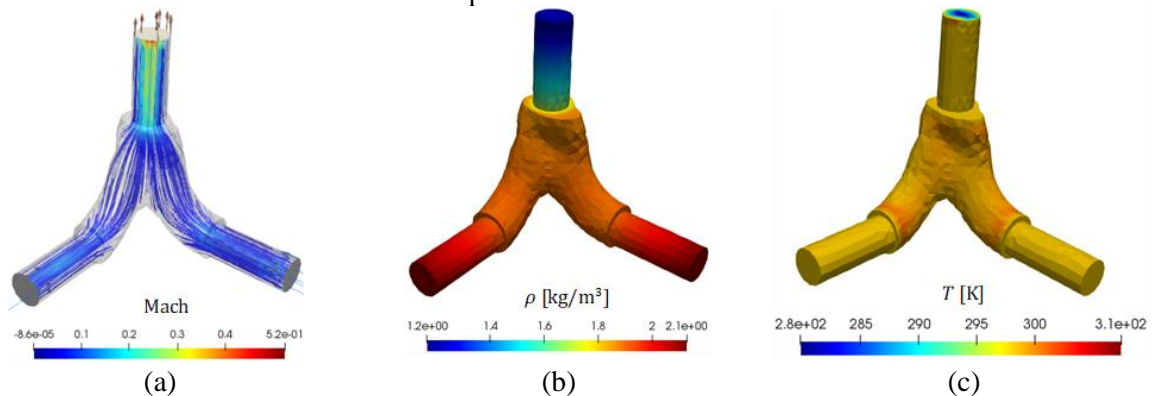
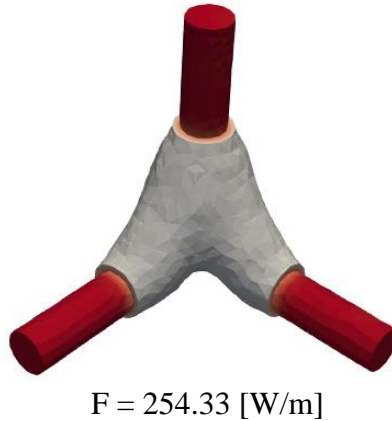


Figure 73. Characteristic fluid flow fields of optimized container: (a) Mach, (b) density and (c) temperature distribution



The optimized topology is cross-checked and validated to an optimized 3D pipe-joint obtained by using incompressible regime conditions (Figure 74). Despite both topologies being similar, the dissipated energy performance of the compressible solver-based optimized container (Figure 73) is 75.2% better.

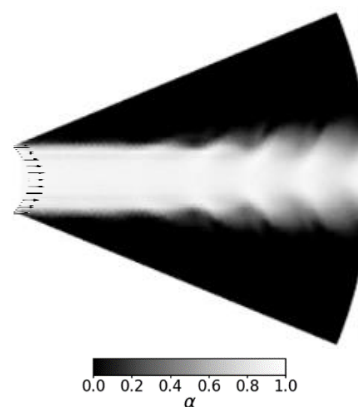
Figure 74. The optimized 3D pipe joint obtained considering incompressible regime



4.2.5. Rotor Example

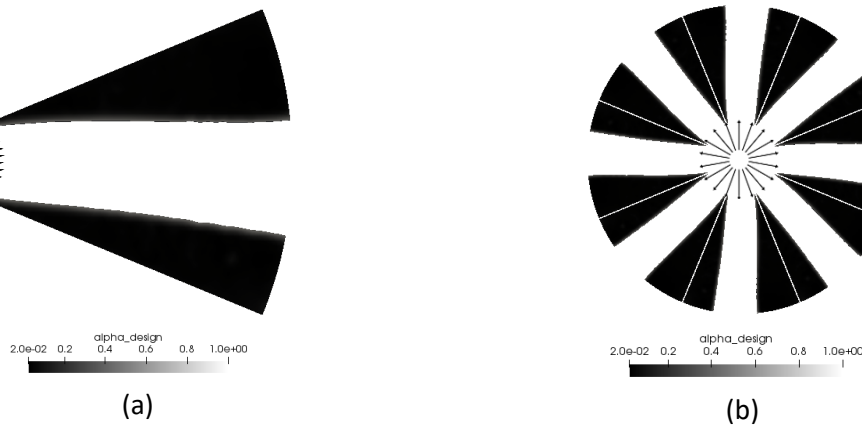
Finally, the developed FEniCS TopOpt FOAM software based on the discrete adjoint methodology is applied to a rotational domain. The rotor cavity case mentioned in section 4.1.6, is tested at compressible turbulent regime by varying the fluid flow properties to $u_{inlet} = 120 \text{ [m/s]}$, $\mu = 5 \times 10^{-4} \text{ [Pa} \cdot \text{s]}$, $n = 400 \text{ [rpm]}$, $T_{inlet} = 298 \text{ [K]}$ and $p_{out} = 101325 \text{ [Pa]}$. The optimization is performed by calibrating the T.O. parameters to $\bar{k}_u = 8 \times 10^5 \left[\frac{\text{kg}}{\text{m}^3 \text{s}} \right]$, and $q_\phi = 0.2112$. The optimized topology layouts are shown in Figure 75, where instabilities are found at the optimized topology due to fluid low viscosity, which is sensible to generate vortexes.

Figure 75. Optimized straight blade rotor cavity under compressible subsonic turbulent regime approximation.



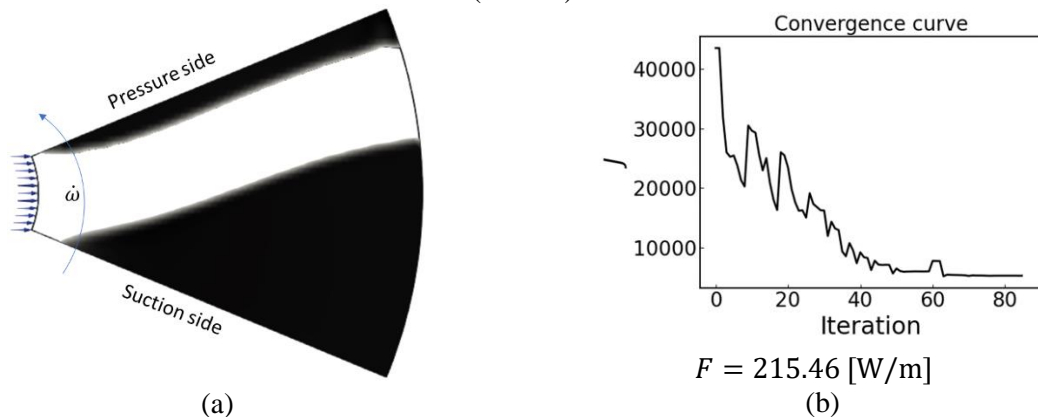
To overcome the vortex generation at the optimized topology, the viscosity continuation methodology is applied: starting with a high viscosity value ($\mu_{\text{start}} = 0.5$ [Pa · s]) and take its topology layout result to start the next optimization process until reaching the desired regime ($\mu_{\text{end}} = 5 \times 10^{-4}$ [Pa · s]). The proposed methodology succeeds, and the instabilities found previously due to vortex generation are not presented anymore (Figure 76).

Figure 76. Topology optimization of straight blade rotor under turbulent compressible regime approximation: (a) 45° section and (b) complete rotor.



The previous domain is tested under the same fluid flow conditions, however, turbulence is solved using the SA turbulence model. Therefore, the material penalization parameters related to the turbulence model are included: $\overline{k_{\phi}} = 1.0$ [kg/m³s], $\overline{k_{\Delta}} = 1 \times 10^{-5}$ [m⁻³], and the optimized topology layout is shown in Figure 77. By solving the turbulence phenomenon, a thinner convex fluid cavity is created, and it is directed to the pressure side of the initial rotor cavity domain (Figure 77).

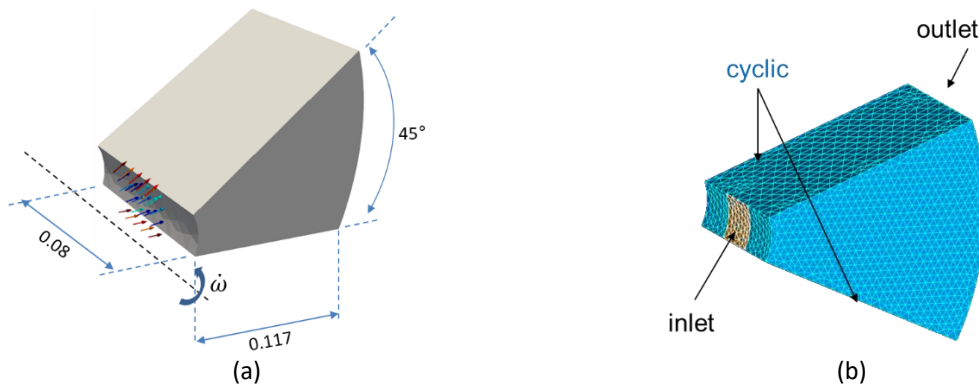
Figure 77. Topology layout of compressible turbulent rotor (a) 45° section and (b) complete rotor (Author)



Finally, the straight blade cavity domain is extended at 3D (Figure 78a), which is discretized by 3.4×10^3 tetrahedral elements (Figure 78b). In the 3D domain, large rotational velocities are tested, which implies the update of the turbulence model, i.e. the use of the Wray-Agarwal turbulence model.

Also, the wall boundaries are replaced with the cyclic boundary conditions (Ltd.) (i.e. ensuring that the outcome flow from one patch is projected equally as the entering flow from the other patch (Ltd.)), to avoid the reverse flow found in Figure 43d. By doing so, the Table 17 boundary conditions are updated to $u_{inlet} = 110$ [m/s] and $\mu_{inlet} = 6 \times 10^{-4}$ [Pa · s] respectively, which imposes a $Re_{inlet} = 3.6 \times 10^3$. Also, each side of the cyclic condition receives a nomenclature of cyclic-1 and cyclic-2 as Table 17 shows. The rotor spins at $n = 1 \times 10^3$ [rpm].

Figure 78. (a) 3D initial domain, and (b) mesh discretization

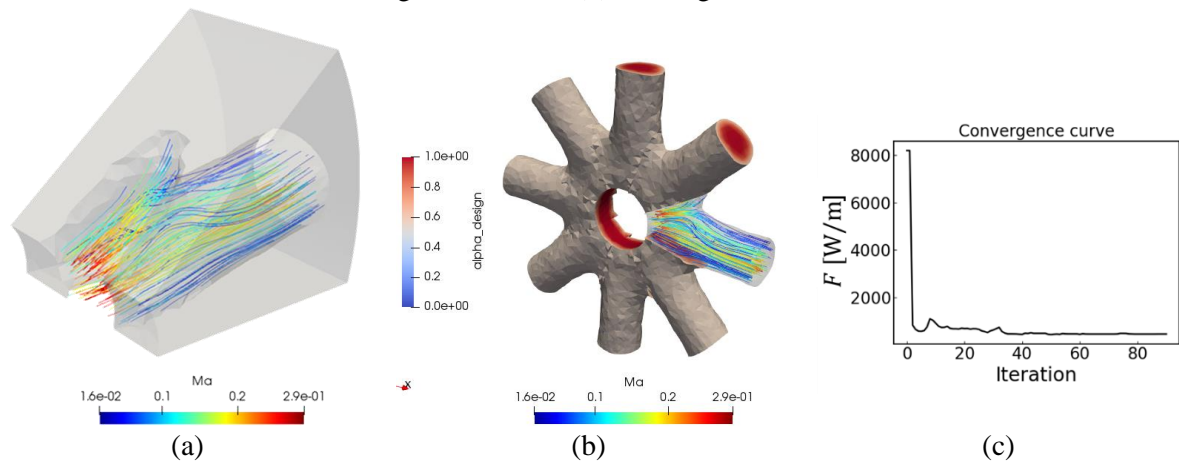


The optimization parameters are calibrated (Table 20), until reaching a well-defined optimized topology shown in Figure 79.

Table 20. Optimization parameters for compressible turbulent flow.

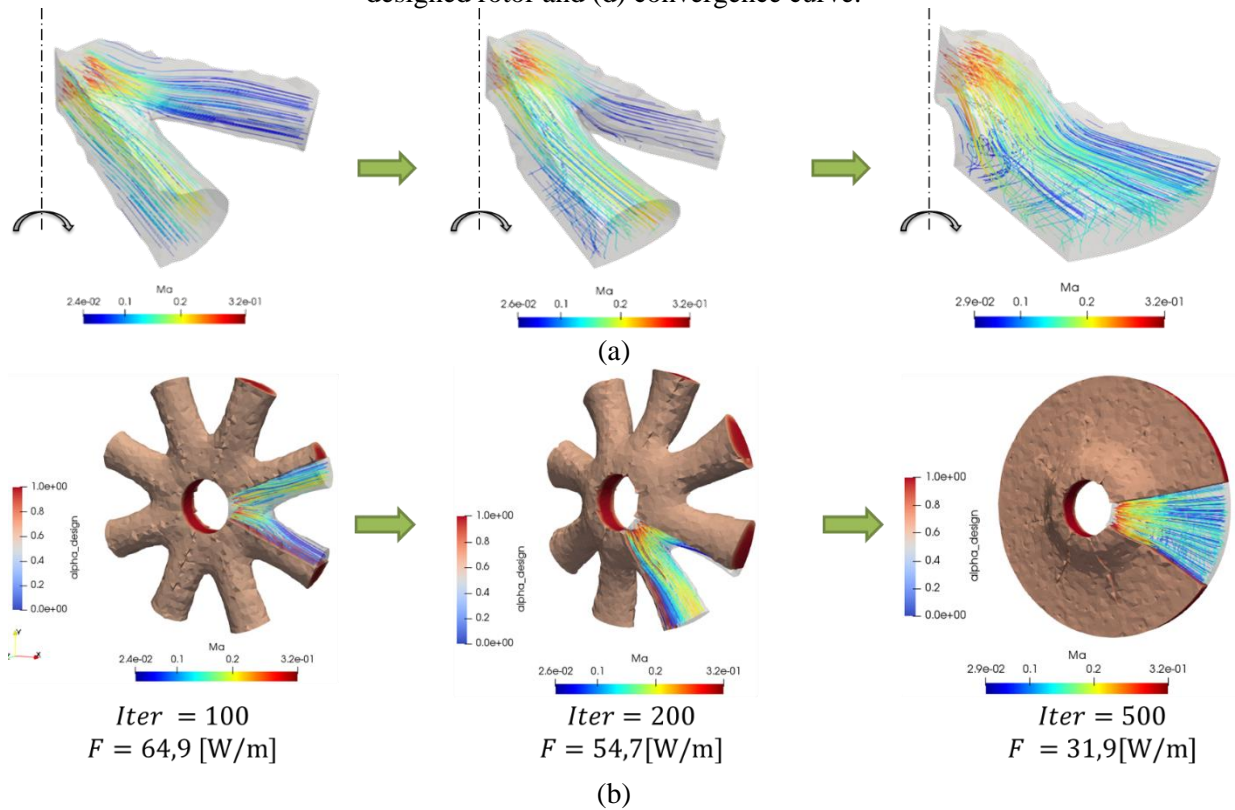
α_{start}	$\bar{V}_{fraction}$ [m ³ /m ³]	q	\bar{k}_u [kg/(m ³ s)]	\bar{k}_T [kg/(m K s ³)]	\bar{k}_ρ [kg/m ³ s]	\bar{k}_Δ [m ⁻³]
0	0.33	0.1	16×10^4	2×10^4	1	1

Figure 79. (a) Optimized 3D straight blade rotor cavity at compressible turbulent subsonic regime (b) designed rotor and (d) convergence curve.



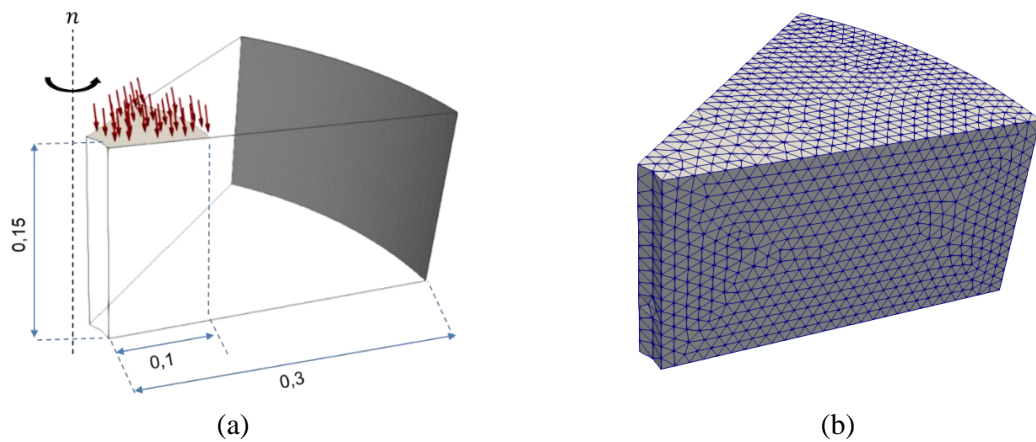
The domain is tested at $n = 4 \times 10^3$ [rpm], and the optimized topology at 500 iterations results in a rotor without blades, similar to a Tesla-type rotor.

Figure 80. (a) Optimized 3D straight blade rotor cavity at compressible turbulent subsonic regime (b) designed rotor and (d) convergence curve.



Therefore, the domain is extended to a real-size rotor discretized by 2.4×10^4 tetrahedral elements (Figure 81). The inlet velocity is considered with an axial direction.

Figure 81. (a) 3D initial domain, and (b) mesh discretization (2.4×10^4 tetrahedral elements)

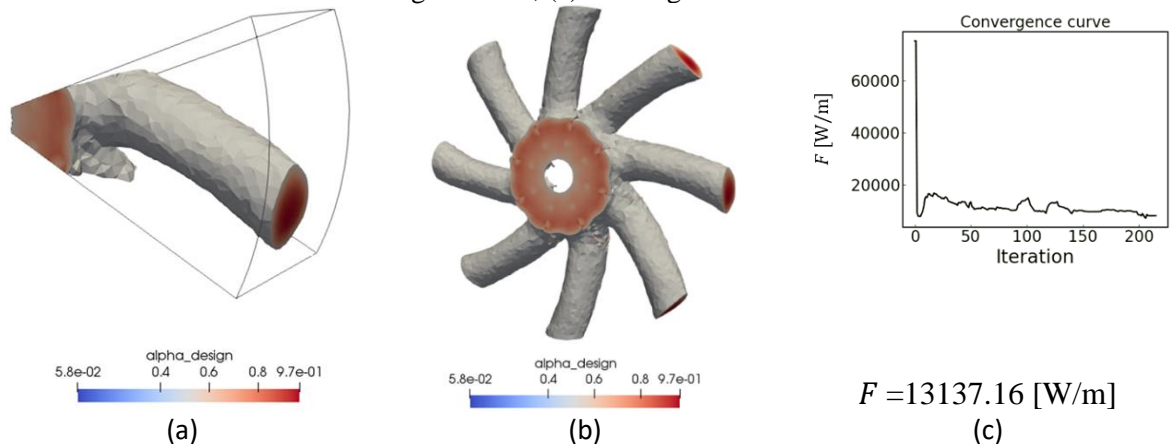


The optimization parameters are calibrated as Table 18 shows, which outcome is the optimized topology shown in Figure 82.

Table 21. Optimization parameters for compressible turbulent flow.

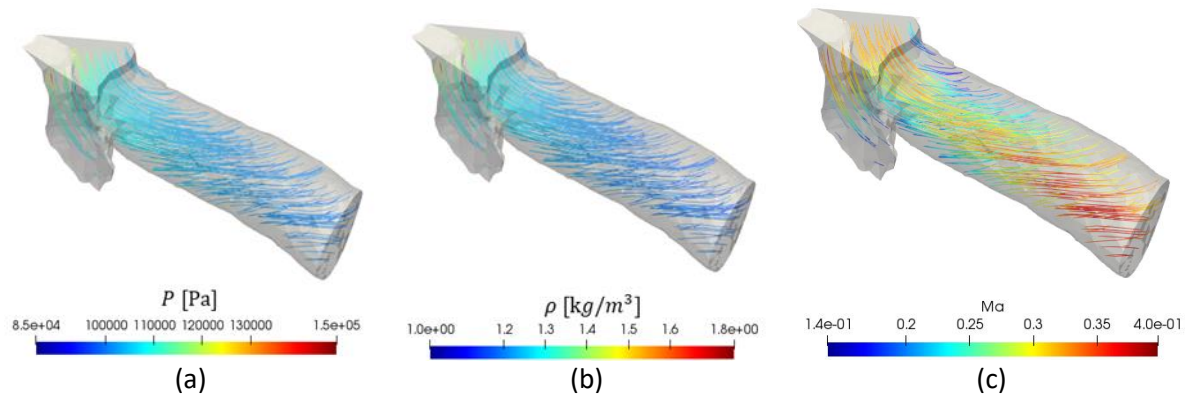
α_{start}	$\bar{V}_{fraction}$ [m ³ /m ³]	q	\bar{k}_u [kg/(m ³ s)]	\bar{k}_T [kg/(m K s ³)]	\bar{k}_R [kg/m ³ s]
0	0.33	0.1	4×10^4	2×10^4	1

Figure 82. (a) Optimized 3D straight blade rotor cavity at compressible turbulent subsonic regime (b) designed rotor, (c) convergence curve



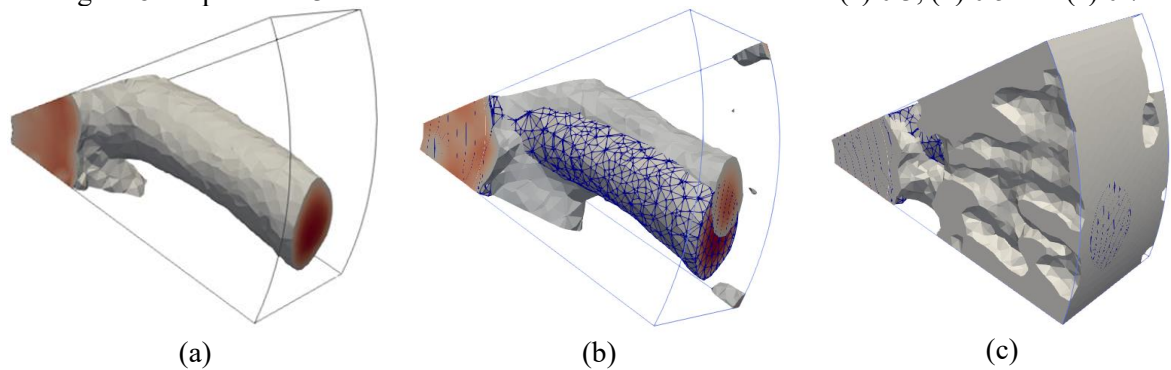
The current domain allows a well-defined optimization of the fluid cavity with a rotor topology overcoming the previous challenge. Figure 83 shows that the optimized rotor at compressible turbulent subsonic regime reaches a Mach number of 0.4 in the entire domain, where its large acceleration is found at the outlet region. The static pressure (Figure 83a) shows a decrease as the fluid flows to the outlet region, which behaviour is similar to the density field (Figure 83b) showing a 44.4% density variation in the whole domain.

Figure 83. Primal fields of optimized rotor under compressible turbulent subsonic regime: (a) pressure, (b) density and (c) Mach number distribution



Different tests are made varying the volume constraint (Figure 84), founding a smooth topology when the 0.3 volume fraction is tested.

Figure 84. Optimized 3D rotor under different volume constraints: (a) 0.3, (b) 0.5 and (c) 0.7



As seen, the study on different volume constraints is necessary to accurately select the optimized topology. Also, the start guess is fundamental to reaching the T.O. goal.

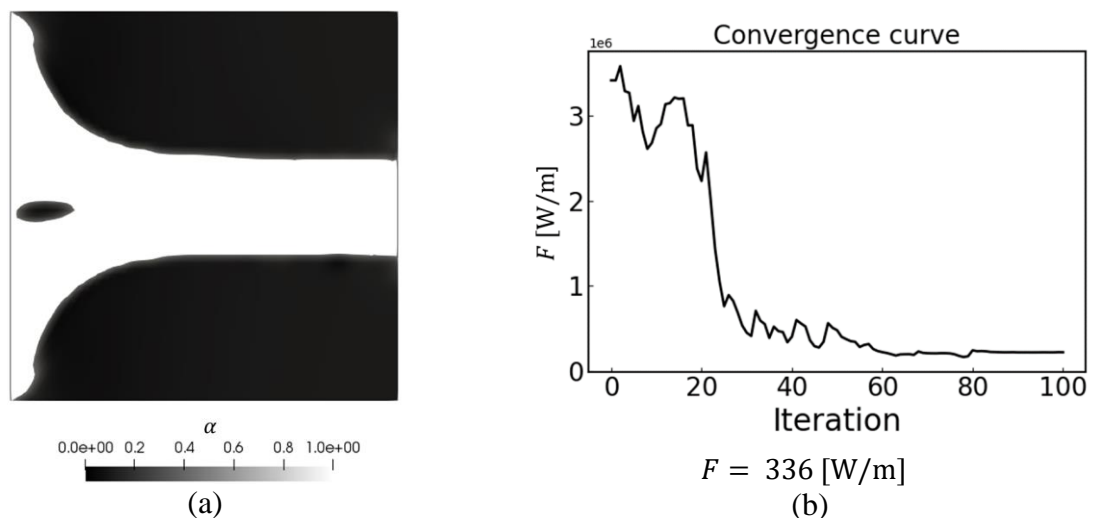
4.3. TOPOLOGY OPTIMIZATION OF COMPRESSIBLE TURBULENT SUBSONIC REGIME FOR REAL GAS CONSIDERING THE DISCRETE ADJOINT APPROACH

After presenting T.O. of compressible turbulent regime assuming perfect-ideal flows, the study is extended to the real gas modelling, where viscosity varies due to temperature interactions and the compressibility of the regime is considered. To do so, the state equations of the following cases include the compressibility factor based on the Peng-Robinson model (Eq.(66)). Also, the dynamic viscosity variation is quantified by Sutherland Law (Eq.(65)).

4.3.1. Converging Nozzle Example

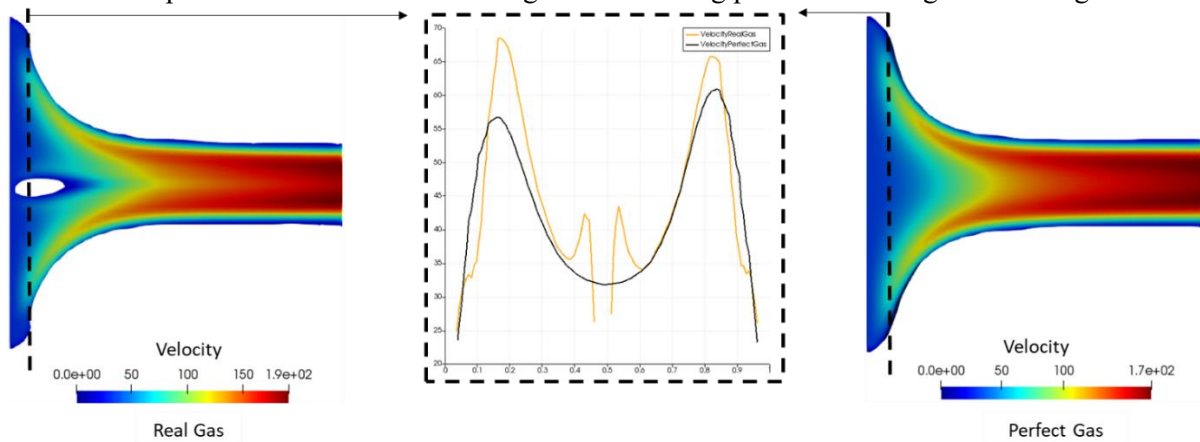
The case considers the Wray-Agarwal turbulence model and its fluid properties are $\mu = 0.03$ [Pa · s], $T_{inlet} = 298.15$ [K], $p_{totaloutlet} = 1 \times 10^5$ [Pa], resulting in a $Re_{inlet} = 1 \times 10^3$. Also, the optimization is performed with $\alpha_{start} = \bar{V} = 0.4$ [m³/m³], $\bar{k}_u = 2.5 \times 10^7$ [$\frac{kg}{m^3s}$], $\bar{k}_T = 1 \times 10^2$ [kg/(m K s³)] and $\bar{k}_R = 1.0$ [kg/m³s], resulting in the layout shown in Figure 85.

Figure 85. Optimized converging nozzle under compressible turbulent subsonic regime and real gas (b) convergence curve.



As seen, the real-gas-based solution can capture the inlet-guide vane, which was also found in the perfect gas solution at $Re_{inlet} = 5 \times 10^3$ (Figure 53). This implies, that the fluid flow is highly accelerated in the real-gas solution. To analyse further the implications, a cross-check validation is made between the perfect and the real-gas solutions (Figure 86).

Figure 86. Velocity field comparison between the optimized converging nozzle designed at compressible subsonic turbulent regime considering perfect and real gas modelling.



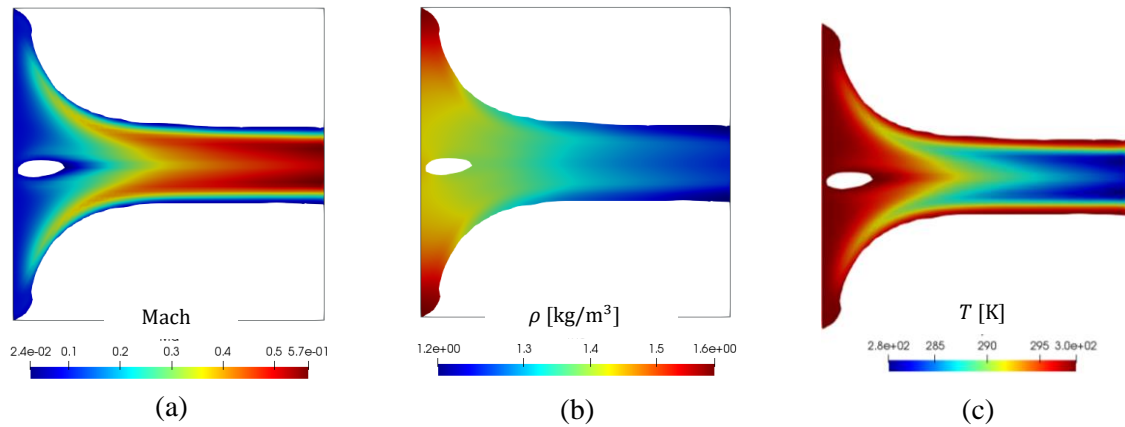
The influence of the real gas modelling and viscosity variation is depicted near the inlet section, where a solid region is created. Its effect can be seen at the velocity field cross-section, which is compared to the previous optimized converging nozzle designed for the perfect gas assumption (Figure 86). The objective function from the perfect gas solution ($F = 248.6$ [W/m]) underestimates the real-gas energy dissipation by 35.2% (Table 22).

Table 22. Cross-check validation between perfect and real gas assumption at optimized nozzle under compressible turbulent regime

Optimized case	Objective Function (F)
Nozzle under perfect gas assumption	248.6 [W/m]
Nozzle under real gas assumption	336.1 [W/m]

The solid region makes the fluid diverges into two paths, which causes an acceleration due to its cross-section reduction. As Figure 86 shows, the fluid peak velocity reaches a maximum of 190 [m/s], which overcomes by 10.5% of the calculated at perfect gas modelling. As seen, the real gas modelling influence is noticeable in the optimization layout. The characteristic flow fields (Figure 87) show that the compressible subsonic regime is reached with a peak Mach number of 0.57, and density variation of 25%, justifying the use of the developed compressible-based T.O. formulation.

Figure 87. Characteristic flow fields of optimized nozzle designed for compressible turbulent subsonic regime considering real gas modelling: (a) Mach, (b) density and (c) temperature distribution



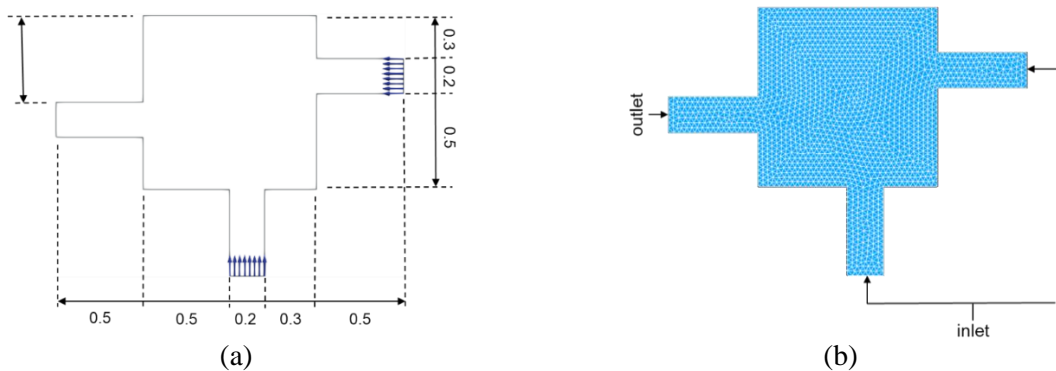
4.3.2. 2D pipe-joint Example

The 2D pipe-joint domain is discretised by 3×10^3 triangular prism (Figure 88a), and the fluid properties are $u_{inlet} = 30$ [m/s], $\mu = 0.03$ [Pa · s], $T_{inlet} = 298.15$ [K], $p_{total,outlet} = 1 \times 10^5$ [Pa], resulting in a $Re_{inlet} = 1 \times 10^3$. The optimization is performed by calibrating the T.O. parameters as Table 23 displays until a smooth optimized topology is reached (Figure 89).

Table 23. 2D pipe-joint optimization parameters for compressible turbulent subsonic flow.

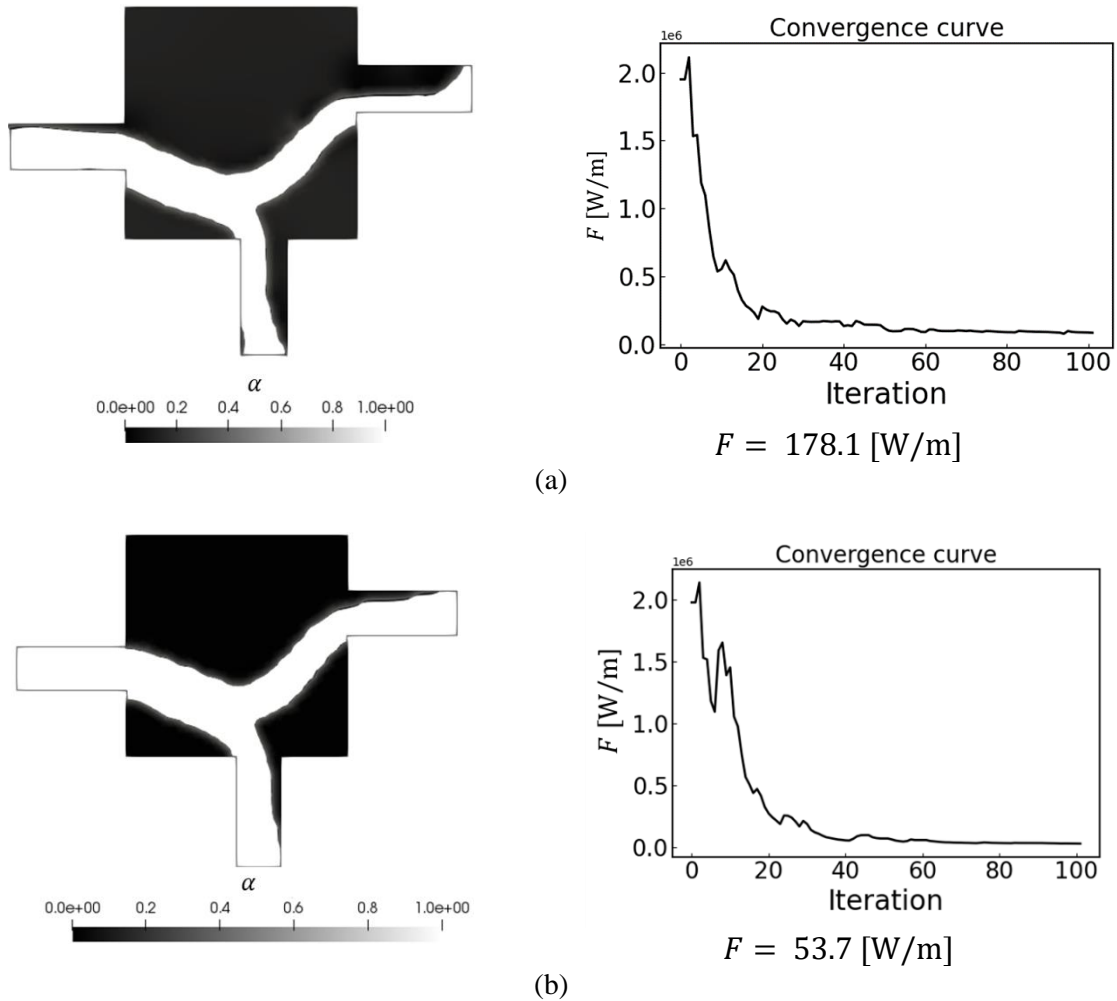
α_{start}	$\bar{V}_{fraction}$ [m ³ /m ³]	q	\bar{k}_u [kg/(m ³ s)]	\bar{k}_T [kg/(m K s ³)]	\bar{k}_R [kg/m ³ s]
0	0.33	0.1	4×10^4	2×10^4	1

Figure 88. (a) 2D pipe-joint domain and its (b) mesh discretization



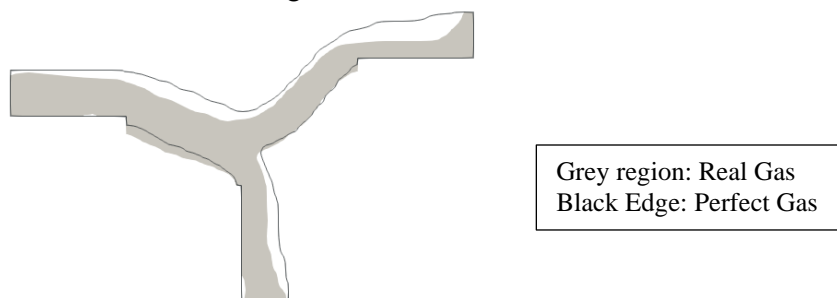
As seen, the two inlet boundaries generate a junction of the fluid path near the outlet region, which is optimized as well into a thinner outlet channel.

Figure 89. Optimized 2D pipe-joint domain under compressible turbulent regime considering (a) real (b) perfect gas modelling



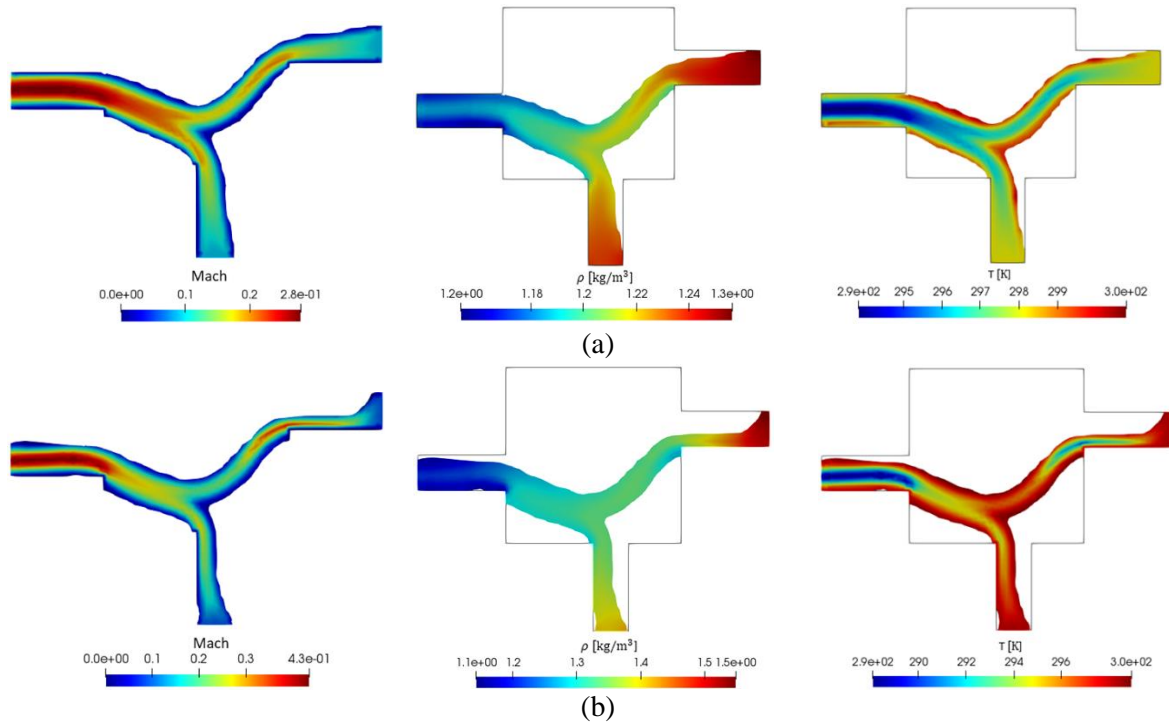
The influence of real gas modelling in the 2D pipe-joint case is checked by comparing its result with the perfect gas assumption (Figure 90). As seen, the real gas solution (Figure 89) is thinner in comparison to the perfect gas state topology layout. This channel thickness influences the objective function, where the perfect-gas solution is 69.8% less than the real-gas solution. The meaning of such different states is that perfect gas modelling underpredicts the real behaviour of the fluid flow, which could affect the real results from the theoretical modelling.

Figure 90. Optimized 2D pipe-joint topology layout comparison between the perfect and real gas modelling



The characteristic fluid flow fields (Figure 91) summarize the difference between the objective functions: at first, the perfect gas-based optimization (Figure 90a), underestimates the gradients of the fluid flow by giving a peak Mach number of 0.28, which is less than the real gas-based formulation of 4.3. Also, the density field comparison shows a 7.69% difference in the perfect gas-based modelling and a 41% difference in the real gas-based solution. The temperature gradient is similar, however, large values are found in the real-gas modelling than in the perfect-gas solution. All these variations consolidate the previous analysis stating that perfect gas optimization underestimates the real fluid flow behaviour at compressible turbulent subsonic flow.

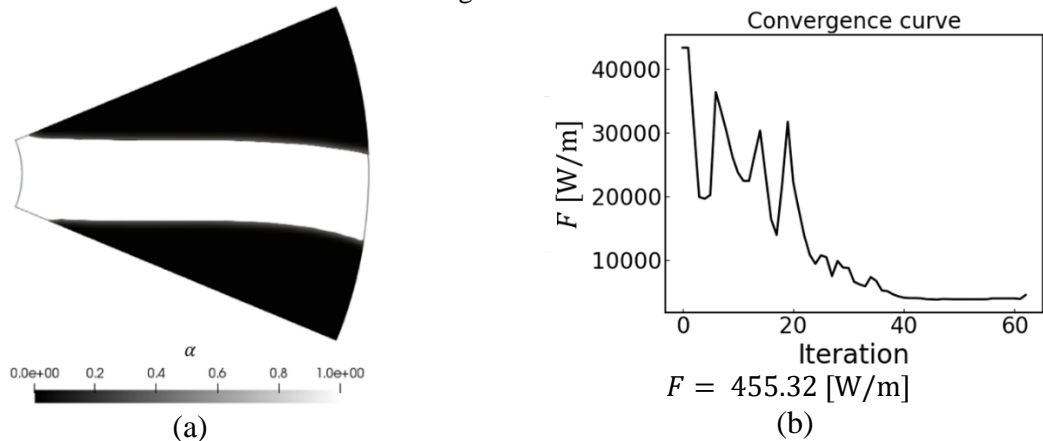
Figure 91. Primal fields of optimized 2D pipe-joint under compressible subsonic turbulent regime considering the (a) perfect gas and (b) real gas state equation.



4.3.3. Rotor Example

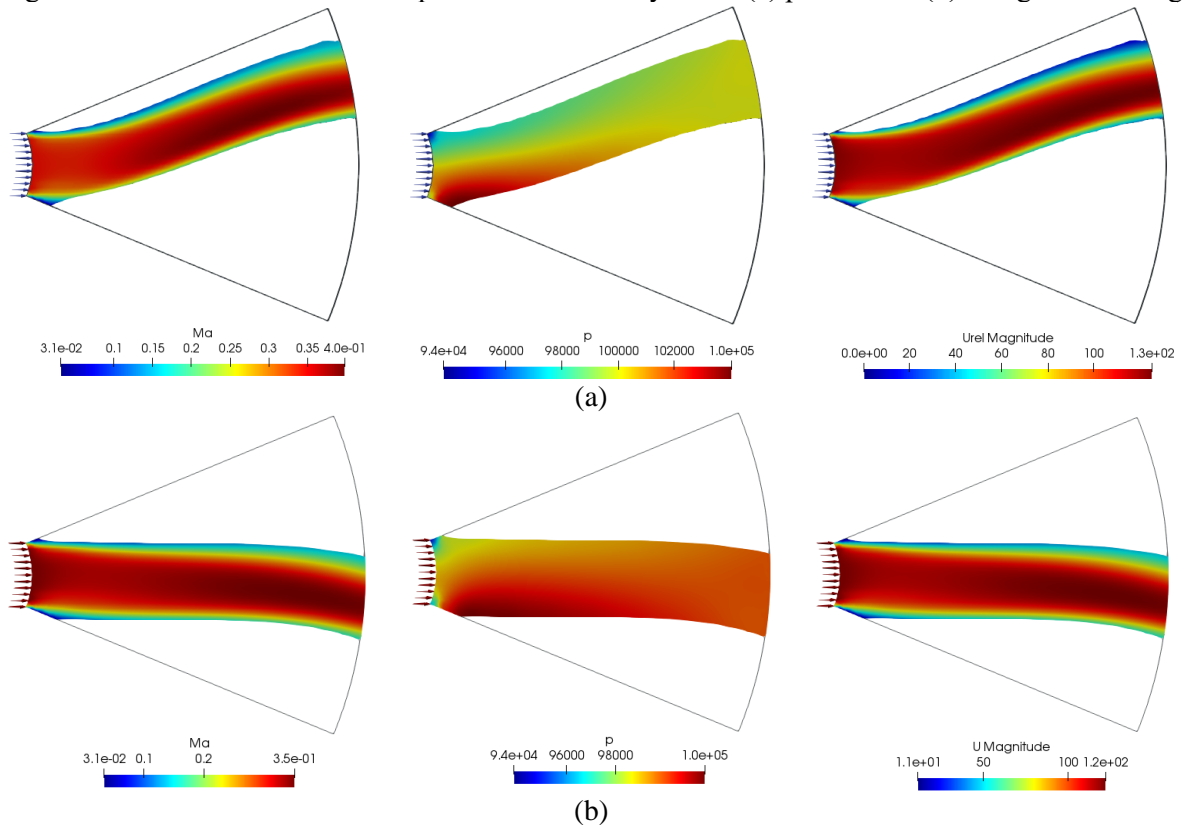
The viscosity variations due to temperature interactions and fluid compressibility are taken. The previous domain is tested under the same flow conditions, i.e. $n = 4 \times 10^3$ [rpm] and $\mu_{inlet} = 5 \times 10^{-4}$ [Pa · s]. The optimization is performed by calibrating the T.O. parameters to $\alpha_{start} = \bar{V} = 0.4$ [m³/m³], $\bar{k}_u = 8 \times 10^5$ [$\frac{kg}{m^3 s}$], $\bar{k}_T = 1 \times 10^2$ [kg/(m K s³)], $\bar{k}_\phi = 1$ [kg/m³s] and $\bar{k}_\Delta = 1 \times 10^{-5}$ [m⁻³], resulting in the optimized rotor of Figure 92.

Figure 92. Optimized rotor under compressible turbulent subsonic regime using real gas modelling (b) convergence curve.



In the current test, non-viscosity continuation is used and the topology does not show vortex generation at the fluid-solid interface as previous tests did (Figure 75), which proves an advantage of using the real gas behaviour. Also, the fluid domain is less sensitive to switching its direction to the pressure side of the rotor blade in comparison to the optimized rotor under perfect gas assumptions (Figure 77). This is adequate in terms of blade structure as a thin solid region is not desired for the blade construction. Despite the thickness of both fluid cavities seeming similar, the objective function difference is around 100% each, meaning that the fluid flow characteristics are not equal (Figure 93).

Figure 93. Flow characteristics of optimized rotor cavity under (a) perfect and (b) real gas modelling



As seen, the real gas flow characteristics are different from the perfect gas assumption. At first, it is fundamental seeing how the pressure distribution is underestimated in the perfect gas modelling, which could significantly impact the design of the rotor stress. Also, the velocity field is underestimated at the perfect gas modelling, giving a peak difference of 8% approximately. The total influence of each variable variation is seen at the Mach number distribution, with a 12.5% difference each.

5. CONCLUSIONS

Topology optimization at compressible turbulent subsonic regime is successfully achieved by considering the discrete adjoint approach from an automatic derivation algorithm. The automatic differentiation allows getting the adjoint model without hand derivation. The numerical results evaluate step by step the desired regime for topology optimization, starting with incompressible regime cases, going through a compressible turbulent approximation, and taking that result as an initial guess to consider the compressible turbulence phenomenon. By doing so, the generation of vortexes is diminished, and smooth topologies are found.

The topology optimization of incompressible turbulent rotating flow is achieved by considering the continuous adjoint approach, which is validated with literature cases and shows its computational cost advantages over the automatic differentiation. At laminar regime, the optimization parameters selection concerning the material distribution update is independent of the optimizer, both the CDV and IDV, respond accurately. Nevertheless, when the turbulence regime is analyzed, the use of IDV optimizer facilitates the optimization parameters selection due to its binary behaviour. Still, in some cases, the CDV optimizer presents smoother topologies layouts despite its difficulties in the T.O. parameter selection. The integer constraint in the IDV approach always leads to explicitly defined fluid-solid interfaces, showing to be convenient in turbulence modelling, such as for computing near-wall distance. For the nozzle case and the 3D pipe-joint example, the CDV optimizer presented a considerably lower computational cost. The CDV approach presented challenges related to optimization parameters calibration and the need for a continuation method, e.g. in the double channel case, the straight pipe solution could not be obtained with the CDV approach even after changing the optimization parameter values, while the IDV approach obtained the straight channels solution immediately. By using the continuation method, the CDV optimizer can reach a straight channel, and despite that, its objective function is larger than the one obtained by the IDV optimizer. In this sense, the IDV approach outperforms the CDV optimizer, mainly in terms of improved fluid-solid wall definition, independence of material penalization parameters and improved objective functions. During the straight blade rotor optimization, its influence becomes larger and changes the topology layout. Also, the use of the Spalart-Allmaras turbulence model becomes challenging as the Reynolds number increases at the rotational

domain, finding its limits to optimize topologies, and suggesting the use of new turbulence models adapted for rotational flow.

The compressible regime is tested firstly with 2D cases, presenting significant results: the converging nozzle portrays a case in which the turbulence does not highly affect the topology layout when compared to turbulence approximation, however, the fluid flow simulation varies significantly and the objective function differs around 40% when turbulence phenomenon is solved. The case is tested at different Reynolds numbers and fluid directors are found between the optimized topology, helping to accelerate the fluid flow. Also, it is found that considering a continuation method is appropriate for domains where the fluid flow faces abrupt changes in its direction to reach an optimized topology, e.g., the pipe-bend case. The topology layout is largely modified when the fluid flow becomes turbulent, and consequently its fluid solution too. Such influence in the turbulence modelling resolution is found too in the diffuser case, where not only the optimized topology layout at turbulent compressible subsonic conditions changes considerably, but also, the solution of the turbulence phenomenon can propose fluid director in the cross-section of the optimized diffuser. Then, the method is successfully applied to a 3D domain, which is compared to a baseline design, showing that the proposed method allows a 79.5% decrease in the energy consumption of a regular design. Simultaneously, the optimization of straight blade rotors in 2D and 3D domains is achieved. The centrifugal forces difficult the optimization parameters calibration, however, the continuation method allows a continuous smooth topology definition. The 3D analyzed domain is enlarged due to the wall boundaries, which were limiting the optimization process. The use of the Wray-Agarwal turbulence model allows the optimization at large rotational velocities than the Spalart-Allmaras turbulence model, as the use of cyclic boundaries instead of wall boundaries too. Finally, the real gas-based influence in the topology optimization of compressible turbulent subsonic flow is studied. The real gas-based formulation considers Peng-Robinson and Sutherland equation to model the compressibility and the viscosity variance due to temperature gradients. It is shown in each 2D case that the perfect gas modelling underestimates the real fluid flow behaviour in compressible turbulent subsonic regime. Large differences are found between the perfect and the real gas-based topologies at the objective function and its fluid flow characteristics, especially the sensitivity to include a fluid director in the cross-section at low Reynolds numbers. Therefore, this first study enhances the importance of using the real gas-based formulation in a compressible turbulent regime to accurately calculate the energy dissipation at the optimized domains.

In future work, the author suggests implementing near-wall mesh refinement with automatic distribution to improve the boundary layer definition. Such a study could improve the optimized topology definition by refining the solid/fluid boundaries section only and avoiding large computational costs. Also, the IDV optimizer presented an advantage over the CDV optimizer, therefore, it should be studied in the compressible turbulent subsonic regime. Another development to be performed is the inclusion of fluid-structure interaction in the rotor design could improve the presented optimization as the resonance frequencies should be avoided at the optimized rotor. Finally, it is suggested to couple large eddy simulations (LES) and direct numerical studies (DNS) in the analysis of turbulence phenomenon influence of topology optimization, as the resolution of the vortexes scales could locate splitters or fluid directors in regions where the vortexes have been averaged only.

6. BIBLIOGRAPHY

- Allmaras, S.R., Johnson, F.T., Spalart, P.R.: Modifications and clarifications for the implementation of the spalart-allmaras turbulence model. 7th Int. Conf. Comput. Fluid Dyn. ICCFD 2012. 9–13 (2012)
- Alnæs, M.S., Logg, A., Ølgaard, K.B., Rognes, M.E., Wells, G.N.: Automated adjoints for FEniCS and Firedrake. *ACM Trans. Math. Softw.* 40, 2018–2019 (2014).
<https://doi.org/10.1145/2566630>
- Alonso, D., Garcia Rodriguez, L.F., Silva, E.C.N.: Flexible framework for fluid topology optimization with OpenFOAM and finite element-based high-level discrete adjoint method (FEniCS / dolfin-adjoint). *Struct. Multidiscip. Optim.* 64, 4409–4440 (2021)
- Alonso, D., de Sá, L.F.N., Saenz, J.S.R., Silva, E.C.N.: Topology optimization based on a two-dimensional swirl flow model of Tesla-type pump devices. *Comput. Math. with Appl.* 77, 2499–2533 (2019). <https://doi.org/10.1016/j.camwa.2018.12.035>
- Alonso, D.H., Romero Saenz, J.S., Picelli, R., Silva, E.C.N.: Topology optimization method based on the Wray–Agarwal turbulence model. *Struct. Multidiscip. Optim.* 65, (2022).
<https://doi.org/10.1007/S00158-021-03106-8>
- Alonso, D.H., Saenz, J.S.R., Silva, E.C.N.: Non-newtonian laminar 2D swirl flow design by the topology optimization method. *Struct. Multidiscip. Optim.* 62, 299–321 (2020).
<https://doi.org/10.1007/S00158-020-02499-2/FIGURES/33>
- Alonso, D.H., Silva, E.C.N.: Topology optimization for blood flow considering a hemolysis model. *Struct. Multidiscip. Optim.* 63, 2101–2123 (2021). <https://doi.org/10.1007/S00158-020-02806-X/FIGURES/19>
- Alonso, D.H., Silva, E.C.N.: Topology optimization applied to the design of Tesla-type turbine devices. *Appl. Math. Model.* 103, 764–791 (2022).
<https://doi.org/10.1016/J.APM.2021.11.007>
- Alvarenga, M.A., Andrade, C.R., Zapparoli, E.L.: Compressible subsonic flow in gas turbine annular diffusers. *Int. Rev. Mech. Eng.* 10, 474–481 (2016).
<https://doi.org/10.15866/ireme.v10i7.8994>
- Arnold, D.N., Brezzi, F., Fortin, M.: A stable finite element for the stokes equations. *Calc.* 1984 214. 21, 337–344 (1984). <https://doi.org/10.1007/BF02576171>
- Bae, S.J., Ahn, Y., Lee, J., Kim, S.G., Baik, S., Lee, J.I.: Experimental and numerical investigation of supercritical CO₂ test loop transient behavior near the critical point operation.

Appl. Therm. Eng. 99, 572–582 (2016).

<https://doi.org/10.1016/J.APPLTHERMALENG.2016.01.075>

Baltadjiev, N.D., Lettieri, C., Spakovszky, Z.S.: An investigation of real gas effects in supercritical CO₂ centrifugal compressors,

<https://asmedigitalcollection.asme.org/turbomachinery/article/137/9/091003/380646/An-Investigation-of-Real-Gas-Effects-in>, (2015)

Borrvall, T., Petersson, J.: Topology optimization of fluids in Stokes flow. *Int. J. Numer. Methods Fluids*. 41, 77–107 (2003). <https://doi.org/10.1002/flid.426>

Brezzi, F., Fortin, M.: *Mixed and Hybrid Finite Element Methods*. Springer New York, New York, NY (1991)

Bueno-Orovio, A., Castro, C., Palacios, F., Zuazua, E.: Continuous adjoint approach for the spalart-allmaras model in aerodynamic optimization. *AIAA J.* 50, 631–646 (2012).

<https://doi.org/10.2514/1.J051307>

Cantwell, B.J.: Fundamentals of compressible flow. In: AA210A. p. 438. Stanford University (2018)

Copyright FEniCS Project: FunctionAssigner — FEniCS Project, <https://fenicsproject.org/olddocs/dolfin/1.4.0/python/programmers-reference/cpp/function/FunctionAssigner.html>

Deshazer, E.W.: An Evaluation of Turbulence Models for Subsonic Compressible Internal Flows, (2007)

Désidéri, J.A., Duvigneau, R.: Parametric optimization of pulsating jets in unsteady flow by multiple-gradient descent algorithm (MGDA). *Comput. Methods Appl. Sci.* 47, 151–169 (2019). https://doi.org/10.1007/978-3-319-78325-3_11

Dewar, B., Tiainen, J., Jaatinen-Värri, A., Creamer, M., Dotcheva, M., Radulovic, J., Buick, J.M.: CFD Modelling of a Centrifugal Compressor with Experimental Validation through Radial Diffuser Static Pressure Measurement. *Int. J. Rotating Mach.* 2019, (2019). <https://doi.org/10.1155/2019/7415263>

Dilgen, C.B., Dilgen, S.B., Fuhrman, D.R., Sigmund, O., Lazarov, B.S.: Topology optimization of turbulent flows. *Comput. Methods Appl. Mech. Eng.* 331, 363–393 (2018)(a). <https://doi.org/10.1016/j.cma.2017.11.029>

Dilgen, S.B., Dilgen, C.B., Fuhrman, D.R., Sigmund, O., Lazarov, B.S.: Density based topology optimization of turbulent flow heat transfer systems. *Struct. Multidiscip. Optim.* 57, 1905–1918 (2018)(b). <https://doi.org/10.1007/s00158-018-1967-6>

Duan, X.B., Ma, Y.C., Zhang, R.: Shape-topology optimization of Stokes flow via variational

- level set method. *Appl. Math. Comput.* 202, 200–209 (2008).
<https://doi.org/10.1016/j.amc.2008.02.014>
- Farrell, P.E., Ham, D.A., Funke, S.W., Rognes, M.E.: Automated derivation of the adjoint of high-level transient finite element programs. *SIAM J. Sci. Comput.* 35, 1–27 (2013).
<https://doi.org/10.1137/120873558>
- Feireisl, E.: Shape Optimization in Viscous Compressible Fluids *. *Appl Math Optim.* 47, 59–78 (2003). <https://doi.org/10.1007/s00245-002-0737-3>
- Ferreira, W.M., Silva, E., Deschamps, C.J.: A parametric optimization procedure for the suction system of reciprocating compressors. In: *IOP conference series: materials science and engineering*. p. 10 (2015)
- Fosas De Pando, M., Schmid ‡ A N, P.J., Lele, D.S.K.: Parametric sensitivity for large-scale aeroacoustic flows. In: *Proceedings of the summer program from the center for turbulent research*. p. 10 (2014)
- Fox, McDonald's, Pritchard, P., Leylegian, J.: *Introduction to fluid mechanics*. John Wiley & Sons Ltd. (2015)
- Funke, S.W.: *The automation of PDE-constrained optimisation and its applications*. (2012).
<https://doi.org/10.13140/2.1.3688.0967>
- Gaetani, P.: *Stator-Rotor Interaction in Axial Turbine: Flow Physics and Design Perspective*. In: *Aircraft Technology*. InTech (2018)
- Gatski, T., Sarkar, S., Speziale, C. eds: *Studies in turbulence*. (2019)
- Gersborg-Hansen, A., Sigmund, O., Haber, R.B.: Topology optimization of channel flow problems. *Struct. Multidiscip. Optim.* 30, 181–192 (2005). <https://doi.org/10.1007/s00158-004-0508-7>
- Giannakoglou, K.C., Papadimitriou, D.I., Papoutsis-Kiachagias, E.M., Kavvadias, I.S., Othmer, C.: *CONTINUOUS ADJOINT METHODS IN SHAPE, TOPOLOGY, FLOW-CONTROL AND ROBUST OPTIMIZATION* Open.
- Grigoriev, I.A.: *Turbulence modeling of compressible flows with large density variation*, (2016)
- Gunzburger, M.: *Perspectives in flow control and optimization*. Society for industrial and applied mathematics (2003)
- Guo, W.: *Centrifugal compressor return channel shape optimization using adjoint method*, (2013)
- Han, X., Rahman, M.M., Agarwal, R.K.: *Development and application of a wall distance free wray-agarwal turbulence model (Wa2018)*. *AIAA Aerosp. Sci. Meet.* 2018. 1–24 (2018).

<https://doi.org/10.2514/6.2018-0593>

Hanifi, A., Alfredsson, P., Johansson, A., Henningson, D. eds: Transition, turbulence and combustion modelling. In: ERCOFTAC. p. 540. , Stockholm (1998)

Haslinger, J., Mäkinen, R.A.E.: Introduction to shape optimization : theory, approximation, and computation. SIAM, Society for Industrial and Applied Mathematics (2003)

He, P., Mader, C.A., Martins, J.R.R.A., Maki, K.J.: DAfoam: An open-source adjoint framework for multidisciplinary design optimization with openFOAM. *AIAA J.* 58, 1304–1319 (2020). <https://doi.org/10.2514/1.J058853>

Iwakiri, K., Honda, H., Tmoita, I., Shiraishi, T.: Shape optimization of centrifugal compressor scroll for turbocharger using adjoint method. *Turbomach. Soc. Japan.* 48, 674–682 (2020)

Jameson, A., Alonso, J., Reuther, J., Martinelli, L., Vassberg, J.: Aerodynamic shape optimization techniques based on control theory. (1998). <https://doi.org/10.2514/6.1998-2538>

Jensen, M.D., Cowan, R.M., Steadman, E.N., Harju, J.A.: Opportunities and challenges associated with CO₂ compression and transportation during CCS activities. *Natl. Energy Technol. Lab.* 42 (2011)

Kaźmierczak, A., Sokolowski, J., Zochowski, A.: Drag minimization for the obstacle in compressible flow using shape derivatives and finite volumes. *Math. Control Relat. Fields.* 8, 89–115 (2018). <https://doi.org/10.3934/mcrf.2018004>

Kim, S.G., Lee, J., Ahn, Y., Lee, J.I., Addad, Y., Ko, B.: CFD investigation of a centrifugal compressor derived from pump technology for supercritical carbon dioxide as a working fluid. *J. Supercrit. Fluids.* 86, 160–171 (2014). <https://doi.org/10.1016/j.supflu.2013.12.017>

Koch, J.R.L., Papoutsis-Kiachagias, E.M., Giannakoglou, K.C.: Transition from adjoint level set topology to shape optimization for 2D fluid mechanics. *Comput. Fluids.* 150, 123–138 (2017). <https://doi.org/10.1016/j.compfluid.2017.04.001>

Kontoleonos, E.A., Papoutsis-Kiachagias, E.M., Zymaris, A.S., Papadimitriou, D.I., Giannakoglou, K.C.: Adjoint-based constrained topology optimization for viscous flows, including heat transfer. *Eng. Optim.* 45, 941–961 (2013).

<https://doi.org/10.1080/0305215X.2012.717074>

Kouhi Esfahani, M.: A contribution to the finite element analysis of high-speed compressible flows and aerodynamics shape optimization, <http://www.tdx.cat/handle/10803/129730>, (2013)

Kuckshinrichs, W.: Carbon capture, storage and use. Springer (2015)

Langlois, T.R., Winter, M., Marino, R.G., Fullmer, W.D., Lopez de Bertodano, M., Fullmer, W.D., Clause, A., Duponcheel, M., Mimouni, S., Fleau, S., Bartosiewicz, Y., ALMGREN,

- A.S., BELL, J.B., SZYMCZAK, W.G., Popinet, S.: Benchmark and Validation of open source CFD codes, with focus on compressible and rotating capabilities. *J. Comput. Phys.* 190, 1213–1227 (2016). <https://doi.org/10.1007/BF03192151>
- Lazarov, B.S., Sigmund, O.: Filters in topology optimization based on Helmholtz-type differential equations. *Int. J. Numer. Methods Eng.* 86, 765–781 (2011). <https://doi.org/10.1002/nme.3072>
- Ltd., C.© 2016-2017 O.: OpenFOAM user guide: Empty, <https://www.openfoam.com/documentation/guides/latest/doc/guide-bcs-constraint-empty.html>
- Ltd., C.© 2016-2017 O.: OpenFOAM - user guide: cyclic boundary condition, <https://www.openfoam.com/documentation/guides/latest/doc/guide-bcs-coupled-cyclic.html>
- Mitusch, S.K., Funke, S.W., Dokken, J.S.: dolfin-adjoint 2018.1: automated adjoints for FEniCS and Firedrake. *J. Open Source Softw.* 4, 1292 (2019). <https://doi.org/10.21105/JOSS.01292>
- Monge, B.: Design of supercritical carbon dioxide centrifugal compressors, (2014)
- Monje, B., Sánchez, D., Savill, M., Pilidis, P., Sánchez, T.: A Design Strategy for Supercritical CO₂ Compressors. *Proc. ASME Turbo Expo.* 3B, (2014). <https://doi.org/10.1115/GT2014-25151>
- Mortensen, M., Langtangen, H.P., Wells, G.N.: A FEniCS-based programming framework for modeling turbulent flow by the Reynolds-averaged Navier-Stokes equations. *Adv. Water Resour.* 34, 1082–1101 (2011). <https://doi.org/10.1016/j.advwatres.2011.02.013>
- Moscatelli, E., Alonso, D.H., de Sá, L.F.N., Picelli, R., Silva, E.C.N.: Topology optimisation for rotor-stator fluid flow devices. *Struct. Multidiscip. Optim.* 65, (2022). <https://doi.org/10.1007/S00158-022-03233-W>
- Munday, S.: Adjoint Spalart-Allmaras. In: *ICON*. pp. 1–20 (2010)
- NASA: Implementing Turbulence Models into the Compressible RANS Equations, <https://turbmodels.larc.nasa.gov/implementrans.html>
- Nejadali, J.: Shape optimization of regenerative flow compressor with aero-foil type blades using response surface methodology coupled with CFD. *Struct. Multidiscip. Optim.* 64, 2653–2667 (2021). <https://doi.org/10.1007/S00158-021-03020-Z/FIGURES/26>
- Nikaido, B.E., Murman, S.M., Garcia, J.A.: OpenFOAM simulations of atmospheric-entry capsules in the subsonic regime. *53rd AIAA Aerosp. Sci. Meet.* 1–14 (2015). <https://doi.org/10.2514/6.2015-0313>
- Ning, F., Xu, L.: Numerical Investigation of Transonic Compressor Rotor Flow Using an Implicit 3D Flow Solver With One-Equation Spalart-Allmaras Turbulence Model. In:

Proceedings of the ASME Turbo Expo. American Society of Mechanical Engineers Digital Collection (2014)

Okubo, C., Silva, E.C.N.: Topology optimization of incompressible and compressible rotating flows using a discrete adjoint approach, (2022)

Okubo, C.M., Sá, L.F.N., Kiyono, C.Y., Silva, E.C.N.: A discrete adjoint approach based on finite differences applied to topology optimization of flow problems. *Comput. Methods Appl. Mech. Eng.* 389, 114406 (2022). <https://doi.org/10.1016/j.cma.2021.114406>

OpenFOAM1912: OpenCFD Release OpenFOAM® v1912, <https://www.openfoam.com/releases/openfoam-v1912/>

Othmer, C.: A continuous adjoint formulation for the computation of topological and surface sensitivities of ducted flow. *Int. J. Numer. Methods Fluids.* 58, 861–877 (2008). <https://doi.org/10.1002/fld>

Papoutsis-Kiachagias, E.M., Giannakoglou, K.C.: Continuous adjoint methods for turbulent flows, applied to shape and topology optimization: industrial applications. *Arch. Comput. Methods Eng.* 23, 255–299 (2016). <https://doi.org/10.1007/s11831-014-9141-9>

Papoutsis-Kiachagias, E.M., Kontoleontos, E.A., Zymaris, A.S., Papadimitriou, D.I., Giannakoglou, K.C.: Constrained topology optimization for laminar and turbulent flows, including heat transfer. *Evol. Determ. Methods Des. Optim. Control.* (2011)

Park, J.H., Cha, J.E., Lee, S.W.: Experimental investigation on performance test of 150-kW-class supercritical CO₂ centrifugal compressor. *Appl. Therm. Eng.* 210, 118310 (2022). <https://doi.org/10.1016/J.APPLTHERMALENG.2022.118310>

Pecnik, Rene and Colonna, P.: Accurate CFD Analysis of a Radial Compressor Operating with Supercritical CO₂. In: *Supercritical CO₂ Power Cycle Symposium.* pp. 1–8 (2011)

Petit, O., Nilsson, H.: Numerical Investigations of Unsteady Flow in a Centrifugal Pump with a Vaned Diffuser. *Int. J. Rotating Mach.* 2013, 1–14 (2013). <https://doi.org/10.1155/2013/961580>

Picelli, R., Moscatelli, E., Yamabe, P.V.M., Alonso, D.H., Ranjbarzadeh, S., dos Santos Gioria, R., Meneghini, J.R., Silva, E.C.N.: Topology optimization of turbulent fluid flow via the TOBS method and a geometry trimming procedure. *Struct. Multidiscip. Optim.* 65, 1–25 (2022). <https://doi.org/10.1007/s00158-021-03118-4>

Picelli, R., Sivapuram, R., Xie, Y.M.: A 101-line MATLAB code for topology optimization using binary variables and integer programming. *Struct. Multidiscip. Optim.* 63, 935–954 (2020). <https://doi.org/10.1007/s00158-020-02719-9>

Pingen, G., Evgrafov, A., Maute, K.: Topology optimization of flow domains using the

lattice Boltzmann method. *Struct. Multidiscip. Optim.* 34, 507–524 (2007).

<https://doi.org/10.1007/s00158-007-0105-7>

Rahman, U.A., Mustapha, F.: Validations of OpenFOAM® steady state compressible solver rhoSimpleFoam. (2015). <https://doi.org/10.15242/iae.iae0215214>

Rinaldi, E., Pecnik, R., Colonna, P.: Steady State Cfd Investigation of a Radial Compressor Operating. 1–11 (2013)

Romero, J.S., Silva, E.C.N.: A topology optimization approach applied to laminar flow machine rotor design. *Comput. Methods Appl. Mech. Eng.* 279, 268–300 (2014).

<https://doi.org/10.1016/j.cma.2014.06.029>

Romero, J.S., Silva, E.C.N.: Non-Newtonian laminar flow machine rotor design by using topology optimization. *Struct. Multidiscip. Optim.* 55, 1711–1732 (2017).

<https://doi.org/10.1007/s00158-016-1599-7>

Sá, L.F.N., Okubo Jr., C.M., Nelli Silva, E.C.: Topology Optimization of Subsonic Compressible Flows. *Struct. Multidiscip. Optim.* 64, 1–22 (2021)(a)

Sá, L.F.N., Romero, J.S., Horikawa, O., Silva, E.C.N.: Topology optimization applied to the development of small scale pump. *Struct. Multidiscip. Optim.* 57, 2045–2059 (2018).

<https://doi.org/10.1007/s00158-018-1966-7>

Sá, L.F.N., Silva, E.C.N.: Topology optimization method applied to laminar flow machine rotor design (master's thesis). 115 (2016)

Sá, L.F.N., Yamabe, P.V.M., Souza, B.C., Silva, E.C.N.: Topology optimization of turbulent rotating flows using Spalart–Allmaras model. *Comput. Methods Appl. Mech. Eng.* 373, 113551 (2021)(b). <https://doi.org/10.1016/j.cma.2020.113551>

Samad, A., Kim, K.Y.: Shape optimization of an axial compressor blade by multi-objective genetic algorithm. In: *Proceedings of the Institution of Mechanical Engineers, Part A: Journal of Power and Energy*. pp. 599–611 (2008)

Sigmund, O., Petersson, J.: Numerical instabilities in topology optimization: A survey on procedures dealing with checkerboards, mesh-dependencies and local minima. *Struct. Optim.* 1998 161. 16, 68–75 (1998). <https://doi.org/10.1007/BF01214002>

Sivapuram, R., Picelli, R.: Topology optimization of binary structures using integer linear programming. *Finite Elem. Anal. Des.* 139, 49–61 (2018).

<https://doi.org/10.1016/j.finel.2017.10.006>

Souza, B.C., Yamabe, P.V.M., Sá, L.F.N., S. Ranjbarzadehá, Picelli, R., Silva, E.C.N.: Topology optimization of fluid flow by using integer linear programming. *Struct. Multidiscip. Optim.* (2020)

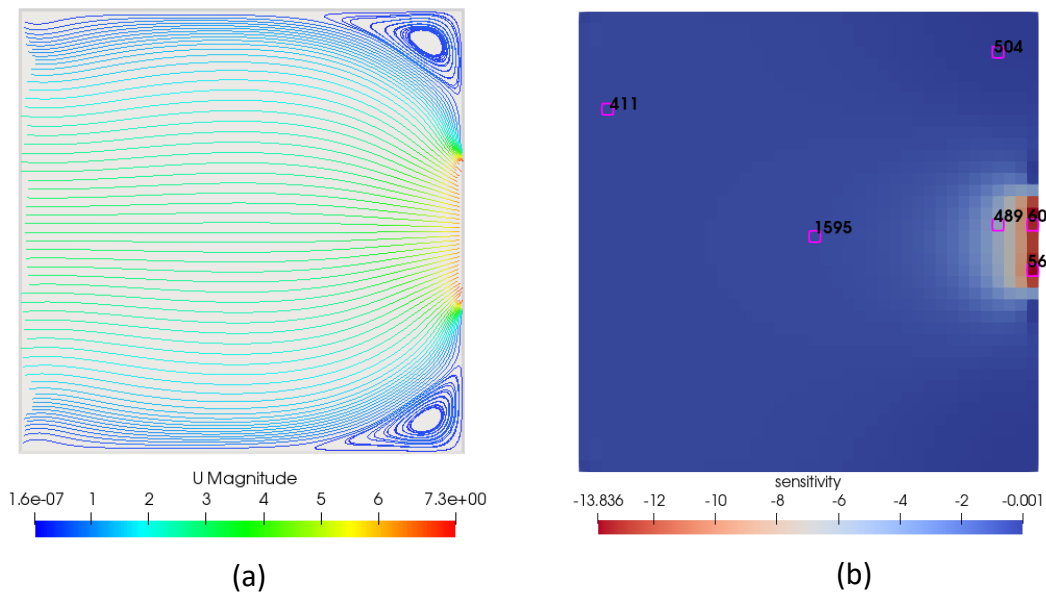
- Spalart, P.R., Allmaras, S.R.: A one-equation turbulence model for aerodynamic flows. *Am. Inst. Aeronaut. Astronaut.* 23 (1992)
- Svanberg, K.: The method of moving asymptotes - a new method for structural optimization. *Int. J. Numer. Methods Eng.* 24, 359–373 (1987)
- Systems, D. office of clean energy: Ramgen power systems. In: Headquarters, N. institute of standards and technology (ed.) *Workshop on Future Large CO₂ Compression Systems*. p. 14 (2009)
- Takagi, K., Muto, Y., Ishizuka, T., Aritomi, M., Kikura, H.: Research on Flow Characteristics of Supercritical CO₂ Axial Compressor Blades by CFD Analysis Kazuhisa. c, 1–8 (2016)
- Towara, M.: Discrete adjoint optimization with OpenFOAM. (2018)
- Tucker, P.G., Rumsey, C.L., Spalart, P.R., Bartels, R.E., Biedron, R.T.: Computations of wall distances based on differential equations. *34th AIAA Fluid Dyn. Conf. Exhib.* 43, (2004). <https://doi.org/10.2514/6.2004-2232>
- Tüzüner, B., Alpman, E., Kavurmacıoğlu, A.: Improved delayed detached eddy simulation of deep cavities at subsonic flow conditions. (2018)
- Vrionis, P.Y., Samouchos, K.D., Giannakoglou, K.C.: Topology optimization in fluid mechanics using continuous adjoint and the cut-cell method. *Comput. Math. with Appl.* 97, 286–297 (2021). <https://doi.org/10.1016/j.camwa.2021.06.002>
- Wachter, A., Biegler, L.: On the implementation of an interior-point filter line-search algorithm for large-scale nonlinear programming. *Math. Program.* 106, 25–57 (2006)
- White, F.M.: *Viscous Fluid Flow*. McGraw Hill (2006)
- Wilcox, D.C.: *Turbulence Modeling for CFD*. (1993)
- Yoon, G.H.: Topology optimization for turbulent flow with Spalart-Allmaras model. *Comput. Methods Appl. Mech. Eng.* 303, 288–311 (2016). <https://doi.org/10.1016/j.cma.2016.01.014>
- Yoon, G.H.: Topology optimization method with finite elements based on the k- ϵ turbulence model. *Comput. Methods Appl. Mech. Eng.* 361, 112784 (2020). <https://doi.org/10.1016/j.cma.2019.112784>

7. APPENDIX

7.1. Sensitivity Validation of the Continuous Adjoint Approach

In T.O., the sensitivity analysis must be validated to guarantee that the design variables are updated correctly. Thus, the sensitivity analysis is validated by comparing the results with the finite difference method, which is a well-established validation method used in T.O. (Dilgen et al. 2018a). The nozzle example presented by (Yoon 2016) is considered here, where boundary conditions and fluid properties are: $|\overline{u}_{inlet}| = 3$ [m/s], $\nu = 1 \times 10^{-3}$ [m²/s], $Re_{inlet} = 3 \times 10^3$. For this case, the velocity streamlines and the sensitivity field are shown at Figure 94.

Figure 94. Sensitivity analysis of the nozzle case: (a) Velocity streamlines and (b) Sensitivity field



Six random cells of the domain are chosen (Figure 94b) and compared to finite-difference calculation. By letting the primal and adjoint systems converge, an initial function value J_0 is obtained. A small perturbation value of the design variable $\Delta\alpha = 0.00001$ is introduced, and a new perturbed function value J is obtained. Both parameters are used to calculate an approximation of the derivative of the objective function considering a finite difference analysis.

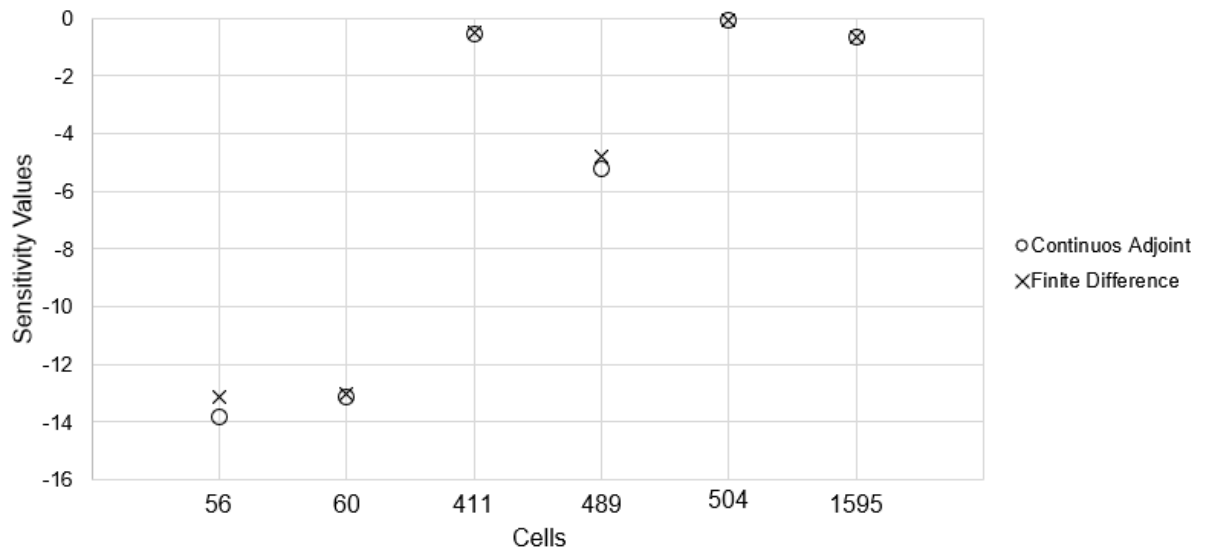
$$\frac{J - J_0}{\Delta\alpha} \cong \frac{\partial J}{\partial \alpha} \quad (109)$$

The objective function calculated without any perturbation is equal to $J_0 = 311.15$. The derivative values of the points shown in Figure 94b, can be seen in Table 24.

Table 24. Sensitivity analysis of the continuous adjoint approach

Design Variable α	Continuous Adjoint $\frac{\partial L_{aug}}{\partial \alpha}$	Perturbed Objective function J	Finite difference $\frac{J - J_0}{\Delta \gamma}$	Difference %
56	-13.8360	311.150575146041	-13.1471	4.98
60	-13.1358	311.150576200357	-13.0416	0.72
411	-0.5238	311.150701383527	-0.5233	0.10
489	-5.2027	311.150658704926	-4.7912	7.91
504	-0.07360	311.150705819222	-0.07976	7.76
1595	-0.6320	311.150700290584	-0.6326	0.10

Figure 95. Sensitivity validation graph of continuous adjoint approach

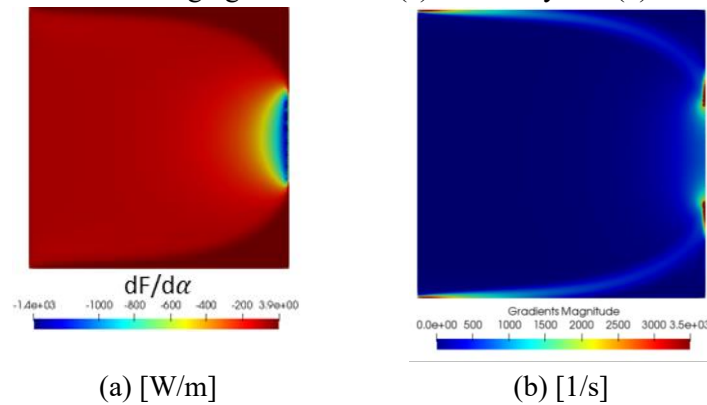


In Figure 95, the values of the second and fourth columns from Table 24 are plotted. Derivatives obtained by the continuous adjoint method implemented in this work are very close to those obtained by the finite difference method.

7.2. Sensitivity Validation Of The Discrete Adjoint Approach

The sensitivity analysis is performed by comparing the results with the finite difference method, which is commonly used in T.O. (Dilgen et al. 2018a). The converging nozzle case under turbulent compressible subsonic conditions (section 4.2.1) is analysed. The initial fluid design variable distribution is considered, and different points along the domain are chosen. The simulation is performed until the SIMPLE algorithm reaches 1×10^4 iterations.

Figure 96. Analysis of the converging nozzle case: (a) sensitivity and (b) velocity gradient field.



After the primal systems converge, an initial function value F_0 is obtained. A small perturbation value of the design variable is introduced ($\Delta\alpha = 1 \times 10^{-5}$), and a new perturbed function value F is obtained. Both parameters are compared via the backward difference scheme, which gives an approximation of the objective function derivative.

$$\frac{dF}{d\alpha} \cong \frac{F(\alpha) - F(\alpha - \Delta\alpha)}{\Delta\alpha} \quad (110)$$

The derivative values in the points shown in Figure 96b, calculated by the adjoint method, can be seen in Table 25.

Table 25. Sensitivity analysis – fluid domain

	Coordinates (x y)	dofin-adjoint $\frac{dF}{d\alpha}$ [W/m]	Finite differences $\frac{F(\alpha) - F(\alpha - \Delta\alpha)}{\Delta\alpha}$ [W/m]	Difference %
1	(0.3 0.25)	-112.23	-113.45	1.093
2	(0.3 0.3)	-112.26	-113.46	1.065
3	(0.3 0.5)	-112.77	-113.69	0.815
4	(0.5 0.5)	-130.49	-132.12	1.253
5	(0.7 0.4)	-178.76	-180.83	1.15
6	(0.9 0.5)	-529.99	-533.51	0.664

The derivatives obtained by the discrete adjoint method are close to those obtained by the finite difference method. The difference increases as the points move to the outlet region, where the fluid flow accelerates, and larger velocity gradients appear (Figure 96c).

7.2.1. Sensitivity validation considering real gas modelling

In this case, the converging nozzle case of section 4.3.1 is analysed. The initial solid design variable distribution is considered as the initial fluid design fluid flow modelling is sensitive to diverging at the first iterations. The sensitivity field is shown in Figure 97, and the simulation is performed until the SIMPLE algorithm reaches 1×10^4 iterations. The system considers the forward scheme approach and the perturbation value $\Delta\alpha = 1 \times 10^{-5}$.

$$\frac{dF}{d\alpha} = \frac{F(\alpha + \Delta\alpha) - F(\alpha)}{\Delta\alpha} \cong \frac{F - F_0}{\Delta\alpha} \quad (111)$$

Figure 97. Converging nozzle sensitivity field under the real gas assumption

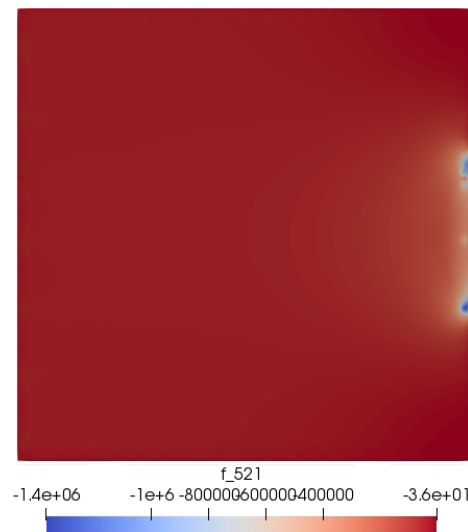


Table 26. Converging nozzle sensitivity validation under compressible turbulent subsonic regime and real gas behaviour

Sensitivity analysis – solid domain

	Coordinates (x y)	dolphin-adjoint $\frac{dF}{d\alpha}$ [W/m]	Finite differences $\frac{F(\alpha+\Delta\alpha)-F(\alpha)}{\Delta\alpha}$ [W/m]	Difference %
1	(0.3 0.25)	-42336.17	-40337.637	4.72
3	(0.3 0.5)	-44139.03	-42093.45	4.63
4	(0.5 0.5)	-47657.53	-45224.88	5.1
5	(0.5 0.3)	-44097.76	-41598.01	5.67
5	(0.7 0.4)	-59758.19	-54803.76	8.29
6	(0.9 0.5)	-13184.88	-120374.88	8.70

The derivative values of the random points are plotted in Table 26, which are compared and validated by the finite differences approach. As seen, the values are relatively close between the finite difference approach and the adjoint calculation, validating the real-gas implementation.

7.3. Derivation Of Weak Form Equations Used At The Discrete Adjoint Approach

Momentum equation:

$$\begin{aligned}
R_W^u &= \int_{\Omega} \left[\frac{\partial}{\partial x_j} (\bar{\rho} \tilde{u}_j \tilde{u}_i) + \frac{\partial}{\partial x_i} \bar{p} + \frac{\partial}{\partial x_j} (\overline{\rho u_i'' u_j''} - \bar{\sigma}_{ij}) + k_u \tilde{u}_i \right] w_{u_j} d\Omega \\
&= \int_{\Omega} \left[\frac{\partial}{\partial x_j} (\bar{\rho} \tilde{u}_j \tilde{u}_i) \right] w_{u_j} d\Omega + \int_{\Omega} \left[\frac{\partial}{\partial x_i} \bar{p} \right] w_{u_j} d\Omega + \int_{\Omega} \left[\frac{\partial}{\partial x_j} (\overline{\rho u_i'' u_j''} - \bar{\sigma}_{ij}) \right] w_{u_j} d\Omega + \int_{\Omega} [k_u \tilde{u}_i] w_{u_j} d\Omega \\
&= \int_{\Omega} \left[\frac{\partial}{\partial x_j} (\bar{\rho} \tilde{u}_j \tilde{u}_i) \right] w_{u_j} d\Omega + \int_{\Omega} \left[\frac{\partial}{\partial x_i} \bar{p} \right] w_{u_i} d\Omega + \int_{\Omega} \left\{ \frac{\partial}{\partial x_j} \left[(\mu - \mu_t) \left(\frac{\partial \tilde{u}_i}{\partial x_j} - \frac{2}{3} \delta_{ij} \frac{\partial \tilde{u}_k}{\partial x_k} \right) \right] \right\} w_{u_j} d\Omega + \\
&\quad \int_{\Omega} [k_u \tilde{u}_i] w_{u_j} d\Omega \\
&= \int_{\Omega} \left[\frac{\partial}{\partial x_j} (\bar{\rho} \tilde{u}_j \tilde{u}_i) \right] w_{u_j} d\Omega + \int_{\Omega} \left[\frac{\partial}{\partial x_i} \bar{p} \right] w_{u_i} d\Omega + \int_{\Omega} \left\{ (\mu - \mu_t) \frac{\partial}{\partial x_j} \left[\left(\frac{\partial \tilde{u}_i}{\partial x_j} - \frac{2}{3} \delta_{ij} \frac{\partial \tilde{u}_k}{\partial x_k} \right) \right] \right\} w_{u_j} d\Omega + \\
&\quad \int_{\Omega} [k_u \tilde{u}_i] w_{u_j} d\Omega \\
&= \int_{\Omega} \left[\frac{\partial}{\partial x_j} (\bar{\rho} \tilde{u}_j \tilde{u}_i) \right] w_{u_j} d\Omega + \int_{\Omega} \left[\frac{\partial}{\partial x_i} \bar{p} \right] w_{u_i} d\Omega + \int_{\Omega} \left\{ (\mu - \mu_t) \frac{\partial}{\partial x_j} \left(\frac{\partial \tilde{u}_i}{\partial x_j} \right) \right\} w_{u_j} d\Omega - \int_{\Omega} \left\{ (\mu - \right. \\
&\quad \left. \mu_t) \frac{\partial}{\partial x_j} \left(\frac{2}{3} \delta_{ij} \frac{\partial \tilde{u}_k}{\partial x_k} \right) \right\} w_{u_j} d\Omega + \int_{\Omega} [k_u \tilde{u}_i] w_{u_j} d\Omega \\
&= \int_{\Omega} \left[\frac{\partial}{\partial x_j} (\bar{\rho} \tilde{u}_j \tilde{u}_i) \right] w_{u_j} d\Omega + \int_{\Omega} \left[\frac{\partial}{\partial x_i} \bar{p} \right] w_{u_i} d\Omega - \int_{\Omega} \left\{ \left(\frac{\partial \tilde{u}_i}{\partial x_j} \right) \frac{\partial}{\partial x_j} w_{u_j} (\mu - \mu_t) \right\} d\Omega + \int_{\Gamma} \left\{ w_{u_j} (\mu - \right. \\
&\quad \left. \mu_t) \frac{\partial \tilde{u}_i}{\partial x_j} n_j \right\} d\Gamma + \int_{\Omega} \left\{ \frac{\partial}{\partial x_k} \tilde{u}_k \frac{\partial}{\partial x_k} \left[\frac{2}{3} \delta_{ij} (\mu - \mu_t) w_{u_j} \right] \right\} d\Omega - \int_{\Gamma} \left\{ \left[\frac{2}{3} \delta_{ij} (\mu - \mu_t) w_{u_j} \right] \frac{\partial}{\partial x_k} \tilde{u}_k n_k \right\} d\Gamma + \\
&\quad \int_{\Omega} [k_u \tilde{u}_i] w_{u_j} d\Omega = 0
\end{aligned}$$

Turbulence Model

$$\begin{aligned}
R_W^{\hat{v}} &= \int_{\Omega} \left(\rho u_j \frac{\partial}{\partial x_j} \hat{v} - \rho c_{b1} \hat{S} \hat{v} + \rho c_{w1} f_w \left(\frac{\hat{v}}{\Delta} \right)^2 - \frac{1}{\sigma} \left[\frac{\partial}{\partial x_j} \left(\rho (v + \hat{v}) \frac{\partial}{\partial x_j} \hat{v} \right) - \rho c_{b2} \frac{\partial^2 \hat{v}}{\partial x_i^2} \right] + k_{\hat{v}} \hat{v} \right) w_{\hat{v}} d\Omega \\
&= \int_{\Omega} \left(\rho u_j \frac{\partial}{\partial x_j} \hat{v} - \rho c_{b1} \hat{S} \hat{v} + \rho c_{w1} f_w \left(\frac{\hat{v}}{\Delta} \right)^2 \right) w_{\hat{v}} d\Omega - \int_{\Omega} \left(\frac{1}{\sigma} \left[\frac{\partial}{\partial x_j} \left(\rho (v + \hat{v}) \frac{\partial}{\partial x_j} \hat{v} \right) - \rho c_{b2} \frac{\partial^2 \hat{v}}{\partial x_i^2} \right] \right) w_{\hat{v}} d\Omega + \\
&\quad \int_{\Omega} (k_{\hat{v}} \hat{v}) w_{\hat{v}} d\Omega \\
&= \int_{\Omega} \left(\rho u_j \frac{\partial}{\partial x_j} \hat{v} - \rho c_{b1} \hat{S} \hat{v} + \rho c_{w1} f_w \left(\frac{\hat{v}}{\Delta} \right)^2 \right) w_{\hat{v}} d\Omega - \int_{\Omega} \left(\frac{1}{\sigma} \frac{\partial}{\partial x_j} \left(\rho (v + \hat{v}) \frac{\partial}{\partial x_j} \hat{v} \right) \right) w_{\hat{v}} d\Omega + \\
&\quad \int_{\Omega} \left(\frac{1}{\sigma} \rho c_{b2} \frac{\partial^2 \hat{v}}{\partial x_i^2} \right) w_{\hat{v}} d\Omega + \int_{\Omega} (k_{\hat{v}} \hat{v}) w_{\hat{v}} d\Omega
\end{aligned}$$

$$\begin{aligned}
&= \int_{\Omega} \left(\rho u_j \frac{\partial}{\partial x_j} \hat{v} - \rho c_{b1} \hat{S} \hat{v} + \rho c_{w1} f_w \left(\frac{\hat{v}}{\Delta} \right)^2 \right) w_{\hat{v}} d\Omega - \int_{\Omega} \left(\frac{1}{\sigma} \frac{\partial}{\partial x_j} \left(\rho (v + \hat{v}) \frac{\partial \hat{v}}{\partial x_j} \right) \right) w_{\hat{v}} d\Omega + \\
&\quad \frac{1}{\sigma} \rho c_{b2} \left[- \int_{\Omega} \left(\frac{\partial}{\partial x_i} \hat{v} \right) \frac{\partial}{\partial x_i} w_{\hat{v}} d\Omega + \int_{\Gamma} w_{\hat{v}} \frac{\partial}{\partial x_i} \hat{v} n_i d\Gamma \right] + \int_{\Omega} (k_{\hat{v}} \hat{v}) w_{\hat{v}} d\Omega = 0
\end{aligned}$$

Eikonal Equation

$$\begin{aligned}
R_W^{\Delta} &= \int_{\Omega} \left[\frac{\partial^2 G}{\partial x_i^2} + \sigma_w G \left(\frac{\partial^2 G}{\partial x_i^2} \right) - (1 + 2\sigma_w) G^4 - k_{\Delta} (G - G_0) \right] w_{\Delta} d\Omega \\
&= \int_{\Omega} \left[\frac{\partial^2 G}{\partial x_i^2} (1 + \sigma_w G) \right] w_{\Delta} d\Omega + \int_{\Omega} [-(1 + 2\sigma_w) G^4 - k_{\Delta} (G - G_0)] w_{\Delta} d\Omega \\
&= \int_{\Omega} \left[-\frac{\partial G}{\partial x_i} (1 + \sigma_w G) \right] \frac{\partial}{\partial x_i} w_{\Delta} d\Omega + \int_{\Gamma} w_{\Delta} \frac{\partial}{\partial x_i} [G(1 + \sigma_w G)] n_i d\Gamma - \int_{\Omega} [(1 + 2\sigma_w) G^4] w_{\Delta} d\Omega - \\
&\quad \int_{\Omega} [k_{\Delta} (G - G_0)] w_{\Delta} d\Omega = 0
\end{aligned}$$

Energy equation

$$\begin{aligned}
R_W^T &= \int_{\Omega} \left[\frac{\partial}{\partial x_j} (\tilde{u}_j \bar{\rho} \tilde{H}) - \frac{\partial}{\partial x_j} (\bar{\sigma}_{ij} \tilde{u}_i - \tilde{u}_i \overline{\rho u_i'' \rho u_j''}) - \frac{\partial}{\partial x_j} \left[-q_l - q_t + \left(\mu + \frac{\mu_t}{\sigma_k} \right) \frac{\partial}{\partial x_j} k \right] + k_T \left(\frac{\tilde{h}}{c_p} - \frac{\tilde{h}_{wall}}{c_p} \right) \right] w_T d\Omega \\
&= \int_{\Omega} \left[\frac{\partial}{\partial x_j} (\tilde{u}_j \bar{\rho} \tilde{H}) - \frac{\partial}{\partial x_j} (2S_{ij} (\tilde{u}_i \mu - \tilde{u}_i \mu_t) - \frac{\partial}{\partial x_j} \left[c_p \frac{\partial \tilde{T}}{\partial x_j} \left(\frac{\mu}{Pr} + \frac{\mu_t}{Pr_t} \right) + \left(\mu + \frac{\mu_t}{\sigma_k} \right) \frac{\partial}{\partial x_j} k \right] + \right. \\
&\quad \left. k_T \left(\frac{\tilde{h}}{c_p} - \frac{\tilde{h}_{wall}}{c_p} \right) \right] w_T d\Omega \\
&= \int_{\Omega} \left[\frac{\partial}{\partial x_j} (\tilde{u}_j \bar{\rho} \tilde{H}) - \frac{\partial}{\partial x_j} \left\{ 2 \left[\left(\frac{\partial \tilde{u}_i}{\partial x_j} \right) - \frac{2}{3} \delta_{ij} \frac{\partial}{\partial x_k} \tilde{u}_k \right] (\tilde{u}_i \mu - \tilde{u}_i \mu_t) \right\} - \frac{\partial}{\partial x_j} \left[c_p \frac{\partial \tilde{T}}{\partial x_j} \left(\frac{\mu}{Pr} + \frac{\mu_t}{Pr_t} \right) + \left(\mu + \frac{\mu_t}{\sigma_k} \right) \frac{\partial}{\partial x_j} k \right] + \right. \\
&\quad \left. k_T \left(\frac{\tilde{h}}{c_p} - \frac{\tilde{h}_{wall}}{c_p} \right) \right] w_T d\Omega \\
&= \int_{\Omega} \left[\frac{\partial}{\partial x_j} (\tilde{u}_j \bar{\rho} \tilde{H}) \right] w_T d\Omega - \int_{\Omega} \left[\frac{\partial}{\partial x_j} \left\{ 2 \left[\left(\frac{\partial \tilde{u}_i}{\partial x_j} \right) - \frac{2}{3} \delta_{ij} \frac{\partial}{\partial x_k} \tilde{u}_k \right] (\tilde{u}_i \mu - \tilde{u}_i \mu_t) \right\} \right] w_T d\Omega - \\
&\quad \int_{\Omega} \left\{ -\frac{\partial}{\partial x_j} \left[c_p \frac{\partial \tilde{T}}{\partial x_j} \left(\frac{\mu}{Pr} + \frac{\mu_t}{Pr_t} \right) + \left(\mu + \frac{\mu_t}{\sigma_k} \right) \frac{\partial}{\partial x_j} k \right] \right\} w_T d\Omega + \int_{\Omega} \left[k_T \left(\frac{\tilde{h}}{c_p} - \frac{\tilde{h}_{wall}}{c_p} \right) \right] w_T d\Omega
\end{aligned}$$

As the Spalart-Allmaras turbulence model is being considered, $\frac{\partial}{\partial x_j} k = 0$

$$\begin{aligned}
R_W^T &= \int_{\Omega} \left[\frac{\partial}{\partial x_j} (\tilde{u}_j \bar{\rho} \tilde{H}) \right] w_T d\Omega - \int_{\Omega} \left\{ \frac{\partial}{\partial x_j} (\tilde{u}_i \mu - \tilde{u}_i \mu_t) \frac{\partial}{\partial x_j} \left[\left(\frac{\partial \tilde{u}_i}{\partial x_j} \right) - \frac{2}{3} \delta_{ij} \frac{\partial}{\partial x_k} \tilde{u}_k \right] \right\} 2w_T d\Omega + \\
&\quad \int_{\Omega} \left\{ \frac{\partial}{\partial x_j} \left[\frac{\partial \tilde{T}}{\partial x_j} \left(\frac{\mu}{Pr} + \frac{\mu_t}{Pr_t} \right) \right] \right\} c_p w_T d\Omega + \int_{\Omega} \left[k_T \left(\frac{\tilde{h}}{c_p} - \frac{\tilde{h}_{wall}}{c_p} \right) \right] w_T d\Omega \\
&= \int_{\Omega} \left[\frac{\partial}{\partial x_j} (\tilde{u}_j \bar{\rho} \tilde{H}) \right] w_T d\Omega - \int_{\Omega} \left\{ \frac{\partial}{\partial x_j} (\tilde{u}_i \mu - \tilde{u}_i \mu_t) \right\} 2w_T d\Omega - \int_{\Omega} \left\{ \frac{\partial}{\partial x_j} \left[\left(\frac{\partial \tilde{u}_i}{\partial x_j} \right) \right] \right\} 2w_T d\Omega + \\
&\quad \int_{\Omega} \left\{ \frac{\partial}{\partial x_j} \left[\frac{\partial}{\partial x_k} \tilde{u}_k \right] \right\} \frac{4}{3} \delta_{ij} w_T d\Omega + \int_{\Omega} \left(\frac{\partial^2 \tilde{T}}{\partial x_j^2} \right) c_p w_T \left(\frac{\mu}{Pr} + \frac{\mu_t}{Pr_t} \right) d\Omega + \int_{\Omega} \left[k_T \left(\frac{\tilde{h}}{c_p} - \frac{\tilde{h}_{wall}}{c_p} \right) \right] w_T d\Omega
\end{aligned}$$

$$\begin{aligned}
&= \int_{\Omega} \left[\frac{\partial}{\partial x_j} (\tilde{u}_j \bar{\rho} \bar{H}) \right] w_T \, d\Omega - \int_{\Omega} \left\{ \frac{\partial}{\partial x_j} (\tilde{u}_i \mu - \tilde{u}_i \mu_t) \right\} 2w_T \, d\Omega + \int_{\Omega} \frac{\partial \tilde{u}_i}{\partial x_j} \frac{\partial}{\partial x_j} (2w_T) \, d\Omega - \int_{\Gamma} 2w_T \frac{\partial \tilde{u}_i}{\partial x_j} n_j \, d\Gamma - \\
&\quad \int_{\Omega} \frac{\partial}{\partial x_k} \tilde{u}_k \frac{\partial}{\partial x_k} \left(\frac{4}{3} \delta_{ij} w_T \right) \, d\Omega + \int_{\Gamma} \frac{4}{3} \delta_{ij} w_T \frac{\partial}{\partial x_k} \tilde{u}_k n_k \, d\Gamma - \int_{\Omega} \left(\frac{\partial \tilde{T}}{\partial x_j} \right) \frac{\partial}{\partial x_j} \left[c_p w_T \left(\frac{\mu}{Pr} + \frac{\mu_t}{Pr_t} \right) \right] \, d\Omega + \\
&\quad \int_{\Gamma} c_p w_T \left(\frac{\mu}{Pr} + \frac{\mu_t}{Pr_t} \right) \left(\frac{\partial \tilde{T}}{\partial x_j} \right) n_j \, d\Gamma + \int_{\Omega} \left[k_T \left(\frac{\tilde{h}}{c_p} - \frac{\tilde{h}_{wall}}{c_p} \right) \right] w_T \, d\Omega = 0
\end{aligned}$$